

SEPARATION OF ZIRCONIUM FROM COMPLEX MATRICES FOR ISOTOPE  
HARVESTING APPLICATIONS

By

JAKE BENCE

A dissertation submitted to the Graduate Faculty in Chemistry in partial  
fulfillment of the requirements for the degree of Doctor of Philosophy, The  
City University of New York

2023

© 2023

JAKE BENCE

All Rights Reserved

APPROVAL

Separation of Zr from Complex Matrices for Isotope Harvesting Applications

By

Jake Bence

This Manuscript Has Been Read and Accepted for The Graduate Faculty in  
Chemistry in Satisfaction of The Dissertation Requirement for the degree of  
Doctor of Philosophy, The City University of New York

Approved: September 2023

Lynn Francesconi, Chair of Examining Committee

Yolanda Small, Executive Officer

Supervisory Committee:

Jennifer Shusterman, Advisor

Lynn Francesconi

Melissa Deri

Benjamin Burton-Pye

THE CITY UNIVERSITY OF NEW YORK

# Abstract

Separation of Zr from Complex Matrices for Isotope Harvesting Applications

By

Jake Bence

Advisor: Dr. Jennifer Shusterman

Zr isotopes have various applications in nuclear science, such as  $^{86}\text{Zr}$  and  $^{89}\text{Zr}$  in nuclear medicine,  $^{88}\text{Zr}$  as a diagnostic isotope relevant to stockpile stewardship, and the fission product  $^{95}\text{Zr}$  useful as an s-process branch nucleus for study in astrophysics. To access these isotopes of interest, dedicated production methods and subsequent processing chemistry are required. Direct production routes can be technically challenging and difficult to obtain enough activity to meet demand. The processing chemistry of Zr isotopes is tedious due to the tendency for Zr to hydrolyze in solution without highly acidic conditions or a strong complexant. With the recent opening of the Facility for Rare Isotope Beams (FRIB), a new avenue is open to obtain Zr isotopes of interest in high yields from beam byproduct accumulation while avoiding hydrolyzing aqueous conditions.

During routine operation of the FRIB, radionuclides will accumulate in both the aqueous beam dump and along the beamline in the process of beam purification. These byproduct radionuclides, many of which are far from stability, can be collected and purified for use in other scientific applications in a process called isotope harvesting. In this work, the viability of

harvesting Zr isotopes from solid components was investigated using several different separation methodologies. Initial work focused on the demonstration of solid-phase harvesting from a secondary  $^{88}\text{Zr}$  beam generated at the National Superconducting Cyclotron Laboratory (NSCL) that was stopped in a series of collectors comprised of Al, Cu, W, and Au foils. Total recovery of  $^{88}\text{Zr}$  was over three times higher recovery than in a previous aqueous-phase harvesting experiment by using anion-exchange and solvent extraction techniques.

Further investigation into other separation methodologies for harvesting Zr at FRIB was conducted to increase the extraction efficiency and target short-lived isotopes of Zr. Due to the complex nature of bulk metal matrices containing radionuclides of Zr, purification methods need to be tested under conditions that are amenable to the isotope harvesting facilities present at FRIB. In this work, a TOPO impregnated resin was synthesized for application to solid-phase isotope harvesting of trace Zr from bulk metal matrices at FRIB.

The chemistry developed for harvesting of Zr was adapted to a supported liquid membrane (SLM) system using 3D-printed microfluidic modules. Performing Zr extractions on the microfluidic scale is a rapid and efficient separation method applicable to harvesting short-lived Zr. The utility of solid-phase isotope harvesting to access elements such as Zr that readily hydrolyze in near-neutral pH aqueous conditions has been demonstrated using several approaches for application to harvesting from solid components at FRIB.

## Acknowledgements

This work would not have been possible without the support of many people. First, I would like to thank my advisor Jennifer Shusterman, who has been such a valuable mentor and friend to me during my time in graduate school both at Hunter and at LLNL. Even through the pandemic, lab floods, and departure from CUNY, she made sure that I could keep moving forward. She has gone above and beyond for myself and her students, and for that I am so grateful.

I would like to thank Lynn Francesconi, who has graciously allowed me to work in her laboratory at Hunter and took over the role as my dissertation committee chair. Her guidance and generosity have helped immensely in making sure I can graduate on time. Thank you to my committee members Benjamin Burton-Pye and Melissa Deri. Their mentorship and positive attitudes throughout my time in graduate school at CUNY have been invaluable.

At LLNL, I would like to express my gratitude to the nuclear and radiochemistry group for not only hosting me as a student intern but for being a great pleasure to work with. Thank you to Tashi Parsons-Davis, John Despotopulos, Kelly Kmak, and Nicholas Scielzo for their contributions to the harvesting work, as well as their guidance during my time at LLNL. Thank you to Narek Gharibyan, Kevin Glennon, and Hector Valdovinos for teaching me about microfluidics work, providing troubleshooting help, and for their fun conversations in the lab. Special thanks go to Enrica Balboni and her student Liuba Williams for the BET analysis on my samples. Thank you to Rachel Lindvall for the ICP-MS analysis. Thank you to Keenan Thomas

and Todd Woody at the NCF for sample analysis, helping with my detector issues and answering the many questions I had with patience.

Thank you to the staff at BNL in MIRP for hosting Jen and I for a summer, including Cathy Cutler, Jasmine Hatcher-Lamarre, and Vanessa Sanders. Thank you to Lisa Muench and Johnathon Fitzsimmons for their help with the ICP-OES.

Thank you to Greg Severin, Kathi, Samridhi, and the many folks in Greg's group for ensuring we could still have a successful beamtime during the Covid-19 pandemic, and for being such excellent hosts during this stressful time. Thank you to Chirag Vyas for going above and beyond helping me with the writing and editing process. Thank you to the staff at the NSCL for providing beam for the harvesting experiment. Thank you to Eric Norman for use of his HPGe detector.

Thank you to my colleagues and friends both in the Shusterman and Francesconi groups and within CUNY that have made graduate school a little easier and a lot more fun. Ramsey, Chrissy, Rachel, Michael, Peña, Dinesh, Will and Shejla, without your support, I do not know how I would have made it through graduate school. Special thanks to Matthew Devany for helping me run NMR samples on a tight timeframe and while I was away at LLNL. Thank you to Sam Groveman from Medgar Evers College for ICP-OES analyses.

I would not have considered graduate school if not for my undergraduate mentors. While at NSU, Dimitri Giarikos was a crucial mentor to me, who introduced me to chemistry research and helped me navigate the graduate school application process. Thank you to Dimitri and Jaclynn Brant, who helped me secure an internship at ORNL and exposed me for the first time to a national laboratory environment. Thank you to my mentor Carter Abney at ORNL, who provided me with valuable advice during my time there. Without these people, I would not have pursued a PhD and made it to where I am today.

I cannot thank my parents and little sister Julianne enough for supporting me throughout graduate school. I moved far away from home, yet they still always encouraged me and were willing to help me during times of great stress.

Thank you to my best friend Adam for his endless support and willingness to proofread my writing, and our many good conversations to help decompress from graduate school.

Thank you to Li for her endless love and support these past five years. Since we first moved to NY together, she was always with me through the worst and best times of this journey, and I am forever thankful for our time together. Thank you to Hero for always being by my side and providing a nice distraction from writing, either by getting me outside to go on a walk or just accepting lots of pets.

This research is supported by the U.S. Department of Energy Isotope Program, managed by the Office of Science for Isotope R&D and Production under contract DE-SC0020161. This work was performed under the auspices of the U.S. Department of Energy by Lawrence Livermore

National Laboratory under Contract DE-AC52-07NA27344. At MSU, this work was supported by the Core R&D Support for Isotope Harvesting at FRIB as part of the DOE-SC-Isotope Program under Contract DE-SC0021220. This work is supported in part by the Horizon-broadening Isotope Production Pipeline Opportunities (HIPPO) program, under Grant DE-SC0022550 from the Department of Energy's Isotope R&D and Production Program.

The introduction and Chapter 1 were adapted from the previously published work by Bence, J. A.; Satija, S.; Domnanich, K. A.; Despotopulos, J. D.; Abel, E. P.; Clause, H. K.; Essenmacher, S.; Kalman, M.; Kleinfeldt, C.; Kmak, K. N.; et al. Solid-phase isotope harvesting of  $^{88}\text{Zr}$  from a radioactive ion beam facility. *Applied Radiation and Isotopes* **2022**, *189*, 110414. DOI: <https://doi.org/10.1016/j.apradiso.2022.110414>

## Contents

List of Tables .....	xiv
List of Figures .....	xv
List of Acronyms .....	xix
Project Goals .....	1
Introduction.....	1
Fundamentals of Isotope Production .....	1
Separation Chemistry Challenges with Isotope Production.....	6
Zr Isotopes .....	7
Isotope Production Facilities.....	8
Accelerators .....	8
Reactors .....	9
Radioactive Ion Beam Facilities .....	10
Isotope Harvesting .....	11
Isotope Harvesting Studies .....	13
Chemical Separation Techniques.....	15
Solvent Extraction .....	15
Ion-Exchange Chromatography .....	16
Solid-Liquid Extraction Chromatography .....	18
Microfluidics.....	19
Supported Liquid Membranes .....	20

Zr Chemistry .....	21
Zr Production and Separation techniques .....	23
Instrumentation .....	25
Gamma-Ray Spectroscopy .....	25
NaI Scintillation Detector .....	27
High Purity Germanium Detector .....	28
ICP-OES Analysis .....	29
Infrared Spectroscopy .....	30
NMR .....	30
Nitrogen Adsorption .....	34
Zr stock solutions .....	36
<sup>88</sup> Zr from LANL for Harvesting Chemistry Development .....	36
<sup>88</sup> Zr from NSCL .....	37
<sup>95</sup> Zr from Fission at LLNL .....	38
Chapter 1: Solid-Phase Harvesting of <sup>88</sup> Zr .....	39
Background .....	39
Chemistry Method Development .....	40
Al Harvesting Method Development .....	40
Cu Harvesting Method Development .....	42
Beam Product Predictions .....	46
Experimental .....	51
Materials and Supplies .....	51

Beamtime at NSCL.....	52
Beam Integration .....	55
Procedure .....	55
Separation of $^{88}\text{Zr}$ and $^{88}\text{Y}$ from Aluminum Foils.....	59
Separation of $^{88}\text{Zr}$ and $^{88}\text{Y}$ from Copper Foils.....	64
Results/Discussion .....	67
Post-Irradiation Analysis .....	67
Harvesting of $^{88}\text{Zr}$ and $^{88}\text{Y}$ from Aluminum foils .....	73
Harvesting of $^{88}\text{Zr}$ and $^{88}\text{Y}$ from Copper Foils .....	76
Conclusion.....	79
Chapter 2: Solid-Liquid Extraction of Zr.....	81
Motivation.....	81
Solvent Extraction Batch Studies.....	83
Studying effects of Acid Concentration .....	85
Effect of TOPO Concentration .....	91
Back Extraction studies .....	96
Extraction from Bulk Cu Solutions .....	99
Synthesis of TOPO Resin .....	104
Characterization of TOPO Resin .....	105
Infrared Spectroscopy .....	105
BET Surface Area.....	111
NMR Analysis .....	112

Batch Extractions of Zr Using TOPO Resin.....	118
Column Studies.....	122
Solid-Liquid Extraction of Zr .....	123
Solid-Liquid Extraction of Zr from Bulk Al.....	134
Solid-Liquid Extraction of Zr from Bulk Cu.....	138
Solid-Liquid Extraction of Zr from Bulk U.....	140
Conclusion .....	142
Chapter 3: Microfluidic SLM Zr separations.....	143
Motivation.....	143
SLM Platform Development.....	145
3D-Printed Modules.....	145
SLM Extraction Procedure .....	147
Materials .....	147
Procedure .....	148
SLM Extraction Parameter Testing .....	151
Adjustment of Feed Solution Acid Concentration.....	151
Matrix Effects .....	156
Separation of Bulk Zr.....	158
Separation from Bulk Cu .....	161
Separation from Bulk U and Fission Products.....	163
Screening Extractants.....	167
HDEHP Chemistry .....	167

Solvent Extraction Methods and Results .....	169
TOPO/HDEHP SLM Extractions .....	172
Kinetics .....	178
Extraction of Zr from Bulk Metals with TOPO and HDEHP .....	181
Separation from Bulk Al .....	181
Separation from Bulk Cu .....	182
Separation from Bulk U .....	184
Comparison to Other Zr Extraction Methods .....	186
Potential Applications .....	187
Conclusion and Future Work .....	188
References .....	191

## List of Tables

Table 1: Stable element impurities reported in $^{88}\text{Zr}$ stock solution, quantified by ICP-OES .....	37
Table 2: LISE ++ predicted ions and their transmission rates based on experimental parameters. .....	47
Table 3: Contents of each solid collector.....	54
Table 4: Associated peaks for Al precipitate and Al standard from IR spectra.....	61
Table 5: Predicted vs experimentally determined ion distribution rates in the Al collector stack. .....	68
Table 6: Experimentally determined total activity, number of atoms, and particle rates of $^{88}\text{Zr}$ for each collector stack. ....	69

Table 7: Total recovery yields for each separation of $^{88}\text{Zr}$ from bulk Al foils. ....	76
Table 8: Total recovery yields for each separation of $^{88}\text{Zr}$ from bulk Cu foils. ....	79
Table 9: Characteristic peaks from IR .....	108
Table 10: Dimensions and volume for each 3D printed half-module.....	146

## List of Figures

Figure 1: Photograph of the target endstation at the NSCL.....	53
Figure 2: (A) Back of the Cu collector. (B) Front side of the Cu collector .....	53
Figure 3: Calibration curve for Al collector irradiation.....	56
Figure 4: Calibration curve for Cu collector irradiation .....	57
Figure 5: Calibration curve for Au collector irradiation.....	58
Figure 6: IR Spectra of $\text{AlCl}_3 \cdot 6\text{H}_2\text{O}$ standard and Al precipitate .....	60
Figure 7: Schematic of the complete separation of $^{88}\text{Zr}$ and $^{88}\text{Y}$ from bulk Al foil. ....	63
Figure 8: Schematic of the complete separation for the extraction of $^{88}\text{Zr}$ and $^{88}\text{Y}$ from bulk Cu foil.....	66
Figure 9: HPGe $\gamma$ -ray spectrum of the Cu collector following removal from the target endstation. .....	70
Figure 10: Distribution of beam products in the Al collector in number of atoms, decay corrected to EOB. ....	71
Figure 11: Distribution of beam products in the Cu collector in number of atoms, decay corrected to EOB. ....	72

Figure 12: Sample elution curves from anion-exchange resin separation of $^{88}\text{Zr}$ from bulk Al in HCl.....	74
Figure 13: Elution curves from DGA resin separation of $^{88}\text{Y}$ from bulk Al in HCl.....	75
Figure 14: Elution curves from DGA resin for separation of $^{88}\text{Y}$ from bulk Cu in $\text{HNO}_3$ and HCl. ....	78
Figure 15: Zr extraction yields from varying HCl concentrations into 0.01 M TOPO in n-dodecane. ....	87
Figure 16: Zr extraction yields from varying $\text{HNO}_3$ concentrations into 0.01 M TOPO in n-dodecane. ....	88
Figure 17: General extraction mechanism for Zr by TOPO. ....	90
Figure 18: The effect of TOPO concentration on Zr extraction yields from 12 M $\text{HNO}_3$ . ....	93
Figure 19: A, top) The effect of TOPO concentration on distribution ratios for Zr extraction. ...	95
Figure 20: Log (D) vs Log [ $\text{HNO}_3$ ] with a linear trendline. ....	96
Figure 21: The percent of Zr back extracted into 1 M HCl vs initial TOPO concentration. ....	98
Figure 22: The percent of Zr back-extracted into 1 M HCl vs initial $\text{HNO}_3$ concentration. ....	99
Figure 23: Zr extraction yields from varying HCl concentration both with and without bulk Cu dissolved in solution. ....	101
Figure 24: Zr extraction yields from varying $\text{HNO}_3$ concentration both with and without bulk Cu dissolved in solution. ....	102
Figure 25: Effect of initial $\text{HNO}_3$ concentration on back extraction into 1 M HCl. ....	103
Figure 26: IR spectra of solid TOPO, XAD-7, TK200 resin, and synthesized resin.....	107
Figure 27: (A) Amberlite XAD-7 monomer structure adapted from specification sheet by Rohm and Haas. <sup>108</sup> (B) Chemical structure of TOPO molecule.....	109
Figure 28: $^{31}\text{P}$ solid-state NMR spectrum of XAD-7.....	115
Figure 29: $^{31}\text{P}$ solid-state NMR spectrum of TOPO resin .....	115

Figure 30: $^{13}\text{C}$ solid-state NMR spectrum of XAD-7 .....	117
Figure 31: $^{13}\text{C}$ solid-state NMR spectrum of TOPO resin .....	118
Figure 32: Batch extractions to study the kinetics of extraction using the TOPO resin. ....	121
Figure 33: TOPO resin extraction of $^{95}\text{Zr}$ compared to XAD-7 from HCl.....	126
Figure 34: TOPO resin extraction of $^{95}\text{Zr}$ compared to XAD-7 from $\text{HNO}_3$ . ....	127
Figure 35: $^{31}\text{P}$ NMR spectrum of 0.5 M TOPO in methanol solution .....	130
Figure 36: $^{31}\text{P}$ NMR spectrum of TOPO resin before (A) and after contact (B) with $\text{HNO}_3$ and HF .....	131
Figure 37: $^{13}\text{C}$ solid-state NMR spectrum of TOPO resin post-acid contact.....	133
Figure 38: $^{13}\text{C}$ solid-state NMR spectrum of TOPO resin post-acid contact.....	134
Figure 39: TOPO resin extraction of $^{95}\text{Zr}$ from a $\approx 1000$ ppm Al solution in $\text{HNO}_3$ . ....	136
Figure 40: TOPO resin extraction of $^{95}\text{Zr}$ from $\approx 8000$ ppm Cu solution in $\text{HNO}_3$ . ....	138
Figure 41: TOPO resin extraction of $^{95}\text{Zr}$ from a 36 ppm U solution in $\text{HNO}_3$ . ....	140
Figure 42: 3D-printed modules with both halves exposing the microchannels.....	147
Figure 43: A fully assembled SLM extraction with two syringe pumps. ....	151
Figure 44: Separation of $^{95}\text{Zr}$ and $^{95}\text{Nb}$ by adjustment of $\text{HNO}_3$ in the feed solution using 0.01 M TOPO in dodecane.....	156
Figure 45: Extraction yields of total Zr and Nb from Zr carrier and carrier free solutions. ....	161
Figure 46: $^{95}\text{Zr}$ yields in the strip solution with bulk Cu and 0.01 M TOPO. ....	163
Figure 47: Extraction yields of detected fission products in the strip solution.....	165
Figure 48: Structure of HDEHP.....	167
Figure 49: Structures of A) TEHA and B) TEHP.....	169

Figure 50: Solvent extractions from HNO <sub>3</sub> solutions with 0.01 M TOPO/0.03 M HDEHP and 0.03 M HDEHP in dodecane diluent. ....	171
Figure 51: Solvent extractions from HCl solutions with 0.01 M TOPO/0.03 M HDEHP and 0.03 M HDEHP in dodecane diluent. ....	172
Figure 52: Comparison of extraction with TOPO and TOPO/HDEHP from 6 M HCl feed and 775pm Zr traced with <sup>95</sup> Zr solution. ....	173
Figure 53: Comparison of extraction with TOPO and TOPO/HDEHP from 12 M HNO <sub>3</sub> feed and 775pm Zr traced with <sup>95</sup> Zr solution. ....	175
Figure 54: <sup>95</sup> Zr and <sup>95</sup> Nb recovery in the 0.1 M HNO <sub>3</sub> /0.1 M HF strip versus the feed solutions of either 6 M HCl or 8 M HNO <sub>3</sub> using TOPO/HDEHP extractants. ....	177
Figure 55: <sup>95</sup> Zr recovery in the 1 M HCl strip versus the flow rate using 0.01 M TOPO. ....	179
Figure 56: <sup>95</sup> Zr and <sup>95</sup> Nb recovery in the 0.1 M HNO <sub>3</sub> /0.1 M HF strip versus the flow rate using 0.01 M TOPO/0.03 M HDEHP extractants from an 8 M HNO <sub>3</sub> feed.....	180
Figure 57: Separation of <sup>95</sup> Zr and <sup>95</sup> Nb from a 500 ppm Al in 6 M HCl solution compared to a solution free of bulk metals.....	182
Figure 58: <sup>95</sup> Zr extraction from a 9870 ppm Cu solution with 0.01 M TOPO compared to 0.01 M TOPO/0.03 M HDEHP. ....	184
Figure 59: Separation of <sup>95</sup> Zr and <sup>95</sup> Nb from a bulk U matrix.....	186

# List of Acronyms

ALARA (As Low as Reasonably Achievable)

Becquerel (Bq)

Brookhaven Linac Isotope Producer (BLIP)

Brunauer, Emmett and Teller (BET)

Magic-angle spinning (MAS)

Coefficient of determination (COD)

Cross-polarization (CP)

Decontamination factor (DF)

Department of Energy Isotope Program (DOE IP)

Dioctylphosphine oxide (DOPO)

Distribution ratio (D)

End of bombardment (EOB)

Exotic Radionuclides from Accelerator Waste for Science and Technology (ERAWAST)

Facility for Rare Isotope Beams (FRIB)

Fluorinated ethylene-propylene (FEP)

Free induction decay (FID)

Bis(2-ethylhexyl) hydrogen phosphate (HDEHP)

High-Purity Germanium Detectors (HPGe)

Inductively Coupled Plasma Optical Emission Spectroscopy (ICP-OES)

International Union of Pure and Applied Chemistry (IUPAC)

Isotope Production Facility (IPF)

Lanthanide (LN)

Lawrence Livermore National Laboratory (LLNL)

Limit of detection (LOD)

Liquid nitrogen (LN<sub>2</sub>)

Los Alamos National Laboratory (LANL)

Magic angle spinning (MAS)

Michigan State University (MSU)

National Isotope Development Center (NIDC)

National Superconducting Cyclotron Laboratory (NSCL)

Nuclear Counting Facility (NCF)

Nuclear magnetic resonance (NMR)

Paul Scherrer Institute (PSI)

Polytetrafluoroethylene (PTFE)

Positron Emission Tomography (PET)

Radioactive ion beam (RIB)

Radiofrequency (RF)

Solvent impregnated resin (SIR)

Strip to feed ratio (S:F)

Supported liquid membrane (SLM)

Tributyl phosphate (TBP)

Trioctylphosphine oxide (TOPO)

Tris(2-ethylhexyl)amine (TEHA)

Tris(2-ethylhexyl)phosphate (TEHP)

Weight distribution ratio ( $D_w$ )

## Project Goals

The initial goal of this work was to investigate for the first time the efficacy of solid-phase isotope harvesting of Zr from a RIB. By creating a  $^{88}\text{Zr}$  beam at the NSCL and impinging it onto solid collectors made of common beamline materials, separation of the  $^{88}\text{Zr}$  can be performed on samples representing those that would be found on solid beamline components at FRIB. The results of this experiment offer a direct comparison to previous aqueous harvesting work of  $^{88}\text{Zr}$ , demonstrating the viability of solid-phase isotope harvesting for Zr from FRIB.

In addition to the solid-phase harvesting demonstration, efforts to improve and expand upon this work were performed by studying two other separation methods to separate Zr: (1) development of a TOPO based resin for solid-liquid extraction chromatography, and (2) investigation into the use of supported liquid membrane system for rapid chemical separation of Zr.

## Introduction

### Fundamentals of Isotope Production

Worldwide demand of isotopes for elements spanning the periodic table increases in tandem with the growth of fields such as nuclear medicine, stockpile stewardship, fundamental nuclear science, and more. The availability of isotopes is a significant challenge due to a wide variety of challenges associated with their production. The field of isotope production describes

the nuclear production and radiochemical purification of desired radionuclides for research and application. Notable challenges in isotope production include the need for specialized facilities, associated costs to produce isotopes of interest, finite shipping ranges from production locations for isotopes with short half-lives, and the limitations of production yields associated with the nuclear and chemical reaction. As a result, demand for many isotopes of interest have outpaced their availability. New methods of producing high yield and purity isotopes of interest are crucial to meet demand and require investment by both the government and private sector. For example, the Department of Energy Isotope Program (DOE IP) helps meet the needs for various isotopes by coordinating US national laboratories and the university laboratories to conduct both research and development and direct production of critical isotopes for availability to the scientific community.

Herein, a general overview of production of radionuclides, defined as a specific radioactive isotope of an element, is described. A radionuclide is often discussed in terms of its “activity,” or number of radioactive decays per second in units of becquerel (Bq). The relationship between activity and number atoms (N) is:

$$A = \lambda N$$

Where  $\lambda$  is the decay constant, which is related to the half-life for a given radionuclide by the equation:

$$\ln(2)/t_{1/2}$$

A radionuclide needs to be produced via a direct nuclear reaction, where a target material is irradiated with a projectile. Alternatively, the parent of a radionuclide can be produced and allowed to decay to the desired radionuclide. Nuclear reactions are processes described by the collision of a projectile and a target nucleus. This is denoted with the notation  $T(P, x) R$ , where  $T$  is the target nucleus,  $P$  the projectile,  $x$  the one or more emitted particles, and  $R$  the residual nucleus.<sup>1</sup> The probability of a reaction occurring is reported as a cross-sectional area in barns (b), where 1 barn is  $10^{-28} \text{ m}^2$ . Each specific nuclear reaction has an associated cross-section ( $\sigma$ ), or probability the reaction will occur. The relationship between a nuclear reaction cross-section and its production rate for a given set of irradiation parameters is shown below.

$$R = \frac{N\sigma\Phi}{t_{\text{irr}}}$$

Where  $R$  is the production reaction rate,  $N$  is the number of target atoms,  $\sigma$  is the cross-section at a particular energy,  $\Phi$  is the projectile flux (particles/cm<sup>2</sup>·s), and  $t_{\text{irr}}$  is the irradiation time.<sup>2</sup> This equation assumes no radioactive decay or limited availability of target material due to burnup, as well as a constant flux and energy for the projectile. For radioactive products, the radioactive decay of the produced radionuclide in an irradiation must be taken into consideration. Therefore, the equation below is used:

$$A = (\sigma n \Delta x \Phi)(1 - e^{-\lambda t})$$

Where  $A$  is the activity of the radionuclide at the end of irradiation in Becquerels (Bq),  $\Delta x$  is the target thickness (cm), and  $n$  is the density (atoms/cm<sup>3</sup>). The latter term ( $1 - e^{-\lambda t}$ ) describes the radioactive decay of the product, which is subtracted from the production rate in the first term. As

the decay term approaches 1 (where  $e^{-\lambda t} \rightarrow 0$ ), the maximum amount of activity for the reaction product is achieved, called the saturation activity. This value puts an upper limit on the amount of product radionuclide that can be produced and can be tuned to minimize contaminants of other side reaction products.

Specific activity, or amount of activity of the radionuclide compared to the total mass of that element in the sample, is reported typically in Bq/g.<sup>3</sup> Specific activity is time dependent due to radioactive decay, so reported values must indicate when the specific activity value was measured. Isotopic impurities in a sample behave the same chemically as the radionuclide of interest, therefore separation of the isotopes is extremely difficult. Isotopic impurities are mitigated by altering the production method since chemical processing is not possible. For example, some isotopic impurities can be other radioactive isotopes, so minimizing their co-production and/or allowing for time for them to decay (typically if the impurities half-lives are shorter than the target radionuclide) are viable options.

Accurate nuclear cross-section data is needed to explore optimal production pathways for a target radionuclide. Individual cross-section values for a specific nuclide describe the probability a specific nuclear reaction will occur at a given incident particle energy. Total cross-section values encompass all different types of exit channels for a given nuclide, including capture and scattering reactions. A limitation here is that many cross-section values on radioactive target nuclei are not experimentally measured, and thus predicted reaction rates rely on theoretically predicted values. If the isotopic composition of a target material is known, as well as the respective cross-sections for the potential nuclear reactions in an experiment, then the conditions can be optimized to

maximize production of the desired radionuclide and minimize co-production of contaminants. As such, careful target consideration and preparation is a necessity to help reduce the number of contaminants that can be produced as well as ensure maximum target radionuclide production.

The presence of stable isotopes of the same element as the radionuclide in the sample, referred to as “isotopic carrier” or “carrier” for short, can often make the radionuclide sample unsuitable for use in the desired application.<sup>4</sup> It is important to note that carrier can be elements other than the analyte, so the type of carrier present should be distinguished.

For example, production of  $^{44}\text{Ti}$  ( $t_{1/2} = 60$  years) is a useful method for generating  $^{44}\text{Sc}$  ( $t_{1/2} = 3.97$  hours) for use in nuclear medicine.  $^{44}\text{Ti}/^{44}\text{Sc}$  generators can be developed by eluting the nuclear medicine relevant  $^{44}\text{Sc}$  grown in from radioactive decay of  $^{44}\text{Ti}$ , which is bound to a column. The  $^{44}\text{Ti}$  can be produced once and last for many years, where it continually decays to the useful and short-lived  $^{44}\text{Sc}$ .  $^{44}\text{Ti}$  is typically produced by proton irradiation of natural Sc target by the reaction  $^{45}\text{Sc}(p,2n)^{44}\text{Ti}$ . For this reaction, favorable cross-sections of approximately 14-40 millibarns (mb) are achieved below 38 MeV proton energies, with a threshold energy of 13 MeV.<sup>5</sup>

<sup>6</sup> The  $^{44}\text{Ti}$  reaction product is chemically separated from the Sc target and used to generate carrier-free  $^{44}\text{Sc}$  through decay. Other methods of producing  $^{44}\text{Sc}$ , such as direct production using proton or deuteron irradiation on  $^{44}\text{Ca}$  targets tend to co-produce other isotopes of Sc, such as  $^{44\text{m}}\text{Sc}$  ( $t_{1/2}=58.6$  h). Direct production of  $^{44}\text{Sc}$  via (p,n) on  $^{45}\text{Sc}$  would not be desirable due to the presence of stable  $^{45}\text{Sc}$ , which is chemically inseparable and results in low specific activity  $^{44}\text{Sc}$ . Therefore these methods are not as favorable compared to the  $^{44}\text{Ti}$  generator method production of  $^{44}\text{Sc}$ .<sup>7,8</sup>

## Separation Chemistry Challenges with Isotope Production

Radiochemical separation of a target radionuclide includes challenges typical in chemistry, such as removal of impurities from the analyte, incorporation of it into a desirable chemical matrix, and proper characterization and quantification of both the analyte and other impurities. However, other factors specific to radiochemistry further complicate the production and purification of a radionuclide. Initially, physically producing the radionuclide is a challenge that requires specialized facilities, typically either accelerators for charged particle production pathways, or reactors for neutron production methods. Radionuclides can have half-lives anywhere from fractions of a second to many years, but many that have strong interest in research and application are anthropogenic with short half-lives that are not found in nature. Therefore, production methods need to be able to produce a radionuclide in sufficient quantity for its desired purpose, taking into consideration its decay time relative to the time needed for travel to the destination and time needed to use it. A workaround for this is to produce the parent radionuclide for the desired product, such as in the previous example with  $^{44}\text{Ti}/^{44}\text{Sc}$  generators.

One of the challenges associated with isotope production is the presence of stable isotopic impurities. For example, in biological studies or medical applications, where the environment is very sensitive to changes in concentration of a metal due to concentration of targeting moieties. If the specific activity is too low, then interfering effects of the stable element become more prominent, such as metal toxicity in the context of nuclear medicine, or self-absorption from sample mass when measuring emissions such as in alpha spectroscopy.

Another challenge in radiochemical separations is the low concentrations typical of radionuclides in a laboratory setting. The number of atoms of the radionuclide of interest is usually multiple orders of magnitude less than standard quantities of elements utilized in a chemistry laboratory. This equates to sub-micromolar or microgram quantities of material, referred to as “trace” amounts. At trace quantities, common chemical characterization methods cannot be used directly unless isotopic carrier is present in quantities above the limit of detection. With trace quantities, the chemical behavior of an element can differ compared to its known chemistry on macro quantities of that element. At trace scales, complex formation can differ from established macroscale chemistry, such as formation of monomeric species instead of polymeric species in solution. Other properties such as adsorption to surfaces, radiocolloid formation, or “carrying” with another species in solution present in macro amounts are typical of trace-scale radionuclides.<sup>9</sup>

## Zr Isotopes

Zr has several radioisotopes of interest in nuclear science, such as <sup>89</sup>Zr in positron emission tomography (PET),<sup>10</sup> <sup>86</sup>Zr as the radioactive parent to the PET isotope <sup>86</sup>Y,<sup>11</sup> and <sup>95</sup>Zr as an s-process branch-point nucleus.<sup>12</sup> <sup>88</sup>Zr ( $t_{1/2}$  = 83.4 days) is relevant for interpreting historic nuclear test data for stockpile stewardship, and it can be used as a tracer for studying Zr chemistry due to its suitable half-life and characteristic  $\gamma$ -ray emission.<sup>13, 14</sup>

<sup>88</sup>Zr is a neutron-deficient isotope that decays by electron capture to <sup>88</sup>Y ( $t_{1/2}$  = 106.63 days) and emits an intense 393 keV  $\gamma$ -ray (I = 97%).<sup>15</sup> Recently, <sup>88</sup>Zr was discovered to have one of the highest neutron-capture cross-sections ever measured.<sup>16</sup> Like the majority of radioactive nuclei,

there are limited cross-section data on  $^{88}\text{Zr}$  due in part to the difficulty in obtaining enough pure target material for a reliable measurement.

## Isotope Production Facilities

### Accelerators

Particle accelerators operate by using an externally applied magnetic field to direct charged particles, such as electrons, protons, deuterons, alpha particles, or heavier ionized atoms onto a target to induce nuclear reactions. In charged particle reactions, cross-section values are typically much lower than neutron-capture cross sections (example values for 1 MeV for  $Z \approx 20$ :  $\sigma < 1$  b versus  $\sigma < 10^4$  b, respectively).<sup>2</sup> The trend of reduced cross-section values for charged particle reactions is due to the need of the incident particle energy to overcome the coulomb barrier and induce a nuclear reaction. They are often used to produce proton-rich isotopes, as these reactions induce the expulsion of one or more neutrons, however charged particles can also be emitted. Types of particle accelerators used in isotope production include cyclotrons, synchrotrons, and linear accelerators. Target selection and design can help minimize the amount of stable isotopic carrier (if eventual application of the produced radionuclide needs to be carrier free or requires a minimum specific activity), facilitate chemistry post-irradiation, maximize production of the radionuclide, and lessen the co-production of contaminants.

Cyclotrons are often used for isotope production with charged particle reactions of light nuclei due to their lower cost and compact design, hence their prevalence in research institutions

and hospitals. The limitations here are that these lower energy cyclotrons can only accelerate light ions, typically protons, up to 20 MeV.<sup>17</sup> Other commercially available cyclotrons exist with available energies up to 100 MeV, however these have a much larger footprint and associated cost. Examples of production reactions induced by cyclotrons are of the form  $(p, xn)$  or  $(p, \alpha)$ , where  $x$  is usually 1 or 2 but can be larger, such as in high energy spallation processes. Cyclotrons that can accelerate ions heavier than protons, such as deuterons and  $\alpha$ -particles (up to ions of uranium) have been used, such as the recently decommissioned K500 and K1200 superconducting cyclotrons at the NSCL.

Linear accelerators typically offer higher energies and intensities than cyclotrons. In the US, these facilities are often at national laboratories, such as the Brookhaven Linac Isotope Producer (BLIP) at Brookhaven National Laboratory (BNL), which can accelerate protons up to 200 MeV with an intensity of 140  $\mu$ A. At the Isotope Production Facility (IPF) at Los Alamos National Laboratory (LANL), proton beams up to 100 MeV and 250  $\mu$ A can be generated.<sup>18</sup> The availability of high energy beams at these facilities make nuclear reactions such as spallation more accessible, while the high beam currents allow for large-scale radionuclide production. They routinely produce isotopes for research and applications, such as  $^{82}\text{Sr}/^{82}\text{Rb}$  generator system for Positron Emission Tomography (PET) in hospitals.<sup>18, 19</sup>

## Reactors

Nuclear reactors can produce controlled neutron fields in which a sample can be placed into to undergo neutron induced reactions. Since the coulomb barrier does not need to be overcome

for a neutron to approach a nucleus, neutron-capture cross section values trend higher than charged particle capture reactions. With reactor produced isotopes, neutron-capture reactions dominate, making neutron-rich isotopes more accessible. Reactors produce neutrons through fission, typically of  $^{235}\text{U}$ . A target can be placed inside a reactor surrounded by U fuel rods to be exposed to the neutron flux produced by the fission reactions. Here, neutrons are typically reflected by a light material such as graphite or Be to increase the neutron flux. The neutrons are strategically reflected to reduce their kinetic energy, typically into the thermal range ( $E_n = 0.025 \text{ eV}$ ) where their average energy matches the energy of the materials in their surroundings. In the thermal neutron energy range, the capture cross-section for the target material is typically larger by orders of magnitude than for higher energy neutrons, as slower neutrons interact more readily with other nuclei.

Using reactors for isotope production requires knowledge of the neutron capture cross-sections of the different nuclei present in the target material. A common neutron capture reaction is  $(n,\gamma)$ , where the target is typically a stable isotope. Emission of a charged particle is possible by formation of a compound nucleus with high enough energy for the charged particle to overcome the coulomb barrier, such as in  $(n,p)$  or  $(n,\alpha)$  reactions.<sup>20</sup>

### Radioactive Ion Beam Facilities

Radioactive ion beam (RIB) facilities generate beams of nuclides produced from fragmentation of stable ion beams for nuclear science research, especially for studying rare isotopes. In the US, The National Superconducting Cyclotron Laboratory (NSCL) and its

successor, the Facility for Rare Isotope Beams (FRIB) at Michigan State University (MSU), produce RIBs through the fragmentation of a stable heavy ion beam (the primary beam) accelerated into a light production target, such as beryllium. The resulting fragmentation products are transferred to an in-flight mass separator to select the desired secondary ions from the primary beam to be delivered to the user experiment, called the secondary beam. Through this process, a broad distribution of fragmentation products are deposited into a beam dump to fully stop the beam and contain the fragmentation products. At FRIB, this is a rotating water target that doubles as a cooling water loop, referred to as the aqueous beam dump.

### Isotope Harvesting

The process of collecting and purifying byproduct radionuclides from RIB facilities for other uses without interruption of the user experiment has been termed “isotope harvesting.” FRIB will produce a wider variety and greater quantity of radionuclides than the NSCL, offering the potential for an unprecedented supply of exotic radionuclides via isotope harvesting.

At FRIB, neutron-deficient isotopes of most elements up to uranium on the periodic table can be generated with beam intensities up to 400 kW and energies up to 200 MeV/nucleon.<sup>21</sup> This is driven by a linear accelerator prior to collision with a target to induce fragmentation. The large variety of fragmentation products generated through these high energy interactions will accumulate at various points within the accelerator. This provides an opportunity to access rare isotopes, many of which are not accessible through other means on Earth. Approximately 90% of the initial primary beam remains unreacted and will be deposited into the aqueous beam dump,

which is designed to capture the excess beam fragments for potential reuse.<sup>21, 22</sup> Aqueous-phase harvesting from the beam dump at FRIB may be challenging due to the large volume of water, wide range of elements present, high activity, and complex redox conditions characteristic of radiolysis in water. A study from Domnanich et al. demonstrated that the radiolytic products generated by irradiating the water in the beam dump with the remaining fragmented beam is lower than expected, but still should be taken into account for aqueous harvesting work.<sup>23</sup> Beam products will accumulate in locations other than the aqueous beam dump, such as beam stops, collimators, exhaust gas, and more.<sup>21</sup> This provides an opportunity for solid and gas-phase isotope harvesting, which may be more amenable options to target radionuclides with difficult aqueous chemistry.

Typical radionuclide production routes involve dedicated irradiations of target material with charged particles at a cyclotron or linear accelerator, or with neutrons at a nuclear reactor. Isotope harvesting at FRIB, however, is a means of production that will occur as a byproduct of other primary user experiments at the facility. FRIB is unique in its incorporation of isotope-harvesting facilities from initial construction; all other RIB facilities have retrofitted the capability to extract radionuclides from existing systems. For example, the Exotic Radionuclides from Accelerator Waste for Science and Technology (ERAWAST) initiative at the Paul Scherrer Institute (PSI), separated long-lived radionuclides from previously irradiated materials.<sup>24</sup> Example radionuclides include  $^{44}\text{Ti}$  from steel,<sup>25</sup>  $^7\text{Be}$  from cooling water,<sup>26</sup> and  $^6\text{Al}$ ,  $^{59}\text{Ni}$ ,  $^{44}\text{Ti}$ ,  $^{53}\text{Mn}$  and  $^{60}\text{Fe}$  from a proton-irradiated copper beam dump.<sup>27</sup> From tantalum and tungsten targets irradiated at the SATURNE II synchrotron of the Laboratoire National Saturne (LNS) at Saclay,  $^{36}\text{Cl}$ ,  $^{129}\text{I}$ ,  $^{146}\text{Sm}$ ,  $^{148}\text{Gd}$ ,  $^{150}\text{Gd}$  (only from tantalum) and  $^{154}\text{Dy}$  have been separated.<sup>28,29</sup> The purified

radionuclides were subsequently used for a variety of applications ranging from nuclear-data measurements to radiopharmaceutical studies.

### Isotope Harvesting Studies

Preliminary isotope harvesting efforts with aqueous matrices have been performed at the NSCL to prepare for harvesting from the aqueous beam dump at FRIB. To date, these experiments have targeted  $^{24}\text{Na}$ ,  $^{47}\text{Ca}/^{47}\text{Sc}$ ,  $^{48}\text{V}$ ,  $^{62}\text{Zn}$ ,  $^{67}\text{Cu}$ , and  $^{88}\text{Zr}$ .<sup>30-36</sup> Aqueous-phase isotope harvesting experiments conducted on  $^{88}\text{Zr}$  and  $^{48}\text{V}$  in near-neutral pH resulted in lower recovery yields than those of the other reported radionuclides.<sup>32,36</sup> Group IV and V elements, including Zr and V, tend to exhibit multiple oxidation states, complex speciation chemistry, and propensity to hydrolyze in aqueous solution, even in acidic matrices. These properties make harvesting isotopes of these elements from near-neutral pH aqueous environments more challenging. For example, V can exist in either cationic or anionic forms in near-neutral pH ranges.<sup>37, 38</sup> Zr readily hydrolyzes, forming inert hydroxide and oxyhydroxide complexes when in aqueous solutions.<sup>39-42</sup>

Solid-phase isotope harvesting is the process of recovering desirable beam fragmentation products from solid materials. It can be implemented in parallel to user experiments and aqueous-phase isotope harvesting at the beam dump. Solid-phase isotope harvesting avoids near-neutral pH aqueous conditions, thus making it desirable for harvesting hydrolysable species.

Isotope harvesting can provide a pathway to access radioactive nuclei that are otherwise difficult to produce, allowing for fabrication of radioactive target materials for subsequent nuclear-data measurements. Radionuclides will deposit at various points along the beamline depending

upon their location. As the beam travels downstream, isotopes are electromagnetically separated in-flight by differences in their magnetic rigidity. For example, near the fragmentation target where the primary beam is fragmented, a wide range of radionuclides up to the mass of the primary beam isotope are found. Moving downstream on the beamline, the mass ranges of radionuclides will narrow around the secondary beam from the mass separation process, resulting in higher relative amounts of isobars relative to the secondary beam. These isotopes may deposit in materials made of different elements, which may lend well to separation chemistry. Isotope harvesting from solid components could occur on a routine basis, where extended time passes before parts can be swapped out while the beam is offline. As such, radionuclides will accumulate over time in these components in measurable quantities, so that once harvesting chemistry is performed, up to mCi amount of activity of various isotopes will be present. For targeting isotopes with long half-lives, this can be an advantage as shorter-lived isotopes of the same element that co-deposit will decay away. For example, if harvesting  $^{88}\text{Zr}$ , isotopes like  $^{86}\text{Zr}$  ( $t_{1/2}= 16.5$  hours) and  $^{89}\text{Zr}$  ( $t_{1/2}=78.4$  hours) that deposit along with  $^{88}\text{Zr}$  will decay after several months of accumulation, while  $^{88}\text{Zr}$  remains. In this case, the challenge lies in separating trace amounts of  $^{88}\text{Zr}$  implanted in a bulk metal matrix. But the benefit is the reduced mass of stable Zr impurity compared to traditional Zr isotope production methods. Once purified from the solid components,  $^{88}\text{Zr}$  or other Zr isotopes of interest can be used for other experiments, such as nuclear cross-section measurements, without the need for dedicated production runs to create the isotope in sufficient quantity.

# Chemical Separation Techniques

## Solvent Extraction

Solvent extraction is a common separation technique where two immiscible liquids (typically one organic phase and the other aqueous) are mixed then separated to preferentially distribute an analyte into the organic phase. This is based on solubility of the analyte in the different phases and can be tuned to cause preferential extraction of the analyte while minimizing co-extraction of impurities. One way to quantify extraction efficiency at equilibrium is by using the distribution ratio (D), as shown in the following equation:

$$D = \frac{[A]_o}{[A]_a}$$

Where  $[A]_o$  = the concentration of the analyte (A) in the organic phase and  $[A]_a$  = the concentration of the analyte in the aqueous phase. A solvent extraction is considered suitable if the value for  $D > 1$ , indicating a majority of the analyte is preferentially soluble in the organic phase. Many factors can affect the distribution ratio, such as temperature, contact time, volume, interface volume, type of diluent, volume ratio of the two phases, pH, and complexants present. It is important to note that the organic phase diluent (the solvent in which the extractant is dissolved in) should be selected based on if it minimizes third-phase formation. Third-phase formation is a

stable emulsion that can form and dissolve the analyte after subsequent mixing of the organic and aqueous phases.

Extractants can be classified based on how they extract metal ion complexes; either by ion-exchange or via solvation. Some extractants form ions in solution, such as dissociation of hydrogens from functional groups, forming an anion. This anionic form can associate with cationic species into solution, pulling them into the organic phase. For example, acidic organophosphorus extractants such as HDEHP tend to dimerize, which can release a  $H^+$  and thus coordinate to a cationic metal. Ion-exchange interactions can be outer-sphere coordination processes, such as in extraction of anionic metal complexes by ion-pair formation with a cationic extractant.

In solvation, no ion formation occurs, but lone pair electrons on an extractant can form inner-sphere interactions with a metal center. Multiple extractant molecules can surround the metal center, increasing its solubility in the organic phase and facilitating phase transfer. One of the most widely studied solvating extractants is tributyl phosphate (TBP), commonly used for separation of U and Pu.<sup>43</sup>

### [Ion-Exchange Chromatography](#)

Chromatography is a separation technique based on the differing affinities species in solution will have for either a solid (stationary) or liquid (mobile) phase. In ion-exchange chromatography, the stationary phase contains charged functional groups that can interact with the oppositely charged ions in the mobile phase that pass through. Depending upon the strength of these interactions with ions in solution, the various ions in the mobile phase can be separated by

their elution time (or lack of elution due to strong binding). Ion-exchange chromatography can either be anion-exchange, where the stationary phase contains positively charged functional groups, or cation-exchange, where the stationary phase is negatively charged to exchange cations in the mobile phase. In some cases, a mixture of the two is used if purifying multiple ions from an eluent is required. Separations of multiple analytes can be performed using ion-exchange chromatography by selecting a stationary phase (typically a commercially available resin) that either will preferentially extract the ion of interest or impurities. Once a stationary phase is selected, then mobile-phase conditions can be adjusted to favorably extract or elute analytes present in the mixture based off their solution chemistry. By adjusting the pH or ionic strength of the mobile phase, the complex formation of the analyte can be altered to change its affinity to the resin and affect elution. Introducing other ions can cause competition with the stationary phase functional groups, releasing the analyte if bound or reducing the chance for it to interact with functional groups on the resin.

In the context of radionuclide separations, the analyte is often present in trace quantities. Therefore, factors such as column capacity, or the maximum amount (such as the theoretical maximum number of moles) a given analyte can be sorbed to the resin, are usually negligible. But given that trace scale radionuclides are often present within a matrix of one or more bulk metals, the capacity factor must be considered, amongst other factors. Theoretical maximum capacity for an ion-exchange resin to uptake a given metal ion can be approximated with the following equation:

$$\frac{[M] * \text{charge}}{\text{column capacity factor} \left( \frac{\text{meq}}{\text{mL}} \right)} = \text{Ion - Exchange Resin capacity}$$

Where [M] is the concentration of the ion in millimole per milliliter, charge is the ionic charge assuming 100% of the analyte present is in this form, or the average charge of multiple charge states present. The column capacity factor is a published value for a resin that is equivalent to the number of ions that can be exchanged per mL volume of resin. Milliequivalents (meq) is the millimole equivalent to H<sup>+</sup> ions, hence the correction in the numerator with the charge of the analyte present to determine the number of ion exchanges that can occur. For example, the published meq/mL value for Dowex 1x8 anion-exchange resin in Cl<sup>-</sup> form used in this work is 1.2 meq/mL. The resin capacity calculated using this equation is the theoretical amount of resin needed for a given analyte concentration. In practicality, this amount is much higher, where a typical ion-exchange column separation uses at least 5 times the calculated volume of resin for one analyte to concentrate analyte and minimize tailing.

### Solid-Liquid Extraction Chromatography

Extraction chromatography operates on a similar premise as ion-exchange chromatography, except for instead of purely ionic interactions, an extractant ligand is used to complex metal species in the mobile phase. Extraction chromatography resins contain an extractant on an inert solid support, such as on fine resins or porous beads. The extractant can be chemically bound to the support, such as through an organic linker, or by physisorption, where the extractant is only held in place by intermolecular forces such as Van der Waals forces or hydrogen bonding. Extraction chromatography can be advantageous over solvent extraction in some cases due to the

much higher surface area availability of the stationary phase, which allows for more exposure of the analyte in the mobile phase to the extractant. Extraction chromatography offers the benefit of producing no mixed organic and aqueous waste while streamlining a separation process compared to solvent extractions. Extraction chromatography resins can be stable in various conditions, depending upon the solubility of the extractant in the mobile phase and chemical resistance to wide pH ranges.

### Microfluidics

Microfluidics is the process of flow chemistry on a micro-scale for a variety of applications. Similar to solvent extraction, microfluidic processes are interface driven processes. They offer an advantage compared to traditional solvent extractions because much higher surface area to volume ratios can be achieved.<sup>44</sup> Additionally, microfluidic processes are attractive for reasons such as low sample volume requirements, enhanced mass transfer, continuous mode of operation, chemical waste reduction, limiting radiation exposure as part of the ALARA principle (As Low as Reasonably Achievable), and reduced cost for specialized facilities.<sup>45</sup> Microfluidic processes allow for processes to be integrated into small systems, which offers benefits such as running multiple processes in parallel, or even adaptation to automation. With automation, reproducibility is more consistent due to the lack of human involvement, which helps increase experiment reliability and product output in radiochemical processes, such as commercial isotope production processes. This has a wide range of utility, such as employing microfluidic processes in laboratory environments to save space and resources dedicated to radiochemical procedures. For example, in a radioisotope production environment, a process can be scaled down to the microfluidic scale, freeing up space

in a fume hood or hot cell, as well as reducing the total amount of required time and cost to carry out the procedure. For facilities where strict quality control procedures must be followed, this can help increase reproducibility of the analyte, especially if adapted for automation.<sup>46-48</sup> The disadvantages here are that solutions of high mass may be restricted by their solubility limit on the microscale and could dictate scale-down feasibility. Solutions of volumes exceeding the  $\mu\text{L}$  regime may require longer separation times or faster flow rates, making the separation impractical. In radiochemistry, small volumes are often desirable and thus make microfluidic separation processes ideal if feasible.

### Supported Liquid Membranes

The use of Supported liquid membranes (SLMs) in metal ion separations are alternatives to traditional separation techniques where factors such as effectiveness at nonequilibrium conditions and combining the extraction and stripping reactions into one step are desirable.<sup>49</sup> In an SLM, a liquid organic containing dissolved extractant(s) is immobilized on an inert microporous membrane support, then two aqueous phases flow over either side both sides. One aqueous phase contains the feed solution and one the strip solution, analogous to the same in solvent extraction. SLMs can be divided into two classes, either flat sheet or hollow fiber type SLMs. In this work, flat sheet type SLMs are utilized in a counter current flow pattern. The aqueous “feed” solution contains analytes and other impurities flow over the top of the membrane to facilitate extraction of the analyte into the organic phase. The aqueous strip solution flows in the opposite direction underneath the membrane, back-extracting analytes from the membrane. Unlike in standard solvent extraction processes, extraction, and back extraction in the SLM occurs simultaneously.

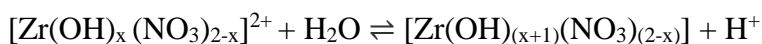
Extractions using SLMs often provide much higher interfacial surface area, which improves extraction efficiency compared to traditional solvent extraction.

## Zr Chemistry

Zr is a group IV element with an electron configuration of  $[\text{Kr}] 5s^2 4d^2$ , where it exists only as the  $\text{Zr}^{4+}$  oxidation state in solution.  $\text{Zr}^{4+}$  has a coordination number of 8 and ionic radius of 0.84 Å.<sup>50</sup> Zr is a hard Lewis acid due to its high charge density, therefore it forms strong complexes with hard Lewis bases. This causes Zr to have high oxophilicity, tending to form an oxide or oxyhydroxide complex that is often insoluble in solution. Aqueous chemistry of Zr is complex, where factors such as acid type and concentration, Zr concentration, and ionic strength all play a role in the predominant form of Zr in solution. Solutions of Zr typically require highly acidic environments to prevent hydrolysis, often only reversible by addition of fluoride ion. Free  $\text{Zr}^{4+}$  in solution can partially hydrolyze, even in mildly acidic conditions, forming species such as  $\text{ZrOH}^{+3}$ ,  $\text{Zr}(\text{OH})^{+2}$ , and  $\text{Zr}(\text{OH})_3^+$ .<sup>40,51</sup> In the presence of a strong acid, such as HCl, Zr can exist in several forms depending on the acid concentration. In HCl concentrations of 0.6-2 M, Zr primarily exists as the tetramer  $[\text{Zr}_4(\text{OH})_8(\text{H}_2\text{O})_{16}]^{+8}$ . Below the 0.6 M acid threshold, the octamer  $[\text{Zr}_8(\text{OH})_{20}(\text{H}_2\text{O})_{24}]\text{Cl}_{12}$  predominates.<sup>52</sup> Over time, Zr under these conditions will polymerize and precipitate as zirconyl chloride/zirconium oxychloride,  $[\text{Zr}_4(\text{OH})_8(\text{H}_2\text{O})_{16}]\text{Cl}_8 \cdot 12\text{H}_2\text{O}$ . However, the precise structure of other extensive Zr polymers has not been fully identified, nor is the mechanism of formation well understood.<sup>39, 41, 53, 54</sup>

Under 6 M HCl, cationic Zr complexes are the primary species in solution. Zr coordinated to various combinations of hydroxyl or water molecules exist in combination with strong anions like Cl<sup>-</sup>, which are in competition for formation of inner sphere complexes with Zr.<sup>53</sup> In this example the coordinating water molecules are gradually replaced with Cl<sup>-</sup> as the HCl concentration increases, such as [Zr(H<sub>2</sub>O)<sub>5</sub>Cl<sub>3</sub>]<sup>+</sup> or [Zr(OH)<sub>2</sub>Cl]<sup>+</sup>. Between 6-7 M HCl, the dominant form of Zr in solution are neutral complexes, such as [Zr(H<sub>2</sub>O)<sub>4</sub>Cl<sub>4</sub>].<sup>55</sup> Beyond 7 M HCl, anionic complexes of Zr dominate.<sup>42</sup> This trend follows with increasing acidity, where the polymers break down and the replacement of bridging or singular hydroxyl groups occurs with Cl<sup>-</sup>. In concentrated HCl, Zr will primarily exist as [ZrCl<sub>6</sub>]<sup>2-</sup>. Over time, the hydroxyl bridges present in the polymer structures can convert to oxo bridges, reducing the reactivity and solubility of the complex. Outside of highly acidic environments, this can cause further polymerization of Zr.

The trend for Zr complexation in HNO<sub>3</sub> solutions between 2- 6 M can be simply described by the equilibrium reaction below.<sup>55</sup>



As the acidity increases, the equilibrium is pushed to the left, reducing the hydrolysis of Zr. As NO<sub>3</sub><sup>-</sup> concentration increases above 6 M, the charge of the Zr complex is reduced with increasing coordinated nitrate (NO<sub>3</sub><sup>-</sup>) groups. This trend follows that of HCl, where hydroxyl and water groups compete with nitrate and form mixed complexes. Full complexation by nitrate results in the complex [Zr(NO<sub>3</sub>)<sub>6</sub>]<sup>2-</sup>. The NO<sub>3</sub><sup>-</sup> groups can also be bidentate, up to a coordination number of 10 with 5 bidentate NO<sub>3</sub><sup>-</sup> in the complex crystallized complex [Zr(NO<sub>3</sub>)<sub>5</sub>]<sup>-</sup>.<sup>56</sup>

In the presence of fluoride ion ( $F^-$ ), Zr forms several strong fluoride complexes. These are strong enough that free, uncomplexed Zr in solution is unlikely with  $F^-$  present and is not easily reversible. Fluoride hinders extraction of Zr, and thus makes for challenging separation chemistry if present at any point in a separation process. Addition of other acids or salts has little effect, but another metal that preferentially binds  $F^-$  can remove it from Zr, such as Al.<sup>57</sup>

At low (trace) Zr concentrations ( $<10^{-6}$  M) in acidic solution, free  $Zr^{+4}$  ion is prevalent due the low number of zirconium atoms present, preventing polymerization.<sup>52, 58, 59</sup> Trace amounts of Zr can readily adsorb to surfaces and form radiocolloids, as is typical with transition metals at trace concentrations. The presence of complexing anions, carrier atoms, and high concentrations of  $H^+$  all minimize this effect. In this case, monomeric complexes of the form  $Zr(OH)^{x-4}$  dominate at low acidities.

## Zr Production and Separation techniques

Zr has four stable isotopes,  $^{90}Zr$ ,  $^{91}Zr$ ,  $^{92}Zr$  and  $^{94}Zr$ , as well as two very long-lived isotopes,  $^{93}Zr$  ( $t_{1/2} = 1.61 \times 10^6$  years) and  $^{96}Zr$  ( $t_{1/2} = 2.35 \times 10^{19}$  years). Several radioactive isotopes of Zr are important in nuclear science, such as  $^{86}Zr$  ( $t_{1/2} = 16.5$  hours) and  $^{89}Zr$  ( $t_{1/2} = 78.41$  hours) in nuclear medicine,  $^{88}Zr$  ( $t_{1/2} = 83.4$  days) for stockpile stewardship, and both  $^{93}Zr$  and  $^{95}Zr$  ( $t_{1/2} = 64.032$  days) in astrophysics and nuclear waste management.<sup>60</sup> Typical production methods for these radioisotopes of Zr are charged particle reactions for neutron-deficient isotopes, or separated from fission products for the neutron-rich isotopes.<sup>61</sup> Several Zr isotopes are formed in high yields as U fission products, such as  $^{93}Zr$ ,  $^{95}Zr$ , and  $^{97}Zr$ . Natural Y is monoisotopic (100% abundance of

$^{89}\text{Y}$ ) which makes proton-rich isotopes of Zr accessible by (p,xn) reactions on Y targets. Y and Zr are easily chemically separable, so complex procedures for target preparation and post-irradiation processing are not needed. For example,  $^{89}\text{Zr}$  is generated by low to medium energy protons (15 MeV) by the reaction  $^{89}\text{Y}(p,n)^{89}\text{Zr}$ , or by deuterons in  $^{89}\text{Y}(d,2n)^{89}\text{Zr}$ .<sup>10</sup>  $^{86}\text{Zr}$  is produced in a similar manner with high energy protons (45-70 MeV) by the reaction  $^{89}\text{Y}(p,4n)^{86}\text{Zr}$ .<sup>11</sup>  $^{88}\text{Zr}$  can be produced by  $^{89}\text{Y}(p,2n)^{88}\text{Zr}$  at proton energies above 14 MeV, or by  $^{89}\text{Y}(d,3n)^{88}\text{Zr}$  above 20 MeV.<sup>62-</sup>  
<sup>64</sup> Due to the similarities in these charged particle induced reactions on Y, multiple Zr isotopes can be co-produced. Thus, tuning the incident energy to optimize for the reaction of interest is critical.

The produced Zr can be separated from the Y target by several methods, such as solvent extraction, extraction chromatography, or ion-exchange chromatography. For  $^{89}\text{Zr}$ , a common method is using a resin with a hydroxamate functional group, commercially available as ZR resin. Here, the Y target is dissolved in hydrochloric acid (HCl), then loaded onto ZR resin to elute the Y and retain Zr. Then, oxalic acid is used to elute Zr in a form suitable for radiolabeling.<sup>10</sup> Zr and Y are also separable by anion-exchange resin, where cationic Y is eluted from the column while anionic Zr is retained in >6 M HCl. This method eliminates the need for an organic complexant, such as oxalic acid, to recover the Zr.

Other methods to produce Zr include alpha particle reactions on natural Sr,<sup>65</sup> alpha ( $\alpha$ ) particle reactions on Y targets,<sup>66</sup> charged particle reactions on natural Nb or natural Zr, photonuclear reactions on Nb or Mo,<sup>67</sup> or spallation of Mo. For example, charged particle reactions on monoisotopic Nb can produce Zr isotopes, such as in the spallation reaction  $^{93}\text{Nb}(p,x)^{89}\text{Zr}$  or  $^{88}\text{Zr}$ .<sup>68</sup> However, the use of Nb targets to produce Zr is not favored due to the difficulty in separating Zr

and Nb. All these methods require dedicated irradiations at facilities, including target preparation and radiochemical post-processing to generate Zr radioisotopes. However, at FRIB, an estimated 630 mCi of  $^{88}\text{Zr}$  will be produced per week from a stable  $^{92}\text{Mo}$  beam.<sup>21</sup> With the unprecedented opportunity at FRIB to harvest isotopes passively from user experiments, it is vital that radiochemical procedures amenable to harvesting Zr isotopes from this facility are developed.

## Instrumentation

### Gamma-Ray Spectroscopy

Gamma-ray or gamma spectroscopy is one of the workhorse methods for characterization and quantification of gamma-ray-emitting radionuclides in radiochemistry. The low number of atoms typical for radioactive species makes standard chemical characterization difficult, however gamma-ray spectroscopy has a much lower limit of detection (LOD). In some cases, a known amount of a radionuclide can be added in for characterization using nuclear counting methods, called a tracer. Many radionuclides emit one or more gamma rays through nuclear decay, and their energy is proportional to the excited state of the nucleus. These gamma-ray emissions are characteristic of the nucleus and can be used for identification. Radiation is emitted in all directions from a radioactive source, so it is treated as a point source when nuclear counting. The solid-angle equation shown below is used to approximate how much radiation from the source the detector receives. This assumes a portion of the radiation strikes a sphere surrounding the source, where the entire surface area of the sphere is  $4\pi$ .

$$\Omega = A/r^2 \quad \text{Equation 7}$$

Multiple photons can strike the detector simultaneously, resulting in sum peaks in a collected gamma-ray spectrum. Therefore, emission energies and intensities for a radionuclide are important to know prior to sample analysis to properly characterize a sample's identity and activity, otherwise sum peaks could cause misidentification. Since gamma-rays are highly penetrating, most materials do not attenuate them sufficiently, which allows for detection through solutions, sample containers, and air. Therefore, gamma spectroscopy is a nondestructive analytical technique, as it only measures the radiation emitted from nuclear decay processes already occurring at a constant rate. However, the attenuation must be accounted for as well as the geometry of the sample relative to the detector for accurate quantification.

Quantification of a given radionuclide can be done using the count rate of a photopeak characteristic to the radionuclide associated with it in a sample. However, not all decays from a radionuclide emit gamma rays, so the intensity of each gamma-ray emission must be used when calculating activity. The efficiency of the detector is also crucial, as only a small portion of the emitted gamma rays will be received by the detector. Not all gamma rays that strike the detector are counted either, such as during the "dead time" of a detector. This is the period of time after receiving a signal from a captured gamma-ray that no other events can be recorded. For high activity samples where the detector dead time exceeds 5% loss of the gamma rays striking it, a correction needs to be made. This can be done via a calculation using the known dead time value or changing the source to reduce the number of gamma rays striking the detector, such as by dilution of the sample or increasing the distance from the detector.

Activity of a radionuclide can be calculated from a gamma-ray count rate using the two equations below:

$$A = \frac{C}{EI}$$

$$A = A_0 e^{-\lambda t}$$

Where A is the activity at a designated point of time,  $A_0$  is the initial activity value,  $\lambda$  is the decay constant, and t is the time in seconds between the two values. In some cases, the decay time does not significantly change the detected activity in an experiment when compared with the half-life of the radionuclide. However, this calculation should be performed to check if significant, and if so then normalize the activity at different time points in an experiment where the decay time can measurably change the initial or final activity values. There are two types of gamma-ray detectors, either scintillation or semiconductor-based detectors, each with their own advantages and drawbacks.

### NaI Scintillation Detector

In this type of scintillation detector, NaI crystals doped with Tl are used to interact with the incoming gamma-rays, which excites an electron due to the photoelectric effect. The electron then deexcites back to the ground state, emitting light proportional to the energy of the incident photon. This is measured by amplifying the signal with a photomultiplier tube, which converts the light to an electrical signal to produce a spectrum for analysis. These types of detectors offer suitable peak resolution for analysis, but not in all cases. For example, peak resolution up to 10% can be observed, which if assumed for a high energy peak such as the 1836 keV gamma emission

from  $^{88}\text{Y}$ , this corresponds to approximately  $\pm 183$  keV from the photopeak. Therefore, if multiple gamma-rays are observed in a sample that overlap due to the poor resolution, characterization and quantification becomes difficult, and thus other spectroscopic methods should be used. However, the efficiency in a NaI detector is very high for gamma-rays, which can range from 10-60%. Another advantage of NaI detectors is that they can operate in a simple setup at room temperature.

### High Purity Germanium Detector

High-Purity Germanium Detectors (HPGe) are a common semiconductor type detector, which offer much higher resolution but poorer efficiency than scintillation detectors. Peak resolutions are often lower than 1%, making them ideal tools for analysis of samples for where peak resolution is crucial. In these detectors, electron-hole pairs in the Ge are created from interaction with a gamma-ray, which excites the electron with enough energy to overcome the band gap and move it from the valence band to the conduction band. These electrons and holes can then move toward the anode and cathode, respectively, with the presence of an applied electric field. These are used to generate a signal proportional to the energy of the deposited gamma-ray. The low band gap of 0.66 eV for Ge requires the Ge crystal to be cryogenically cooled with liquid nitrogen, which prevents electrons from leaking into the conduction band by thermal excitation.<sup>1</sup> This requirement as well as the low efficiency of often <5% are drawbacks to using HPGe detectors, but their utility is still highly valuable and widely used.

## ICP-OES Analysis

Inductively Coupled Plasma Optical Emission Spectroscopy (ICP-OES) was used throughout this work to identify and quantify stable metals present in samples. In ICP-OES, atoms in a sample are excited via a plasma, typically made from ionized argon. Excited electrons deexcite to a lower energy level, which emits measurable radiation from the atoms. The light is emitted at a wavelength specific to the energy level gap. Since energy levels between electron orbitals are specific to each element and the energy levels within that element, these transitions can be used to identify elements present in a sample.

An ICP is produced by induction heating of argon gas to temperatures up to 10,000 K. The energy needed to generate the plasma is produced by flowing current through a coil to generate a magnetic field, which imparts energy into the plasma. The field holds the plasma in a small area, called the plasma torch. The torch is hot enough to ionize most elements and induce electron excitation. An aqueous sample is nebulized into the plasma, which evaporates the solvent and causes electrons in the atoms in the sample to excite. This light is measured using a charge coupled device (CCD) to measure the intensity of light at each specific wavelength it receives. The intensity of the light at a given wavelength is directly proportional to the concentration of the element being analyzed, which is used to quantify the element in the sample. To do so, a calibration curve must be generated with a plot of the intensity of the signal versus concentration in samples of known concentration of the same element. This calibration curve is wavelength specific and must be analyzed prior to each sample analysis, as the intensity of light measured is dependent on the

plasma torch intensity. ICP-OES is sensitive enough to measure  $\mu\text{g}$  quantities of metals in a sample.<sup>69</sup>

## Infrared Spectroscopy

Infrared (IR) spectroscopy is a chemical characterization technique that exploits the property of molecules where radiation is absorbed at wavelengths characteristic of their structure, revealing the identity of functional groups. To do so, a sample is exposed to an IR beam, resulting in partial absorption of the infrared radiation by the sample's molecules. The remaining radiation is detected, and the resulting spectrum is plotted as a function of wavenumber (reciprocal of wavelength) versus percent of the incident light absorbed. The motion of atoms leads to different types of vibrations, such as stretching, bending, or twisting, which can occur symmetrically or asymmetrically, and each motion corresponds to a specific frequency. This can be used to determine the presence of different functional groups in a sample or observe shifts from a known absorption wavenumber to probe differences in bonding environment between samples.

## NMR

Nuclear magnetic resonance (NMR) spectroscopy is used to study molecular structure by analyzing the spin state of nuclei with magnetic moments in the presence of an externally applied magnetic field. Not all nuclei are NMR active, as the nucleus must be paramagnetic with an odd number of nucleons. When a paramagnetic liquid sample is placed inside a strong, constant magnetic field, the spin states of the nuclei change from random orientations to either align with ( $\alpha$ -spin state) or against ( $\beta$ -spin state) the external field. The  $\beta$ -spin states are less populated than

the  $\alpha$ -spin states, as it requires more energy to align against the magnetic field. This difference in energy is proportional to the strength of the external magnetic field. In an externally applied magnetic field, the nuclei spin at a precession rate called the Larmor frequency that is specific to each type of nucleus. Energy specific to the Larmor, or resonance frequency can be applied to the sample to promote the  $\alpha$ -spin states to  $\beta$ -spin states. This energy difference is small and falls in the radio frequency radiation energy spectrum and is referred to herein as radiofrequency (RF) radiation. The RF can be applied as an oscillating magnetic field or in single pulses. Reverting back to the original  $\alpha$ -spin state releases RF radiation.<sup>70, 71</sup> The relationship between the energy difference of the two spin states, the magnetic field and the inherent magnetic properties of the nucleus are shown in the equation below.

$$\Delta E = h\nu = \frac{\gamma}{2\pi} hB_0$$

Where  $\Delta E$ = energy difference between  $\alpha$  and  $\beta$ -spin states,  $h$ = Plank's constant,  $\nu$ = operating frequency of the spectrometer,  $\gamma$ = gyromagnetic ratio for a specific type of nucleus,  $B_0$ = strength of the applied magnetic field in tesla (T). Plank's constant can be cancelled from both sides of the equation, which leaves a direct relationship between the operating frequency of the spectrometer and strength of the applied magnetic field required to produce a signal from a nucleus with a known gyromagnetic ratio (ratio of magnetic moment to angular momentum characteristic to a type of nucleus, denoted as  $\gamma$ ).

A second relaxation process occurs simultaneously with the spin-state realignment to the magnetic field. When nuclei absorb the RF at the exact Larmor frequency, they become excited.

They deexcite with a long delay, typically on the order of 0.1 to 10 seconds, and release RF radiation. This process is called free induction decay (FID). The time of applying an RF pulse and measuring the FID is called the acquisition time. NMR instruments today utilize pulsed RF radiation and convert changes in signal intensity over time to intensity versus frequency spectrum in a process called Fourier transform (FT).

The measured frequency differs depending on the electron environment around the nucleus. The electrons surrounding the nucleus in an atom are charged and moving, therefore they alter the magnetic field of the nucleus. If a nucleus has higher electron density from its surrounding bonding environment, then it is said to be “shielded” due to the shift in its resonance frequency to the right (upfield) from the weakened effect of the externally applied magnetic field on the nucleus. The opposite effect is deshielding, where electron density is pulled away from the nucleus, increasing the chemical shift to the left (downfield) because of the increased effect the magnetic field has on the nucleus. This shift is measurable (in ppm) compared to the expected value for a specific nucleus, which allows for the chemical environment around a nucleus to be determined.

Solid-state NMR spectroscopy utilizes the same fundamental properties of nuclear spin on atomic nuclei as in solution-state NMR. Three types of nuclear magnetic interactions dictate NMR frequencies: dipolar spin coupling, chemical shift anisotropy, and quadrupolar coupling. Dipolar spin coupling results from the distance between nuclei. Chemical shift anisotropy is dictated by the chemical bonding environment between nuclei. Quadrupolar coupling arises from quantum spin states larger than  $\frac{1}{2}$ , which have a non-spherical charge distribution and thus have an electric quadrupole moment in addition to the magnetic dipole moment. All these interactions influence

the resonance frequency of a nuclear spin state, and thus directly influence peak resolution in NMR spectroscopy. Solid samples are anisotropic, exhibiting magnetic dipole-dipole magnetic interactions (dipolar spin coupling) that do not average out like in solution-state NMR samples. This is corrected for by a technique called magic-angle spinning (MAS), where samples are spun around an axis with frequencies typically >1 kHz, tilted at the magic angle  $54.7^\circ$  relative to the applied magnetic field.<sup>72</sup> At this angle, the dipolar spin coupling spin is reduced to 0 because of the relationship between the bond angle relative to the external magnetic field

$$3\cos^2(\theta) - 1 = 0 \quad (\text{Equation 11})$$

Once the sample is spun at the magic angle, the only remaining influences on the resonance frequency are the chemical shift anisotropy and quadrupolar coupling, which can be used to probe molecular structure. A result of spinning the sample at high frequencies is a phenomenon called spinning sidebands, which appear at frequencies offset from the chemical shifts equal to the spinning frequency. Sidebands result from spinning the sample at a frequency slower than the chemical shift frequency, which incompletely averages the interaction. This can be minimized or removed entirely by spinning the sample at a faster rate.<sup>71</sup>

$^{31}\text{P}$  nuclei are useful in NMR spectroscopy because it is monoisotopic (natural abundance=100%), has a spin of  $\frac{1}{2}$ , and a high gyromagnetic ratio ( $\gamma$ ), 40.5% of  $^1\text{H}$ . Spectra can be collected with proton decoupling since spin-spin coupling is rarely observed.<sup>73</sup> Both solution and solid-state  $^{31}\text{P}$  NMR spectroscopy was utilized in this work to analyze the stability of a resin containing an organophosphorus extractant.<sup>74</sup>

Solid-state  $^{13}\text{C}$  NMR spectroscopy can be conducted to discern structural information; however, it typically requires cross-polarization to enhance the signal due to its low natural abundance of 1.1%.  $^{13}\text{C}$  has a spin of  $\frac{1}{2}$ , and a low gyromagnetic ratio of 25% relative to  $^1\text{H}$ . Cross-polarization (CP) is used with MAS to improve the signal from low abundance nuclei by transferring magnetization from high abundance nuclei, typically  $^1\text{H}$  by the heteronuclear dipolar interaction. This occurs only at the RF frequency where the Hartmann-Hahn condition applies, giving the relationship:<sup>75</sup>

$$(B_{1,I})\gamma_I = (B_{1,S})\gamma_S \quad (\text{Equation 12})$$

Where  $B$  is the external magnetic field strength,  $\gamma$  is the gyromagnetic ratio,  $I$  denotes the abundant nuclei ( $^1\text{H}$ ) and  $S$  denotes the less abundant nuclei ( $^{13}\text{C}$ ). This is conducted by following a pulse sequence, where a pulse is applied to the more abundant nuclei ( $^1\text{H}$ ), then an RF pulse matching the Hartmann-Hahn condition is applied to cause the magnetization transfer to the less abundant nuclei ( $^{13}\text{C}$ ). Then the signal from decay of the  $^{13}\text{C}$  is recorded. With cross-polarization, signal intensities and various relaxation times are not proportional to the number of  $^{13}\text{C}$  atoms, so quantification is not possible.

## Nitrogen Adsorption

Brunauer, Emmett and Teller (BET) surface area theory was developed as a commonly employed method for surface area analysis of materials.<sup>76</sup> Adapted from the Langmuir theory of adsorption, which describes the sorption of gas molecules onto a monolayer surface, BET theory extrapolates gas sorption to multiple layers of material. To measure the surface area of a sample,

they are degassed using heat and vacuum exposure to remove adsorbed air and water. The weight of the dry and degassed sample is recorded, then saturated with a non-reactive gas, typically nitrogen. Nitrogen is used primarily because it is cheap and easily available in high purity, not chemically reactive, and known to readily adsorb to solids. The amount of gas adsorbed to the degassed material can be measured by first cooling the sample to liquid nitrogen (LN<sub>2</sub>) temperature, then subjecting it to vacuum and exposing it to known amounts of nitrogen gas. LN<sub>2</sub> is used so that the amount of nitrogen adsorbed can be measured accurately and keep the sample held at a constant temperature, typically the boiling point of nitrogen (77 K). Once the saturation pressure is achieved (where no more gas adsorption occurs even with increasing pressure), the adsorbed gas can be quantified. The volume of gas adsorbed is plotted against the pressure at a constant temperature, called an isotherm. This isotherm is then used to calculate the BET surface area value. While there are six types of isotherms recognized by the International Union of Pure and Applied Chemistry (IUPAC), the BET surface area measurements in this work pertain to type IV for mesoporous materials. In type IV isotherms, capillary condensation occurs, where the adsorbed gas condenses into the pores below the saturation pressure of the gas.<sup>77</sup>

In BET analysis, several assumptions are made, as follows: Gas adsorption theory can apply to each layer independently, and can occur indefinitely; gas adsorption only occurs via weak intermolecular interactions, not chemical bonding; the layers do not interact with one another; the energy associated with each gas molecule adsorbing to the material requires the same amount of energy; the adsorption and desorption process is reversible; the pressure difference of the adsorbed gas is directly proportional to the volume adsorbed to the material.

## Zr stock solutions

### $^{88}\text{Zr}$ from LANL for Harvesting Chemistry Development

$^{88}\text{Zr}$  used for method development of  $^{88}\text{Zr}$  harvesting prior to the NSCL beamtime was procured from the National Isotope Development Center (NIDC) through the DOE Isotope Program. It was generated by proton induced spallation on natural Nb at LANL. The  $^{88}\text{Zr}$  was chemically separated from the target material and quantified by gamma ray emission from its strong 393 keV emission. The  $^{88}\text{Zr}$  was stored in 1.58 mL of 0.1 M HCl, with a total decay corrected activity of 0.8 mCi/mL to the shipping date, then shipped to Hunter College. To note,  $^{88}\text{Zr}$  decays to  $^{88}\text{Y}$ , which has a half-life of 106.626 days.  $^{88}\text{Y}$  has two strong gamma-ray emissions of 898 keV and 1836 keV, so it can be easily tracked and quantified. Chemical impurities and total stable Zr content was determined by ICP-OES and the results are shown in Table 1 below. This sample was diluted 50 times in concentrated HCl by aliquoting 100 ul of the source solution and placing in 4.5 mL of concentrated HCl. The needle used to aliquot from the  $^{88}\text{Zr}$  source vial was washed several times with 0.1 M HCl to make a total stock volume of 5 mL. This new stock solution was to store the  $^{88}\text{Zr}$  in a higher acid concentration easily workable for separation method development.

Separate working stock solutions were generated for experiments from this diluted  $^{88}\text{Zr}$  solution by diluting the 5 mL with 2 mL of additional concentrated HCl to bring the approximate HCl concentration above 11 M. This was then loaded onto an anion-exchange column (2 mL column volume) using Dowex 1x8 anion-exchange resin (100-200 mesh) pre-conditioned with

concentrated HCl. Here, the Zr adheres to the resin, while the daughter  $^{88}\text{Y}$  elutes in concentrated HCl. Three, 10 mL fractions of concentrated HCl were collected, then 2, 10 mL fractions of 6 M HCl following that to collect a majority of the  $^{88}\text{Zr}$ . The  $^{88}\text{Zr}$  in 6 M HCl was then used as the new stock solution and reconstituted in the appropriate acids for future experiments as needed. While the grown in  $^{88}\text{Y}$  is removed, it can be assumed that the other residual stable metal impurities are still present, including carrier levels of stable Zr likely in the high ppb range.

Table 1: Stable element impurities reported in  $^{88}\text{Zr}$  stock solution, quantified by ICP-OES

and reported as concentration values in ppm.

Element	Concentration (ppm)
Cu	0.22
Fe	8.13
Ga	>200
Nb	>200
Ni	0.438
Zr	6.24

### $^{88}\text{Zr}$ from NSCL

$^{88}\text{Zr}$  produced at the NSCL was generated by fragmentation of a stable  $^{92}\text{Mo}$  beam on a Be target. Using the A1900 magnetic separator system, the  $^{88}\text{Zr}$  secondary beam was selected for and further electromagnetically purified before delivery to the solid collector stack system.  $^{88}\text{Zr}$  was chemically separated from the solid collectors as described in Chapter 1 to produce carrier-free  $^{88}\text{Zr}$ .

## <sup>95</sup>Zr from Fission at LLNL

<sup>95</sup>Zr is a U fission product and was used as a tracer to study Zr chemistry in the SLM methodologies outlined in Chapter 3. Uranium was fissioned through proton bombardment at the Center for Accelerator Mass Spectrometry (CAMS) at LLNL. Zr was separated from the U and other fission products by elution from LN resin (Eichrom), which contains HDEHP as the functional group, with 0.1 M HNO<sub>3</sub>/0.1 M HF. <sup>95</sup>Zr (t<sub>1/2</sub>= 64.032 days) decays to <sup>95</sup>Nb (t<sub>1/2</sub>=34.991 days), which decays to stable <sup>95</sup>Mo. <sup>95</sup>Zr and <sup>95</sup>Nb are in transient equilibrium because of the shorter half-life of <sup>95</sup>Nb.

Studies were conducted on <sup>95</sup>Zr either received as is from the initial separation from fission products, or by further purification using anion-exchange. In both cases, <sup>95</sup>Zr solutions were boiled down and reconstituted in either HNO<sub>3</sub> or HCl to use as stock solutions for experiments and drive off excess fluoride. <sup>95</sup>Zr was purified by removing an aliquot of the stock solution and reconstituting in concentrated HCl. Then, this was loaded onto an anion-exchange column using strong-base Dowex 1x8 200-400 mesh. A majority of the <sup>95</sup>Zr sorbs to the column, however a significant portion (up to 30%) elutes due to the strong, neutral Zr-F complexes that do not retain on the resin. The sorbed Zr is eluted using 6 M HCl and quantified using an HPGe detector and the 724 keV gamma-ray emission of <sup>95</sup>Zr. For <sup>95</sup>Zr stocks in HNO<sub>3</sub>, a portion of the <sup>95</sup>Zr in 6 M HCl was boiled down and reconstituted in 12 M HNO<sub>3</sub> a minimum of three times in a plastic tube on a hot water bath with a heat lamp to minimize <sup>95</sup>Zr losses to irreversible sorption to glassware.

# Chapter 1: Solid-Phase Harvesting of $^{88}\text{Zr}$

## Background

The solid collector foils used in this work were Al, Cu, W, and Au, chosen to represent solid beamline materials that may accumulate byproduct radionuclides during routine operations at FRIB, or that may be desirable for implementation as fragment catchers. For example, Al is commonly used for solid components due to its high durability, low density, and low cost. Cu is useful for its ductility and both thermal and electrical conductivity. W is dense and has a high melting point, thus typically used for radiation shielding or beam stops in nuclear science experiments. Au can be rapidly dissolved and separated from many other elements because of its unique chemistry, making it a promising material for a fragment catcher for short-lived radionuclides. By dissolving each of these collectors in highly acidic matrices prior to radiochemical separation, hydrolyzing conditions are avoided, ideally improving Zr recovery yields. The previous aqueous-phase isotope harvesting experiment of  $^{88}\text{Zr}$  reported a total recovery of  $(26 \pm 2) \%$  of  $^{88}\text{Zr}$  deposited into an aqueous target.<sup>36</sup> In this work, solid-phase isotope harvesting of  $^{88}\text{Zr}$  is investigated for a direct comparison to the aqueous-phase isotope harvesting study. The solid-phase isotope harvesting methods described below provide a methodology for collection of  $^{88}\text{Zr}$  which can subsequently be applied to group IV and other elements with complex aqueous chemistry.

## Chemistry Method Development

Initial chemical separation methods for application to harvesting of trace Zr implanted into Al and Cu metal foils were investigated, with the context of several challenges in mind: Dissolution of metal foils and their appropriate workup for chemical separation that avoids hydrolyzing conditions, separation of a trace analyte from bulk materials, and the separation of Zr from other co-contaminant trace radionuclides present from  $^{88}\text{Zr}$  secondary beam.

Initial work looking at spallation of Mo to produce  $^{88}\text{Zr}$  was performed at BNL as a surrogate experiment for isotope harvesting of Zr from solid materials. Here, samples containing trace quantities of  $^{88}\text{Zr}$  were produced from spallation of stable  $^{\text{nat}}\text{Mo}$  foils using a high energy (200 MeV) proton beam produced at the BLIP. This was performed to generate foil samples containing trace amounts of implanted  $^{88}\text{Zr}$  for harvesting chemistry development that were more applicable to what would be generated at the NSCL from a  $^{88}\text{Zr}$  secondary beam.

### Al Harvesting Method Development

The starting point to try and isolate trace Zr deposited into Al foils was with anion-exchange chromatography, for multiple reasons. A typical separation method in radiochemistry is ion-exchange chromatography, which has been proven to be effective even with trace scale analytes. Al is known to exist predominantly as cationic  $\text{Al}^{3+}$  in aqueous solutions, typically  $[\text{Al}(\text{H}_2\text{O})_6]^{3+}$ . Also, Al has been shown to have no retention on anion-exchange resin in all concentrations of HCl.<sup>78</sup> Since Zr forms anionic complexes in high concentrations hydrochloric

acid with high retention to anion-exchange resin, this seemed to be a good starting point for separations method development.<sup>78</sup>

With the context of avoiding hydrolyzing conditions for Zr, dissolution of the Al foils was the first task for separation from Zr. Ideally, the Al foils will be dissolved in a matrix suitable for direct loading onto an anion-exchange column without any workup needed. Al metal is known to dissolve in hydrochloric acid, however, its purity has an observable effect on its dissolution. Al metal of less than trace metal grade purity dissolves faster with increasing concentrations of hydrochloric acid, and is more resistant to oxidizing acids such as nitric acid due to the formation of a passivation layer. Trace metal purity Al is more resistant to hydrochloric acid, and this was observed with initial dissolution studies for this work. 99% purity Al scrap metal dissolved rapidly with addition of several drops of concentrated hydrochloric acid, however trace metal grade Al had no noticeable degradation, even after several hours of exposure. To keep the solution in predominantly HCl matrix, additions of small amounts of nitric acid along with mild heat were found to dissolve the Al foil completely within an hour. Since the Al and Zr need to be in concentrated HCl solution to perform the separation, this solution must be boiled down and reconstituted in concentrated HCl several times to remove the nitric acid. It is important to note that this is performed in a plastic container to prevent trace Zr from irreversibly adsorbing to the container walls, which can happen easily in glassware even if not taken to complete dryness.

## Cu Harvesting Method Development

For separation of implanted Zr from the Cu foils, initial efforts were focused on anion-exchange separation following dissolution of the foils in the appropriate acid, similar to the separations from Al foils. Cu metal is known to readily dissolve in nitric acid ( $\text{HNO}_3$ ), however, the  $\text{HNO}_3$  needs to be removed prior to performing a separation. Zr adsorption to a strong base anion-exchange column is favorable in HCl concentrations above 6 M, however in nitric acid media, the distribution coefficient (kD) values are low for all concentrations.<sup>79, 80</sup> Even though Zr hydrolysis is less likely to occur with increasing acid concentrations, low kD values make use of this method in nitric acid media impractical due to Zr elution from incomplete sorption to the resin.<sup>79</sup> Due to this, initial efforts to dissolve the Cu metal foils in HCl were conducted so that the Zr could dissolve in a solution appropriate for direct loading onto an anion-exchange resin. Cu metal does not dissolve in concentrated hydrochloric acid on its own. Addition of heat and long exposure time is ineffective, but small additions of 30% hydrogen peroxide can help oxidize the Cu and force dissolution in concentrated HCl without formation of a passivation layer. Peroxide can destroy the organic resin, so this solution needed to be boiled down and reconstituted in concentrated HCl to remove the residual peroxide through both peroxide decomposition and evaporation. However, once the solution was boiled down and reconstituted, high losses of  $^{88}\text{Zr}$  were observed by irreversible sorption to the solution container, which would occur both in glassware and plastic. These losses can be mitigated by careful boiling down the solution without going to complete dryness to help retain Zr in solution.

Another challenge with anion-exchange separation of Zr from the Cu is due to the speciation chemistry of Cu in HCl solutions. While readily soluble, Cu in high concentrations of HCl can exist as several anionic complexes, depending on redox conditions. Typically, Cu is stable in solution as  $\text{Cu}^{2+}$ , forming hydrated  $[\text{Cu}(\text{H}_2\text{O})_6]^{2+}$ , but forms predominantly  $\text{CuCl}_4^{2-}$  in high concentrations of HCl.  $\text{Cu}^{1+}$  is present in reducing conditions, forming  $\text{CuCl}_2^{1-}$  and  $\text{CuCl}_3^{2-}$ . Therefore, the Cu complexes will show some sorption to the anion-exchange resin in HCl. Loading these solutions of high Cu concentration resulted in elution times exceeding several hours and >30 CVs of acid required to elute the bulk amount of Cu material. Also, due to the high concentration and mass excess of Cu compared to the trace levels of Zr, it carried the Zr through the resin and co-eluted in the initial concentrated HCl load fractions. While unclear the cause, it is likely that the initial column experiments testing this separation had exceeded the resin capacity, where anion-exchange sites on the resin were blocked by other Cu complexes and thus reduced the chance for the trace  $^{88}\text{Zr}$  to interact with the resin. For a given Cu mass of 50 mg (approximate mass of foil used in harvesting experiment), and assuming all Cu complexes in solution are of charge 2<sup>-</sup>, the calculated minimum resin required is 1.90 mL. Note, resin capacity is merely a minimum estimate, typically column dimensions are made to exceed the column capacity by 5-10 times to account for other factors that contribute to retention. Therefore, the actual amount of anion-exchange resin to use to not exceed capacity and perform correctly is approximately 10-20 mL. This value was determined using the ion-exchange resin capacity equation (Equation 6). Where 1 meq = equivalent number of cationic sites that can exchange with 1 mmol of  $\text{Cl}^-$  (or any singly charged anion). For Dowex 1x8 strong base anion-exchange resin, the capacity is 1.2 meq/mL. Note that the capacity should only be accounted for metals that form anionic complexes under the

given conditions. This value is for one metal, so if multiple metals are present, these must be summed to determine if column capacity is exceeded. Also, resin capacity is not the only metric that will affect retention, as column diameter and length must be taken into account as well. However, since resin volumes used in these separation tests ranged from 2- 5 mL, the resin capacity was exceeded and resulted in much of the Zr not retaining on the column. The Cu elution exhibited slow tailing in >20 CVs due to the slight retention to the resin. Since anion-exchange column separations in this geometry already required many column volumes (CVs) of solution and several hours of eluting time, scale up to retain the Zr would not make this procedure practical.

Increasing the column size theoretically should mitigate Zr bleed through, however, due to the weak adsorption of anionic Copper-chloride complexes to the resin, this would require very long column times exceeding several hours, and >100 mL of acid to completely elute the Cu target material. Also, this may not solve the problem with trace amounts of Zr carrying with the bulk Cu, even if there are enough cationic resin sites available to interact with, which was observed upon column scale up to exceed the capacity value.

To decrease retention time of the anionic Cu-chloride complexes, reduction of  $\text{Cu}^{2+}$  to  $\text{Cu}^{1+}$  using a reductant was investigated. This was to convert the Cu in solution to predominantly the monoanionic complex  $\text{CuCl}_2^{1-}$  instead of  $\text{CuCl}_4^{2-}$ , which has a lower overall charge and thus lower affinity to the resin in solutions above concentrations of 8 M HCl.<sup>79</sup> Since Zr is well retained on anion-exchange resin above 6 M HCl, this separation may be possible by first eluting the reduced Cu first while retaining Zr, then selectively eluting the Zr later by reducing the HCl concentration. Several reductants were screened to reduce Cu in solution upon dissolution, and were confirmed

colorimetrically with UV-Vis absorption analysis. Solutions of  $[\text{Cu}(\text{H}_2\text{O})_6]^{2+}$  are blue, but readily undergo ligand exchange with  $\text{Cl}^-$  according to the hard-soft acid-base theory, so conversion to the chloride form  $\text{CuCl}_4^{2-}$  turns the solution green. Upon reduction to  $\text{CuCl}_2^{1-}$ , the solution becomes clear. Reductants tested were ascorbic acid, citric acid, and hydroxylamine hydrochloride. While ascorbic acid is known to readily reduce Cu in solution, the concern was how long Cu will be reduced to  $\text{Cu}^{1+}$ , degradation of the ascorbic acid in concentrated HCl, and unwanted chelation of Zr. Thus, initial testing was performed prior to reducing irradiated Cu foil samples. Ascorbic acid completely reduced Cu in a minimum 1:1 molar ratio in solution, so all reductants tested were held at this concentration ratio. Hydroxylamine hydrochloride did not reduce  $\text{Cu}^{2+}$  in these conditions tested, but citric acid and ascorbic acid did readily with small additions to solution. However, citric acid is a known complexant for Zr, and ascorbic acid is not under high acid concentrations.<sup>9</sup> This is due to the pH of solution being well below the first pKa value for ascorbic acid of 4.7, causing the complex to be protonated, preventing metal complexation. At high concentrations of Cu, such as in this case where concentrations typically exceed 1000 ppm and approach the solubility limit, the solutions are deep in color. Practically, this can be used to confirm the reduction of Cu before column separation by reducing with dropwise additions of ascorbic acid to the dissolved  $\text{Cu}/^{88}\text{Zr}$  solution until completely clear with no visible green remaining.

An important note is that solutions of  $\text{Cu}^{1+}$  are not stable and will disproportionate over time. In this context, complete oxidation to  $\text{Cu}^{2+}$  solution was observed after 1 hour from initial reduction. Therefore reduction of Cu solutions were performed right before loading onto the anion-exchange column. Notably, the bulk Cu material eluted much faster than previous separations.

However, the ascorbic acid decomposes in concentrated HCl, forming a black insoluble substance on the resin and in the initial loading solution container. Post-separation analysis showed that a majority of the  $^{88}\text{Zr}$  had not eluted in the 6 M HCl fractions as expected, and was either lost by carrying with the bulk Cu in the initial fractions or by adsorption to the black decomposition products of ascorbic acid. After several attempts, anion-exchange column separation with ascorbic acid proved to be ineffective as a majority of the Zr was unrecoverable, so this method for harvesting Zr from Cu foils was not pursued any further.

### Beam Product Predictions

Software to model ion beam products and their transmission rates at radioactive ion beam facilities such as the NSCL, called LISE++, was used to predict ion transmission rates of  $^{88}\text{Zr}$  and other primary beam fragmentation products through the A1900 prior to delivery to the target irradiation chamber. Experimental parameters were modeled to minimize contaminants in the  $^{88}\text{Zr}$  secondary beam, however it is still likely that nuclides close in mass to  $^{88}\text{Zr}$  pass through the magnetic purification process and make up a portion of the beam. However, these potential byproducts could be identified using Lise++ code, along with their likely transmission rates prior to the beamtime. These nuclides and their transmission rates are shown in Table 2 below. Since these ions can include both radioactive and stable isotopes of a given element, their half-lives are included as well. Knowing what other radionuclides may be implanted into the collectors along with  $^{88}\text{Zr}$  can help guide the harvesting chemistry development for  $^{88}\text{Zr}$  purification. For example, these predictions show that other transmitted Zr isotopes include  $^{86}\text{Zr}$ ,  $^{87}\text{Zr}$ ,  $^{89}\text{Zr}$ , and stable  $^{90}\text{Zr}$  and  $^{91}\text{Zr}$ . However, these isotopes (except for stable  $^{90}\text{Zr}$  and  $^{91}\text{Zr}$ ) all have half-lives on the order

of minutes or hours, compared to 83 days for  $^{88}\text{Zr}$ . Therefore, these radionuclides should not be of concern for purification of  $^{88}\text{Zr}$ , because even though they behave the same chemically, they will be decayed away during the delay between post-irradiation and when harvesting chemistry begins. However, it can be assumed that some stable Zr isotopes may be present with the  $^{88}\text{Zr}$ .

Table 2: LISE ++ predicted ions and their transmission rates based on experimental parameters.

Total ion transmission rates are approximate and do not sum to 100%.

Radionuclide	Half-Life	(units)	Predicted Ion Production Rate (pps)	Total predicted ion transmission rate (%)
$^{90}\text{Mo}$	5.56	h	4.91E+01	0.002
$^{91}\text{Mo}$	15.49	m	1.29E+03	0.012
$^{92}\text{Mo}$	stable		N/A	N/A
$^{93}\text{Mo}$	4000	y	5.57E+03	5.304
$^{94}\text{Mo}$	stable		2.13E+00	1.016
$^{88}\text{Nb}$	14.55	m	4.19E+03	0.101
$^{89}\text{Nb}$	2.03	h	3.05E+04	0
$^{90}\text{Nb}$	14.6	h	6.57E+05	5.205
$^{91}\text{Nb}$	680	y	3.63E+06	48.255
$^{92}\text{Nb}$	3.47E+07	y	3.58E+02	0.476
$^{93}\text{Nb}$	stable		1.97E-01	0.131
$^{85}\text{Zr}$	7.86	m	1.26E+02	0.007

$^{86}\text{Zr}$	16.5	h	1.63E+04	0
$^{87}\text{Zr}$	1.68	h	6.24E+04	0.443
$^{88}\text{Zr}$	83.4	d	1.56E+06	25.568
$^{89}\text{Zr}$	78.41	h	8.43E+05	25.34
$^{90}\text{Zr}$	stable		5.78E+03	0.599
$^{91}\text{Zr}$	stable		1.36E+01	0.141
$^{83}\text{Y}$	7.08	m	1.27E+03	0.06
$^{84}\text{Y}$	39.5	m	1.62E+04	0.025
$^{85}\text{Y}$	2.68	h	3.13E+05	7.383
$^{86}\text{Y}$	14.74	h		32.499
				not
$^{86\text{m}}\text{Y}$	47.4	m	1.01E+06	differentiated in software from $^{86}\text{Y}$
$^{87}\text{Y}$	79.8	h		16.102
				not
$^{87\text{m}}\text{Y}$	13.37	h	2.60E+05	differentiated in software from $^{87}\text{Y}$
$^{88}\text{Y}$	106.626	d	3.08E+03	0.581
$^{89}\text{Y}$	stable		3.08E+00	0.003

<sup>80</sup> Sr	106.3	m	5.97E+01	0.005
<sup>81</sup> Sr	22.3	m	2.95E+03	0
<sup>82</sup> Sr	25.34	d	1.05E+04	0.06
<sup>83</sup> Sr	32.41	h	4.01E+05	13.951
<sup>84</sup> Sr	stable		4.29E+05	23.898
<sup>85</sup> Sr	64.849	d	8.11E+04	9.363
<sup>86</sup> Sr	stable		2.20E+03	0.725
<sup>87</sup> Sr	stable		5.42E+00	0.008
<sup>78</sup> Rb	17.66	m	1.13E+02	0.008
<sup>79</sup> Rb	22.9	m	3.40E+03	0.134
<sup>80</sup> Rb	33.4	s	4.59E+03	0
<sup>81</sup> Rb	4.572	h	5.08E+04	2.243
<sup>82</sup> Rb	1.2575	m	2.19E+05	17.856
<sup>83</sup> Rb	86.2	d	3.14E+04	5.91
<sup>84</sup> Rb	32.82	d	1.11E+03	0.61
<sup>85</sup> Rb	stable		3.79E+00	0.008
<sup>76</sup> Kr	14.8	h	2.40E+00	0
<sup>77</sup> Kr	74.4	m	1.60E+03	0.062
<sup>78</sup> Kr	1.50E+21	y	2.01E+03	0.077
<sup>79</sup> Kr	35.04	h	4.96E+02	0.006
<sup>80</sup> Kr	stable		3.58E+04	4.111

<sup>81</sup> Kr	2.29E+05	y	1.21E+04	3.402
<sup>82</sup> Kr	stable		4.62E+02	0.391
<sup>83</sup> Kr	stable		3.17E+00	0.01
<sup>75</sup> Br	96.7	m	5.51E+01	0.002
<sup>76</sup> Br	16.2	h	7.98E+02	0.036
<sup>77</sup> Br	57.036	h	1.34E+02	0.01
<sup>78</sup> Br	6.45	m	2.34E+02	0.037
<sup>79</sup> Br	stable		4.56E+03	1.951
<sup>80</sup> Br	17.68	m	2.46E+02	0.331
<sup>81</sup> Br	stable		1.67E+00	0.008
<sup>74</sup> Se	stable		6.90E+01	0.004
<sup>75</sup> Se	119.78	d	5.21E+01	0.005
<sup>76</sup> Se	stable		1.92E+00	0
<sup>77</sup> Se	stable		9.22E+01	0.06
<sup>78</sup> Se	stable		8.32E+01	0.184
<sup>79</sup> Se	3.26E+05	y	8.47E-01	0.007
<sup>80</sup> Se	stable		2.11E-02	0.001
<sup>73</sup> As	80.3	d	9.47E+00	0.001
<sup>74</sup> As	17.77	d	1.50E+00	
<sup>75</sup> As	stable		6.25E-02	
<sup>76</sup> As	1.0942	d	5.97	0.021

<sup>77</sup> As	38.83	h	5.82E-01	0.009
<sup>78</sup> As	90.7	m	1.26E-02	0.001
<sup>74</sup> Ga	stable		1.06E-02	0.001
<sup>75</sup> Ge	82.78	m	1.24E-01	0.003
<sup>76</sup> Ge	stable		6.16E-03	0.001

## Experimental

### Materials and Supplies

The Al (99.45%, 0.025 mm thick, Alfa Aesar), Cu (99.8%, 0.025 mm thick, Alfa Aesar), W (99.95%, 0.05 mm thick, Alfa Aesar), and Au (99.95 %, 0.025 mm thick, Goodfellow) foils were all cut into a circle with a diameter of 2.54 cm, cleaned with isopropanol (99.99%, Fisher), and scored to label before loading into the collectors. The mass of one foil was approximately 36 mg for Al, 80 mg for Cu, and 250 mg for Au. For the Al and Cu studies, hydrochloric acid (Trace Metal grade, 36–38%, Fisher), nitric acid (metals basis, 65–70%, Alfa Aesar), 18.2 MΩ-cm water (Barnstead GenPure Pro MilliQ water system), n-dodecane (Alfa Aesar, >99%), Tri-n-octylphosphine oxide (ReagentPlus 99%, Aldrich) were all used without further purification. Commercial resins utilized in this work were Dowex 1x8 (100-200 mesh, Cl form), DGA resin-normal (50-100 μm, Eichrom) and pre-packed Pb resin cartridges (2 mL, 50-100 μm, Eichrom).

## Beamtime at NSCL

The  $^{88}\text{Zr}^{39+}$  secondary beam was generated by fragmentation of a stable 140-MeV/nucleon  $^{92}\text{Mo}$  primary beam on a 446-mg/cm<sup>2</sup> Be target. Using the A1900 fragment separator,  $^{88}\text{Zr}$  was selected with a 2% momentum acceptance and delivered to the target endstation (Figure 1). The  $^{88}\text{Zr}$  beam was implanted in the collector attached to the target endstation, which contained the foils of interest (Figure 2). The circular foils were mounted as stacks and clamped with an aluminum ring to an aluminum KF40 flange blank, making up a collector. The collector foils were Al, Cu, W, and Au, with each collector only containing foils of one of these metals. Ten to twenty foils comprised a single collector stack for each material, determined by modeling the stopping ranges using LISE++ and SRIM; tantalum backing foils, to ensure the  $^{88}\text{Zr}$  beam was completely stopped in the collector stacks, and degraders (for Al, Cu, Au) were also used (Table 3). Tantalum degraders and backing foils were included to ensure the beam was fully stopped in the collector foil stacks. Each collector was irradiated for approximately 8 hours with the  $^{88}\text{Zr}$  beam. To monitor the  $^{88}\text{Zr}$  beam current on target over the course of the experiment, an intercepting Faraday cup located immediately upstream of the endstation was periodically inserted to read the beam current.

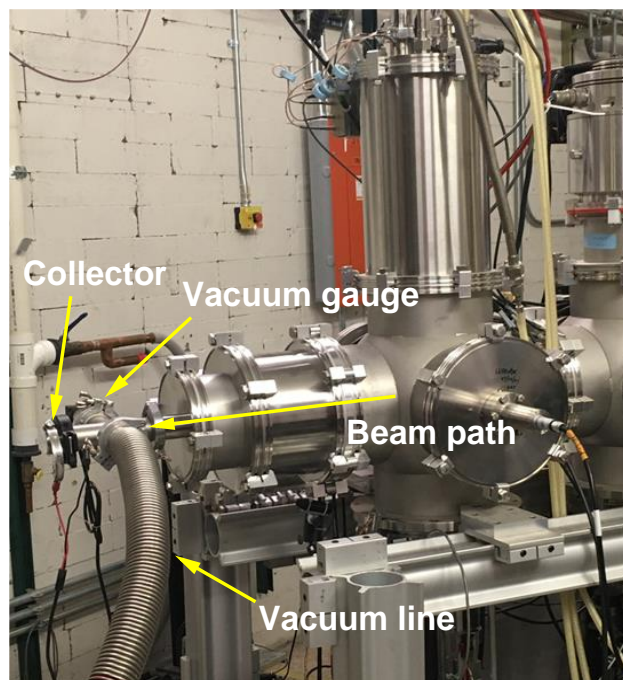


Figure 1: Photograph of the target endstation at the NSCL. Each collector containing the foil stacks for a particular element was secured to the beamline, as shown, and held under vacuum during irradiation with the secondary  $^{88}\text{Zr}$  beam.

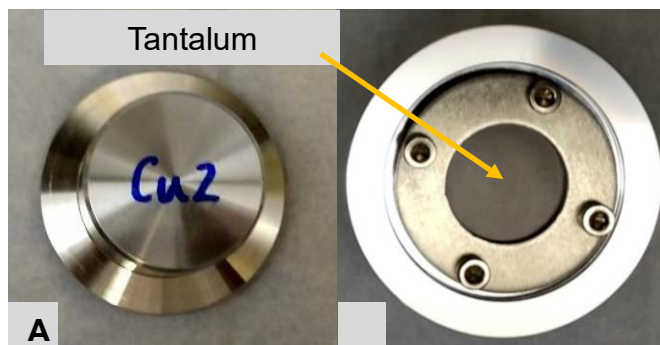


Figure 2: (A) Back of the Cu collector. (B) Front side of the Cu collector with part of the Ta degrader showing, beneath which lies the stack of Cu foils all secured with an aluminum ring and screws. This was mounted onto the end of the beamline as depicted in Figure 1.

Table 3: Contents of each solid collector, where Ta degraders (0.127 mm thick each) were placed upstream of the target stack and ta backings were placed downstream behind the foils.

Material	Aluminum (Al)	Copper (Cu)	Tungsten (W)	Gold (Au)
Number of foils in collector	20	16	10	16
Thickness of each foil (mm)	0.025	0.025	0.05	0.025
Purity (%)	99.45	99.8	99.95	99.95
Number of Tantalum Degraders	3	2	None	1
Number of Tantalum Backings	1	1	1	1

Collector stacks were counted on a PHDS Fulcrum portable HPGe  $\gamma$ -ray detector outside of the vault within 10 minutes of end of bombardment (EOB) to identify short-lived species. A typical  $\gamma$ -ray spectrum collected immediately after EOB is shown in Figure 9. In addition to  $^{88}\text{Zr}$ , other detected radionuclides include:  $^{86}\text{Zr}$  ( $t_{1/2}$ = 16.5 hours),  $^{89}\text{Zr}$  ( $t_{1/2}$ = 78.41 hours),  $^{86}\text{Y}$  ( $t_{1/2}$ = 14.74 hours),  $^{87}\text{Y}$  ( $t_{1/2}$ = 79.8 hours),  $^{87\text{m}}\text{Y}$  ( $t_{1/2}$ = 13.37 hours), and  $^{90}\text{Nb}$  ( $t_{1/2}$ = 14.6 hours).<sup>81-84</sup> Within 24 hours of EOB, the collector stacks were transported from the NSCL to the radiochemistry laboratory in the MSU Department of Chemistry for further analysis. Each collector was disassembled, and the individual foils were counted on a shielded HPGe detector to determine the identity and distribution of beam products in the stacks. After the initial analysis, the W collector foils remained at MSU while the Cu and Al collector foils were shipped to Hunter College and the Au collector foils were shipped to Lawrence Livermore National Laboratory (LLNL) for subsequent separation chemistry for the extraction of  $^{88}\text{Zr}$  and  $^{88}\text{Y}$ .

## Beam Integration

Periodically during each collector irradiation with the secondary  $^{88}\text{Zr}$  beam, an intercepting Faraday cup (F157) was inserted into the primary beam to record the beam current. Simultaneously, multiple non-intercepting detectors were used to monitor the secondary beam current. These values were used for calibration of the beam current to ultimately determine the number of  $^{88}\text{Zr}$  ions that were delivered through the A1900 spectrometer. On average over every 30 minutes over the course of an 8-hour irradiation, the Faraday cups were inserted and the measured current value along with the value from the nearest non-intercepting detector was recorded, just after the Be target used to fragment the beam (denoted Z013). The time inserted, and how long it was intercepting the beam was also recorded for future beam integration. The Z013 records the beam current every 5 seconds during each irradiation. When the F157 is inserted, the beam is blocked and not irradiating the target. After irradiation and analysis of the total yield of  $^{88}\text{Zr}$  in the collectors determined by gamma-ray spectroscopy, the particle rates of  $^{88}\text{Zr}$  delivered to each collector stack per particle nano-Ampere of the primary  $^{92}\text{Mo}$  beam (pps/pnA) passing through the A1900 were calculated as follows:

## Procedure

To make a calibration curve, a segment of datapoints was chosen during a period when the F157 was inserted (typically a 2–3-minute time span) for each collector. The F157 versus Z013

readings during this time were plotted against one another, then fit with a trendline. These plots are shown in Figure 3, Figure 4, and Figure 5 below.

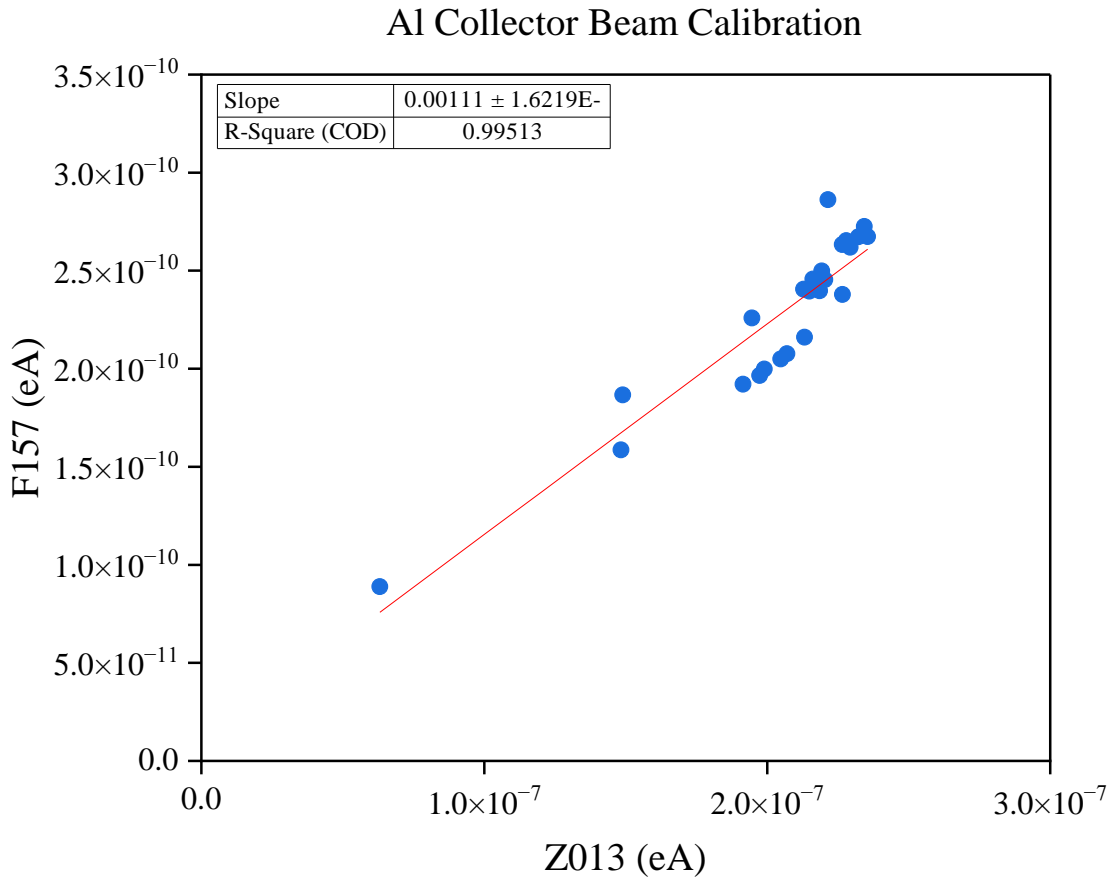


Figure 3: Calibration curve for Al collector irradiation

### Cu Collector Beam Calibration

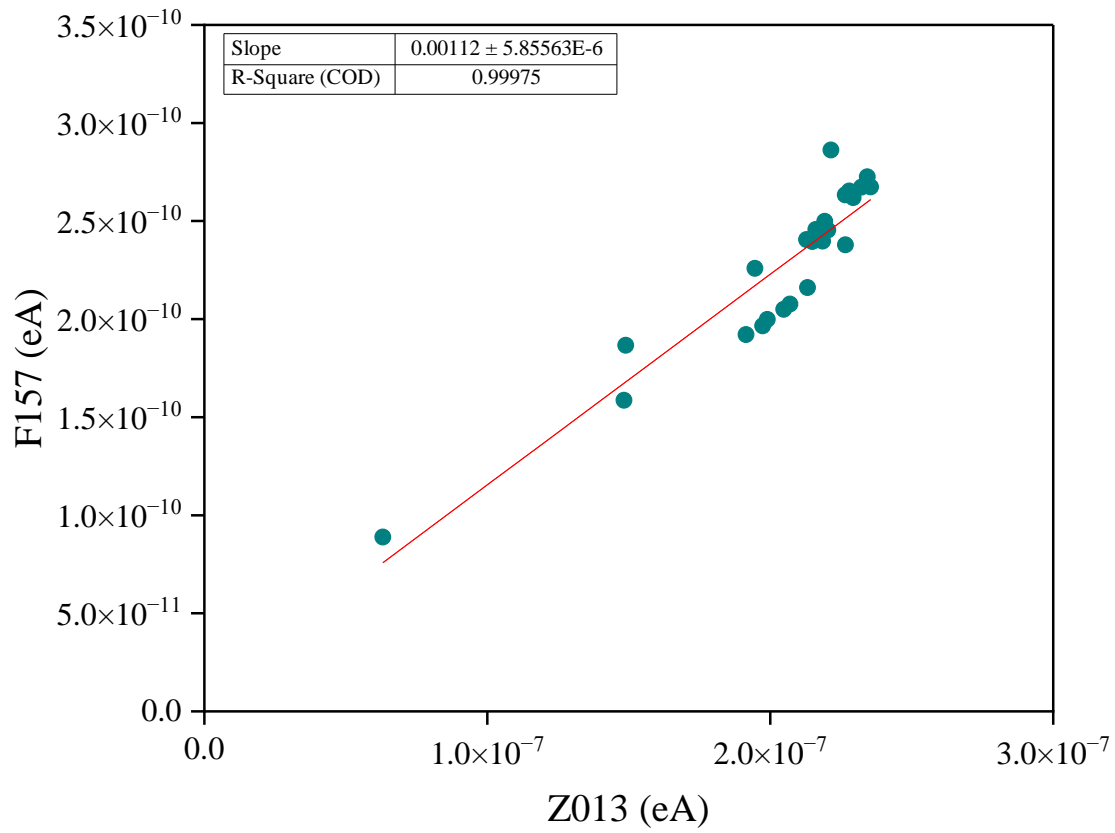


Figure 4: Calibration curve for Cu collector irradiation

### Au Collector Beam Calibration

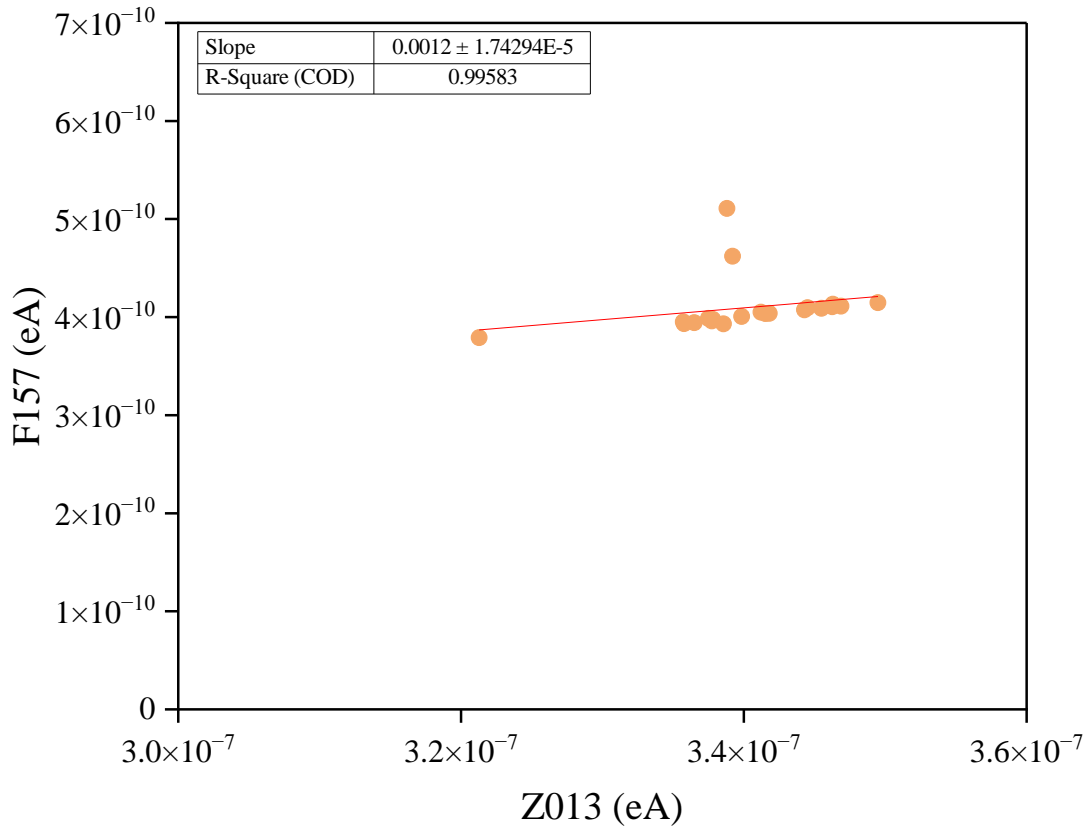


Figure 5: Calibration curve for Au collector irradiation

To solve for the delivered beam current over the entire irradiation time, the beam current recorded by the Z013 for each collector's whole irradiation time was summed, then input into the trendline equation to solve for the summed primary beam current. Values recorded from the experiment at the NSCL are in electrical current (eA), which neglects the charge state of the beam (assuming it is singly charged). Therefore, these values were converted to pA by dividing by 39 for the  $^{88}\text{Zr}$  secondary beam charge state of  $39^+$  (the average charge state of the beam recorded by

the NSCL operators, whereas fully ionized Zr beam should be 40<sup>+</sup>), then multiplied by 10<sup>9</sup>. This relationship is shown in the equation below:

$$eA = pA * Z$$

where pA= pps \* e, Z= charge state of ion, pps= particle rate in particles/second, e= charge of electron. The integrated time beam was on each collector was determined by summing the time beam was on for that period, then subtracting for the time when the F157 that intercepted the beam was inserted. The total amount of <sup>88</sup>Zr atoms in each collector (including <sup>88</sup>Zr that was found in the ring clamp) determined by gamma-ray spectroscopy and decay corrected to end of bombardment, was divided by total integrated irradiation time to find the average rate of <sup>88</sup>Zr (pps). The final ion rate was determined by dividing the rate by the summed beam current, resulting in the reported values in pps/pnA.

### Separation of <sup>88</sup>Zr and <sup>88</sup>Y from Aluminum Foils

Harvesting from the Al foils was performed 1 month after EOB; therefore, the only remaining detectable radionuclides were <sup>88</sup>Zr (t<sub>1/2</sub>= 83.4 d), its daughter <sup>88</sup>Y (t<sub>1/2</sub>= 106.626 days), and <sup>85</sup>Sr (t<sub>1/2</sub>= 64.849 days).<sup>15</sup> Foils were counted on an Ortec GEM60P4 HPGe detector. Those containing deposited <sup>88</sup>Zr were cut in halves or quarters for subsequent chemical processing.

Each Al foil fragment was dissolved in 500 μL of concentrated HCl with 10 μL of concentrated HNO<sub>3</sub> in a hot water bath with stirring for 1 hour. The Al solution was evaporated to a wet residue and reconstituted in concentrated HCl several times to remove residual nitric acid and keep <sup>88</sup>Zr in solution as a free anionic complex. During this step, a portion of the Al precipitates

as insoluble hydrated aluminum chloride, confirmed by IR spectroscopy relevant to a known standard (Figure 6). Associated bond vibrations are shown in Table 4.

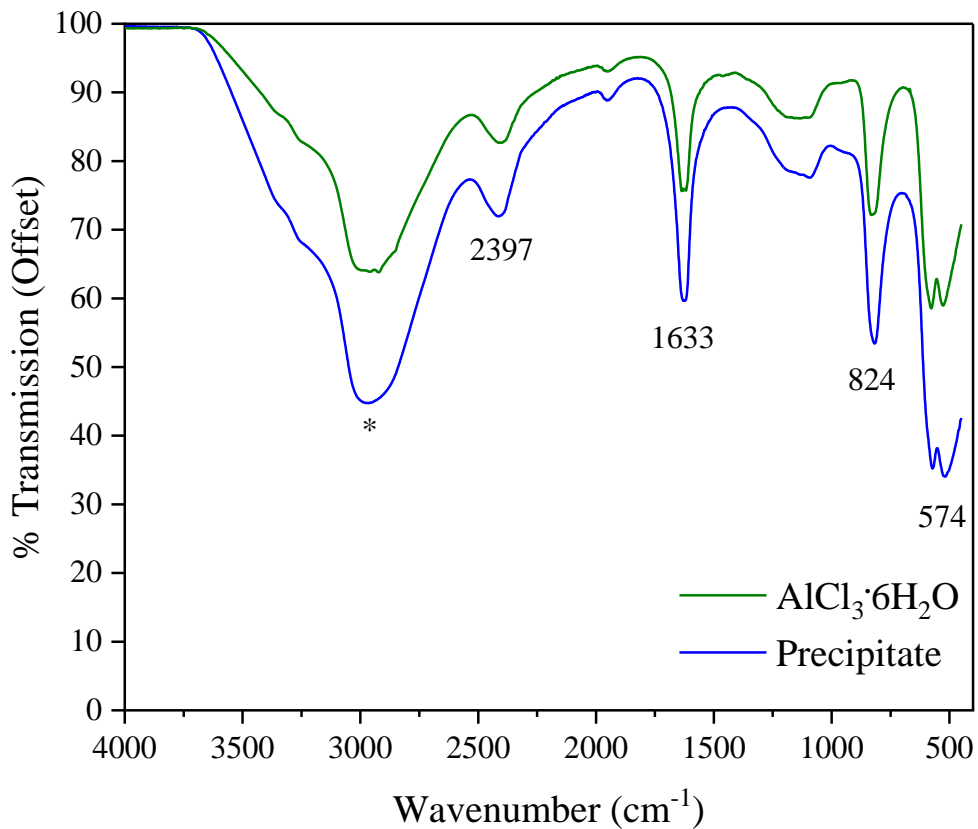


Figure 6: IR Spectra of AlCl<sub>3</sub>·6H<sub>2</sub>O standard and Al precipitate after wash with ether

Table 4: Associated peaks for Al precipitate and Al standard from IR spectra.

Absorption (cm <sup>-1</sup> )	Group
574 (doublet)	Octahedral Al
824	C-O ether
1633	H <sub>2</sub> O
2397	CO <sub>2</sub> Al(H <sub>2</sub> O) <sub>6</sub> stretch
3000*	O-H stretch H <sub>2</sub> O C-H ether

Approximately 500  $\mu$ L of supernatant was removed and allowed to cool, counted on a 1.1 x 2 cm NaI well detector (Alpha Spectra Inc.), then loaded onto a prepared strong-base anion-exchange resin (Dowex 1x8 100-200 mesh Cl<sup>-</sup> form, 2 mL column volume, 4 cm x 0.8 cm). The column was prepared by slurry loading resin preconditioned with 1 M HCl, then washed with >10 column volumes (CVs) of concentrated HCl with gravity flow. The loading solution vial was rinsed twice with an additional 500  $\mu$ L of concentrated HCl and added to the column to ensure all the <sup>88</sup>Zr was loaded. The column was washed with concentrated HCl for a total of 22.5 mL (>11

CVs) to elute both cationic  $\text{Al}^{3+}$  and  $^{88}\text{Y}^{3+}$ . A total of 25 mL (>12 CVs) of hot 6 M HCl was used to elute the  $^{88}\text{Zr}$ . Each fraction was counted on the NaI detector in the same geometry as the load solution to determine final recovery of  $^{88}\text{Zr}$ . An identical, non-radioactive surrogate experiment without  $^{88}\text{Zr}$  or  $^{88}\text{Y}$  was performed to determine the elution profile of Al. Al was quantified using ICP-OES with a Shimadzu ICPE-9000 Multitype ICP Emission Spectrometer at 258 nm wavelength for each collected fraction.

To isolate the  $^{88}\text{Y}$ , fractions containing  $^{88}\text{Y}$  that co-eluted with Al in the initial anion-exchange column were loaded onto normal DGA resin, which has a N,N,N',N'-tetra-n-octyldiglycolamide functional group that strongly binds to trivalent rare earths and high field strength elements.<sup>85-87</sup> DGA resin has a high affinity for  $\text{Y}^{3+}$  in a wide range of hydrochloric and nitric acid concentrations, while Al exhibits low sorption to the resin in all acid concentrations.<sup>86</sup> DGA resin was pre-wetted with 1 M HCl for 24 hours and slurry loaded into a column yielding a 0.5 mL CV (0.4 cm x 1 cm), then pre-conditioned with 10 CVs of concentrated HCl. Fractions containing  $^{88}\text{Y}$  and Al in concentrated HCl from the previous  $^{88}\text{Zr}$  separation (1.5 mL each) were counted on a NaI detector, then loaded directly onto the prepared column under gravity flow. The column was washed with concentrated HCl, collecting the 12 mL of load and wash eluate together. The  $^{88}\text{Y}$  was eluted in 9 mL of 1 M HCl followed by 4 mL of water. The full separation scheme for  $^{88}\text{Zr}$  and  $^{88}\text{Y}$  is shown in Figure 7. Decontamination factors (DF) of the target nuclide ( $^{88}\text{Zr}$  and  $^{88}\text{Y}$ ) from the Al, Cu and Au foils were calculated using the equation below:

$$DF = \frac{\left(\frac{\text{mol}_{88\text{Zr}}}{\text{mol}_M}\right)_{\text{Final}}}{\left(\frac{\text{mol}_{88\text{Zr}}}{\text{mol}_M}\right)_{\text{Initial}}}$$

Where ‘M’ indicates the bulk metal. The limit of quantification of the ICP-OES for Al and Cu was 10 ppb, and thus used as a minimum value for determining mol of Al and Cu for samples with a concentration below this value. For the Au separations,  $^{88}\text{Y}$  was recovered only from decay of purified  $^{88}\text{Zr}$ , therefore decontamination factors of  $^{88}\text{Y}$  from Au were not calculated.

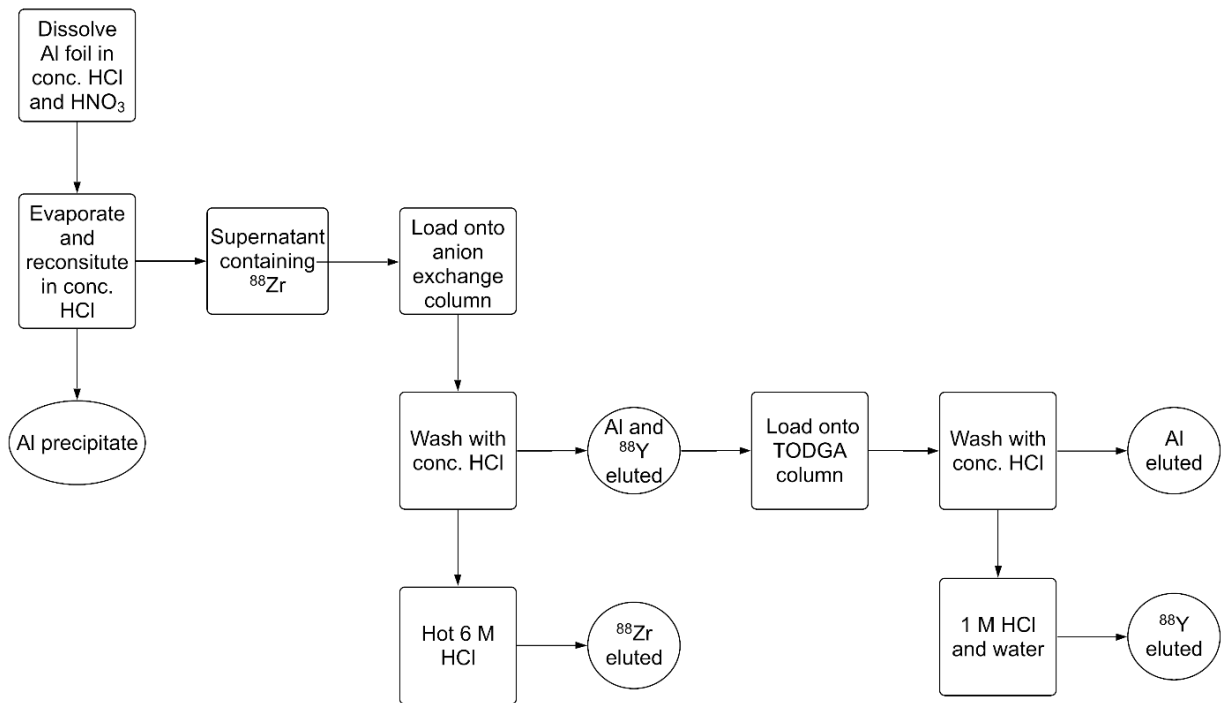


Figure 7: Schematic of the complete separation of  $^{88}\text{Zr}$  and  $^{88}\text{Y}$  from bulk Al foil.

## Separation of $^{88}\text{Zr}$ and $^{88}\text{Y}$ from Copper Foils

Cu foils were cut in half, dissolving each half in 500  $\mu\text{L}$  of prepared 12 M  $\text{HNO}_3$ . The dissolved Cu solution was counted on a NaI detector prior to the separation procedure. 2 mL of 0.01 M trioctylphosphine oxide (TOPO) in n-dodecane was pre-equilibrated with 2 mL of 12 M  $\text{HNO}_3$  by mixing each together for 3 minutes, then allowing to settle for 30 minutes. The solution was centrifuged for 2 minutes, then 500  $\mu\text{L}$  of the organic layer was removed and added to the dissolved Cu solution (1:1 volume ratio) for selective extraction of the  $^{88}\text{Zr}$  into the organic layer. The two phases were mixed with a vortex mixer for 3 minutes, followed by 3 minutes of centrifugation. The phases were separated with a pipette and the organic layer counted on a NaI detector. The organic layer was washed 3 times with 12 M  $\text{HNO}_3$  by adding the organic layer to 500  $\mu\text{L}$  of 12 M  $\text{HNO}_3$ , vortex mixing for 3 minutes, and centrifuging for 2 minutes for each wash. By this method, the  $^{88}\text{Y}$  and the Cu remained in the 12 M  $\text{HNO}_3$  aqueous phase while a majority of the  $^{88}\text{Zr}$  was extracted into the organic layer. This process constituted one pass, which was repeated once more with another 500  $\mu\text{L}$  of 0.01 M TOPO in n-dodecane. The organic phases from passes 1 and 2 containing  $^{88}\text{Zr}$  were combined and the  $^{88}\text{Zr}$  back-extracted by vortex mixing with an equal volume of 1 M HCl for 3 minutes, separating by centrifugation for 2 minutes, and repeating 3 times. The full scheme is shown in Figure 8.

Following  $^{88}\text{Zr}$  extraction,  $^{88}\text{Y}$  and Cu remained in the initial 12 M  $\text{HNO}_3$  aqueous phase (500  $\mu\text{L}$ ). To separate the  $^{88}\text{Y}$  from the Cu, the mixture was loaded on a DGA resin column, prepared in the same manner as previously described for Al, but here pre-conditioned with 10 CVs

of 12 M HNO<sub>3</sub>. After loading, the column was washed with 10 CVs 12 M HNO<sub>3</sub>, and eluted sequentially with 20 CVs 0.1 M HNO<sub>3</sub>, 20 CVs 1 M HCl, and 20 CVs water.

Identical non-radioactive surrogate experiments without <sup>88</sup>Zr or <sup>88</sup>Y were performed for both the solvent extraction and column separations to determine the Cu concentration of the solutions at each step in the procedure. Cu was quantified using ICP-OES at 225 nm wavelength for each sample.

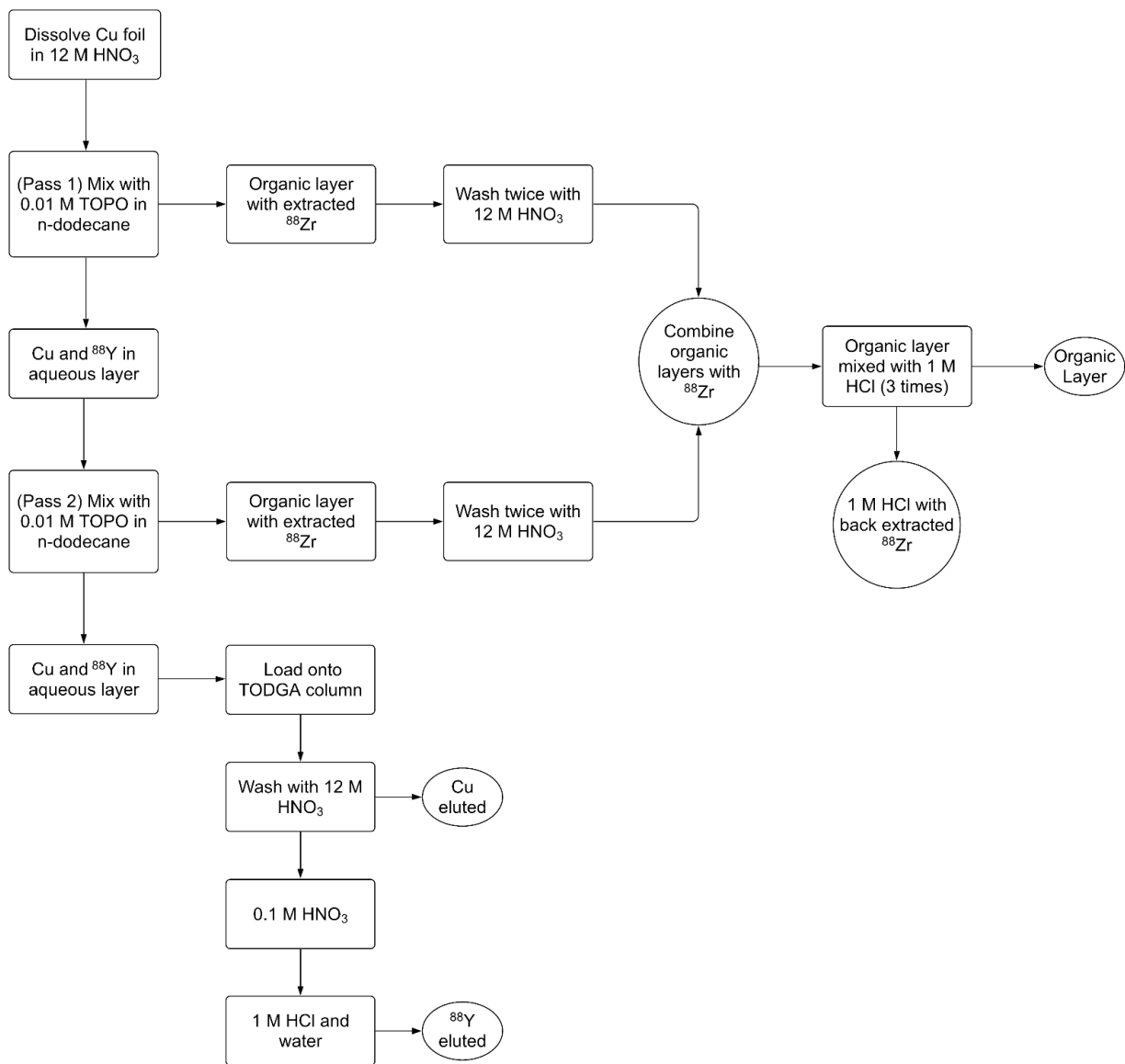


Figure 8: Schematic of the complete separation for the extraction of  $^{88}\text{Zr}$  and  $^{88}\text{Y}$  from bulk Cu foil.

## Results/Discussion

### Post-Irradiation Analysis

Once chemistry on the foils began about one month after EOB, most of the beam products other than  $^{88}\text{Zr}$  and its decay product  $^{88}\text{Y}$  had decayed to below detectable levels. The exception was  $^{85}\text{Sr}$ , which was detected several months post-irradiation in all three collector materials, however detailed quantification was only possible for the Au foil stack. The beam product deposition agreed with the stopping range calculations with the  $^{88}\text{Zr}$  collecting in foils #6-11 for the Al stack, #12-15 for the Cu stack, and #1-13 foils for the Au stack (Figures 7, 8, and 9 for Al, Cu, and Au, respectively). The number of atoms of  $^{88}\text{Zr}$  deposited in the collectors exceeded other products by at least one order of magnitude. The predicted ion transmission rate into a collector for  $^{88}\text{Zr}$  from LISE++ software was  $1.56 \times 10^6$  particles per second (pps).

Radionuclide deposition locations in the collector stacks were predicted based on their mass to charge ratios (m/q). Since heavy ions with high energy can predictably penetrate materials due to electrostatic and nuclear interactions, their stopping power can be estimated by comparing their m/q. Table 5 shows the mass to charge ratios for the predominant radionuclides found in the Al collector stack, as well as both their predicted and experimentally determined locations. The predictions did not completely match the actual outcome for a majority of these products, however this may be due to decay of short-lived beam products with these radionuclides as part of their decay chains. This will result in incorrect assumptions that these products were produced directly from primary beam fragmentation and deposited into the foils based on their momentum, and not

their radioactive parent's momentum. Other factors could contribute to this distribution of beam products as well, such as differences in energies due to collisions with collector materials or incomplete ionization of the ions.

Table 5: Predicted vs experimentally determined ion distribution rates in the Al collector stack. Order is described from #1-5, where a lower m/q ratio should deposit earlier in the collector stack more upstream from the beam, and a higher m/q ratio ion should deposit more downstream.

Nuclide	Atomic mass	charge (q)	m/q ratio	Predicted order	Actual order
<sup>86</sup> Zr	86	39	2.21	1	1
<sup>88</sup> Zr	88	39	2.26	3	4
<sup>89</sup> Zr	89	39	2.28	4	2
<sup>86</sup> Y	86	38	2.26	3	5
<sup>87</sup> Y	87	38	2.29	5	3
<sup>90</sup> Nb	90	40	2.25	2	2

The decay corrected total activity of <sup>88</sup>Zr deposited into the collector stacks are shown in Table 6. The difference in deposited activity in the collectors is due to the variations in integrated particle rates from collector to collector. The average particle rates (in atoms of <sup>88</sup>Zr per second, pps) of Al and Cu were  $(2.12 \pm 0.13) \times 10^7$  and  $(1.82 \pm 0.09) \times 10^7$ , respectively, as determined by  $\gamma$ -ray spectroscopy analysis decay corrected to end of bombardment. While no <sup>88</sup>Zr was detected in the KF40 flange, Ta degrader foils, Ta backing foils, or metal screws,  $(5.6 \pm 2.2) \%$  and  $(4.1 \pm$

2.3) % of the total  $^{88}\text{Zr}$  activity was deposited onto the Al ring clamp for the Al and Cu collectors, respectively.

Table 6: Experimentally determined total activity, number of atoms, and particle rates of  $^{88}\text{Zr}$  for each collector stack.

Collector	Activity of $^{88}\text{Zr}$ at EOB (Bq)	Number of $^{88}\text{Zr}$ atoms at EOB	Integrated beam on target time (hours)	Average particle rate of $^{88}\text{Zr}$ (pps)
Al	$(5.72 \pm 0.36) \times 10^4$	$(5.94 \pm 0.37) \times 10^{11}$	7.78	$(2.12 \pm 0.13) \times 10^7$
Cu	$(3.87 \pm 0.20) \times 10^4$	$(4.02 \pm 0.21) \times 10^{11}$	6.15	$(1.82 \pm 0.09) \times 10^7$
Au	$(6.41 \pm 0.22) \times 10^4$	$(6.66 \pm 0.23) \times 10^{11}$	7.75	$(2.39 \pm 0.08) \times 10^7$

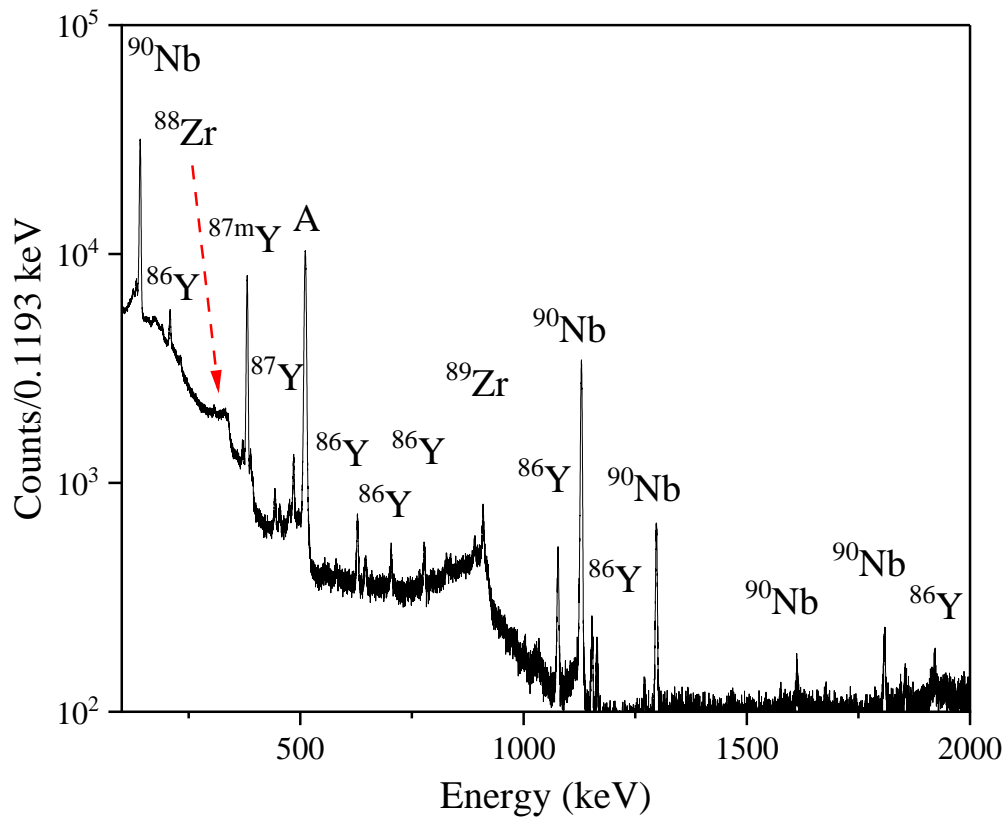


Figure 9: HPGe  $\gamma$ -ray spectrum of the Cu collector following removal from the target endstation. The spectrum was collected within 30 minutes of EOB and is not decay corrected. Beam products

co-deposited with the  $^{88}\text{Zr}$  shown in the spectrum include  $^{86}\text{Zr}$ ,  $^{89}\text{Zr}$ ,  $^{86}\text{Y}$ ,  $^{87}\text{Y}$ ,  $^{87\text{m}}\text{Y}$ , and  $^{90}\text{Nb}$ . The peak labeled “A” is the 511 keV annihilation peak.

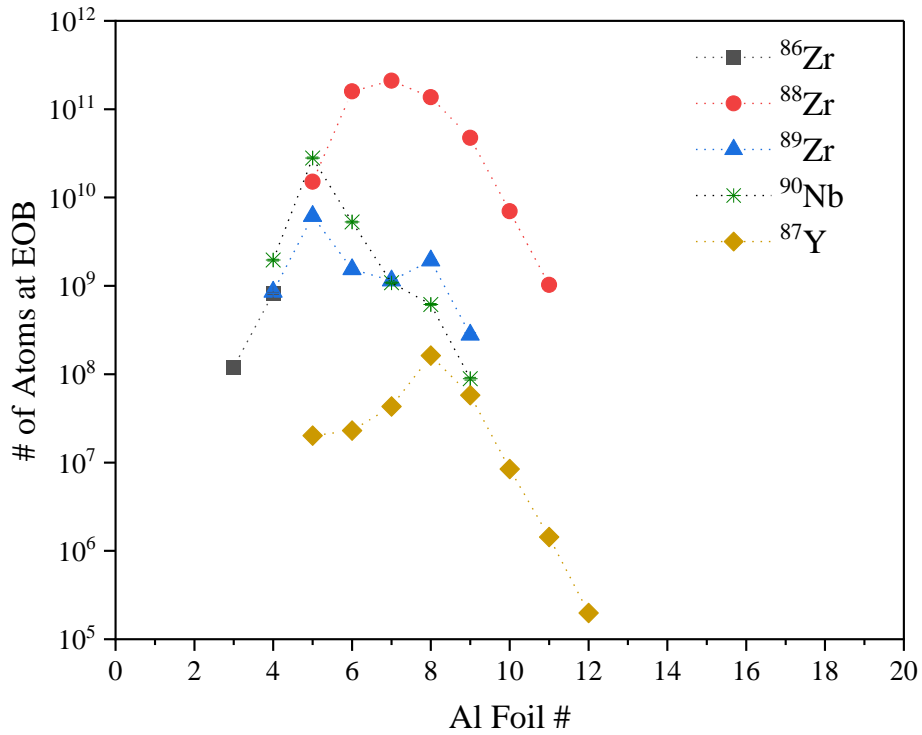


Figure 10: Distribution of beam products in the Al collector in number of atoms, decay corrected to EOB. Counting of the individual Al foils began within 6 hours from EOB. The x-axis represents each foil in the stack, with foil #1 the most upstream and first to be hit by the beam, and foil #20 the most downstream. Note that the Ta degraders and backing foils have been left out of this figure

as no activity was detected on these components. No activity was detected on foils #1, 2, or 13-20.  $^{88}\text{Zr}$  was detected in foils #5-11, denoted by stars.

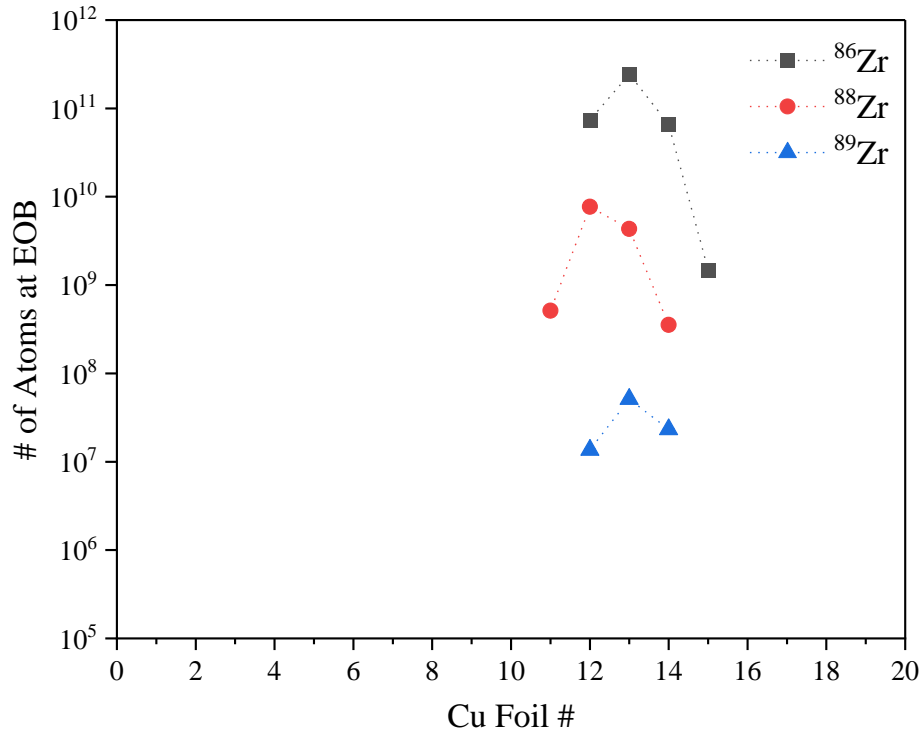


Figure 11: Distribution of beam products in the Cu collector in number of atoms, decay corrected to EOB. Foils were counted 9 days after EOB, so many of the short-lived species had decayed away before they could be detected. The x-axis represents each foil in the stack, with foil #1 the most upstream and first to be hit by the beam, and #16 the most downstream. Note that the Ta degraders and backing foils have been left out of this figure as no activity was detected on these

components. At 9 days post EOB, no activity was detected in foils #1-10 or 16.  $^{88}\text{Zr}$  was detected in foils #12-15, denoted by stars. Cu and Au foils, however, were not analyzed the same day as EOB, resulting in fewer short-lived beam products detected compared to the Al foils.

### Harvesting of $^{88}\text{Zr}$ and $^{88}\text{Y}$ from Aluminum foils

In concentrated HCl, Zr is predominantly in the form  $[\text{ZrCl}_6]^{2-}$ , which is strongly adsorbed on the anion-exchange resin. In 6 M HCl, neutral complexes such as  $\text{ZrCl}_4$  are the dominant form and weakly adhere to the resin, allowing for elution of  $^{88}\text{Zr}$  from the column in this matrix.<sup>79,53</sup> ICP-OES analysis of Al in the non-radioactive surrogate experiments showed  $(56 \pm 6.7)$  % of the total Al mass was removed via the initial precipitation, with the remainder being separated from the  $^{88}\text{Zr}$  in the concentrated HCl elution from the anion-exchange column. prior to the anion-exchange step. The total recovery of  $^{88}\text{Zr}$  was  $(86.6 \pm 5.4)$  % over five trials, with an average decontamination factor of  $2.2 \times 10^5$  (Table 7). While no Al was detected in the final  $^{88}\text{Zr}$  fractions, the limit of quantification of 10 ppb for Al in the ICP-OES for each fraction set the upper limit of Al concentration used for decontamination factor calculations. The unrecovered  $^{88}\text{Zr}$  remained with the Al precipitate (~2%) or was retained on the column (~11%).

After separation with DGA, the average  $^{88}\text{Y}$  recovery from Al over 3 trials was  $(93.1 \pm 4.5)$  % with a decontamination factor of  $2.8 \times 10^5$ . Unrecovered  $^{88}\text{Y}$  was retained on the DGA column with no other losses. Chromatograms of Al,  $^{88}\text{Y}$ , and  $^{88}\text{Zr}$  from anion-exchange and DGA separations are shown in Figures 11 and 12, respectively. A typical  $\gamma$ -ray spectrum of one of these fractions is shown in Figure S1, where the only nuclide other than  $^{88}\text{Zr}$  was the in-grown daughter

$^{88}\text{Y}$ , present from decay during the time between column elution and counting the fractions. The non-radioactive surrogate experiment showed  $(102 \pm 5.7)$  % elution of Al from the DGA column in the concentrated HCl column fractions. No Al was detected in the fractions where 1 M HCl and water was used as eluent.

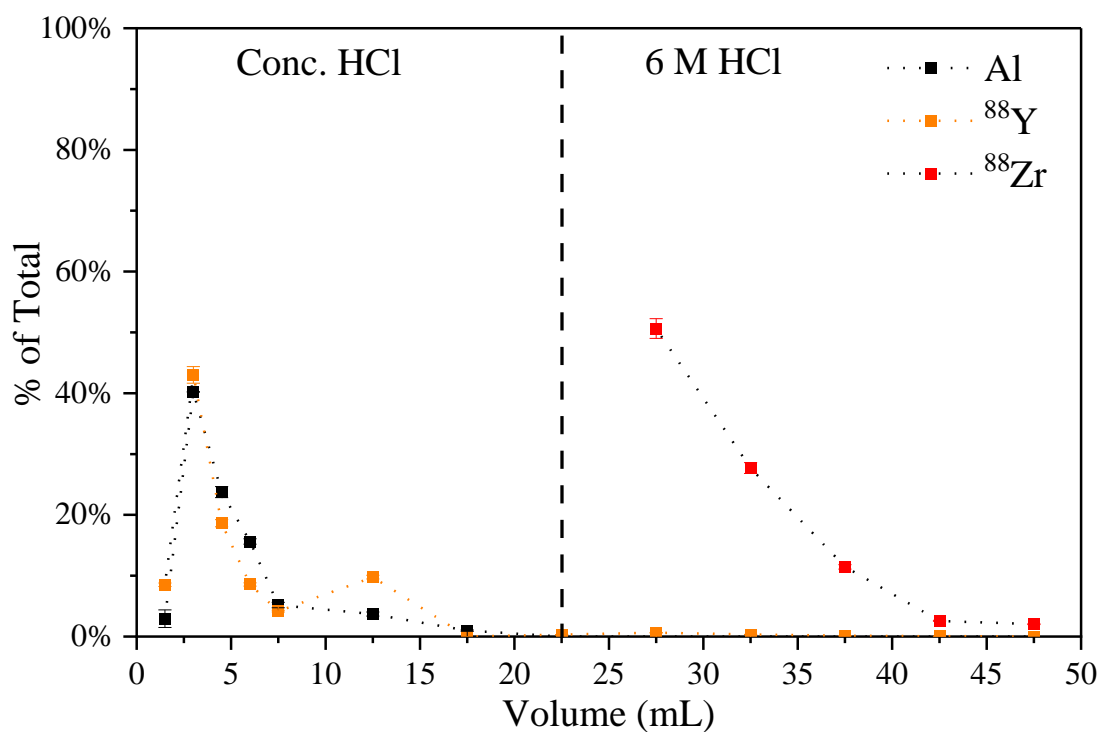


Figure 12: Sample elution curves from anion-exchange resin separation of  $^{88}\text{Zr}$  from bulk Al in HCl. Y-axis values are reported as percent of total Al content by mass or percent of the total activity of  $^{88}\text{Zr}$  and  $^{88}\text{Y}$ . The Al data were collected in a separate non-radioactive separation run

under identical conditions to the radioactive samples to allow for ICP-OES analysis. Lines are only to guide the eye.

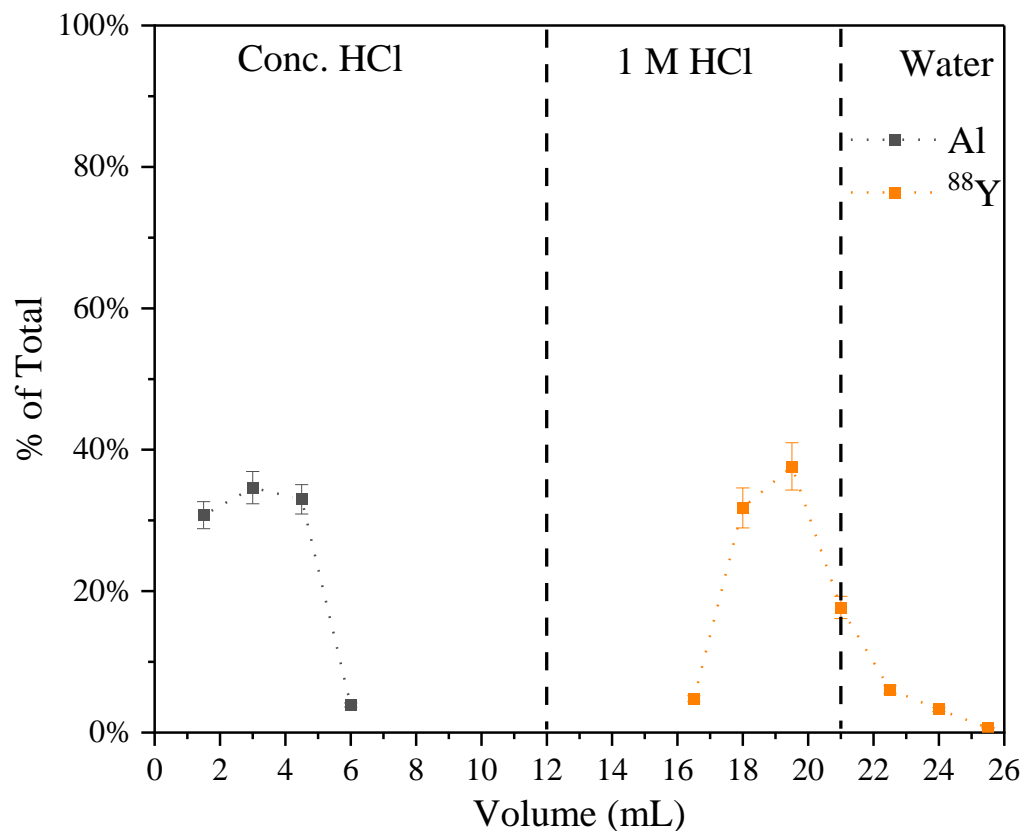


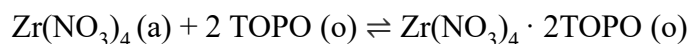
Figure 13: Elution curves from DGA resin separation of <sup>88</sup>Y from bulk Al in HCl. Y-axis values are reported as percent of total Al content by mass or percent of the total activity of <sup>88</sup>Y. The Al data were collected in a separate, non-radioactive separation under identical conditions to the radioactive samples to allow for ICP-OES analysis. Lines are only to guide the eye.

Table 7: Total recovery yields for each separation of  $^{88}\text{Zr}$  from bulk Al foils.

Trial #	Mass of Al (mg)	Total $^{88}\text{Zr}$ activity (Bq)	$^{88}\text{Zr}$ recovered (%)	Decontamination Factor
Al #1	10.9	$55 \pm 3$	$82.5 \pm 5.5$	$1.8 \times 10^5$
Al #2	9.7	$223 \pm 14$	$91.6 \pm 6.3$	$1.8 \times 10^5$
Al #3	9.6	$1060 \pm 59$	$89.4 \pm 5.6$	$1.7 \times 10^5$
Al #4	16.0	$2420 \pm 110$	$81.1 \pm 4.5$	$2.6 \times 10^5$
Al #5	17.5	$1640 \pm 81$	$88.6 \pm 5.0$	$3.1 \times 10^5$

#### Harvesting of $^{88}\text{Zr}$ and $^{88}\text{Y}$ from Copper Foils

From acidic solutions, Zr can be complexed by both acidic or neutral organophosphorus extractants.<sup>88-90</sup> This property has been exploited in many applications for selective solvent extraction of Zr from mixtures, such as in the separation of Zr from Hf.<sup>53</sup> The neutral trioctylphosphine oxide (TOPO, also known as Cyanex 921) ligand has been used to extract Zr from acidic solutions of hydrochloric or nitric acid into the organic phase.<sup>57, 89-91</sup> The extraction typically follows the following solvating scheme:



Where (a) is the aqueous phase and (o) is the organic phase containing the TOPO extractant.<sup>53, 57</sup>

The strong extraction of  $Zr^{4+}$  with TOPO in n-dodecane from acidic matrices combined with poor extraction of divalent and trivalent metals allowed for separation of Zr from both Cu and its decay product  $^{88}Y$ .  $^{88}Zr$  was quantitatively extracted from the 12 M  $HNO_3$  to the organic phase with 0.01 M TOPO solution after two passes. 12 M  $HNO_3$  was determined to be the best nitrate medium that struck a balance between extraction efficiency and back-extraction efficacy; higher concentrations of  $HNO_3$  improved extraction effectiveness of  $^{88}Zr$  but decreased back-extraction in 1 M HCl. Lower concentrations of  $HNO_3$  decreased extraction efficiency and increased likelihood of  $^{88}Zr$  hydrolysis. ICP-OES analysis showed <0.5% of the original Cu mass present in the first  $HNO_3$  wash solution, followed by <0.05% in the second of the three  $HNO_3$  washing solutions, likely due to co-extraction from the first pass of TOPO. No Cu was detected in the third  $HNO_3$  wash or any of the 1 M HCl solutions used for back extraction. The limit of quantification of 10 ppb for the ICP-OES for Cu in each sample set the upper limit of Cu concentration used for decontamination factor calculations. The average yield of  $^{88}Zr$  recovered from Cu was  $(88.4 \pm 5.4) \%$  with a decontamination factor of  $3.3 \times 10^5$  (Table 8). The unrecovered  $^{88}Zr$  remained in the nitric acid wash solutions as well as in the organic phase after back extraction.

After subsequent separation with DGA, the average  $^{88}Y$  recovery from Cu over 4 trials was  $(96.2 \pm 4.1) \%$  with a decontamination factor from Cu of  $3.7 \times 10^5$ . Unrecovered  $^{88}Y$  remained adhered to the walls of vials used to dissolve the Cu foils. The elution curves for Cu and  $^{88}Y$  are shown in Figure 14. Similar to the separation of Al and  $^{88}Y$ , DGA resin has poor uptake of Cu complexes in nitric acid, allowing for selective chelation of  $^{88}Y$ , which is strongly retained in high concentrations of  $HNO_3$ .

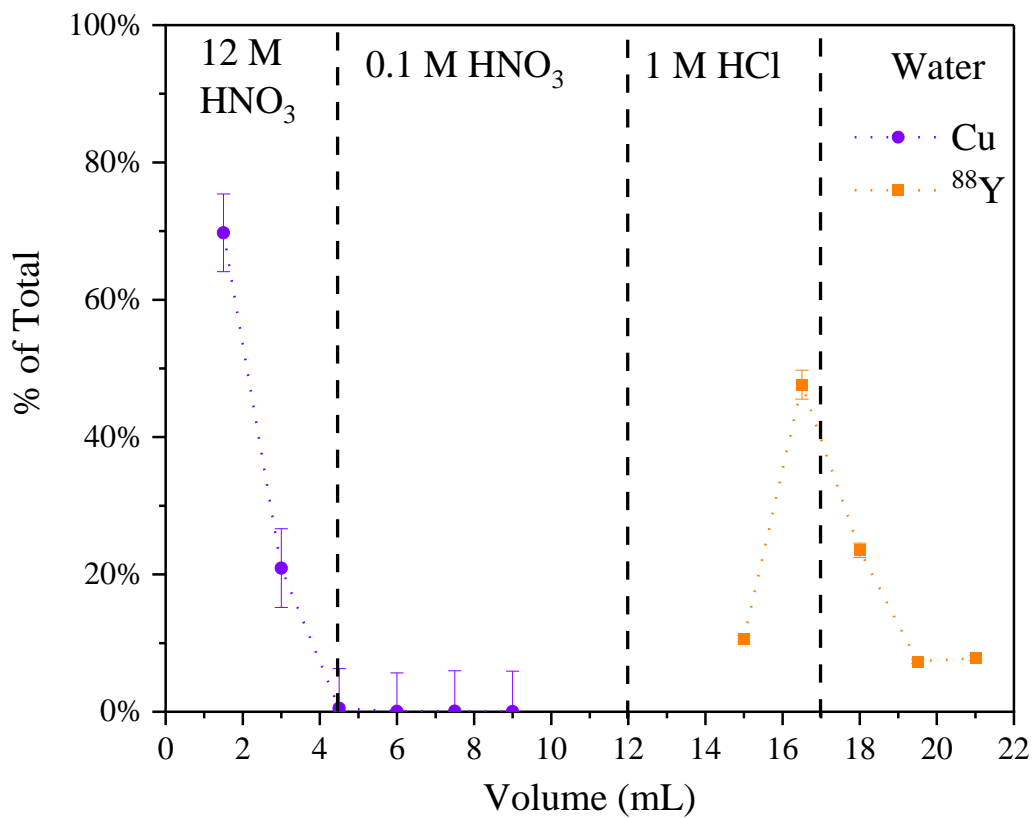


Figure 14: Elution curves from DGA resin for separation of  $^{88}\text{Y}$  from bulk Cu in  $\text{HNO}_3$  and  $\text{HCl}$ .

Y-axis values are reported as percent of total Cu content by mass or percent of the total activity of

<sup>88</sup>Y The Cu data were collected in a separate non-radioactive separation under identical conditions to the radioactive samples to allow for ICP-OES analysis. Lines are only to guide the eye.

Table 8: Total recovery yields for each separation of <sup>88</sup>Zr from bulk Cu foils.

Trial #	Mass of Cu (mg)	Total <sup>88</sup> Zr activity (Bq)	<sup>88</sup> Zr recovered (%)	Decontamination Factor
Cu #1	43.3	754 ± 41	90.2 ± 5.4	3.3 x 10 <sup>5</sup>
Cu #2	46.0	2260 ± 112	89.3 ± 4.9	3.5 x 10 <sup>5</sup>
Cu #3	43.7	77 ± 4	89.6 ± 5.7	3.3 x 10 <sup>5</sup>
Cu #4	42.6	58 ± 3	84.5 ± 5.6	3.1 x 10 <sup>5</sup>

## Conclusion

Total yields of <sup>88</sup>Zr were (86.6 ± 5.4) % from Al and (88.4 ± 5.4) % from Cu. The average decontamination factor was 2.6 x 10<sup>5</sup>. The solid-phase collection in this work showed more than three times increase in <sup>88</sup>Zr recovery compared to previous aqueous-phase isotope harvesting efforts. The higher recoveries of <sup>88</sup>Zr are attributed to maintaining the extractable Zr<sup>4+</sup> species in highly acidic conditions once in solution to avoid formation of hydrolysis products. The only detectable radioactive contaminant present at time of separation was the in-grown <sup>88</sup>Y daughter, which was also successfully separated from both <sup>88</sup>Zr and the bulk collector materials. Yields of <sup>88</sup>Y were (93.1 ± 4.5) % from Al and (96.2 ± 4.1) % from Cu. The average decontamination factor of <sup>88</sup>Y from Al and Cu was 3.3 x 10<sup>5</sup>. The average time from dissolution to finished separation of

both  $^{88}\text{Zr}$  and  $^{88}\text{Y}$  from Al and Cu was 6 hours and 4 hours, respectively. This timeline could be shortened with the use of a peristaltic pump or even future adaptation to a liquid chromatography system, potentially improving the efficiency of the separations without compromising the high recovery yields.

A proof-of-concept experiment for solid-phase isotope harvesting of  $^{88}\text{Zr}$  from Al, Cu, W, and Au collectors was demonstrated at the NSCL for application to FRIB. Foil stacks of each material were irradiated with an  $^{88}\text{Zr}$  secondary beam, then chemically processed to recover and purify the deposited  $^{88}\text{Zr}$  using a combination of anion-exchange chromatography, extraction chromatography and solvent extraction techniques. These separation methodologies developed for  $^{88}\text{Zr}$  provide a framework for harvesting Zr isotopes, other group IV elements, or elements with complex aqueous chemistry that may be better suited for solid-phase isotope harvesting. The separations here were aided by the decay of the short-lived species, however, they represent some of the dominant species even at EOB. Future experiments targeting shorter-lived products may require more complex separations schemes to accommodate the presence of more radionuclides, such as Nb isotopes in the case of harvesting neutron-deficient Zr. With FRIB recently commencing operation, expanding the isotope harvesting toolkit will make a wider array of radionuclides available to the nuclear-science community.

## Chapter 2: Solid-Liquid Extraction of Zr

### Motivation

Compared to solvent extraction, extraction chromatography resins do not need organic solution, require fewer steps in the separation process, and are less sensitive to matrix effects, which all contribute to making a more efficient separation process for a given analyte. Extraction resins can have various kinetic differences due to relying on diffusion of a solution through the resin, compared to the mixing that drives separation in solvent extraction. But due to high surface areas in a resin, extraction yields can be improved over solvent extractions with similar conditions. In radiochemical extractions, factors such as the half-lives of the radionuclides present, their decay products, and relative concentration (trace or macroscale) can significantly alter the methodologies standard in traditional chemical separation techniques. For harvesting Zr isotopes from bulk metal matrices, a faster and simpler separation method was desired compared to the previously developed, multistep solvent extractions.

Trioctylphosphine oxide (TOPO) has been used extensively in solvent extractions of Zr, which motivated this work to test TOPO-based resins as an alternative to solvent extraction.<sup>57, 89-92</sup> TOPO and other organophosphorus reagents are known to extract Zr via solvation, such as the widely studied tributyl phosphate (TBP). But TOPO is more basic than TBP ( $K_H = 8.9$  versus  $K_H = 0.17$ , respectively) where  $K_H$  is a measure of basicity called the nitric acid uptake equilibrium constant.<sup>93</sup> The increased basicity may improve Zr extraction from acidic matrices. TOPO is a

solvating extractant, so the pH of the solution will not affect its extraction capability as with other acidic organophosphorus extractants that rely on deprotonation. In this work, a TOPO-impregnated extraction chromatography resin was synthesized and used to extract Zr to improve upon the procedures outlined in the solid-phase harvesting of  $^{88}\text{Zr}$  studies.

A commercially available TOPO-based resin, called TK200 by Eichrom Technologies, is primarily used for actinide separations and radiopharmaceutical preparations of Ga isotopes. It is reported to have a weight distribution ratio (Dw) for Zr greater than 10 for all concentrations of nitric and hydrochloric acid.<sup>94</sup> Notably, the structure of the polymer backbone and subsequent synthetic process is not reported, but the published particle size range is 50-150  $\mu\text{m}$ . While the polymer support that makes up the resin backbone is proprietary, it is assumed that the resin is likely coated with TOPO, and not functionalized. Therefore, a need for an extraction chromatographic resin optimized for Zr recovery under harvesting conditions motivated this work. The synthesized resin in this work uses a mesoporous, inert polymer called Amberlite XAD-7 impregnated with TOPO. This resin has a large pore diameter (90  $\text{\AA}$ ) and surface area (450  $\text{m}^2/\text{g}$ ), which can allow for an extractant like TOPO, to fill the pores easily. The large particle size (20-60 mesh) allows for eluent to flow quickly, which is suitable for rapid and scaled-up separations required for isotope harvesting from metal components at FRIB.

In this work, a TOPO solvent impregnated resin (SIR) was created using XAD-7 acrylic polymer resin. The resin can hold large quantities of ligand while also not requiring a complex synthetic procedure. With the solvent impregnation technique, a ligand (such as TOPO) is dissolved in a diluent and mixed with the polymer backbone. Then the solvent is evaporated off,

leaving the ligand coating the support. The SIR requires no synthesis pathway to graft the extractant to the surface of a polymer, yet still provides a robust solid-liquid extraction chromatographic resin. The XAD series of resins have been used to generate SIRs containing various extractants, including TOPO, for various extraction applications. Examples include separations of selenium and arsenic, removal of cadmium from water, U adsorption, and isolation of other heavy metals.<sup>95-99</sup> Other sources report using solvent impregnated XAD resins for Zr separation, albeit with extractants other than TOPO.<sup>100</sup> Described here is the first work to the best of my knowledge where a TOPO impregnated resin using XAD-7 was used for Zr extractions relevant to radiochemical separations. Specifically, this work focused on the extraction of <sup>88</sup>Zr from bulk metals using TOPO impregnated resin, aiming to improve separation efficiency compared to traditional ion-exchange or solvent extraction methods. Once fully optimized, the resin could be scaled up and adapted for Zr harvesting. If proven effective, the TOPO based resin may be a viable option easily amenable to separating Zr from bulk metal matrices for isotope harvesting.

## Solvent Extraction Batch Studies

Before synthesis and testing of a TOPO based resin, the chemistry of TOPO extraction needed to be further explored to identify ideal extraction conditions for Zr. The trend in extraction of Zr from acidic solutions should be similar in solvent extraction compared to that of a solid-phase extraction because the largest contributing factor Zr extraction is its complex formation. However, the kinetic effects on Zr extraction will differ due to the difference in turbulent mixing

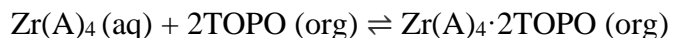
in solvent extraction versus the diffusion flow of a solid-liquid separation. Therefore, an important question to answer is if the increased surface area contact of an extraction resin will provide better or worse extraction capability compared to solvent extraction. Exploratory solvent extractions will offer insight into what acid concentrations provide significant extraction of Zr, which will guide the ideal conditions when translated to solid-liquid extractions.

Trace Zr speciation in acidic aqueous solutions (absent of any strong organic complexants) is dependent upon the type of acid present and its concentration due to the complexation chemistry of the conjugate base. For example, in hydrochloric acid concentrations of 4-6 M HCl, Zr begins to form predominantly neutral complexes such as  $ZrCl_4$ , whereas above 6 M HCl anionic complexes dominate.<sup>88,53</sup> Extractability of Zr can also be enhanced by addition of an anion from salts, such as NaCl for  $Cl^-$  when controlling for HCl concentration. The general trend reported in the literature for stability constants of the following anions with Zr decreases in the order of  $OH^- > F^- > SO_4^{2-} > NO_3^- > Cl^-$ , which is correlated with their decreasing trend in pKa values.<sup>53</sup> Zr extraction using neutral organophosphorus extractants from nitric and chloride media has been thoroughly explored for applications in nuclear science.<sup>53, 101</sup> Zr extraction by neutral organophosphorus reagents is highly dependent on acid type and concentration, as the complex formation of Zr must be neutral to be extracted.<sup>57</sup> In addition, the initial solid-phase harvesting work detailed in chapter 1 utilized TOPO for extraction from 12 M  $HNO_3$  solutions and subsequent back extraction into 1 M HCl, yielding 85% extraction of Zr ( $D=5.7$ ) with 3 minutes of contact time. This developed procedure was suitable for solvent extraction and thus was extrapolated to solid-liquid extraction chromatography. Herein, more detailed analysis into the extraction

chemistry of Zr from nitric and chloride matrices was investigated for application in solid-phase extraction of Zr using a TOPO based resin.

### Studying effects of Acid Concentration

Previous work demonstrated increasing extraction of Zr with increasing [HNO<sub>3</sub>] with 0.01 M TOPO in dodecane, discussed in chapter 1 (Figure 16). This matches the reported trend in the literature for extraction of macro-amounts of Zr from HNO<sub>3</sub> solutions where D>1 above 2 M HNO<sub>3</sub>.<sup>90</sup> This trend is different than that of HCl, which peaks in extraction yield in the 4-6 M HCl range due to the predominant formation of neutral Zr complexes in this range. However, due to the complexity of Zr speciation chemistry, differences in Zr concentration, ionic strength, pH, and Zr starting material, conflicting extraction trends have been observed and thus makes normalizing Zr extraction conditions to compare to this work difficult.<sup>53, 89, 102</sup> With TOPO, the reported mechanism of extraction is through the following solvation scheme:<sup>101</sup>



Zr solvation by TOPO proceeds when four coordination sites are occupied by a conjugate base (A), such as Cl<sup>-</sup> or NO<sub>3</sub><sup>-</sup>. Here, the NO<sub>3</sub><sup>-</sup> can be mono or bidentate. However, the following mechanism is more likely if Zr has a coordinated O, as shown below.<sup>103,102</sup>



TOPO molecules in the organic phase can solvate, or coordinate with the Zr<sup>4+</sup> nitrate complex in the aqueous phase, which causes solubility of the Zr complex in the organic phase.

Solubility in organic phase is attributed to the lower charge density of the neutral complexes.<sup>104</sup> A 1:1 molar ratio of Zr to TOPO in extraction has been reported from HCl as  $\text{ZrCl}_4 \cdot \text{TOPO}$ .<sup>91</sup> From  $\text{HNO}_3$ , a 1:1 ratio may be attributable to bidentate chelation by  $\text{NO}_3^-$  to  $\text{ZrO}$ .

To determine the extraction trend of Zr, solvent extractions using 0.01 M TOPO in n-dodecane were performed on trace  $^{88}\text{Zr}$  solutions in varying concentrations of mineral acid. The organic phase was pre-equilibrated with the appropriate acid for each extraction for a minimum of 30 minutes of contact time. The solutions were mixed on a vortex mixer each for 3 minutes with a 1:1 volume ratio of organic: aqueous phase, then separated by pipette for nuclear counting. Samples were counted on a NaI scintillation gamma-ray spectrometer. The extraction yields plotted as a function of acid concentration for hydrochloric and nitric acids are shown in Figure 15 and Figure 16 below. Yields were taken as ratio measurements of the  $^{88}\text{Zr}$  count rates in the aqueous solution after relative to the initial count rate before contact with the organic extractant solution. Associated uncertainties are mostly attributed to random counting statistics and uncertainty from imperfect phase separation of the aqueous and organic phases. Uncertainties were propagated using the relative uncertainty for each error contribution to the total measurement and were within  $1\sigma$  uncertainty.

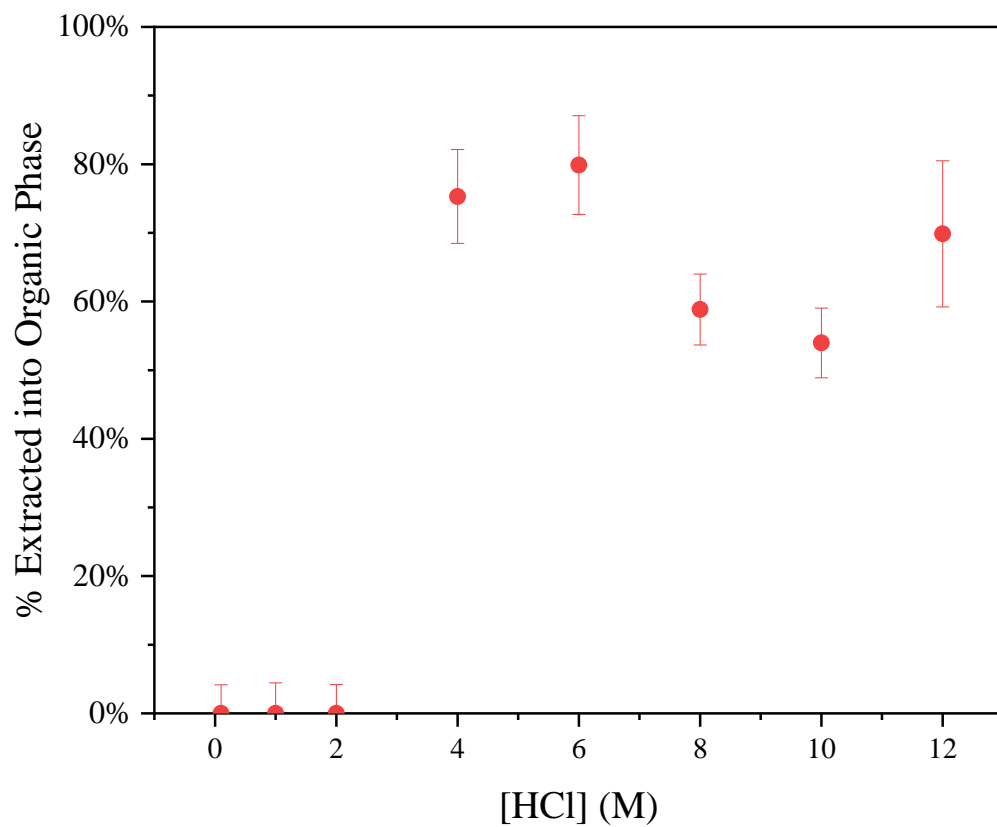


Figure 15: Zr extraction yields from varying HCl concentrations into 0.01 M TOPO in n-dodecane. Error bars represent propagated uncertainties dominated by nuclear counting statistics and sampling volumes.

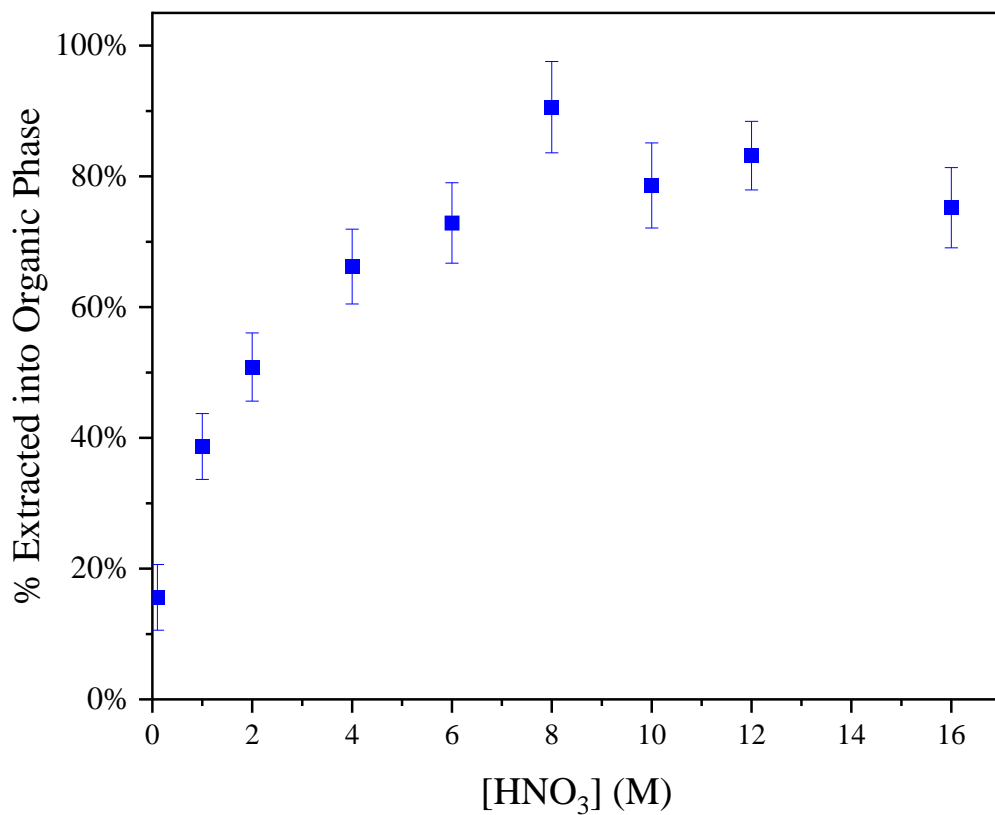


Figure 16: Zr extraction yields from varying HNO<sub>3</sub> concentrations into 0.01 M TOPO in n-dodecane. Error bars represent propagated uncertainties dominated by nuclear counting statistics and sampling volumes.

Stability constants for Zr in chloride and nitrate matrices were compiled from Wang et al at an ionic strength of 2. These were calculated by the following formula:

$$\beta = \frac{[\text{Zr}(\text{A})_n]^{4-n}}{[\text{Zr}^{4+}][\text{A}^-]^n} \quad \text{Equation 15}$$

Where A= Cl<sup>-</sup> or NO<sub>3</sub><sup>-</sup>. For all values of n, the stability constants (β) were below 1, indicating favoring of the reactant side of the equilibrium.<sup>53</sup> This shows predominant formation of uncomplexed Zr<sup>4+</sup> in solution. As such, higher concentrations of HCl and HNO<sub>3</sub> will drive the equilibrium to the right and form more complexed Zr species.

From HCl, the highest extraction yields occur in the range of 4-6 M HCl as seen in Figure 15. In this concentration range, Zr forms neutral chloride complexes, which allow for solvation by TOPO. Here, two active sites likely contain coordinated water molecules to the metal center that the oxygen in the phosphine oxide (P=O) bond from TOPO can displace to coordinate to the Zr<sup>4+</sup> metal center (Figure 17). In concentrations above 6 M HCl, more Cl<sup>-</sup> atoms are coordinated to the metal center (up to six, ZrCl<sub>6</sub><sup>2-</sup>, in concentrated HCl), which are not easily displaced by the TOPO ligand. Below 4 M HCl, cationic Zr complexes form, which are thought to be mixtures of complexes such as [Zr(H<sub>2</sub>O)<sub>x</sub>(OH)<sub>y</sub>]<sup>4-y</sup> · 4-yCl<sup>-</sup>, [Zr(H<sub>2</sub>O)<sub>x</sub>Cl<sub>y</sub>]<sup>4-y</sup> · 4-yCl<sup>-</sup>, or various Zr(OH)<sub>x</sub><sup>4-x</sup> (x=1-6) when not polymerized, and thus are not able to be coordinated by the TOPO ligand. Here, x+y=6 since Zr (IV) has a coordination number of 6.

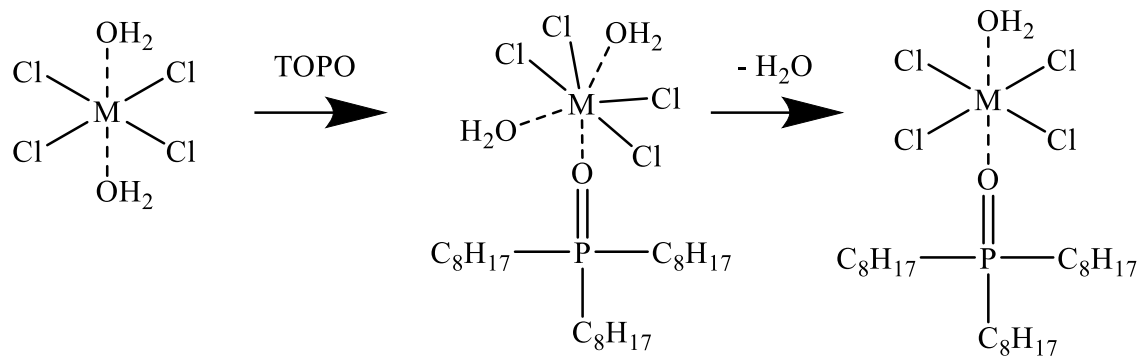
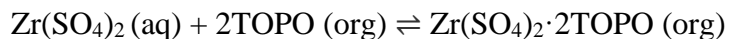


Figure 17: General extraction mechanism for Zr by TOPO.

The increase in nitric acid concentration increases the extraction yield of Zr approaching a maximum from concentrated acid. This is attributed to formation of  $ZrO(NO_3)_2$  or  $Zr(NO_3)_4$  complexes with higher concentrations of  $NO_3^-$ . Just as from HCl, the TOPO molecule can coordinate these neutral complexes through the O of the P=O bond. Other studies confirmed that the  $H^+$  has no effect on the Zr extraction, implying that  $H^+$  does not participate in the extraction and that it must be the  $NO_3^-$  concentration that affects TOPO coordination to Zr.<sup>102</sup> One factor that can change this extraction trend is competition with  $NO_3^-$  for extraction by TOPO or other organophosphorus based extractants.<sup>102</sup> This only holds true for macro-concentrations of Zr where the number of TOPO molecules does not exceed the amount of anions and Zr by multiple orders of magnitude. Kinetically, Zr may exhibit faster extraction in nitric acid compared to hydrochloric acid due to the lower charge density of nitrate groups than chloride, causing preferential distribution into the organic phase.<sup>104</sup>

Zr has a much higher stability constant with  $SO_4^{2-}$  than  $Cl^-$  and  $NO_3^-$ . Therefore, extraction with an organic extractant such as TOPO is less favorable from sulfuric acid solutions, as the

TOPO ligand is unable to displace the sulfate anion. In 0.25 M H<sub>2</sub>SO<sub>4</sub>, Zr(SO<sub>4</sub>)<sub>2</sub> is the dominant species, which is extracted by TOPO.



Above 0.25 M, anionic Zr(SO<sub>4</sub>)<sub>3</sub><sup>2-</sup> becomes more prevalent, which are not extractable via solvation.<sup>53, 105</sup>

### Effect of TOPO Concentration

The concentration of TOPO in dodecane has a profound effect on both the extraction and back extraction of Zr from aqueous solutions. Solutions of 12 M HNO<sub>3</sub> containing a known quantity of <sup>88</sup>Zr were created and then contacted with various concentrations of TOPO in n-dodecane solutions for 3 minutes. The organic phase was then counted on a NaI well detector in the same geometry as the initial <sup>88</sup>Zr to analyze how much was extracted. As shown in Figure 18, the minimum concentration tested that extracted Zr was 1 mM TOPO with 0.1mM TOPO showing no Zr extraction. At 0.01 M TOPO, extraction yields were approximately 85%, approaching an asymptote in extraction yield up to 0.05 M TOPO. These same extractions gave a distribution ratio above 1 when the TOPO concentration exceeded 1mM TOPO (Figure 19A). A common method for determining an extractant to metal ratio is by plotting the Log (D) versus the log of the extractant concentration in M ([extractant]), where the slope of a linear fit can determine the approximate ratio of the dominant extracted complex. When plotting the log (D) versus log [TOPO], a line of best fit was attempted to fit the data to determine the TOPO:Zr ratio during extraction (Figure 19B). However, this data did not show a strong linear correlation. Under these

conditions, a cubic polynomial function best fit the data, with a coefficient of determination (COD), or  $R^2$  value of 0.9995. This deviation from linearity might be attributable to marginal improvements in extraction with increasing TOPO concentration above 0.005 M TOPO. The Zr extraction from nitric acid is also highly dependent on the free  $\text{NO}_3^-$  concentration, therefore the  $\log(D)$  versus  $\log [\text{HNO}_3]$  was plotted and fit with a trendline (Figure 20). Here, a linear fit is suitable with an  $R^2=0.94$ . If the outlier D value for concentrated  $\text{HNO}_3$  is removed, a stronger fit with  $R^2=0.97$  is achieved. It is unclear why concentrated nitric had a reduced distribution ratio and requires repeating to verify if there is a downward trend within error. One hypothesis is that  $\text{HNO}_3$  is competing with Zr for extraction by TOPO, so above 12 M  $\text{HNO}_3$  a reduced extraction yield of Zr is observed. Based on these trends, it is confirmed that the extraction of Zr with TOPO depends strongly on the complexant ( $\text{NO}_3^-$  or  $\text{Cl}^-$ ) concentration in solution, however the precise ratio of TOPO:Zr in the extracted complex is not confirmed. No fit was identified with HCl, as the extraction yields were irregular and only nonzero at 4 M HCl and above.

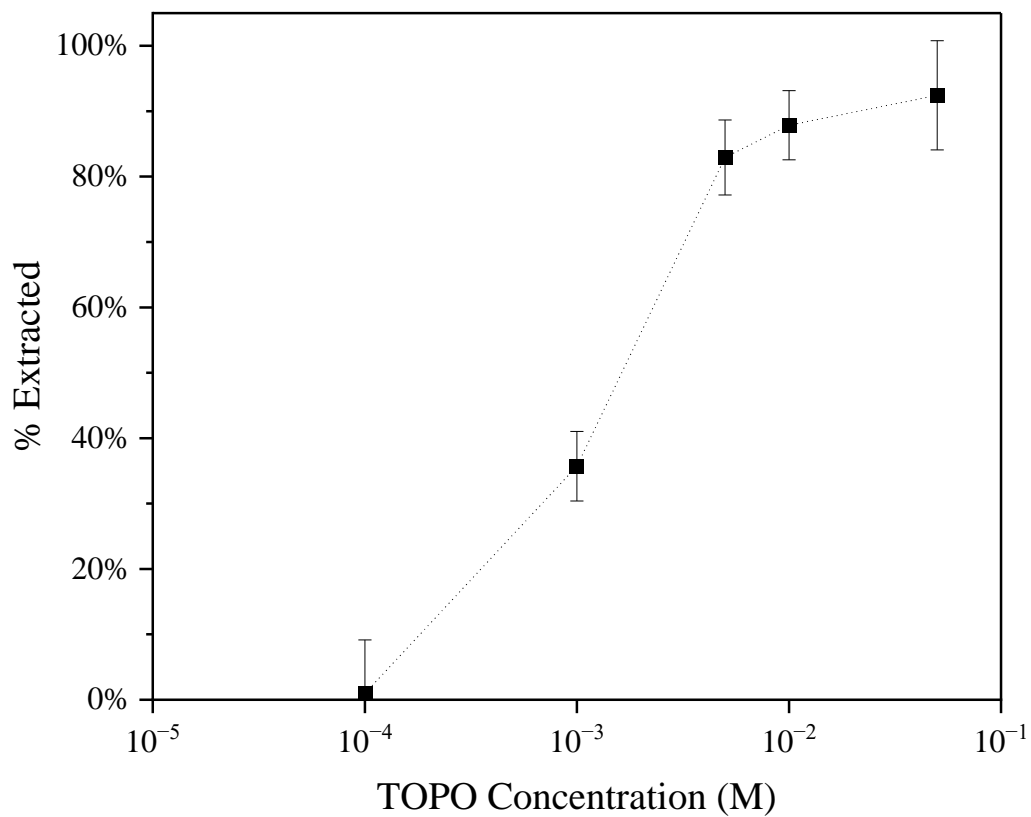
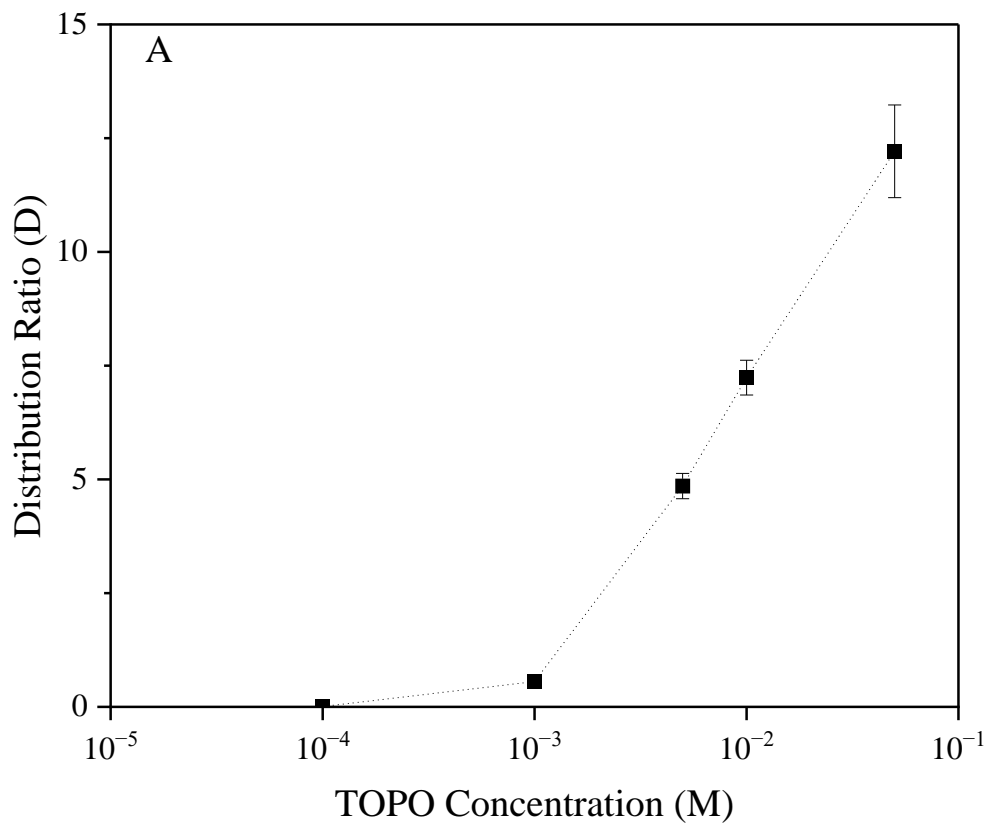


Figure 18: The effect of TOPO concentration on Zr extraction yields from 12 M HNO<sub>3</sub>. 3 minutes of contact time, 1:1 o:a volume ratio



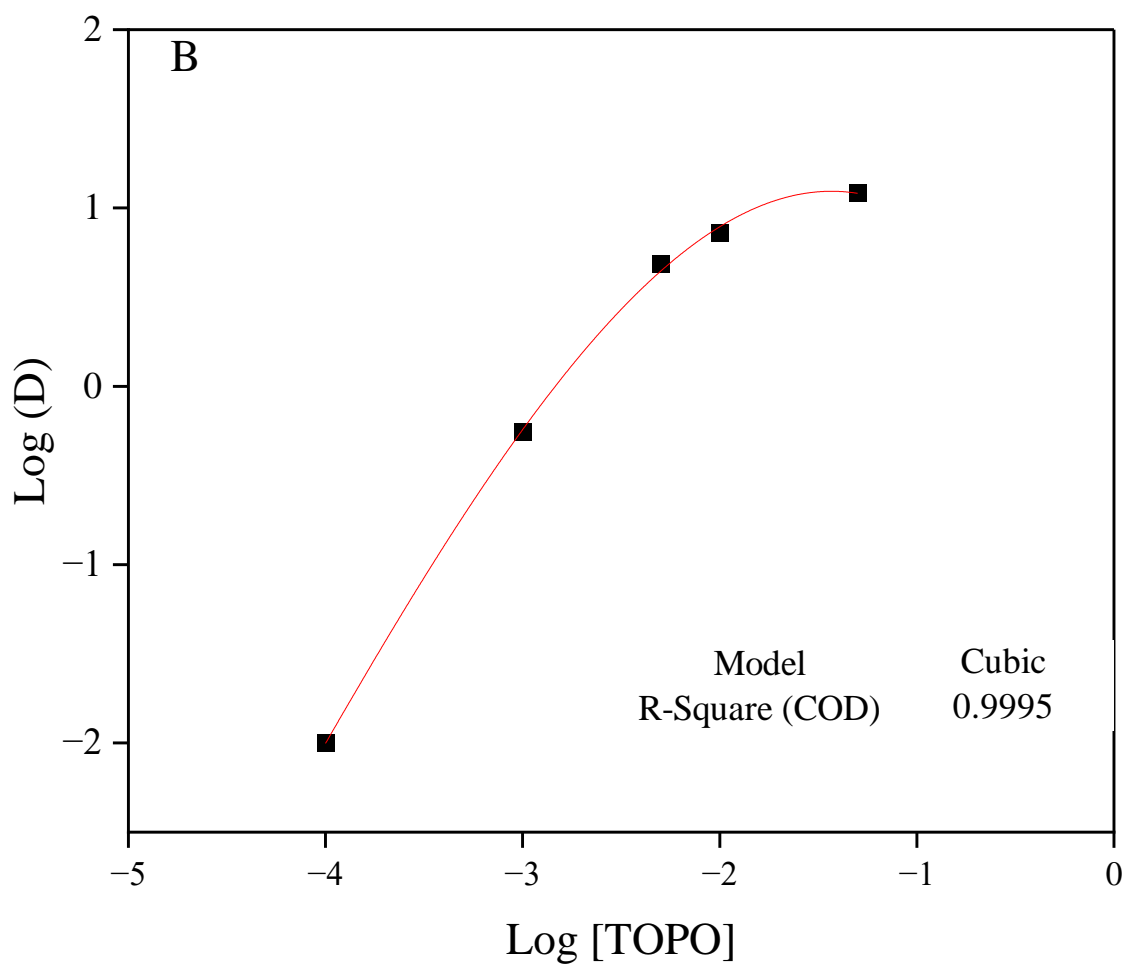


Figure 19: A, top) The effect of TOPO concentration on distribution ratios for Zr extraction. B, bottom) Log (D) vs Log (TOPO concentration) fit with a cubic polynomial function.

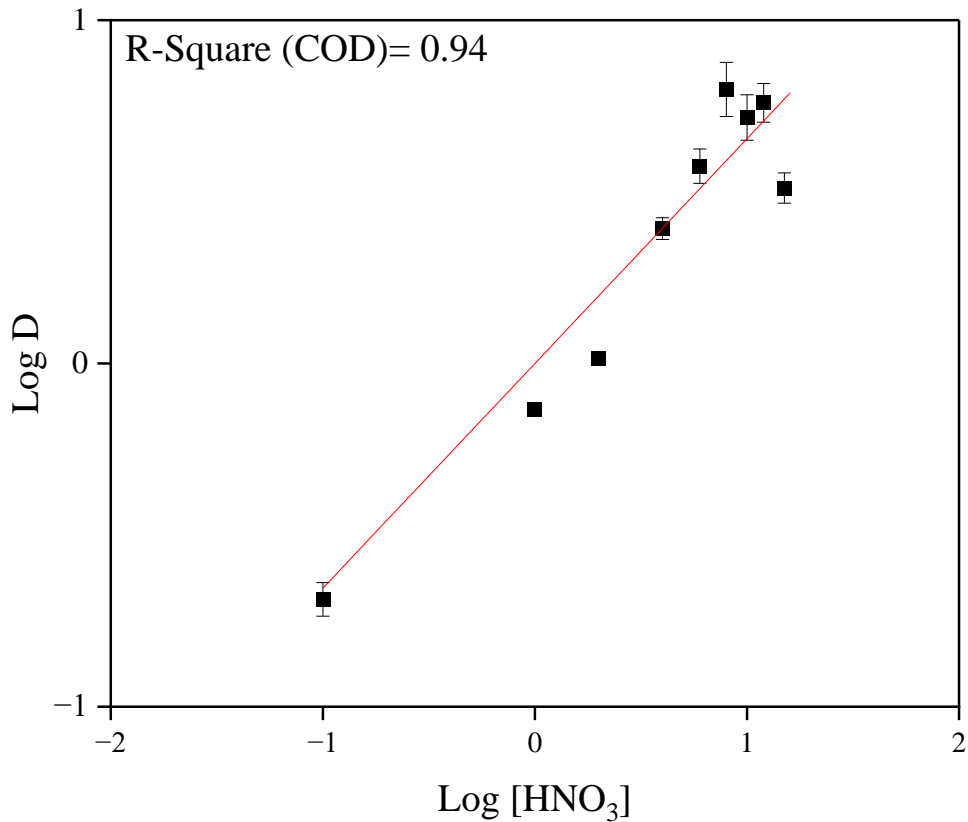


Figure 20: Log (D) vs Log [HNO<sub>3</sub>] with a linear trendline.

### Back Extraction studies

When determining the best conditions for Zr extraction using TOPO, the TOPO concentration should be considered if back extraction of Zr into an aqueous phase is required. TOPO binds strongly to Zr, so release from the extractant back into an aqueous phase is

thermodynamically and kinetically limited. In back extraction, low retention is desirable since the goal is to remove Zr from the solvated complex in the organic phase and cause it to transfer into the aqueous phase. Therefore, low HCl concentrations below 4 M HCl were chosen to back-extract Zr. 1 M HCl was suitable for back extraction from 0.01 M TOPO with a minimum of 3 passes at 3 minutes each to yield >85% of the Zr back in the aqueous phase. When the TOPO concentration is increased to 0.05 M, the total yield of Zr back extracted after 3 passes decreases to 50% ( Figure 21). Subsequent extractions were performed with 0.01 M TOPO as it was the best balance of extraction and back extraction yields. No correlation was observed between the back extraction yields and initial HCl concentration Zr was extracted from, further demonstrating that the TOPO concentration drives the back extraction yields of Zr.

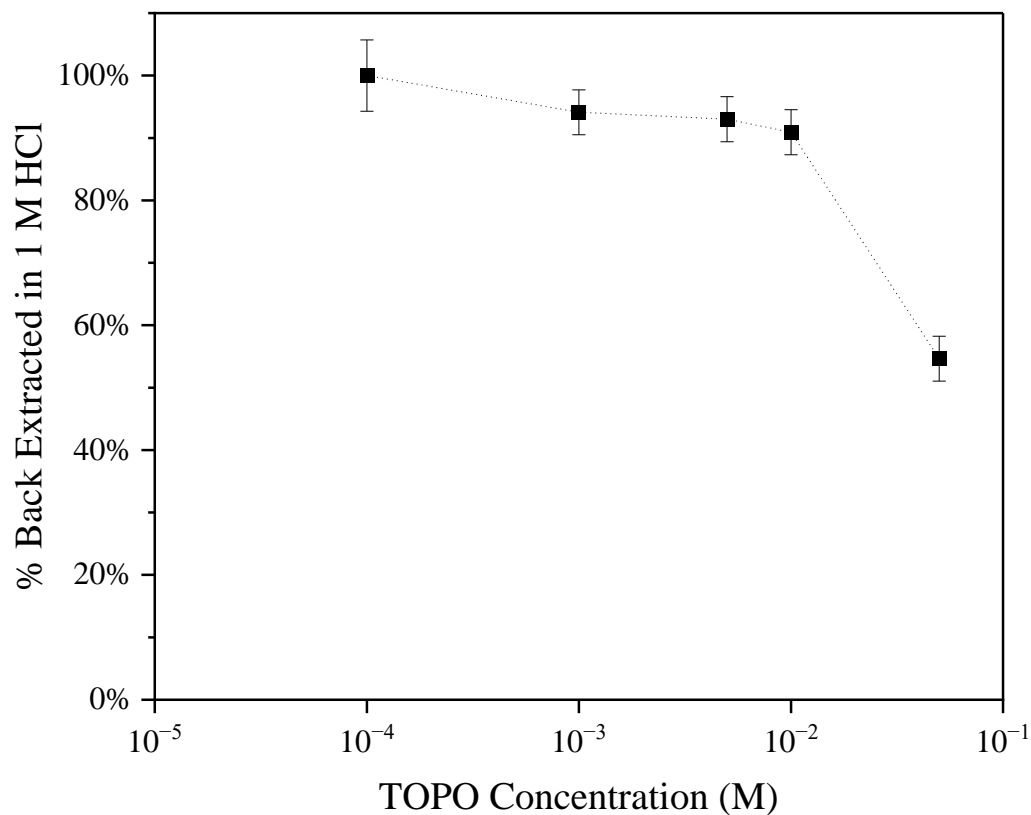


Figure 21: The percent of Zr back extracted into 1 M HCl vs initial TOPO concentration.

Organic solutions used to test the effect of  $\text{HNO}_3$  concentration on Zr extraction were used to test the back-extraction of Zr into 1 M HCl and plotted in Figure 22. Here, the amount of Zr back extracted into solution is relative to the amount of Zr in the organic phase. In this study, the initial concentration of  $\text{HNO}_3$  seems to not affect the back extraction into 1 M HCl above 2 M  $\text{HNO}_3$ , implying that the extracted Zr species is the same  $>2$  M  $\text{HNO}_3$ . Because of this, the effect

of increasing  $\text{HNO}_3$  concentration improving the Zr extraction into the organic phase is likely due to formation of more  $\text{Zr}(\text{NO}_3)_4$  complexes that can be extracted.

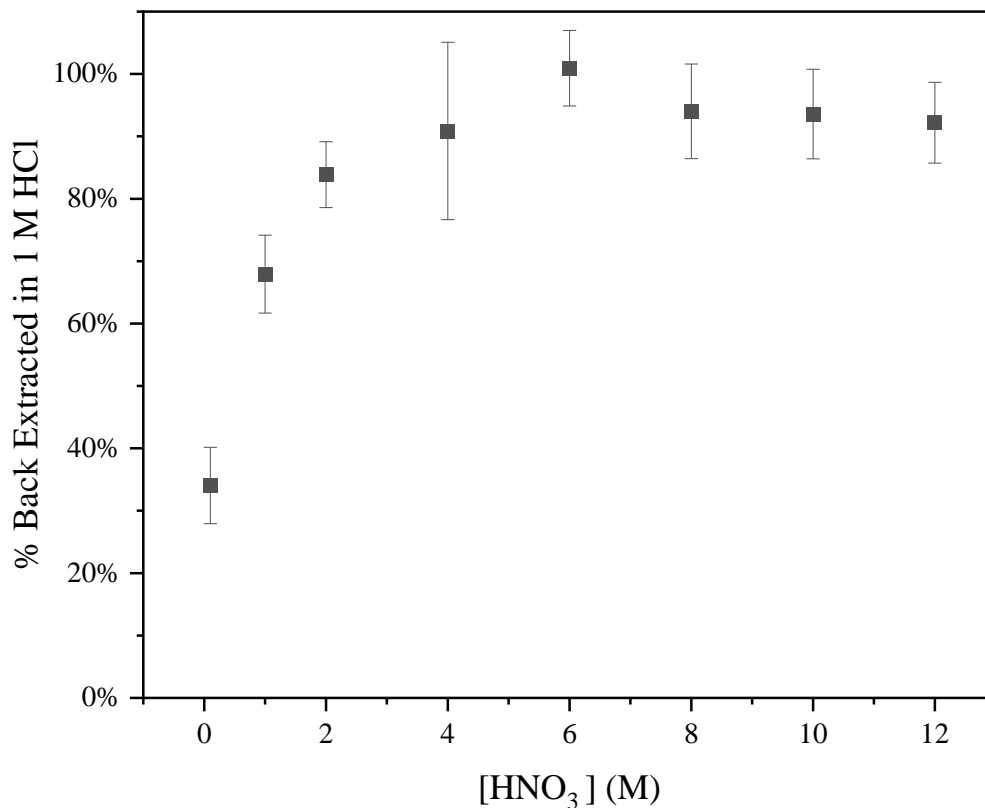


Figure 22: The percent of Zr back-extracted into 1 M HCl vs initial  $\text{HNO}_3$  concentration.

#### Extraction from Bulk Cu Solutions

Extractions of Zr from bulk Cu matrices were tested to see if the difference in ionic strength and presence of a bulk metal would interfere with Zr recovery. Results from HCl are

shown in Figure 23 and those from  $\text{HNO}_3$  in Figure 24. Cu was chosen as the bulk metal as a continuation from the solid-harvesting work, and was made by dissolving 42-47 mg in 500  $\mu\text{L}$  of acid to make approximately 80,000 ppm Cu solutions. From HCl, no significant difference was observed in Zr extraction up to 6 M HCl. However, deviations were observed above 6 M HCl, where the presence of Cu hinders Zr extraction. Cu and Zr both form anionic chloride complexes in this range, which are not extractable by TOPO. However, neutral copper chloride complexes that are square planar/tetrahedral in geometry can be extracted by TOPO and compete with Zr extraction.<sup>106</sup> Cu is partially extracted by TOPO above 7 M HCl, but not in any  $[\text{HNO}_3]$ .<sup>107</sup> Cu can also hinder extraction by blocking interactions between the Zr and TOPO since it is multiple orders of magnitude higher in concentration in solution than Zr. In  $\text{HNO}_3$ , a slight enhancement in Zr extraction occurs with the presence of Cu. This is due to the formation of hydrated Cu complexes, which pull water molecules out of solution. This can drive up the free  $\text{NO}_3^-$  concentration and cause more formation of extractable Zr nitrate species.

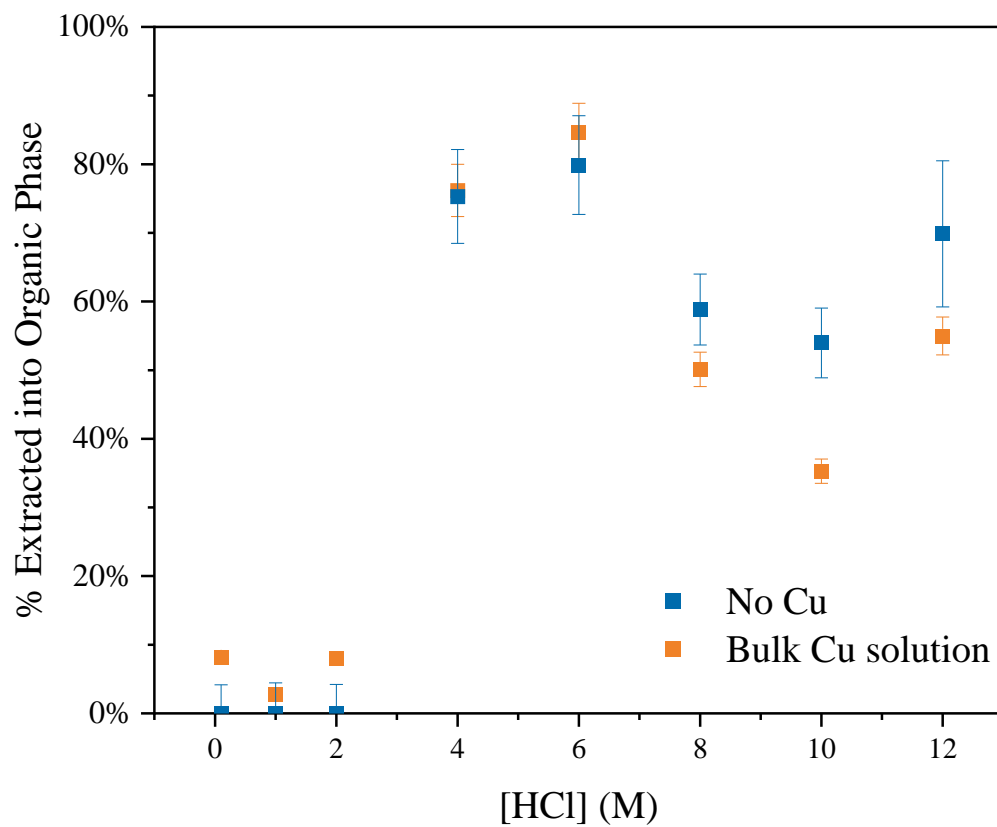


Figure 23: Zr extraction yields from varying HCl concentration both with and without bulk Cu dissolved in solution.

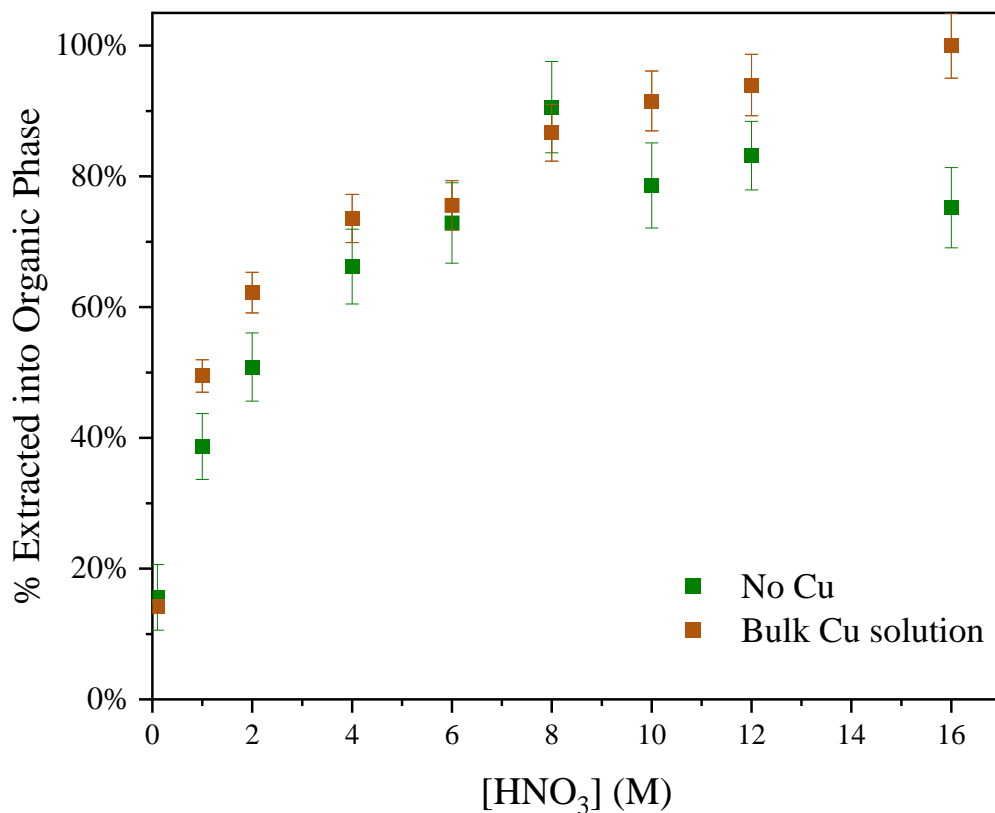


Figure 24: Zr extraction yields from varying HNO<sub>3</sub> concentration both with and without bulk Cu dissolved in solution.

Since the back extraction step is kinetically limited, the presence of Cu may inhibit back extraction of Zr if it was co-extracted or incompletely separated from the organic phase. Therefore, back-extractions from various HNO<sub>3</sub> solutions containing bulk Cu were also plotted to see the effect of Cu. With Cu present, the back-extraction is significantly hindered as seen in Figure 25.

The reduced back extraction yield of Zr into 1 M HCl may be due higher amounts of Cu in the organic phase, which limits phase transfer of Zr back into the aqueous phase.

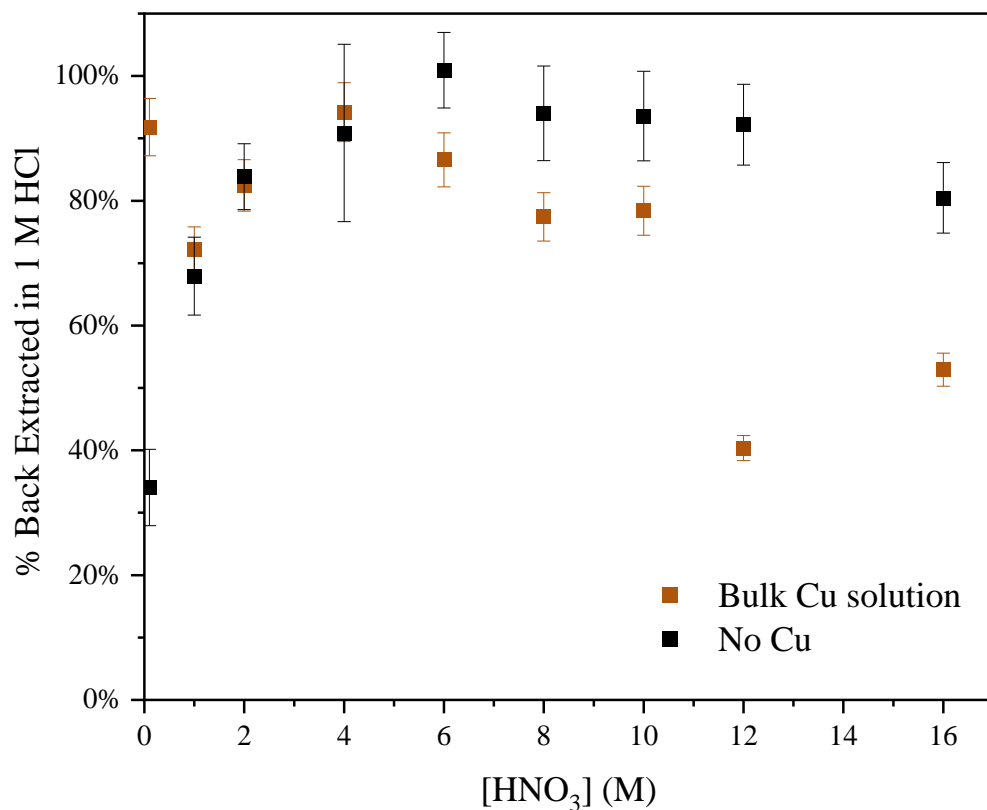


Figure 25: Effect of initial HNO<sub>3</sub> concentration on back extraction into 1 M HCl.

## Synthesis of TOPO Resin

Solvent impregnated resins (SIRs) have a wide range of uses and are relatively simple to make compared to functionalized resins. In functionalized resins, the ligand is chemically attached to the resin surface, either directly or by grafting to a linker that bonds to the resin. In SIRs, the resin merely coats and fills the pores of a resin, typically held in place by weak intermolecular interactions like Van der Waals forces or hydrogen bonding. The general approach to make a SIR is to mix the extractant dissolved in an organic solvent with the polymeric resin for a period of time, then evaporate the solvent off, which leaves the extractant behind on the polymer. With SIRs, a robust polymer backbone can be combined with a wide range of extractants to create a resin suitable for solid-phase extraction of a given analyte for a wide range of applications.

To make the TOPO SIR, the XAD-7 resin backbone must first be conditioned. This is to remove the salts and excess water that the resin is stored with to prevent bacterial growth. To do so, the resin is mixed thoroughly with purified water and decanted. Then, the resin is washed with 0.1 M HNO<sub>3</sub>, followed by water until the decanted solution registers neutral. Finally, the resin is washed with methanol or acetone several times and filter dried with vacuum to remove residual water. In this state, the XAD-7 is considered conditioned and is notably electrostatically charged compared to the resin before washing. Up to 70% mass loss is observed with one washing procedure, so a majority of the resin by mass contains, water, salts, and likely excess monomer. A second wash yields less than 10% mass loss, so repeated conditioning is not necessary.

Once conditioned, the TOPO can be impregnated into the resin. Previously reported TOPO SIR synthetic methods recommend not exceeding 40% loading of extractant by mass, as this can cause crystallization of the extractant on the surface of the resin and leeching when used in column format.<sup>97</sup> To load the TOPO into the resin, conditioned XAD-7 is weighed and placed in a polypropylene tube. Solid TOPO is weighed separately at approximately 50% of this recorded mass value. A 50% TOPO to XAD-7 mass ratio was utilized for synthesis due to losses of TOPO during the synthetic process. The TOPO is then dissolved in acetone or methanol by adding the solvent in a minimum ratio of 5 mL per 500 mg of XAD-7 and mixing on a vortex mixer for several minutes until completely dissolved. This solution is added to the XAD-7 then mixed overnight on a sample rotator. More solvent can be added to ensure proper mixing. Once mixed overnight, the solvent is removed by filtering and air drying. However, this does cause significant losses of TOPO and takes several hours of time, so it can be more efficiently removed without losses by using a rotary evaporator. This procedure, modified and experimentally tested from those reported in the literature, yields approximately 30-35% TOPO loaded by mass in the resin after losses during the process.<sup>97</sup>

## Characterization of TOPO Resin

### Infrared Spectroscopy

Once a resin is impregnated with TOPO, IR spectroscopy is used to identify characteristic chemical bonds present. Vibrational modes from the TOPO molecule that are not present in the XAD-7 acrylic backbone are ideal for characterization of the synthesized resin. For example,

tertiary phosphine oxide bonds ( $R_3P=O$ ) show absorbance in the 1100-1200  $cm^{-1}$  range, which was experimentally confirmed with IR absorbance of TOPO crystals that show a strong absorbance at 1155  $cm^{-1}$ . While the XAD-7 acrylic backbone should not contain phosphorus, a broad absorbance overlapping with the trialkyl phosphine oxide stretch in the range of approximately 1070-1200  $cm^{-1}$  was observed. This is likely due to C-O bonds that exist in the resin or a phosphorus impurity. Carbonyl (C=O) bonds also in the resin are present as a sharp peak at 1724  $cm^{-1}$ . However, the XAD-7 does not show strong absorbance around 2900-3000  $cm^{-1}$ , even with the presence of  $sp^3$  hybridized C-H bonds. TOPO does show absorbance in this range due to the octyl groups. These changes in absorbance between pure TOPO and XAD-7 are enough to give context on whether the synthesized resin contains TOPO. A lack of vibrational shifts in absorbance at the P=O (1100-1200  $cm^{-1}$ ) and C=O peaks (1724  $cm^{-1}$ ) shows that no formal bonding is occurring, as expected in a SIR. The IR spectra of interest for the XAD-7 backbone, synthesized TOPO impregnated resin, and solid TOPO are all shown in Figure 26, with the associated characteristic peaks in Table 9: Characteristic peaks from IR.

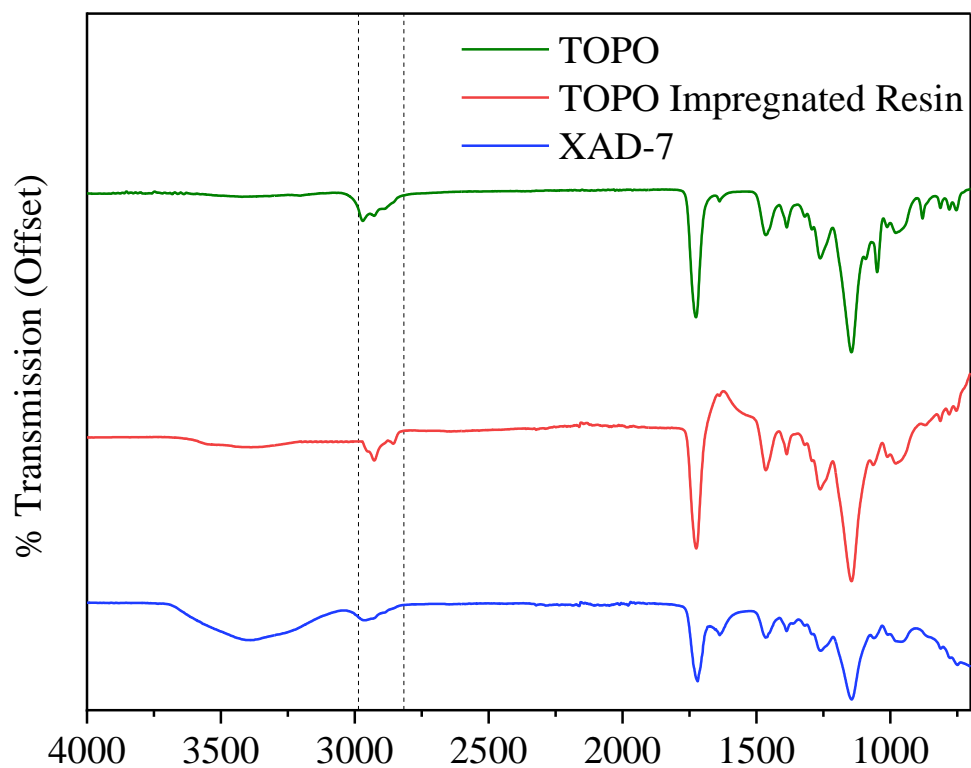


Figure 26: IR spectra of solid TOPO, XAD-7, TK200 resin, and synthesized resin. The solids were rinsed with acetone before IR analysis to remove impurities such as salts and water particularly present in the XAD-7. absorbance differences in the range of 2900-3000  $\text{cm}^{-1}$  between the different samples are indicated with vertical dashed lines.

Table 9: Characteristic peaks from IR

Absorbance ( $\text{cm}^{-1}$ )	Group
1155	P=O
1070-1200	C-O
1455	CH <sub>2</sub> Bending
1724	C=O
3000	C-H sp <sup>3</sup>
3000-3500	O-H stretch from H <sub>2</sub> O impurity

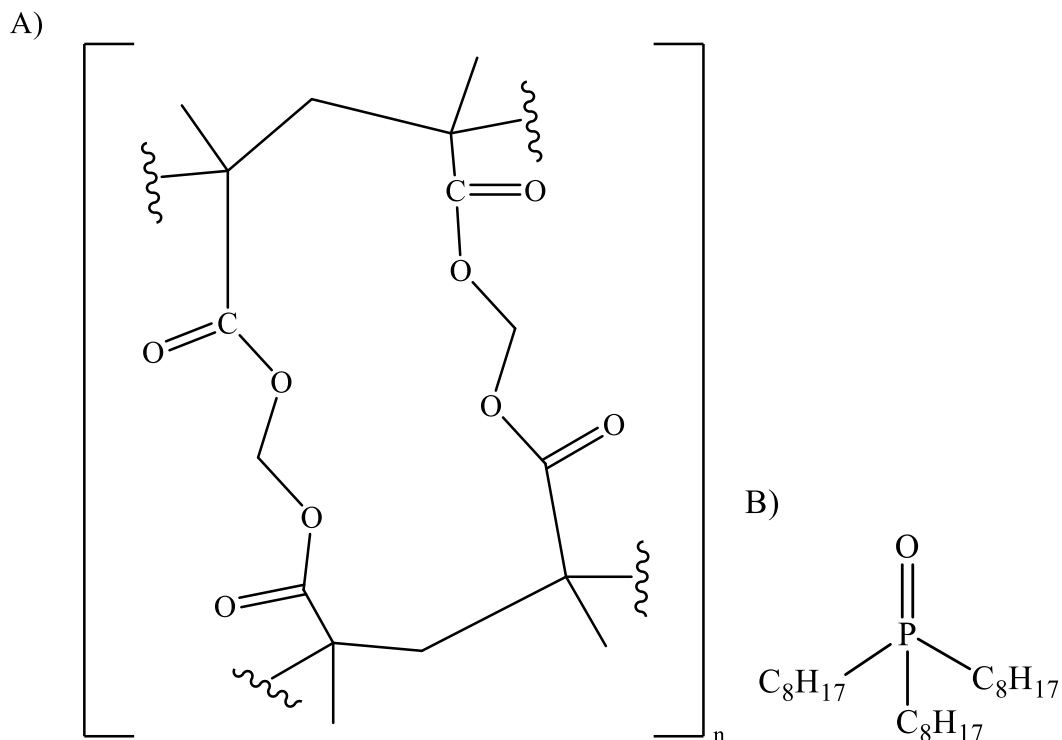


Figure 27: (A) Amberlite XAD-7 monomer structure adapted from specification sheet by Rohm and Haas.<sup>108</sup> (B) Chemical structure of TOPO molecule.

As the intended application of the impregnated resin is to be used in a gravity flow column format for separation and purification chemistry, characterizing physical properties of the resin when packed into a column is necessary to assess its utility. Parameters such as particle size, free column volume (FCV) or column volume (CV), and bed volume (BV) are commonly reported values given for a column separation. Particle size has a direct effect on the flow rate of an eluent through a column. Typically, particle sizes less than 100  $\mu\text{m}$  require a vacuum to elute, otherwise columns with particle sizes greater than 100  $\mu\text{m}$  can flow by gravity. Separation efficiency is

heavily influenced by the bed volume (BV), or the total volume of a packed resin inside a column that varies with height and width, approximated by the equation for volume of a cylinder:

$$V = \pi r^2 h$$

The BV does not account for the empty space between resin particles, which can vary drastically depending on mesh size and porosity and affect the column flow rate. Columns are typically kept at minimum bed volumes appropriate to achieve separation of the analyte to reduce elution time. Larger bed volumes can be exploited to improve separations that contain high relative quantities of matrix material or contain analytes and contaminants with small differences in distribution ratios. However, a major tradeoff with increasing bed volume is increasing the time for separation and required eluent volumes. The FCV is the sum of the volume of the interstitial space between the resin particles when packed in the column and the volume inside the pores of the resin, which totals to the volume of eluent inside of a column. This value normalizes the separation efficiency of a given column separation by reporting the volume of the column and the number of column volumes of eluent was needed to elute an analyte, as the actual volume of eluent can vary depending on these factors.

The particle size of the XAD-7 backbone has a published harmonic mean (to mitigate effect of large outliers in the average) of 578  $\mu\text{m}$  and surface area of 450  $\text{m}^2/\text{g}$ . About 2.3% of the particles are reported to be under 300  $\mu\text{m}$ .<sup>108</sup> Since the particle size is large compared to many other commercially available resins (20-60 mesh versus 200-400 mesh), there is a large amount of empty space between the spherical beads when packed tightly into a column. As such, the flow rate of a column with this resin is qualitatively fast and must be attended to diligently to prevent

the column from drying out while collecting column fractions. Columns were tested with various sizes and eluents without any analytes present to gauge the flow rate by gravity flow before performing a separation of radioactive Zr. Preliminary separations with the TOPO impregnated resin were investigated with Eichrom 2 mL disposable plastic columns of 0.8 cm internal diameter and  $1.5 \pm 0.3$  cm bed height. Initially with this column geometry, grinding the resin to reduce the particle size was investigated. This was to determine if better packing efficiency and thus both improved flow rates and separation of Zr could be achieved. After grinding by hand with a mortar and pestle, the particle size was measured using molecular sieves. However, one consistent particle size was not obtainable, so particle sizes ranged from approximately 90- 250  $\mu\text{m}$ . Molecular sieves with sizes of 90, 106, 150, and 250  $\mu\text{m}$  all contained resin. Resins described herein were not ground due to the inconsistent sizing, risk of removing the TOPO impregnated in the pores of the resin, and reduced surface area of the resin.

### BET Surface Area

The TOPO resin was analyzed to determine the average surface area compared to the conditioned XAD-7 to act as a control. It is expected that the surface area and pore diameter will be much lower in the TOPO resin compared to the XAD-7 due to filling of the pores with TOPO.<sup>98</sup> However, the resin is not of uniform size, so reported values are merely an average of a representative set of particles. Samples were weighed and dried at 50°C overnight, then degassed for 24 hours at 110 °C with a Quantachrome Instruments FloVac Degasser. The dry weight of the degassed sample was recorded, then placed on a Micromeritics Gemini VII instrument for analysis.

The published surface area value of XAD-7 is 450 m<sup>2</sup>/g, and the measured value here was validated at 417 ± 13 m<sup>2</sup>/g for comparison to the impregnated resin.

The BET surface area of the TOPO resin was measured at approximately 87 ± 0.35 m<sup>2</sup>/g, with a Langmuir surface area value of 135 ± 0.55 m<sup>2</sup>/g. This is expected due to the theory of BET surface area, which is a measurement that extrapolates the nitrogen adsorption to multiple layers. Langmuir surface area assumes that only a monolayer of material can absorb the gas, hence why it is typically a larger value. The measured average pore diameter of the impregnated resin was 0.98 nm (9.8 Å), whereas the published pore diameter for bare XAD-7 is 9 nm (90 Å). Therefore, a nearly 10 times reduction in average pore volume was observed with TOPO present.

### NMR Analysis

Solid-state NMR spectroscopy of <sup>13</sup>C and <sup>31</sup>P was utilized to analyze the TOPO resin compared to the XAD-7 backbone to confirm the presence of TOPO, as well as determine if any P containing impurities were present. NMR spectra were obtained on the resin sample after exposure to acids as described in the column separations section to determine if any structural degradation occurs. Also, solution-state NMR of the eluent from a column separation of the TOPO resin was performed to determine if the extractant leached from the resin during conditions used for separation. These NMR spectra and discussion of degradation analysis are contained in the solid-liquid extraction section.

Solid-state NMR spectra were acquired at 162 MHz for <sup>31</sup>P and 101 MHz for <sup>13</sup>C on a 400 MHz Bruker NMR at Hunter College. Here, samples were packed into a 4 mm zirconia rotor and

packed with a Kel-F (Polychlorotrifluoroethylene polymer) cap, then subjected to spin rates from 10-15 kHz to produce a suitable signal to noise ratio and partitioning from the spinning side bands characteristic of MAS solid-state NMR. Due to the different spin rates, as well as cross-polarization on the  $^{13}\text{C}$  NMR spectra, detailed quantitative analysis is not possible. Proton  $90^\circ$  pulse widths of 109.4 or 140.0  $\mu\text{s}$ , with 2 ms of contact time and 5 s of recycle delay were used to acquire the cross-polarization (CP)  $^{13}\text{C}$  NMR spectrum. However, chemical shifts (in ppm) characteristic of the resin backbone and TOPO molecule will show a direct shift if chemically altered or absent if not present, so qualitative observations can still be made comparing the spectra of different samples. Solution-state  $^{31}\text{P}$  NMR at 202 MHz was performed using a 500 MHz Bruker NMR at Hunter College. Chemical shifts are reported in ppm relative to an external 5 mM phosphoric acid ( $\text{H}_3\text{PO}_4$ ) standard solution.

For  $^{31}\text{P}$  analysis, the XAD-7 resin backbone was analyzed and compared to the TOPO resin. Figure 28 shows the XAD-7 backbone NMR spectrum, while Figure 29 shows the TOPO resin NMR spectrum with a strong peak at 46 ppm indicating the presence of TOPO. While the TOPO peak is absent in the XAD-7 spectrum, there is a  $^{31}\text{P}$  peak of unknown origin at -21 ppm, as shown in Figure 28. This is thought to be phosphate salt impurities, since the XAD-7 resin is shipped containing water and salts to prevent bacterial growth. While the XAD-7 is conditioned to remove these residual salts, some may still be present after washing. The only salts reported are sodium chloride and sodium carbonate, so these salts may be impure and contain phosphates.<sup>109</sup> However, expected chemical shifts for group I and group II phosphate salts are typically above 0. A chemical shift of approximately -20 more closely matches  $\text{AlPO}_4$ .<sup>74, 110</sup> This impurity likely is

not washed away in the resin conditioning process due to its insolubility in water. Otherwise, the impurity may be organic phosphates with functional groups that donate electron density and shield the nucleus, resulting in a chemical shift below 0. These compounds may be present in the water or acids used during the conditioning and separation procedures

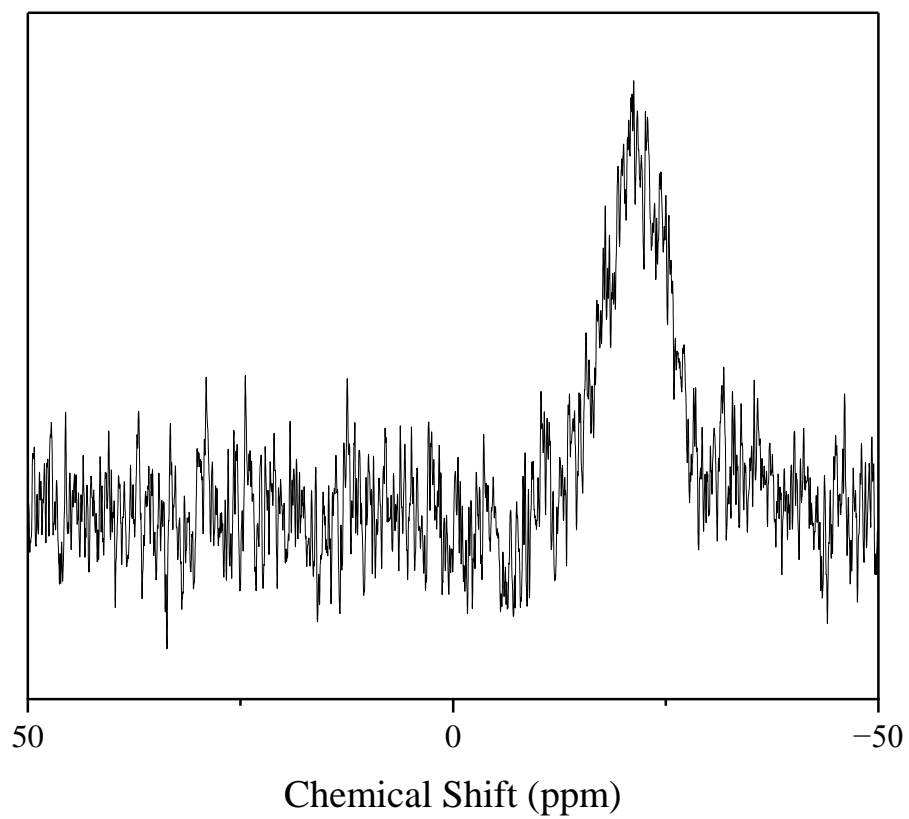


Figure 28:  $^{31}\text{P}$  solid-state NMR spectrum of XAD-7 collected at 162 MHz with 10 kHz spinning, 1024 scans, and single pulse sequence.

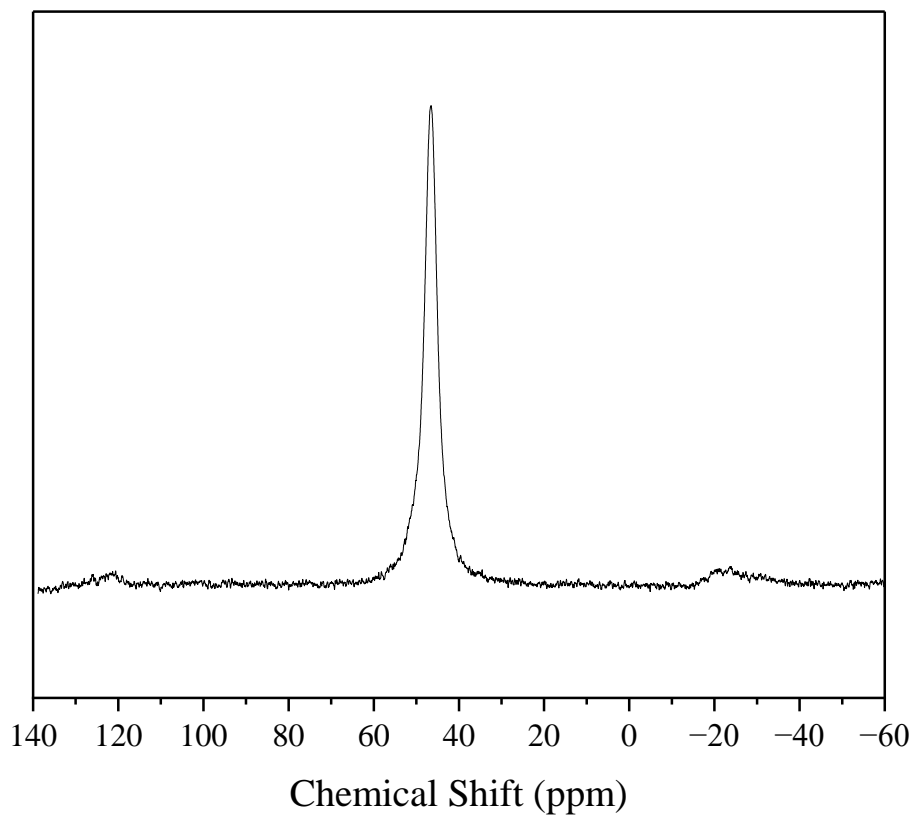


Figure 29:  $^{31}\text{P}$  solid-state NMR spectrum of TOPO resin collected at 162 MHz with 12 kHz spinning, 1024 scans, and single pulse sequence.

$^{13}\text{C}$  of the XAD-7 resin backbone (Figure 30) contains several broad peaks, including multiplets that are hard to distinguish due to the cross-linking polymerization of the resin. However, the peaks present from the XAD-7 backbone were compared to the peaks present from the octyl groups on

TOPO to verify the presence of TOPO in the resin. In a TOPO molecule, there are two distinct types of carbon atoms that will produce a different signal from one another, one being the  $\alpha$ -carbon bound to the phosphine oxide functional group, and the other the  $\beta$ -carbon adjacently bound to the  $\alpha$ -carbon. These peaks have chemical shifts of approximately 10 and 18 ppm in Figure 31 from the  $\text{CH}_3$  and  $\text{CH}_2$  carbons in the octyl chains, respectively. Since the carbons in the carbon chain experience a higher chemical shift when closer to or bound to the electronegative phosphine oxide bond, the  $\text{CH}_2$  groups are slightly downfield from the  $\text{CH}_3$ . By this same reason, the adjacent peaks between 20-40 ppm in Figure 31 (and 5-35 ppm in the XAD-7 spectrum, Figure 30) could be  $\alpha$ -carbons to the ester groups associated with the resin backbone, with certain shifts producing multiplets due to the various crosslinking of the polymeric structure. In addition, the chemical

shifts observed at 160 and 170 ppm likely correspond to the C=O carbons present in the ester groups of the XAD-7 resin.

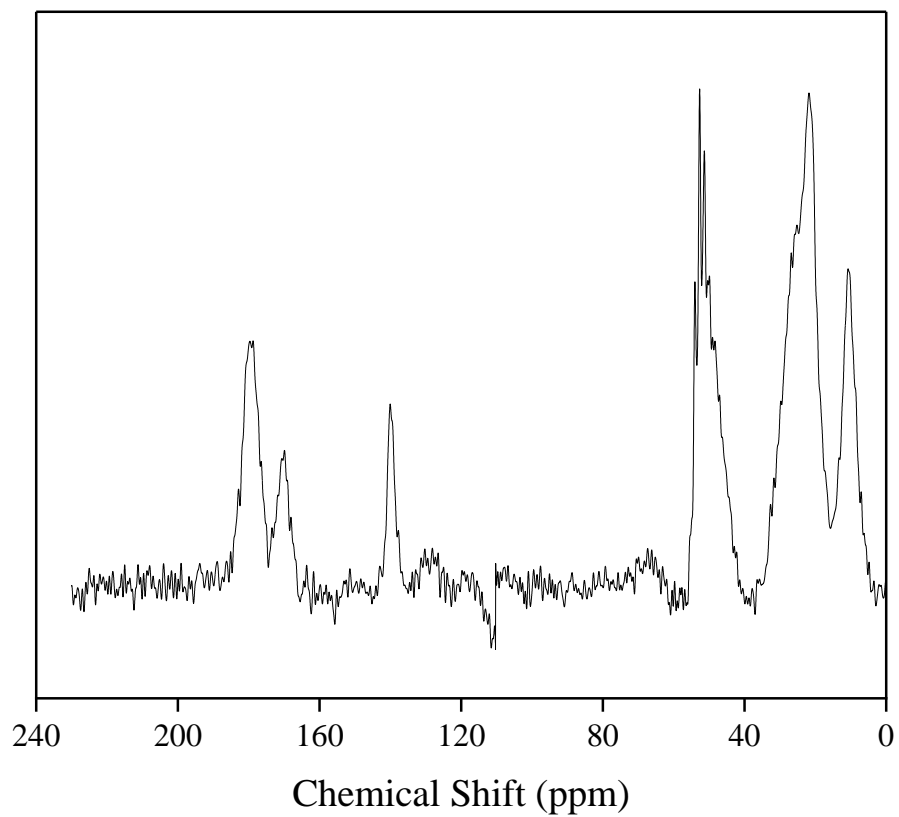


Figure 30:  $^{13}\text{C}$  solid-state NMR spectrum of XAD-7 collected at 101 MHz with 12 kHz spinning, 12,000 scans, and single pulse sequence.

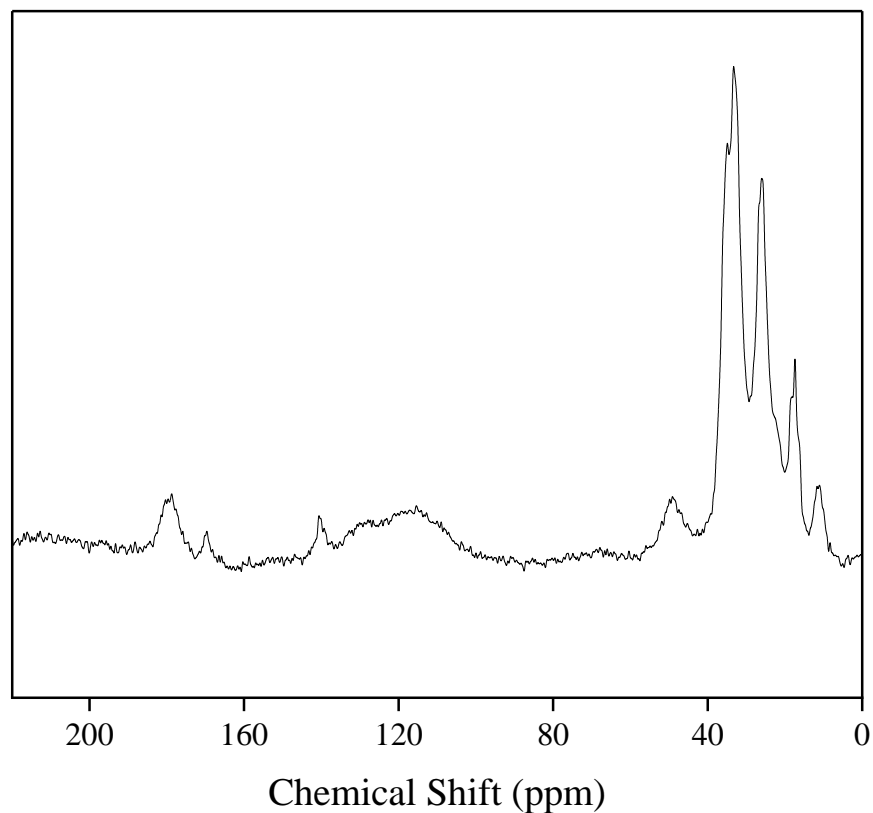


Figure 31:  $^{13}\text{C}$  solid-state NMR spectrum of TOPO resin collected at 101 MHz with 15 kHz spinning, 12,000 scans, and single pulse sequence.

#### Batch Extractions of Zr Using TOPO Resin

The TOPO resin's extraction capability was tested in batch studies to compare to the solvent extractions, as well as determine feasibility for use in a solid-phase extraction column format. Known quantities of resin were weighed and pre-equilibrated with the appropriate acid by mixing for at least 30 minutes and up to overnight. An aliquot of  $^{88}\text{Zr}$  solution in the same acid

concentration was added to the conditioned resin suspension and mixed for a set amount of time. This solution was then separated from the resin using a syringe filter, then both the resin and separated solution were counted on a NaI detector. To quantify the amount of  $^{88}\text{Zr}$  adsorbed onto the resin, an aliquot of the  $^{88}\text{Zr}$  stock solution in the same geometry as the post-extraction samples to determine relative percent of  $^{88}\text{Zr}$  extracted and remaining in the solution. Control batch extractions were performed both with the XAD-7 backbone containing no TOPO extractant in an identical manner, as well as with no resin to determine if  $^{88}\text{Zr}$  was adhering to the vials or syringe filters.

Batch extractions were conducted from 6 M HCl with the TOPO resin at several different mass scales: the first was with sub 5 mg of resin in 1 mL of solution, and the next was scaled up to approximately 40 mg of resin per 10 mL of solution, then 80 mg per 20 mL of solution. This was to follow a ratio of approximately 4 mg of resin for every 1 mL of solution. For kinetics studies, samples were mixed on a sample rotator at 40 rpm at time scales from 3 minutes to over 24 hours, where the contact time between adding the  $^{88}\text{Zr}$  to the resin solution or prompt removal from the rotator for analysis was negligible.

Batch extraction studies were conducted with varying contact times, and the amount of  $^{88}\text{Zr}$  extracted by the resin was quantified relative to the initial  $^{88}\text{Zr}$  concentration in solution before contact with the resin (Figure 32). At least 10 minutes of contact time is needed for 50% of the  $^{88}\text{Zr}$  to be extracted by the resin under the conditions tested. A maximum uptake value was not observed within 24 hours due to the lack of an asymptote in the plot of % Zr extracted versus contact time. The resin extracts higher amounts of Zr than solvent extraction below 10 minutes of

contact time. However, the extraction trends between the two methods coalesce above this point. At approximately 24 hours of resin contact time, the  $^{88}\text{Zr}$  extracted is  $78\% \pm 14\%$ , where the  $1\sigma$  uncertainty is due to low counting statistics for  $^{88}\text{Zr}$  in the supernatant solution propagated with pipetting volume error. Weight distribution ratios (Dw) were calculated based on the following equation:

$$Dw = \frac{(A_0 - A_s)}{W_{(g)}} / \left( \frac{A_s}{V_{(mL)}} \right)$$

Where  $A_0$  is the initial activity of the analyte in solution ( $^{88}\text{Zr}$ ),  $A_s$  is the activity in the supernatant after separation from the resin,  $A_0 - A_s$  is the activity of the analyte sorbed to the resin,  $W_{(g)}$  is the mass of the resin in grams, and  $V_{(mL)}$  is the total volume of solution.

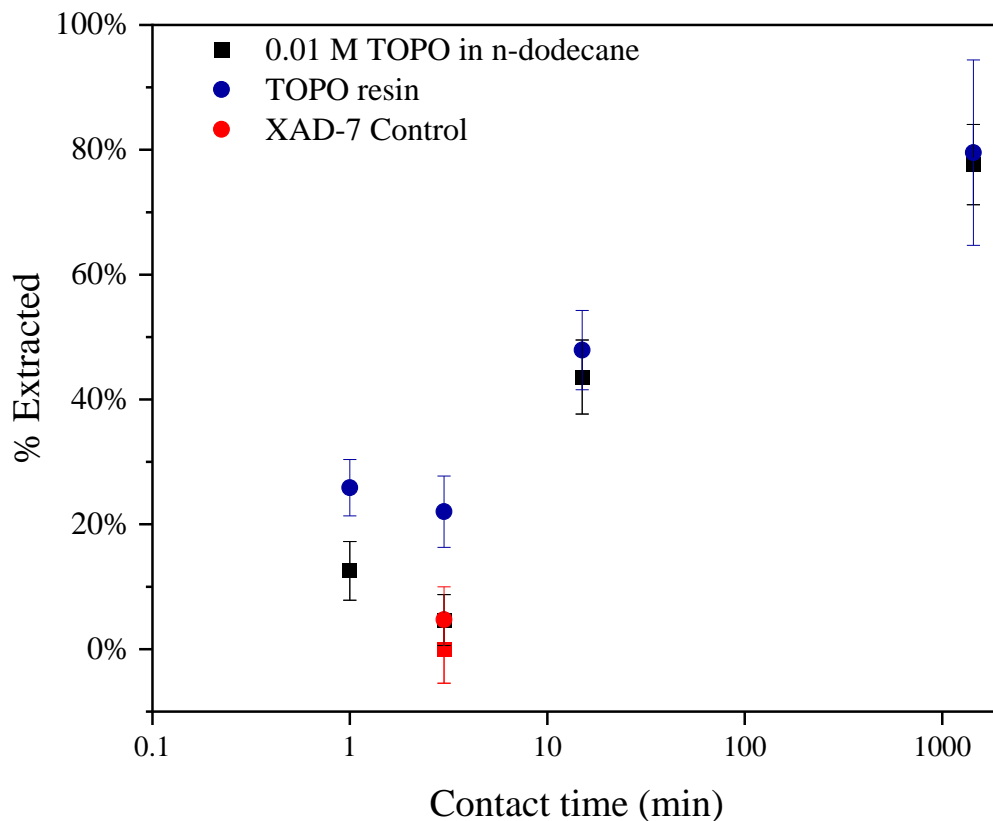


Figure 32: Batch extractions to study the kinetics of extraction using the TOPO resin.

In the various batch extractions tested,  $D_w$  values exceeded 1000 for all cases, including in the control study with XAD-7 only. With the XAD-7, typically 35-40% of the initial  $^{88}\text{Zr}$  sorbed to the resin in 6 M HCl and up to 12 M  $\text{HNO}_3$ . This is likely due to the various oxygen containing functional groups on the resin, such as carboxyl group impurities, to which Zr has a strong affinity. However, there is still a significant increase in the  $^{88}\text{Zr}$  extracted, and a two-to-three-fold increase in  $D_w$  (>3000  $D_w$  value) for the TOPO based resin. Therefore, up to 40% of the  $^{88}\text{Zr}$  removed from

solution is not extracted by the TOPO but sorbed to the XAD-7 backbone. Notably, the vortex mixing intensity and ratio of resin to Zr is a significant factor in extraction efficiency. Several extractions with resin were performed with a vortex mixer at timescales of 5 minutes or below, resulting in higher extraction yields compared to the sample rotator. For practicality, extraction studies longer than 5 minutes were performed with a sample rotator with the known tradeoff of reduced extraction yields. For example, with an excess amount of resin (249 mg), 3 minutes of vortex mixing with 2 mL volume yielded 100%  $^{88}\text{Zr}$  removed from solution. Exhaustive batch extractions were not performed, as this was to act as a screening test for feasibility of solid-phase extraction of Zr using the developed TOPO resin.

### Column Studies

Disposable, 2 mL plastic columns were used for initial column experiments at Hunter College. Columns were packed with approximately 250-300 mg dry synthesized resin, to a bed height of 1.5 cm (BV= 0.75-0.9 cm<sup>3</sup>). Continuation of the column studies with this resin were performed at LLNL, and here column geometries were changed to 0.5 cm diameter and  $7 \pm 1$  cm resin height (BV= 1.3-1.6 cm<sup>3</sup>), which equates to 220-250 mg of resin to achieve slower and more manageable flow rates.

The resin was experimentally tested to estimate the free column volume by washing the column with HCl and testing the column eluent with pH strips. A plastic 2 mL column was slurry packed with 300 mg of synthesized resin in water. Once packed, the column was eluted continuously until sufficiently wetted with water, then 6 M HCl was added in known aliquots of

100  $\mu\text{L}$ . The eluent leaving the column was tested with pH strips regularly until acidic. Thereafter the free column volume was estimated to be 150-250  $\mu\text{L}$ .

In the smaller diameter column geometry, a similar procedure was followed to determine the FCV. In this experiment, the column dimensions were 0.5 cm diameter and 7 cm resin height ( $\text{BV} = 1.3 \text{ cm}^3$ ) with 220 mg of resin. 0.1 M  $\text{HNO}_3$  was added to the top of the resin bed and the eluent was collected in a weighed vial containing 1 mL of water. This solution was continuously monitored with pH strips until they read acidic, then promptly removed from collecting column eluent. This was weighed again to calculate the amount of solution eluted from the column before registering acidic, which yields an approximate FCV of 70  $\mu\text{L}$ .

## Solid-Liquid Extraction of Zr

The TOPO impregnated resin was used in a column format to test the extraction efficiency of Zr from solution in either nitric acid or hydrochloric acid. Prior to each experiment, the resin was weighed dry, then wetted with 0.1 M  $\text{HNO}_3$  or 0.1 M  $\text{HCl}$ , depending on if the separation was carried out with either acid. The loading solution contained  $^{95}\text{Zr}$  in either 12 M  $\text{HNO}_3$  or 6 M  $\text{HCl}$ . All stock solutions containing  $^{95}\text{Zr}$ , including those containing bulk metals, were thoroughly mixed and allowed to equilibrate for at least several hours prior to separation. Each column was slurry loaded with the TOPO resin (or XAD-7 in the control extractions, which were wetted and pre-equilibrated in the same manner) and continuously rinsed with dilute acid to minimize large air pockets and prevent drying. Glass wool was packed on both the top and bottom of the column to prevent small resin particles from washing through with the column fractions, and to keep the resin

tightly packed. Once packed in the column, the resin was washed with several bed volumes of 12 M HNO<sub>3</sub> or 6 M HCl (5-10 mL) to match the loading solution acid concentration. The loading solution was added in 500 µL or less of total volume to the top of the resin bed once exposed to minimize analyte tailing. An aliquot of the initial stock used for the loading solution was counted in the same geometry as column fractions on an HPGe detector. The stock aliquot was diluted and analyzed with ICP-OES to verify the stable metal loading solution concentration in the applicable experiments, which was used to calculate the relative percent of <sup>95</sup>Zr and stable metals eluted in each fraction. The <sup>95</sup>Zr decay product <sup>95</sup>Nb was not quantified or included in the elution curves as its chemistry was not the focus of this work. The loading solution container was rinsed three times to ensure all the loading solution was added to the column. Column fractions were collected with approximately 1.5 mL volume in each, which equates to one CV. Eluent was added in order from more to less concentrated acid to minimize hydrolysis of the Zr and swelling of the resin.

Stable metal content of each column fraction and loading solution were analyzed with ICP-OES, except for the separation from bulk U experiment. In the U experiment, a solution of <sup>238</sup>U was traced with <sup>237</sup>U (t<sub>1/2</sub>= 6.75 days) and quantified using the 208 keV gamma ray emission (I= 21 %) from <sup>237</sup>U decay and known specific activity (<sup>237</sup>U/<sup>238</sup>U). Decontamination factors (DF) from the bulk metal were calculated for the column fractions containing eluted <sup>95</sup>Zr as described in chapter 1 (Equation 14). In experiments where the stable metal was below the LOD for a sample, the DF is calculated assuming the LOD concentration to calculate a minimum DF from <sup>95</sup>Zr.

Initial extractions of <sup>95</sup>Zr using the TOPO resin were conducted from both nitric acid and hydrochloric acid, with the load solution adjusted to the concentration of the associated acid (12

M HNO<sub>3</sub> or 6 M HCl) that yields the highest Zr uptake as established in previous experiments. Control experiments were also performed in an identical geometry and equilibration procedure with the XAD-7 backbone, which was conditioned in the same procedure as outlined in the resin synthesis process. As expected, based on the batch studies, up to 40% of the total <sup>95</sup>Zr adheres to the XAD-7. In nitric acid, this is less prominent with only about 15% of the <sup>95</sup>Zr sorbing to the resin. This is due to the stronger complexation of Zr by NO<sub>3</sub><sup>-</sup> groups than Cl<sup>-</sup>. Otherwise, a majority of the <sup>95</sup>Zr elutes in the first two column fractions. The TOPO resin binds the Zr strongly, as no bleed through of <sup>95</sup>Zr is observed in any of the HCl or HNO<sub>3</sub> concentrations tested (0.01-12 M). Therefore, a complexant was needed to elute the <sup>95</sup>Zr. A mixture of 0.01 M HF and either 0.01 M HNO<sub>3</sub> or 0.01 M HCl was added to the column to elute the <sup>95</sup>Zr and keep it in a nitrate or chloride matrix. Recovery yields of <sup>95</sup>Zr were >80% in hydrochloric acid and >90% in nitric acid matrices. <sup>95</sup>Zr was predominantly eluted in three column fractions. Elution curves from either HCl (

Figure 33) or HNO<sub>3</sub> (Figure 34) are shown below. Some yields for <sup>95</sup>Zr or the bulk metals exceed 100%, likely due to variations in column fraction counting geometry compared to the loading solution.

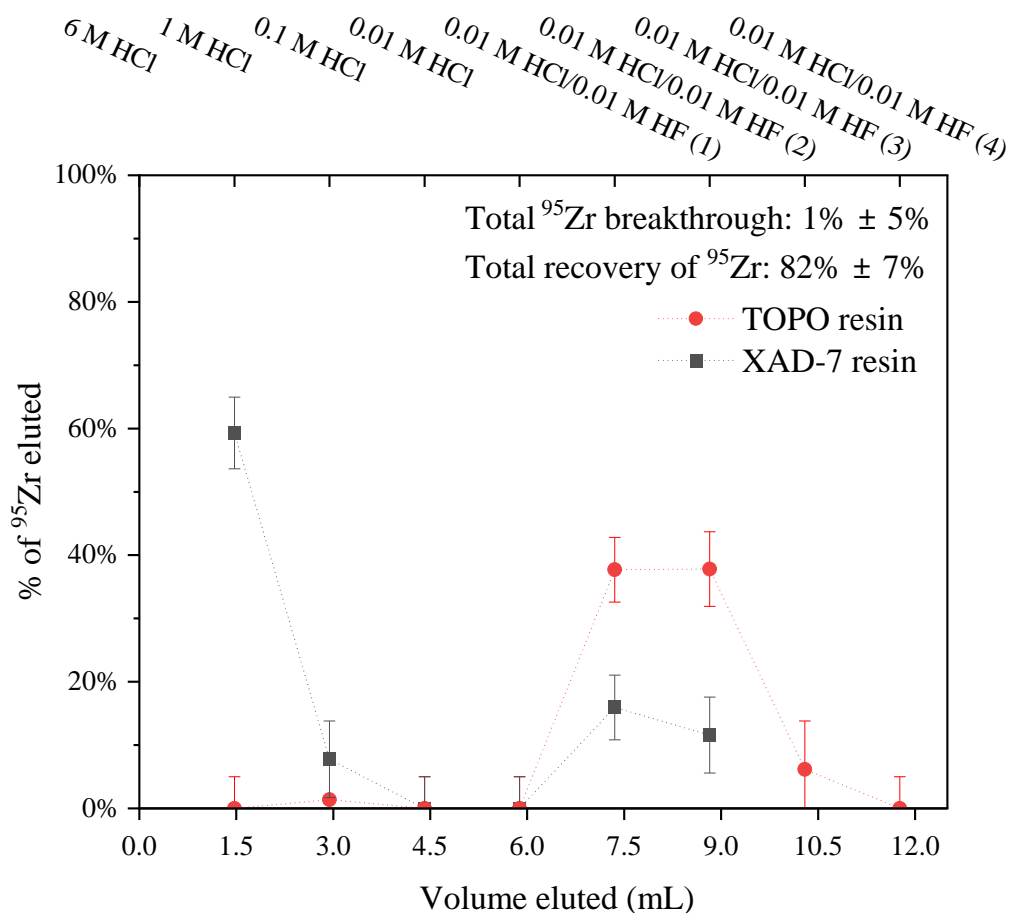


Figure 33: TOPO resin extraction of <sup>95</sup>Zr compared to XAD-7 from HCl. The top x-axis shows the volume of total eluent corresponding to the acid concentration on the bottom x-axis. Lines are only shown to guide the eye.

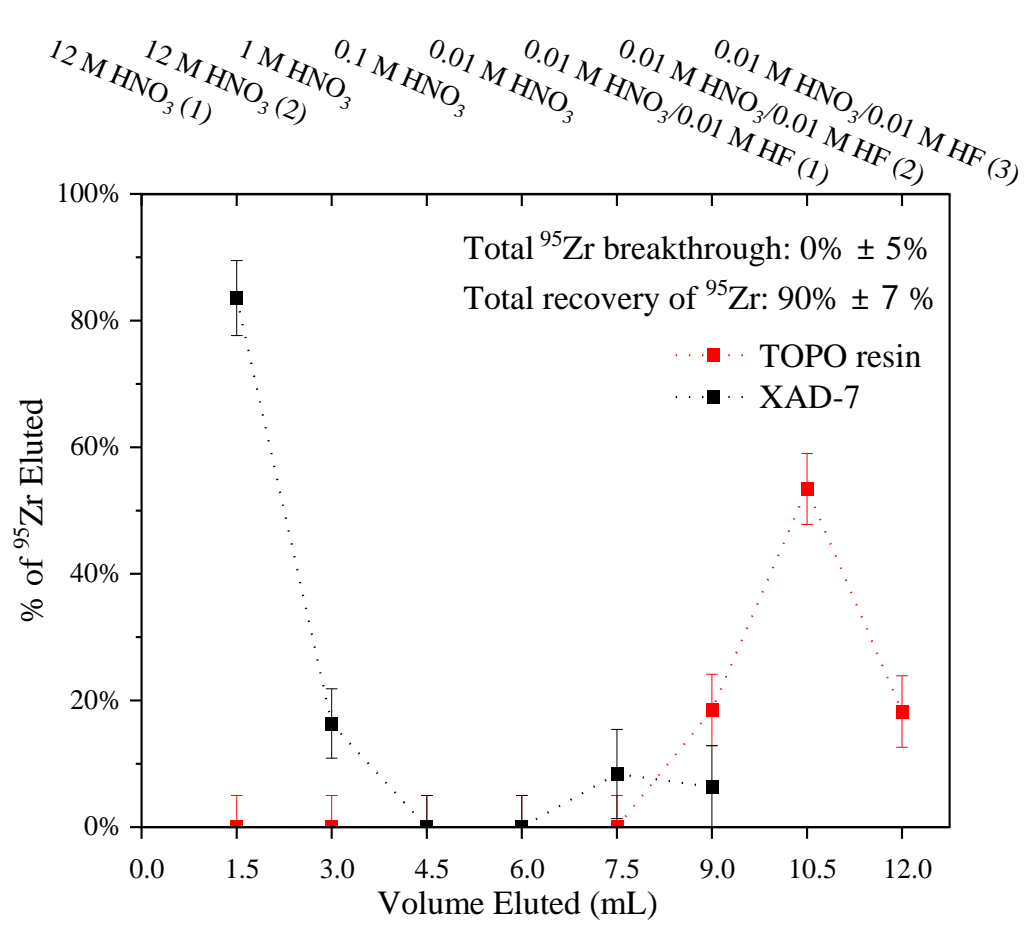


Figure 34: TOPO resin extraction of <sup>95</sup>Zr compared to XAD-7 from HNO<sub>3</sub>. The top x-axis shows the volume of total eluent corresponding to the acid concentration on the bottom x-axis. Lines are only shown to guide the eye.

A cold surrogate column with 233 mg of resin was run using water, 6 M HCl, and 1 M HCl as eluents to determine if TOPO would leach off the resin. Fractions of approximately 1.5 mL each were collected in the following order: The first 2 fractions were water, fraction 3 was 6 M HCl transition fraction, fraction 4 was 6 M HCl, fraction 5 was 6 M and 0.1 M HCl transition fraction,

then fraction 6 was 0.1 M HCl. Column fractions were analyzed by diluting 1 mL of the fraction into 4 mL of methanol for a 5 times dilution factor. TOPO is highly soluble in methanol, and not soluble in water or acids. Therefore, careful observation of precipitate formation in the column fractions was noted, however no solid precipitate was observed. Quickly after fraction collection, the solution was mixed then an aliquot taken for dilution. These solutions were pipetted into an NMR sample tube along with a sealed capillary tube containing a solution of 5 mM H<sub>3</sub>PO<sub>4</sub> in 50% deuterated methanol and water to act as an external reference, where the <sup>31</sup>P peak from H<sub>3</sub>PO<sub>4</sub> is set to 0 ppm for all spectra. Figure 35 shows the <sup>31</sup>P NMR spectra of a 0.5 M TOPO solution in 50% deuterated methanol, where the large peak at approximately 55 ppm is indicative of the TOPO molecule. Here the much weaker bands present at 59 ppm and within 0.5 ppm of the large 55 ppm chemical shift are likely attributable to other alkylphosphorus impurities known to be present in small quantities with commercially purchased TOPO, such as dioctylphosphine oxide (DOPO).<sup>111</sup>

No <sup>31</sup>P containing compounds were detected in the 6 column fractions, therefore the TOPO resin is assumed to be stable up to 6 M HCl within these parameters described. A limitation here is that no HF or HNO<sub>3</sub> solution was introduced to the column, so the leaching of TOPO off the resin should be investigated with solution-state NMR in these acids. However, TOPO is stable and insoluble in both acids, and did not exhibit behavior indicative of degradation in the experiments described thus far, so it is unlikely that leaching off the resin would occur in these experiments due to intrinsic properties of TOPO. What is more likely is altering of the chemical structure of the resin backbone due to the strong acid exposure, such as acid catalyzed hydrolysis reactions, which could affect the Van der Waals interactions that help hold the TOPO extractant in the resin

or mechanically alter the resin structure. Therefore, solid-state NMR spectra was measured on the TOPO resin both before and after contact with HNO<sub>3</sub> up to 12 M HNO<sub>3</sub>, then sequentially down to 0.01 M HNO<sub>3</sub>/0.01 M HF identical to the column separation method. In this stability experiment, the resin was contacted with 12 M HNO<sub>3</sub> for 2-3 hours before pipetting off most of the acid solution. Then, water was added in to allow resin to sink and dilute the acid before sitting overnight. The next day, the resin was washed with 1 M HNO<sub>3</sub>, then 0.1 M HNO<sub>3</sub>, then rinsed several times with water. Finally, 0.01 M HNO<sub>3</sub>/0.01 M HF was added, briefly mixed, and sat for approximately 5 hours. This solution was removed, then the resin was washed multiple times with water and tested with pH strips until registered neutral. The excess water was removed, and the resin dried overnight at 60 °C before packing into the solid-state NMR probe.

As shown in Figure 36, the TOPO peak at 46 ppm is still present with the same intensity after contacting the resin with HNO<sub>3</sub> and HF compared to the pre-contacted resin. This implies no significant degradation of the TOPO in the resin after contacting the acids. However, a weak, unknown peak at 21 ppm appears in the <sup>31</sup>P spectrum of the post-acid contacted resin. This might be due to formation of degradation products from the TOPO or other organophosphorus impurities in the resin reacting with the acids.

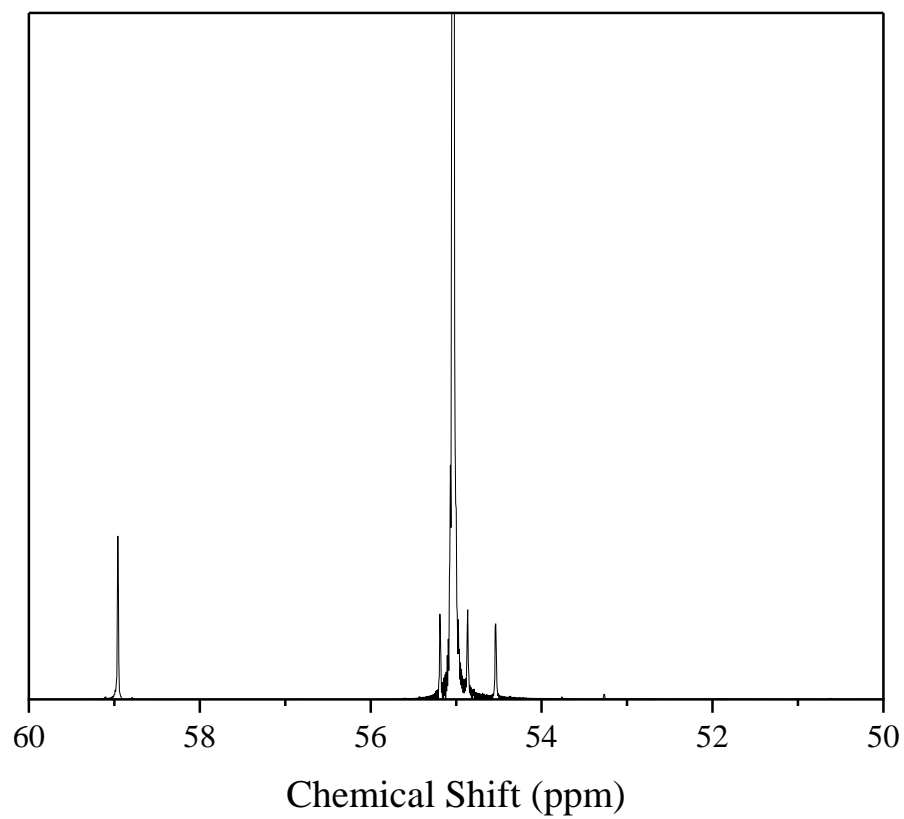


Figure 35:  $^{31}\text{P}$  NMR spectrum of 0.5 M TOPO in methanol solution referenced to 5 mM  $\text{H}_3\text{PO}_4$  solution. Spectrum was acquired at 202 MHz with 128 scans on a 500 MHz Bruker NMR.

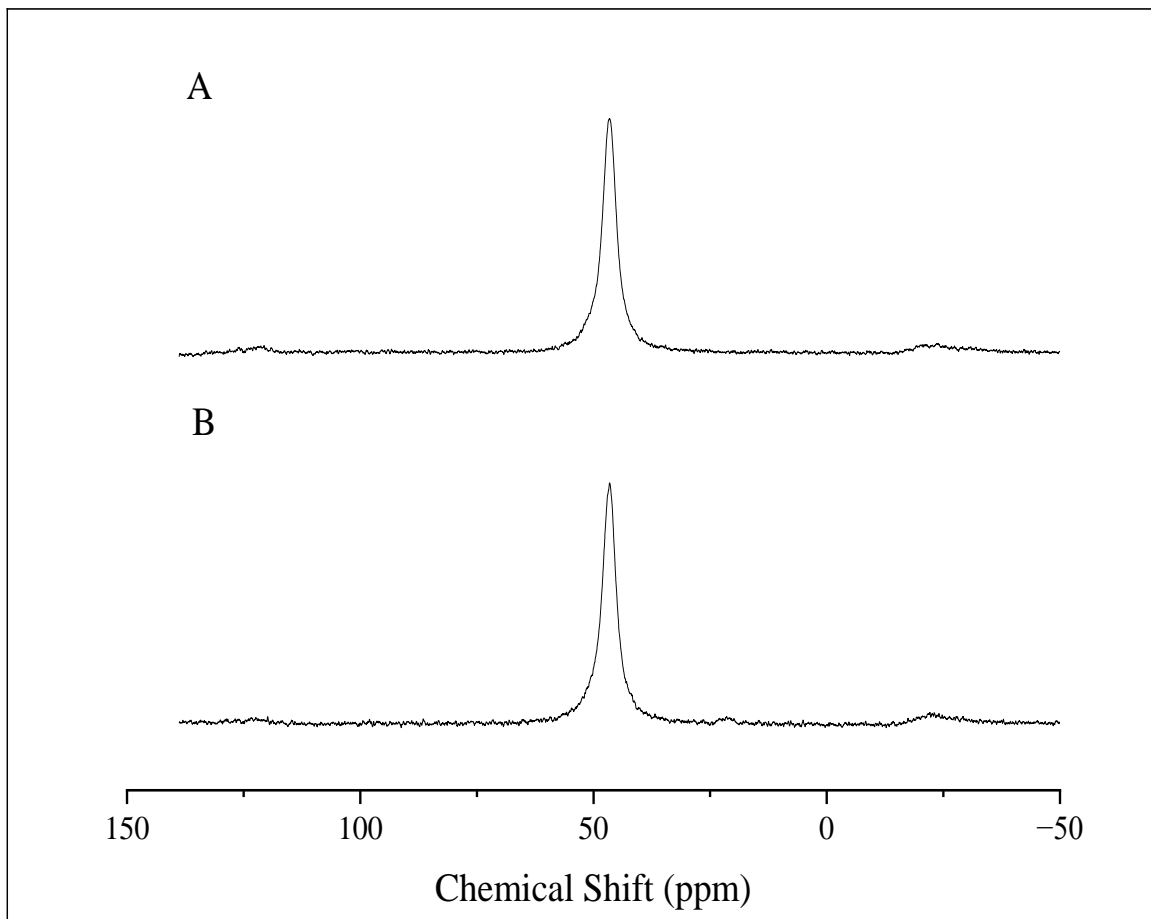


Figure 36:  $^{31}\text{P}$  NMR spectrum of TOPO resin before (A) and after contact (B) with  $\text{HNO}_3$  and  $\text{HF}$ , measured with 12k spinning, 1024 scans each. Single pulse.

When comparing the  $^{13}\text{C}$  NMR spectra of the TOPO resin, no peak shifts were observed in the resin pre-acid contact (Figure 31) and post-acid contact (Figure 38). Since no peak shifts were observed, it is likely that no chemical changes are occurring in the XAD-7 backbone or the octyl groups on the TOPO molecules from exposure to  $\text{HNO}_3$  or  $\text{HF}$ . The acid exposure times tested on the resin far exceed the timescale for a typical column separation, so it is safe to assume that the

resin is stable in acidic conditions up to 12 M HNO<sub>3</sub> and in dilute 0.01 M HF. This implies the resin could be used more than once without regeneration or sustain much larger elution volumes than tested in this work, however more experiments to test the limitations of the resin need to be performed.

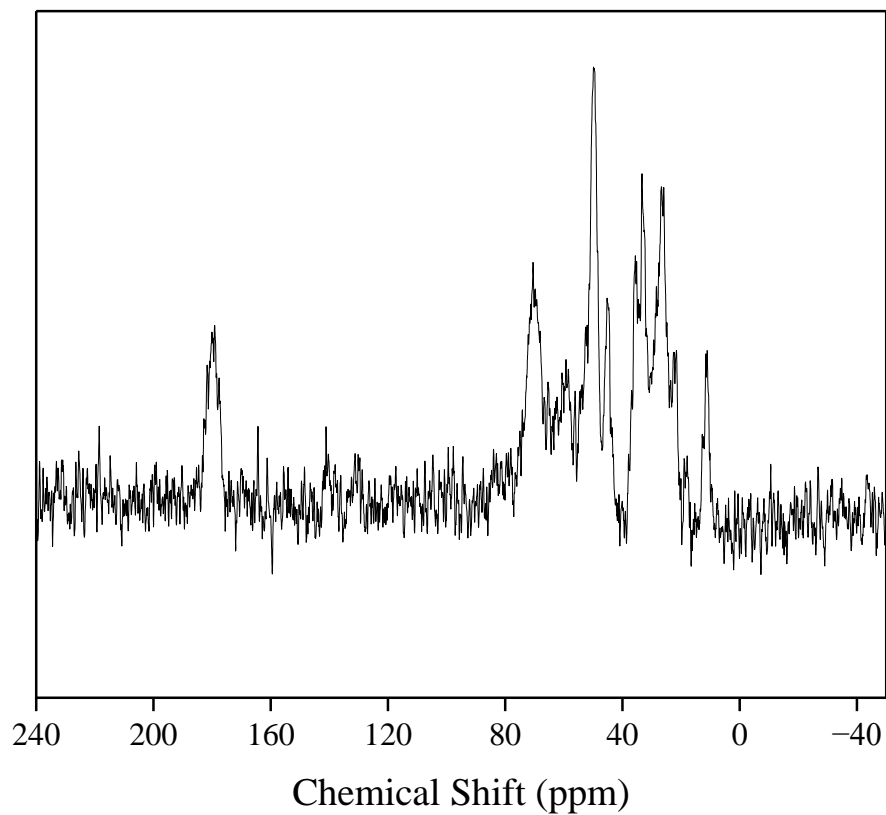


Figure 37:  $^{13}\text{C}$  solid-state NMR spectrum of TOPO resin post-acid contact collected at 101 MHz with 14.5 kHz spinning, 128 scans, and a cross-polarization pulse sequence of  $90^\circ$  proton pulse widths of 109.4 or 140.0  $\mu\text{s}$ , with 2 ms of contact time and 5 s of recycle delay.

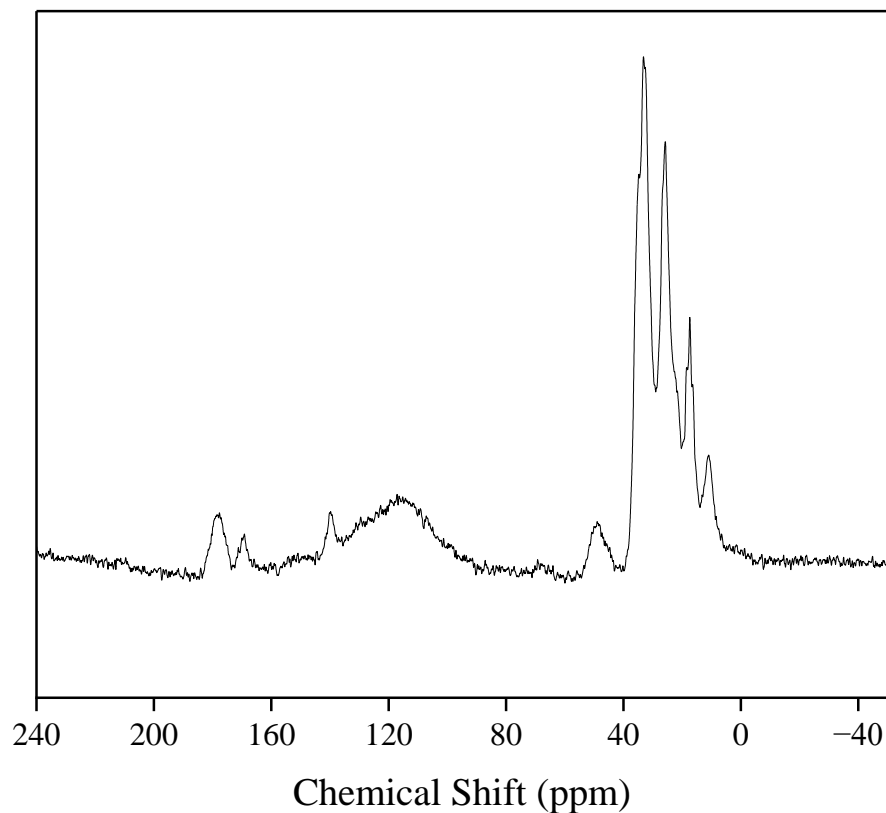


Figure 38:  $^{13}\text{C}$  solid-state NMR spectrum of TOPO resin post-acid contact collected at 101 MHz with 14.5 kHz spinning, 12,000 scans, and single pulse sequence.

#### Solid-Liquid Extraction of Zr from Bulk Al

A 300  $\mu\text{L}$  solution containing estimated 1000 ppm of Al and trace  $^{95}\text{Zr}$  in 12 M  $\text{HNO}_3$  was added to a pre-conditioned TOPO resin column (7.0 cm tall and internal diameter of 0.5 cm). After loading, the column was washed with 3 mL of 12 M  $\text{HNO}_3$ . The initial Al concentration was approximate until confirmed by ICP analysis post-separation. The initial loading solution

concentration was determined to be 1165 ppm by ICP-OES and used for the relative percent eluted values. Then, sequential additions of 1 M, 0.1 M, and 0.01 M HNO<sub>3</sub> were collected in 1.5 mL fractions each before collecting four fractions of 0.01 M HNO<sub>3</sub>/ and 0.01 M HF. <sup>95</sup>Zr was only detected in the four column fractions containing HF, and the total sum of activity exceeded the activity quantified in the loading solution, so percent yields for each fraction are normalized to sum to 100%. Therefore, losses of <sup>95</sup>Zr were minimal. Elution curves for <sup>95</sup>Zr and Cu are shown in Figure 39. Al was quantified post-separation by diluting the column fractions with a 150 times dilution factor and analyzing with ICP-OES. Here, all the Al was eluted in the first four column fractions, with a normalized total recovery of 100 ± 9.1% and >85% in the first fraction. This is expected since Al forms hydrated cations in acidic solution and is not known to be extracted by neutral organophosphorus extractants. A minimum decontamination factor of 2.2 x 10<sup>2</sup> for <sup>95</sup>Zr from Al was calculated based off the LOD value for Al in the ICP-OES. This value was 10 ppb for the diluted samples analyzed with ICP-OES, which equates to 1.5 ppm Al in the original samples. The actual DF likely exceeds this since all the loaded Al is accounted for in the initial few fractions that do not contain <sup>95</sup>Zr.

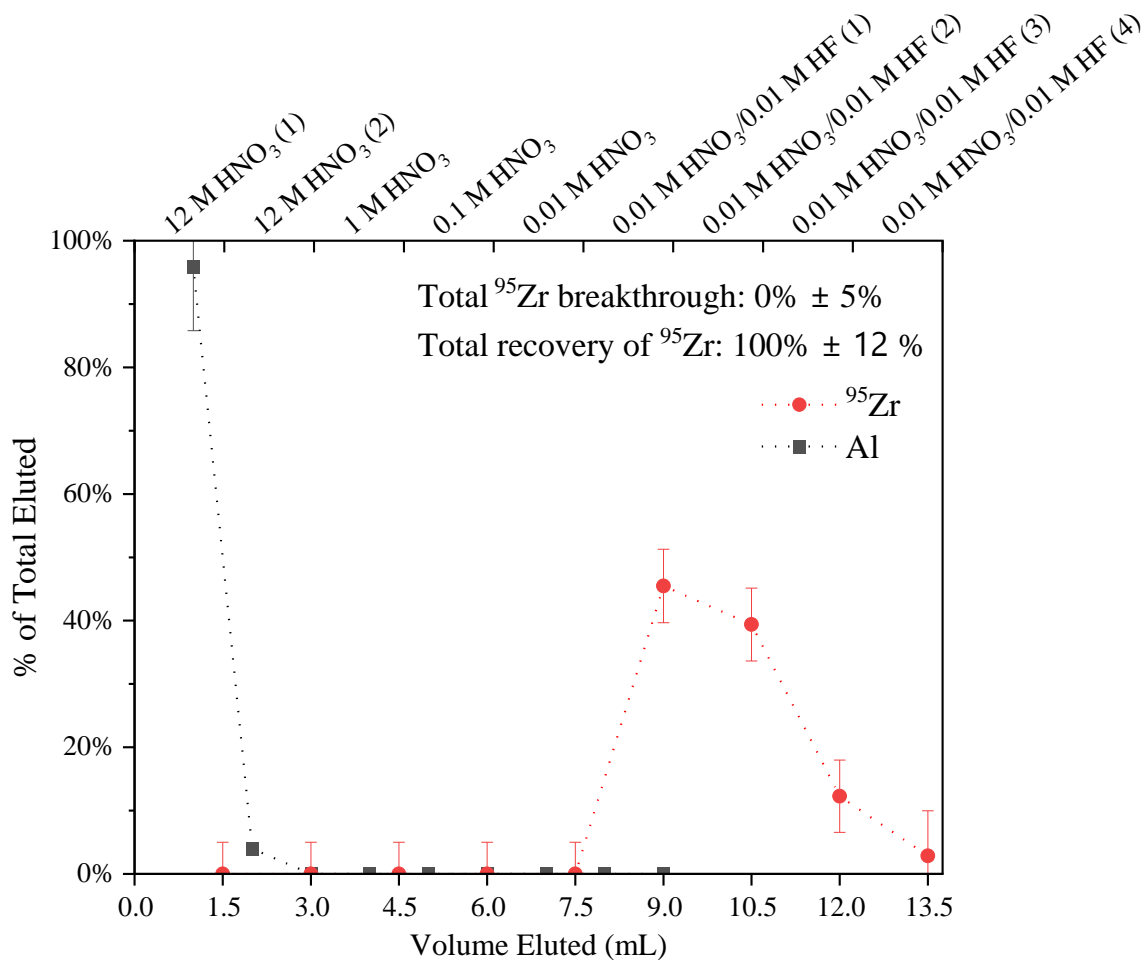


Figure 39: TOPO resin extraction of  $^{95}\text{Zr}$  from a  $\approx 1000$  ppm Al solution in  $\text{HNO}_3$ . Column yields are normalized. The bottom x-axis shows the volume of total eluent corresponding to the acid concentration on the top x-axis. Lines are only shown to guide the eye.

To note, a column experiment to extract  $^{95}\text{Zr}$  from a 1000 ppm Al solution in HCl was attempted. A 500  $\mu\text{L}$  solution containing 1000 ppm Al in 6 M HCl was prepared and spiked with  $^{95}\text{Zr}$ , then loaded onto a column 7.3 cm tall and internal diameter of 0.5 cm. This was pre-conditioned with several mL of 6 M HCl prior to loading. After loading, 3 mL of 6 M HCl wash

were added and collected, followed by additions of 1 M, 0.1 M, and 0.01 M HCl, collected in 1.5 mL fractions each. Then four fractions of 0.01 M HCl/ and 0.01 M HF were collected to recover  $^{95}\text{Zr}$ , however a total of <5% of the  $^{95}\text{Zr}$  loaded was detected in the four column fractions containing HF. This is attributed to adsorption of  $^{95}\text{Zr}$  to Al complexes in solution that may have irreversibly stuck to the column. For example, hydrated  $\text{Al}^{3+}$  in solution can convert to insoluble  $\text{AlF}_3$  upon addition of HF, which Zr can adsorb to.

## Solid-Liquid Extraction of Zr from Bulk Cu

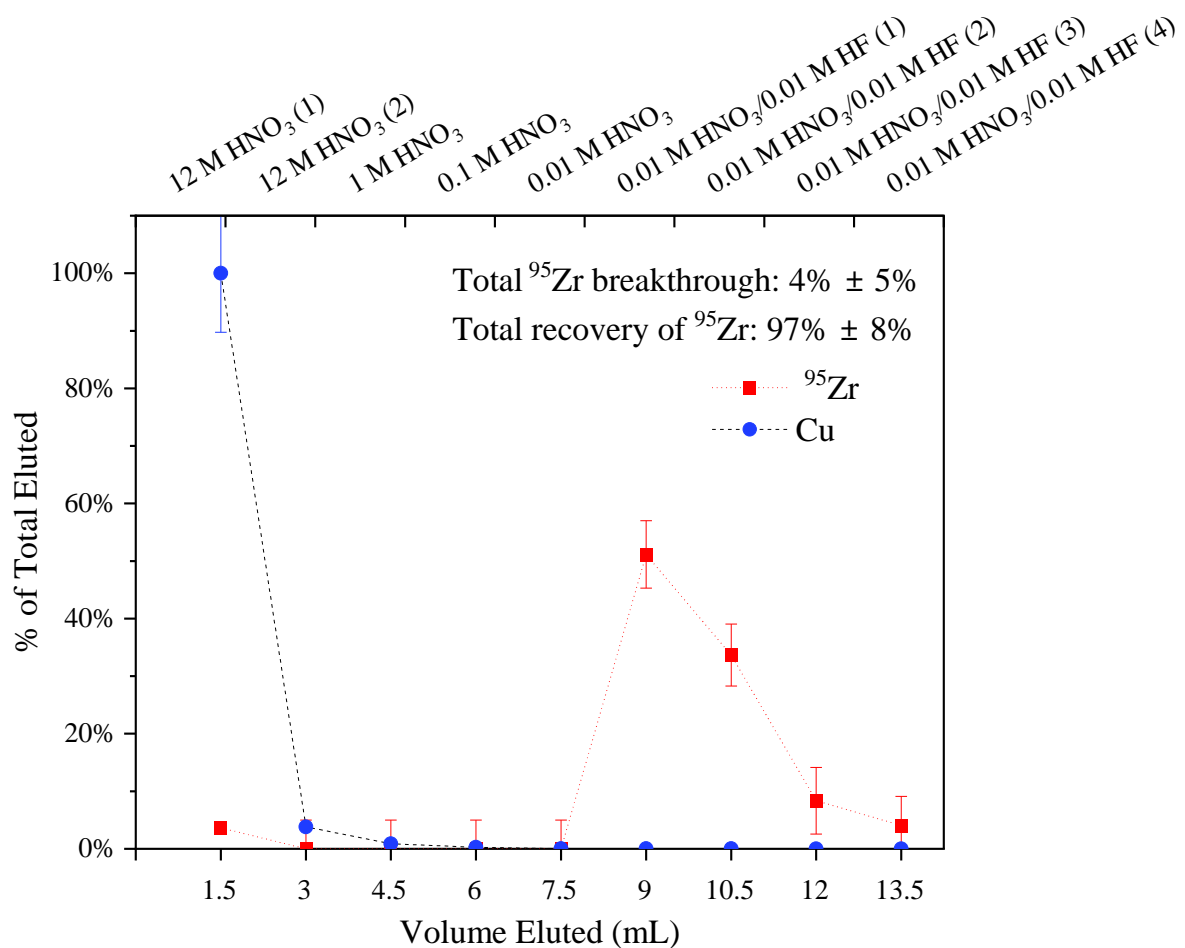


Figure 40: TOPO resin extraction of <sup>95</sup>Zr from ≈8000 ppm Cu solution in HNO<sub>3</sub>. Column yields are normalized. The bottom x-axis shows the volume of total eluent corresponding to the acid concentration on the top x-axis. Lines are only shown to guide the eye.

A 400 μL solution containing approximately 8000 ppm Cu and trace <sup>95</sup>Zr in 12 M HNO<sub>3</sub> was added to a pre-conditioned TOPO resin column. The loading solution concentration of Cu determined by ICP-OES was 7897 ppm and used for the relative percent eluted values. The column

was initially washed with 3 mL of 12 M HNO<sub>3</sub>, then, sequential additions of 1 M, 0.1 M, and 0.01 M HNO<sub>3</sub> were collected in 1.5 mL fractions each before collecting four fractions of 0.01 M HNO<sub>3</sub>/ and 0.01 M HF elution curves for <sup>95</sup>Zr and Cu are shown in Figure 40. A majority of the <sup>95</sup>Zr was detected in the four column fractions containing HF, and the total sum of activity was 97 ± 8% of the original loading solution concentration prior to running the separation. The <5% of <sup>95</sup>Zr not recovered was co-eluted with the Cu, likely due to the large mass of Cu blocking the TOPO active sites from extracting the <sup>95</sup>Zr. Cu was quantified post-separation by diluting the column fractions with 300 times dilution factor for the first fraction, which was bright blue in color and thus highly concentrated, and then diluting the remaining fractions 300 then 30 times to analyze with ICP-OES. Here, the normalized total of Cu was 100 ± 10.8% that eluted in the first three column fractions, with the remaining samples falling below LOD. A minimum decontamination factor of 2.6 x 10<sup>4</sup> for <sup>95</sup>Zr from Cu was calculated based off the LOD value for Cu in the ICP-OES. This value was 10 ppb for the diluted samples analyzed with ICP-OES, which equates to 0.3 ppm Cu in the original samples. The actual DF likely exceeds this since all the loaded Cu is accounted for in the initial few fractions, and the small amount of <sup>95</sup>Zr that co-eluted with Cu was not included in the recovery yield.

## Solid-Liquid Extraction of Zr from Bulk U

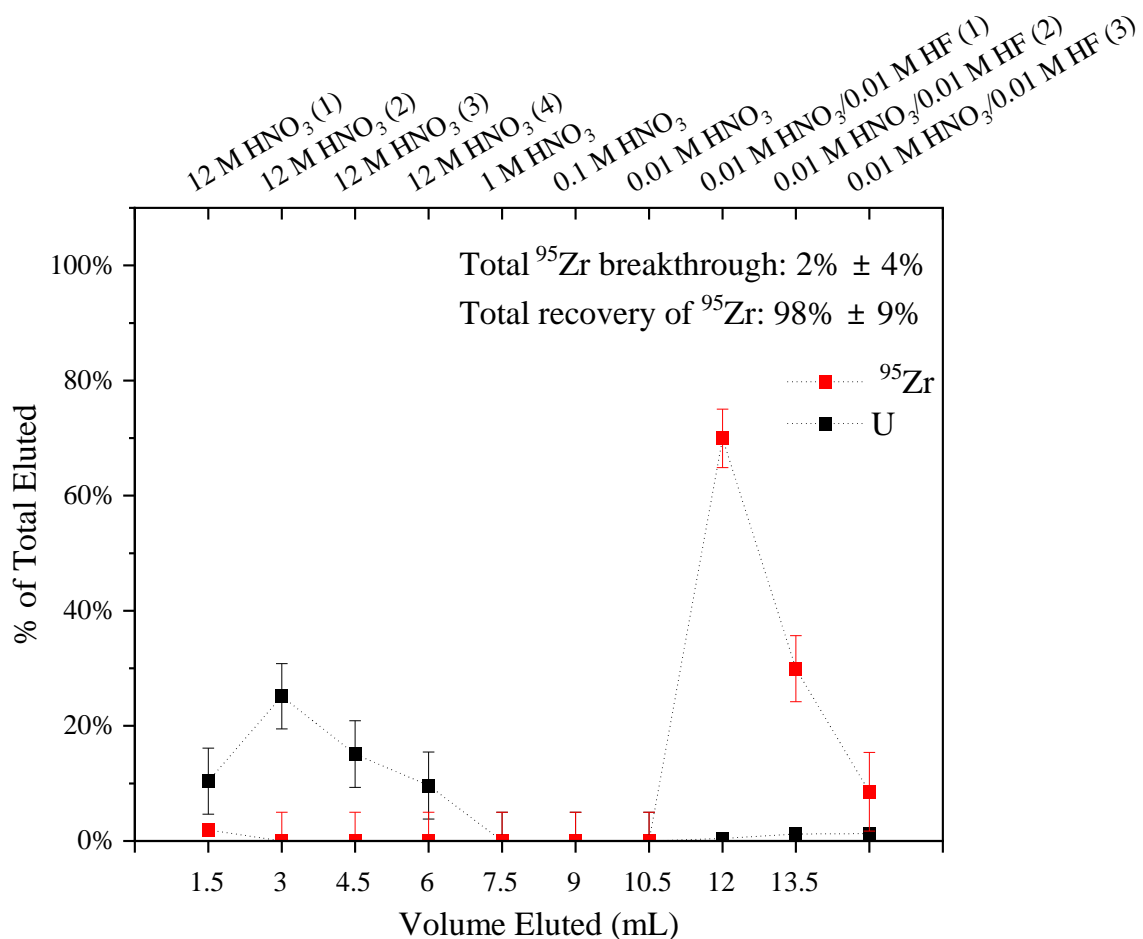


Figure 41: TOPO resin extraction of  $^{95}\text{Zr}$  from a 36 ppm U solution in  $\text{HNO}_3$ . Column yields are normalized. The bottom x-axis shows the volume of total eluent corresponding to the acid concentration on the top x-axis. Lines are only shown to guide the eye.

While the TOPO resin has demonstrated a high extraction efficiency and suitable separation from bulk metals like Al and Cu, an experiment was performed to test the efficacy of the resin if the bulk metal matrix is also extracted by TOPO. The resin was tested to see if  $^{95}\text{Zr}$

could still be extracted when competing with another metal, using a bulk U solution containing trace  $^{95}\text{Zr}$ .

U is extracted by TOPO in  $\text{HNO}_3$  and  $\text{HCl}$ , although with a trend inverse of Zr where the distribution coefficient decreases with increasing acid concentration.<sup>98</sup> However, with all concentrations of  $\text{HNO}_3$  and  $\text{HCl}$ ,  $D > 10$  for U, with  $D > 10^2$  for all  $\text{HCl}$  concentrations. Above 7 M  $\text{HNO}_3$ , the distribution ratio for U is between 10-100.<sup>107</sup> Therefore, Zr separation from bulk U was conducted in 12 M  $\text{HNO}_3$ . A 250  $\mu\text{L}$  solution containing approximately 36 ppm total U traced with  $^{237}\text{U}$ , and trace  $^{95}\text{Zr}$  in 12 M  $\text{HNO}_3$  was added to a pre-conditioned TOPO resin column. The column was initially washed with 3 mL of 12 M  $\text{HNO}_3$ , but a majority of the U remained on the column and was eluted slowly in all of the column fractions. Therefore, to try and elute the U first, two more column fractions of 12 M  $\text{HNO}_3$  were collected for a total of four fractions (90 FCV, 4 BV). Then, sequential additions of 1 M, 0.1 M, and 0.01 M  $\text{HNO}_3$  were collected in 1.5 mL fractions each before collecting three fractions of 0.01 M  $\text{HNO}_3$  and 0.01 M HF. Elution curves for  $^{95}\text{Zr}$  and U are shown in Figure 41. A majority of the  $^{95}\text{Zr}$  was detected in the three column fractions containing HF, and the total sum of activity was  $98 \pm 9\%$  of the original loading solution concentration prior to running the separation.  $2 \pm 12\%$  of  $^{95}\text{Zr}$  not recovered eluted in the first few fractions, likely due to carrying with the bulk U. A total of  $60 \pm 10.7\%$  of the total U eluted across all the column fractions, with the  $^{95}\text{Zr}$  fractions containing in total  $< 3\%$  of the original U concentration. Decontamination factors from each fraction for  $^{95}\text{Zr}$  from U were calculated to be less than 10 due this co-elution of U. Therefore, the extraction conditions tested were useful for debulking the U from the trace  $^{95}\text{Zr}$  with minimal loss, however the separation is not complete due

to co-elution of the U and  $^{95}\text{Zr}$ . Collection of more fractions with 12 M  $\text{HNO}_3$  would not be the practical solution here due to slight extraction of the U by TOPO molecules in the resin causing tailing of the U. Therefore, conditions would need to be altered to ensure complete elution of the U prior to eluting the  $^{95}\text{Zr}$  with HF, or follow this separation procedure with another method to further purify the  $^{95}\text{Zr}$  from the remaining U.

## Conclusion

In this work, a TOPO impregnated resin was synthesized and used to purify trace Zr using solid-phase extraction. The TOPO resin's effectiveness in separating Zr from different bulk metal matrices of Al, Cu, and U were tested to compare to initial solvent extraction purification procedures outlined in chapter 1. The TOPO impregnated resin provides a way to effect rapid purification of trace Zr from solutions of high interfering metal concentrations with minimal time commitment and elution volumes. The resin strongly binds Zr and needs a strong complexant such as  $\text{F}^-$  to remove, which allows for a wide range of acidic solutions to be loaded onto the resin without workup to extract Zr. The TOPO resin can be synthesized in advance and used to harvest Zr present in complex matrices in a wide variety of experimental conditions. This allows for an easily amenable solution to harvesting Zr isotopes from dissolved metal parts at RIB facilities, and its efficacy has been demonstrated here. More studies would need to be performed with the TOPO based resin to make it a practical method for isotope harvesting, such as testing highly radioactive conditions that could degrade the resin or create redox conditions that may affect the Zr extraction chemistry.

## Chapter 3: Microfluidic SLM Zr separations

### Motivation

Extractions utilizing supported liquid membranes (SLM) on the microfluidic scale can be an advantageous method for radionuclide extractions due to small volume requirements and short separation times. In an SLM, there are multiple processes occurring simultaneously, which are as follows: 1) The extraction of the analyte from the feed solution into the membrane, 2) Diffusion of the analyte in the membrane, 3) Release of the analyte from the membrane into the strip solution. The diffusion process is driven by the chemical gradient, and further enhanced with an extractant present in the diluent used to impregnate the porous membrane.<sup>112</sup> SLM extraction is limited by the extraction kinetics and interfacial diffusion of the analyte, not by chemical equilibrium.<sup>113, 114</sup> Flat sheet-supported liquid membranes (FS-SLM) are utilized in this work, where the feed solution flows counter-currently to the strip solution on the opposite side of the SLM. Here, the analyte diffuses downward through the SLM with gravity. Compared to traditional solvent extraction methods, SLMs provide several advantages. The large surface area to volume ratio (273 cm) for <100  $\mu\text{L}$  of liquid provides more surface area for mass transport of the analyte into the membrane, increasing the number of interaction points for metal ions to be extracted. The extraction and back extraction steps occur simultaneously with continuous flow, unlike in a solvent extraction where extraction and back extraction are two distinct steps in most systems. As such, SLM extractions can proceed much faster than traditional separation methods. SLM systems can exploit kinetic differences between analytes with similar extraction thermodynamics to achieve separation, such

as group IV and group V metals with identical complexation chemistry. When reduced to the microfluidic scale, SLM extractions can increase separation efficiency with minimal required volumes. The microfluidic 3D-printed modules used in this work were developed previously to provide a field-deployable means for separation of U and Pu for nuclear forensics.<sup>113, 115, 116</sup> They are cheap, disposable and simple to produce in quantity, which reduces the aversion to utilizing microfluidic SLM methods for radionuclide separations that traditionally require reusable setups prone to contamination. SLM systems could lend well to automation, especially in routine separation processes at isotope production facilities. Automated SLM extractions could improve reproducibility of separations, reduce the total cost, be conducted during online operations, and lower the radiation dose to workers by reducing total “hands on” time required to carry out the separation.

There is little reported work in the literature utilizing microfluidic FS-SLMs for radionuclide separations, and scarce work on using SLMs at present for isotope harvesting.<sup>113, 117</sup> In this work, the developed Zr harvesting chemistry is adapted to a FS-SLM system using previously developed 3D-printed microfluidic modules to provide another method for isotope harvesting of Zr. Ideal conditions for Zr extraction using these systems are investigated and compared to both traditional methods outlined in the literature and the other methods in this work. The SLM extractions of Zr were tested from several bulk metal matrices to ensure their effectiveness for applications to solid-phase harvesting.

## SLM Platform Development

### 3D-Printed Modules

Modules used in this work were developed by Servis et al.<sup>113, 118</sup> and Glennon et al.<sup>115</sup> at LLNL. The 3D printed modules were printed with clear type resin from Formlabs, Inc. A photo of the top and bottom halves of the modules used are shown in Figure 42, with associated dimensions and volumes shown in Table 10. To note, the modules shown are printed with black type resin for visual clarity, but the modules used in the experiments were all printed with clear resin, even though structurally they are the same. These were designed using FreeCAD software and printed in batches of four, where four top halves and four bottom halves are arranged on one printing block in a Formlabs 3 printer. One batch takes approximately 12 hours to print, but they can be made and stored in advance prior to use in experiments. Once printed, they are washed for 30 minutes in an isopropanol bath, then promptly removed to flush the fluid channels with more isopropanol. This step is crucial to remove any excess liquid resin and ensure the channels are open. Once the modules are washed and channels dried with nitrogen flow, they are UV cured for 60 minutes with a Formlabs Form Cure machine to harden the resin.

These modules were tested for chemical resistance against hydrochloric and nitric acids by placing printed resin cubes in concentrated hydrochloric and 12 M nitric acid overnight. The blocks were weighed before and after acid exposure, and no mass difference or visual degradation was observed. The modules were also flowed with 6 M HCl and 12 M HNO<sub>3</sub> feed solutions for up to 1 hour, exceeding the exposure time a module under a typical experiment using these acids would

be exposed to. Vials to collect the feed and strip solution were weighed prior to the experiment, then weighed again after collecting 300  $\mu\text{L}$  at 5  $\mu\text{L}/\text{min}$  for 60 minutes. Using the density of these acids at room temperature (1.088 g/mL for 6 M HCl, 1.33 g/mL for 12 M  $\text{HNO}_3$ ), the volume eluted was calculated based off the mass of eluted solution. The eluted volumes were within 5 % of the expected value based off the syringe pump flow rate and time spent eluting. No visual degradation was observed, and the solutions flowed as expected with no leaking.

Table 10: Dimensions and volume for each 3D printed half-module.

Dimensions (mm)	Volume of channel ( $\mu\text{L}$ )	Total Path Length (mm)	Channel dimensions	Total Volume ( $\mu\text{L}$ )	Surface area-to-volume ratio
$50 \times 50 \times 10$ (L $\times$ W $\times$ H)	8.43	192.3	100 $\mu\text{m}$ depth, 1.2 mm wide	35.5	273 cm

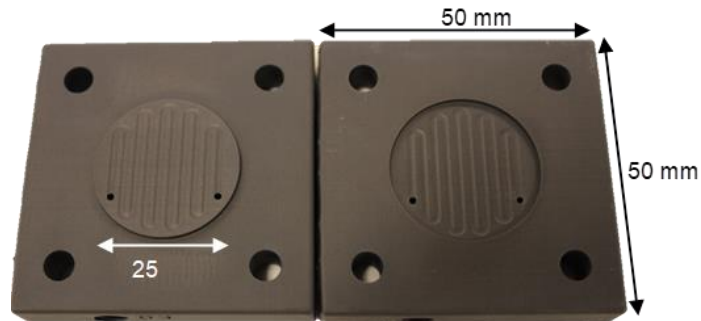


Figure 42: 3D-printed modules with both halves exposing the microchannels. The half-module on the lefthand side is the top half with the convex channel stage, and the right half is the bottom with a concave channel stage. Photo courtesy of K. Glennon (LLNL).

## SLM Extraction Procedure

### Materials

Syringe pumps were NE-1000 SyringeONE pumps from New Era Instruments. Syringes were 3 mL Luer-Lock type with 8.52 mm internal diameter. Hydrophobic Polytetrafluoroethylene (PTFE) membranes used were purchased from Advantec MFS, Inc and were 25 mm in diameter, 80  $\mu\text{m}$  thick with 0.2  $\mu\text{m}$  pores. All tubing used was 1/16" outer diameter, 0.01" inner diameter fluorinated ethylene-propylene (FEP) tubing. Fittings were Luer-Lock 1/4"-28 adapters for connecting the syringes and modules to the tubing along with a ferrule to secure the tubing inside.

## Procedure

Experimental conditions for extractions using the SLM systems are described using syringe pumps; however, they can be easily modified to fit a peristaltic pump system. Syringe pumps were placed in the correct position (see Figure 43). Flow rates and syringe internal diameter settings were set to match the conditions needed for the experiment. Extractant solutions (either 0.01 M TOPO in dodecane, or 0.01 M TOPO/0.03 M HDEHP in dodecane) were pre-equilibrated for at least 30 minutes with the same type of acid used in the feed solution for the experiment. Syringes were filled with appropriate solutions for experiment; The strip solution, such as 1 M HCl or 0.1 M HNO<sub>3</sub>/HF, a “cold” feed solution containing no analytes (typically 8 M HNO<sub>3</sub> or 6 M HCl), and a “hot” feed solution of identical acid concentration as the cold feed, but contains <sup>95</sup>Zr and other analytes (<sup>95</sup>Nb daughter, bulk metals, etc.). Tubing was cut for the two outlet lines and two for the inlet lines. The outlet lines are approximately 3-5 cm to extend into the collection vials from the SLM module. The inlets are approximately 15-20 cm to connect the syringes once placed on the syringe pump to the SLM module. Modules were printed and prepared as described in the previous section “3D-Printed Modules.” The two solution outlet fittings were assembled by pushing the outlet tubing through a ferrule, then through a fitting with a small part of the tubing exposed. An O-ring was fit onto the exposed portion of tubing, which will be screwed into the threaded outlet holes on the module. Two inlet tubing lines were assembled with a fitting containing a ferrule and O-ring on one end to secure to the module, and the other end with a Luer-Lock tightened onto a threaded adapter to secure to one of the syringes containing solution feed or strip solution. A PTFE membrane was placed to sit flat in the concave stage on the bottom half of a 3D-printed module,

covering the microchannels. Several drops (100-200  $\mu\text{L}$ ) of organic extractant solution were cast onto the membrane, ensuring it is completely coated. The top-half of the module was placed in the correct orientation (the outlet holes on both modules should be on the same side, facing the syringe pumps) on top of the bottom half module containing the extractant soaked membrane. These were sealed together with #8 screws with a washer and pushed through each of the four screw holes through the assembled module. Another washer was secured on the underside of the module onto the end of the screw with a nut and hand tightened. Using a screwdriver and wrench to brace, each screw and washer was sealed tightly to hold the modules together. The outlet tubing was attached with connections securely to the outlet holes. Then the inlet fittings were attached to the feed inlet and strip inlet holes. Once all secured, the lines were connected to the feed and strip solution syringes, then secured onto the syringe pump. Care was taken to ensure minimal air and no bubbles were in the syringes prior to connecting. The pump positions were set using the “purge” or “draw” buttons to fit the syringes and secure them prior to beginning pumping. The volume dispensed values on the pumps were reset and the syringes checked to ensure they are tightly secured on the track. The flow rates were set to the desired flow rate for the washing step. Typically, initial flow rates were set to 25  $\mu\text{L}/\text{min}$  to push excess air out and flow the feed and strip solutions completely through the modules, then reduced to the same flow rate as used for the experiment for a total of 150-200  $\mu\text{L}$  dispensed. To begin the experiment, both pumps were started at the same time, then the solution flow monitored as it flows through to check that no leaks occur and that the solutions were flowing correctly. Once all the air was pushed out and no leaks or bubbles were present, solutions were continued flowing through for the desired amount of volume to “wash” the membrane. This step pushes excess air and organic solution out of the lines and acts as a check for

leaks prior to connecting analyte solution. Once washed and all checks were passed, the pumps were paused and the feed solution was swapped out (typically an acidic solution of the same concentration as the feed solution but does not contain any analyte). The connections were checked again to ensure they were secure, and that minimal air and bubbles are present in the syringe. Both the feed and strip solutions were started to pump again. Regular monitoring of the flow of the feed and strip solutions was performed throughout the experiments to monitor for leaks. Once the solutions exited the microchannels, steady-state equilibration began. After the solution was fully contacting the membrane and had almost exited the microchannels, the collection vials were swapped out. These vials were weighed prior to the experiment and counted like the sample collection vials for later analysis. Typically, 50  $\mu\text{L}$  of solution at 5  $\mu\text{L}/\text{min}$  was collected from both the feed and strip lines, then the pumps were paused. The collection vials were swapped out for pre-weighed sample collection vials before beginning pumping again at the desired flow rate for the experiment, carefully minimizing time that the pumps are paused.

After collection time was over, the vials were visually checked that the volumes match 100  $\mu\text{L}$  for both vials. A discrepancy here indicates a leak or insufficient pumping occurred. If weighed before the experiment, these can be weighed to determine the mass of solution that eluted from the modules. Using the known density of the feed and strip solutions, the volume of solution eluted can be determined to verify the correct amount of solution eluted. The eluted solutions were collected for the desired amount of time over the course of the experiment. Unless otherwise noted, 110  $\mu\text{L}$  of solution is collected at a rate of 5  $\mu\text{L}/\text{min}$ , which equates to 22 minutes of total collection time. After the collection period was over, the collection vials were replaced with waste vials and

syringes of water were used to flow through the lines for cleaning. The screws were removed and the entire module is disposed of. A 100  $\mu\text{L}$  aliquot of the feed and strip solutions was taken and placed in separate vials for nuclear counting. The aliquots were counted with an HPGe in the same geometry as the initial feed solution aliquot prior to running the experiment. The count rates for  $^{95}\text{Zr}$  and  $^{95}\text{Nb}$  in the feed and strip solution post-extraction were related to those in the initial feed for extraction analysis.



Figure 43: A fully assembled SLM extraction with two syringe pumps.

## SLM Extraction Parameter Testing

### Adjustment of Feed Solution Acid Concentration

Initial experiments using the SLM systems were conducted using the same conditions used for Zr separation via solvent extraction. Conditions ideal for extraction of Zr as investigated

previously used 0.01 M TOPO in dodecane to extract from 6 M HCl (Figure 15), or from concentrations of HNO<sub>3</sub> above 2 M, ideally 12 M (Figure 16). Therefore, the initial experiment was set up with NCA <sup>95</sup>Zr dissolved in 12 M HNO<sub>3</sub> and flowed over an SLM soaked with 0.01 M TOPO in dodecane at a flow rate of 5 μL/min for 22 minutes as described in the procedure section. The strip solution in this case was 1 M HCl, which flowed countercurrently on the underside of the SLM at the same flow rate and was collected for the same amount of time. Unless otherwise noted, these are the standard conditions utilized for each SLM extraction of <sup>95</sup>Zr using TOPO described in this work. One metric of success used here is not just the total % of total <sup>95</sup>Zr recovered in the strip solution, but also the strip to feed ratio (S:F). Similar to a distribution ratio, a value above 1 indicates a majority of the Zr was extracted into the strip solution. However, the limitation here is that a S:F ratio above 1 may show preference of Zr in the strip versus the feed, however it does not account for total % of Zr accumulated in the membrane itself. Therefore, S:F ratios and % of total <sup>95</sup>Zr in the strip are both reported. The results were 85 ± 5% of the total <sup>95</sup>Zr extracted into the strip solution, with 15 ± 5% remaining in the feed solution. This matches the solvent extraction data under the same conditions using trace NCA <sup>88</sup>Zr, within uncertainty. Compared to a control extraction with the same conditions but with no TOPO dissolved in the diluent, 62 ± 6% of the <sup>95</sup>Zr remained in the feed, and the remaining 38 ± 6% migrated into the membrane with no <sup>95</sup>Zr recovery in the strip. However, the control solvent extraction data shows no <sup>95</sup>Zr uptake in the organic phase with any acid concentration. This is due to phase transfer of slightly nonpolar Zr(NO<sub>3</sub>)<sub>4</sub> complexes into the membrane via diffusion.

Using a 6 M HCl feed, no Zr extraction into the strip solution was observed. This matched the control experiment with no TOPO present in the SLM, where approximately  $65 \pm 7\%$  of the initial  $^{95}\text{Zr}$  activity remained in the feed solution and the remainder of the activity diffused into the membrane. Zr extraction from aqueous solution is largely dependent on the initial TOPO concentration, acid concentration, and contact time. However, the back extraction step is significantly reduced with increasing TOPO concentration. Therefore, higher TOPO concentrations were not used in the membrane to increase Zr recovery, as this would likely cause  $^{95}\text{Zr}$  to accumulate in the membrane and not be recovered in the strip solution without a strong complexant. The HCl concentration is already optimized for the highest recovery, so the lack of extraction points to the poorer extraction kinetics of Zr from HCl compared to  $\text{HNO}_3$ . The approximate residence time of the  $^{95}\text{Zr}$  feed is 1.7 minutes (101 seconds) for a flow rate of 5  $\mu\text{L}/\text{min}$ , which is much less than the  $>10$  minutes of time needed to achieve a distribution ratio above 1 as in the solvent extraction experiments from 6 M HCl with trace Zr. It is likely that the increased surface area the FS-SLM provides compared to solvent extraction is not sufficient to overcome the slow extraction kinetics for Zr from HCl under these conditions tested.

It is important to note that while 12 M  $\text{HNO}_3$  is effective for  $^{95}\text{Zr}$  extraction as demonstrated, it results in higher failure rates using either the syringe pumps or a peristaltic pump system. Since nitric acid has a higher density and viscosity than water, the pumps do not push with enough pressure to dispense the correct volume. This creates a pressure differential on the membrane since the strip solution flows at a faster rate. The standard procedure is to flow the feed and strip solutions at the same flow rate to equalize the pressure on the SLM, however when the

viscosities and densities of the fluids differ significantly, the pressure on the SLM is unequally applied. This causes the membrane to push upward from the higher pressure applied on the underside from the strip solution, which causes a portion of the feed solution to leak into the strip solution channels. In some cases, a leak is not observed, but the feed volume is still lower than anticipated and thus introduces more error in quantifying results of an extraction. 12 M HNO<sub>3</sub> (54 w/w%) used in this work has an experimentally determined density of 1.33 g/mL, which was diluted from concentrated nitric acid with a concentration of 15.025 M (67% w/w%). The approximate published density and viscosity for 12 M HNO<sub>3</sub> (54% w/w) is 1.33 g/mL and 2.0 mPa·s at 20 ° C, respectively.<sup>119, 120</sup> The density of 12 M HNO<sub>3</sub> was experimentally confirmed as well for each stock solution. Water is approximately 1 g/mL and 1.0 mPa·s at 20 ° C. 6 M HCl (18% w/w) has a density and viscosity of approximately 1.1 g/mL and 1.3 mPa·s, respectively.<sup>121</sup> However, no observable issues have been observed using HCl of any concentration over the course of this work. This implies a threshold value above the density and viscosity of water where the pumps fail to deliver the correct volume through the assembled 3D-printed modules, within standard . Therefore, experiments using feed solutions with lower HNO<sub>3</sub> concentrations than 12 M were attempted to identify if suitable <sup>95</sup>Zr extraction could still be achieved while reducing the number of pump failures. Experiments without activity were tested with various HNO<sub>3</sub> concentrations up to 8 M HNO<sub>3</sub>, and no leaks were observed. No degradation of tubing was observed with extended use of 8 M HNO<sub>3</sub> as well. Modules were tested for leaks by visually confirming that the correct volume was eluted in both the strip and feed collection vials, as well as measuring the mass of the solutions eluted to ensure the volume eluted was within 5% error. After testing the effect of HNO<sub>3</sub> feed concentration on <sup>95</sup>Zr extraction, 8 M HNO<sub>3</sub> was selected as

the ideal feed concentration for suitable extraction yield in the remaining experiments and will be further discussed in later sections. Below 8 M HNO<sub>3</sub> for the feed concentration, the <sup>95</sup>Zr extraction efficiency becomes unfavorable. Only 45% of the <sup>95</sup>Zr is extracted into the strip solution with the remainder of the <sup>95</sup>Zr in the feed solution with 7 M HNO<sub>3</sub>. This yields a strip to feed ratio of 0.83, with no accumulation in the membrane. However, the reduced yield of Zr in the strip may be useful for separation of Zr and Nb, as 100% of the <sup>95</sup>Nb remained in the feed, and the only <sup>95</sup>Nb found in the strip solution was from extracted <sup>95</sup>Zr (Figure 44). <sup>95</sup>Nb extraction was much lower than <sup>95</sup>Zr in all extraction conditions tested, likely due to an order of magnitude difference in distribution ratios of Zr and Nb extraction by TOPO from HNO<sub>3</sub>.<sup>90</sup> Slower extraction kinetics can explain this difference in extractability of Zr and Nb, but further experiments are needed to confirm this.

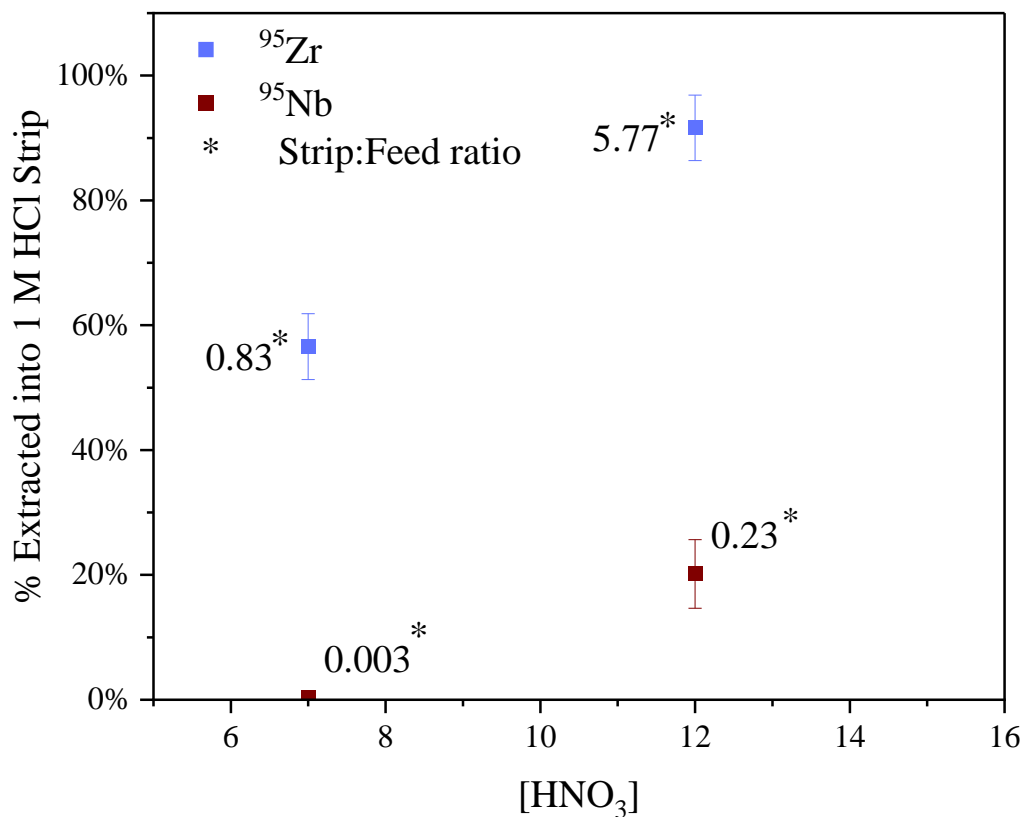


Figure 44: Separation of <sup>95</sup>Zr and <sup>95</sup>Nb by adjustment of HNO<sub>3</sub> in the feed solution using 0.01 M TOPO in dodecane.

### Matrix Effects

Several extractions resulted in little to no detectable <sup>95</sup>Zr in the strip solution, even under conditions where <sup>95</sup>Zr S:F ratios are greater than 1 under ideal conditions. Replicate extractions were tested with various HNO<sub>3</sub> feed concentrations at 6, 8 and 12 M HNO<sub>3</sub> at 5 μl/min with 1 M HCl strip solution and 0.01 M TOPO in dodecane diluent. In these experiments, results closely

resemble the control extractions without TOPO, where <5% of the total  $^{95}\text{Zr}$  is present in the strip product solution. The lower yield of  $^{95}\text{Zr}$  that diffused into the membrane is different from the control. At most,  $20 \pm 6\%$  of the  $^{95}\text{Zr}$  diffused into the membrane, compared to the control value of  $38 \pm 6\%$ , both determined via duplicate extractions.  $^{95}\text{Zr}$  stock solutions were purified via anion-exchange as described previously in methods. However, further purification via solvent extraction was conducted to generate a new stock solution with 0.01 M TOPO and back extracted into 0.1 M  $\text{HNO}_3$ , then acidified back to 8 M  $\text{HNO}_3$ . This new stock was used to run a SLM extraction again as described, but 100% of the  $^{95}\text{Zr}$  remained in the feed solution after flowing through the SLM. While unclear what might be the cause here, there are several possibilities: 1) the presence of fluoride or other salts present in mass far exceeding the  $^{95}\text{Zr}$  concentration in solution, which can carry the  $^{95}\text{Zr}$  and prevent TOPO molecules from binding to the  $^{95}\text{Zr}$ ; 2) when the stock solutions were boiled down and reconstituted during their initial preparation, unknown salts were present and quickly dissolved back in  $\text{HCl}$  or  $\text{HNO}_3$ ; 3) presence of residual Zr-F complexes, which are not extracted by the TOPO due to the strong complexing power of  $\text{F}^-$ ; 4) presence of residual complexants, such as HDEHP from the lanthanide (LN) resin separation of  $^{95}\text{Zr}$  from fission products prior to generating the  $^{95}\text{Zr}$  stocks for this work; 5) Zr could have hydrolyzed over time in solution. However, this is unlikely due to the low pH, trace concentrations of Zr, and trace amounts of fluoride present. Most of the other extractions were successful with stock solutions generated in the same manner, even without additional purification. Therefore, it is unlikely residual fluoride, salts or complexants were a significant factor in the hindered extraction yields of  $^{95}\text{Zr}$  from these experiments, as these effects would be present in all extractions described in this work. It is more probable that hydrolysis was the cause, especially from the purification

process with back extraction into dilute acids, which increases the chance for  $^{95}\text{Zr}$  to hydrolyze. Zr is known to hydrolyze with time, and form colloids with increasing pH.<sup>58</sup> This would need to be confirmed through further experimentation and is outside of the scope of this work. Practically, this can present an issue with using TOPO as an extractant in the FS-SLMs, as extraction yields may be significantly reduced depending upon the age of the solution and if other ions are present. These issues did not present in the exploratory solvent extractions on various Zr solutions. In those studies, no HF or other fluoride sources were used in the separation process. Studies were conducted on both trace and mass concentrations of Zr, including with interfering ions such as excess concentrations of group I and II salts with minimal effect on extraction yields. This points to the FS-SLM extraction method with TOPO to be much more sensitive to matrix effects than solvent extractions or solid-phase extraction. However, Zr hydrolysis is always a concern and likely contributes to the reduced extraction yields.

### Separation of Bulk Zr

Several experiments of Zr extraction were carried out with carrier added Zr to test if the membrane becomes saturated with Zr. The theoretical maximum amount of Zr that can be complexed by TOPO was calculated by assuming TOPO extracts Zr exclusively in a 2:1 ratio, and that once complexed it does not release Zr. 100  $\mu\text{L}$  of 0.01 M TOPO solution was added to the SLM before sealing the module. This equates to approximately  $6.0 \times 10^{17}$  TOPO molecules present. Assuming a 2:1 TOPO:Zr ratio,  $3.0 \times 10^{17}$  Zr complexes can be extracted at maximum. With a feed solution containing 775 ppm Zr solution traced with  $^{95}\text{Zr}$  flowing at 5  $\mu\text{L}/\text{min}$ , approximately  $2.6 \times 10^{16}$  Zr atoms will flow through the SLM per minute. Therefore, the theoretical

point of membrane saturation would be 12 minutes with this feed solution but is likely much higher due to TOPO releasing Zr into the strip solution simultaneously with the initial extraction from the feed. However, over the course of the experiment time of approximately 22 minutes (110  $\mu\text{L}$  at 5  $\mu\text{L}/\text{min}$ ),  $^{95}\text{Zr}$  yields in the strip averaged over duplicate experiments were  $23 \pm 5\%$ , shown in Figure 45. Assuming membrane saturation at 12 minutes of flow time, the Zr extraction yield is estimated to be  $>50\%$ . The  $^{95}\text{Nb}$  yields were reduced as well down to 2% extracted into the strip. Hydrolysis of the Zr may be the cause, where predominantly cationic Zr hydroxide complexes form irreversibly during stock preparation. These complexes are not extractable by TOPO, but remain in solution. This explains why the majority of the Zr remained in the feed solution. The Zr was not sorbed to the polypropylene vial used to contain the stock solution, as this was aliquoted and counted on an HPGe immediately prior to using it for the feed solution in the separation experiment. The first experiment showed no Zr accumulation in the membrane, as mass balance of total Zr was reached between the feed and strip solutions, while the second trial experiment had approximately  $34 \pm 8\%$  accumulation. All variables were kept consistent between the two experiments, however the second experiment where accumulation in the membrane was observed was conducted 6 days later than the first. It is possible that the presence of mass quantities of Zr in the 12 M  $\text{HNO}_3$  solution without fluoride began polymerizing. Zr tetramers are known to form even in acidic solutions.<sup>52</sup> These polymers could have reduced polarity which may enable diffusion into the membrane. The reduced extraction yield of  $^{95}\text{Zr}$  into the strip with this 775 ppm solution implies saturation of the SLM, and thus would require longer residence times or a larger membrane surface area to achieve extraction yields comparable to the NCA Zr yields.

A separate experiment was performed using the same  $^{95}\text{Zr}/\text{Zr}$  stock solution, but in 6 M HCl by boiling and reconstituting a portion of the stock. Here, only  $15 \pm 6\%$  of the Zr was transferred to the strip, with no accumulation in the membrane. Since this work was focused on purification of trace Zr in the context of isotope harvesting, further experiments were not pursued to determine this maximum uptake value of Zr under these conditions. Using TOPO as an extractant in a FS-SLM for Zr extractions shows limitations with matrix effects, such as bulk metals or interfering ions, as well as being kinetically limited predominantly in the initial extraction step. Also, the presence of various Zr species, such as hydrolyzed Zr complexes can cause reduced extraction yields. Therefore, other extractants were investigated to overcome these matrix effects in the SLM systems.

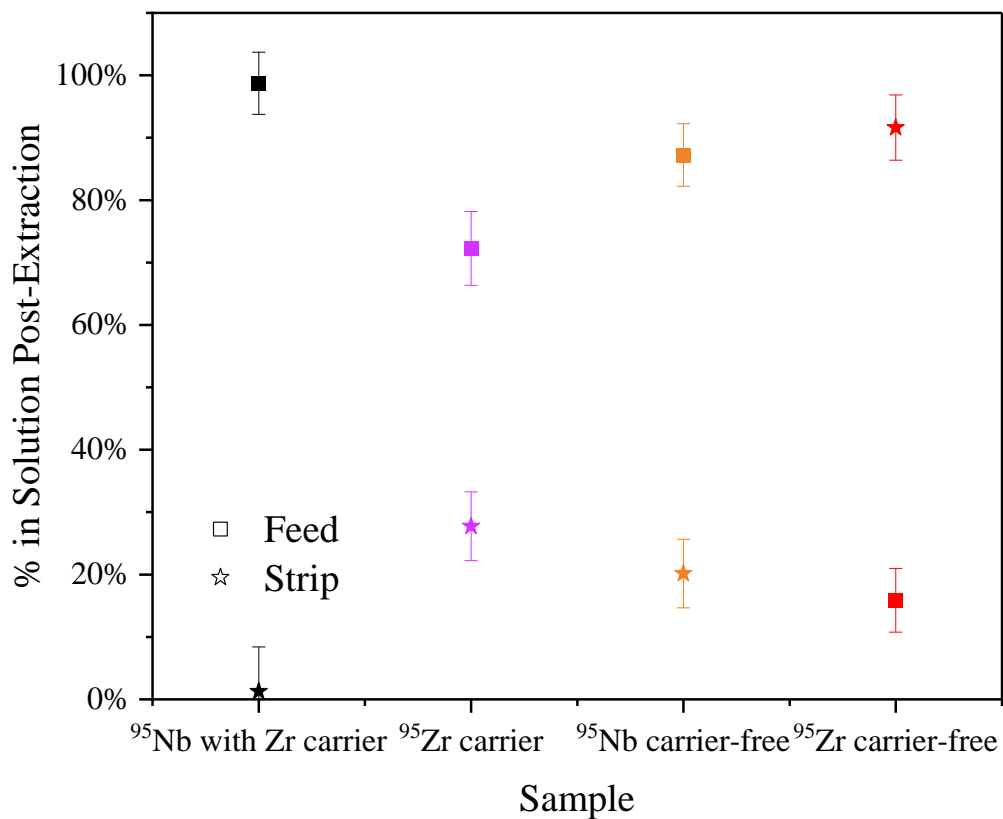


Figure 45: Extraction yields of total Zr and Nb from Zr carrier and carrier free solutions. Squares represent the % of the analyte remaining in the feed solution post-extraction, stars represent the strip solutions. The x-axis indicates Zr and Nb extraction from stable Zr carrier and carrier-free solutions. Data points are colored for visual clarity.

### Separation from Bulk Cu

Once  $^{95}\text{Zr}$  extraction conditions were established with TOPO, extractions were conducted with  $^{95}\text{Zr}$  in solution with Cu as a bulk metal to compare to the solvent extraction and solid-phase

extraction methods. Here, Cu solutions were made by dissolving a known mass of solid Cu metal (TM grade) in 12 M HNO<sub>3</sub>, then diluting to make solutions of 10 ppm Cu and 1000 ppm Cu. <sup>95</sup>Zr in 12 M HNO<sub>3</sub> was spiked in and mixed thoroughly, then 100 μL was counted on an HPGe in the same vial geometry as samples collected from SLM eluted samples. After running an SLM extraction using the standard procedure with this <sup>95</sup>Zr/Cu stock solution, the extraction yields were measured by relative count rates of aliquots of the feed and strip post-extraction. The yields of <sup>95</sup>Zr in the strip solution are plotted in Figure 46 below versus the Cu concentration in the feed. The <sup>95</sup>Zr yield is significantly reduced from both Cu solutions (27 ± 6% for 10 ppm Cu, 34 ± 5% for 1000 ppm Cu) compared to the extraction yield of 85 ± 5% from 12 M HNO<sub>3</sub> without Cu present. No accumulation of <sup>95</sup>Zr in the membrane was observed in either experiment. Cu(II) is not reported to be extracted by neutral organophosphorus extractants in HNO<sub>3</sub>, which suggests the presence of Cu in excess is likely carrying the <sup>95</sup>Zr and hindering its diffusion/extraction into the membrane. Alternatively, the Cu ions could be competing with Zr for coordination with TOPO in the membrane. In either case, the presence of other interfering ions are many orders of magnitude higher in concentration (≈10<sup>6</sup>) compared to the <sup>95</sup>Zr in solution, which hinders extraction of Zr from the feed into the membrane, as the Zr that transfers into the membrane near completely transfers into the strip solution. Compared to the control, <sup>95</sup>Zr transfer from the feed is similar at approximately 30%, but accumulation in the membrane is much more likely with minimal (<5%) <sup>95</sup>Zr phase transferring out of the membrane into the strip solution. This supports the role of TOPO in the extraction, as it greatly enhances extraction of Zr into the SLM from the feed, but also enhances the transfer of Zr into the strip compared to diffusion alone.

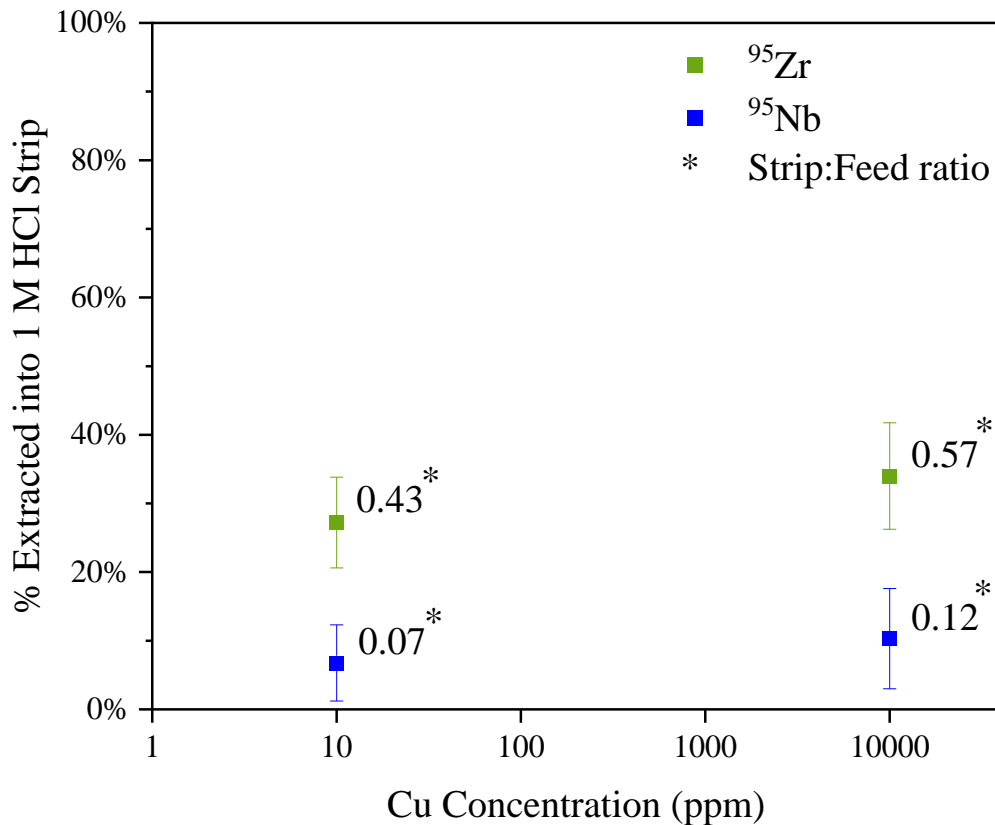


Figure 46:  $^{95}\text{Zr}$  yields in the strip solution with bulk Cu and 0.01 M TOPO.

### Separation from Bulk U and Fission Products

Extraction of  $^{95}\text{Zr}$  from a mixture of  $^{235}\text{U}$  fission products and bulk U was attempted. The yields of  $^{95}\text{Zr}$  and co-extracted radionuclides in the strip solution from dozens of fission products are shown in Figure 47 below. This followed the original extraction procedure with 0.01 M TOPO in dodecane in the SLM, 12 M  $\text{HNO}_3$  feed, 1 M HCl strip and a flow rate of  $5 \mu\text{L}/\text{min}$ .  $^{95}\text{Zr}$  was spiked in to achieve suitable count rates, and the solution was counted in the same geometry as the

samples prior to running the SLM extraction. Some  $^{237}\text{U}$  tracer was present and was used to track the U chemistry using its 208 keV (21%) gamma-ray emission. Samples were counted at the Nuclear Counting Facility (NCF) at LLNL and analyzed with GAMANAL software.<sup>122</sup> The yield of  $^{95}\text{Zr}$  was reduced to  $31 \pm 5\%$  from 85%, likely due to competition with bulk U to permeate into the membrane. The remaining  $^{95}\text{Zr}$  was in the feed solution and not extracted into the membrane. However, no  $^{237}\text{U}$  was detected in the strip solution due to a combination of the poor extraction and stripping kinetics with a high  $\text{HNO}_3$  feed and HCl strip, respectively. The minimal co-extraction of other metals present in solution demonstrates the selectivity for Zr under these conditions with the SLM system.

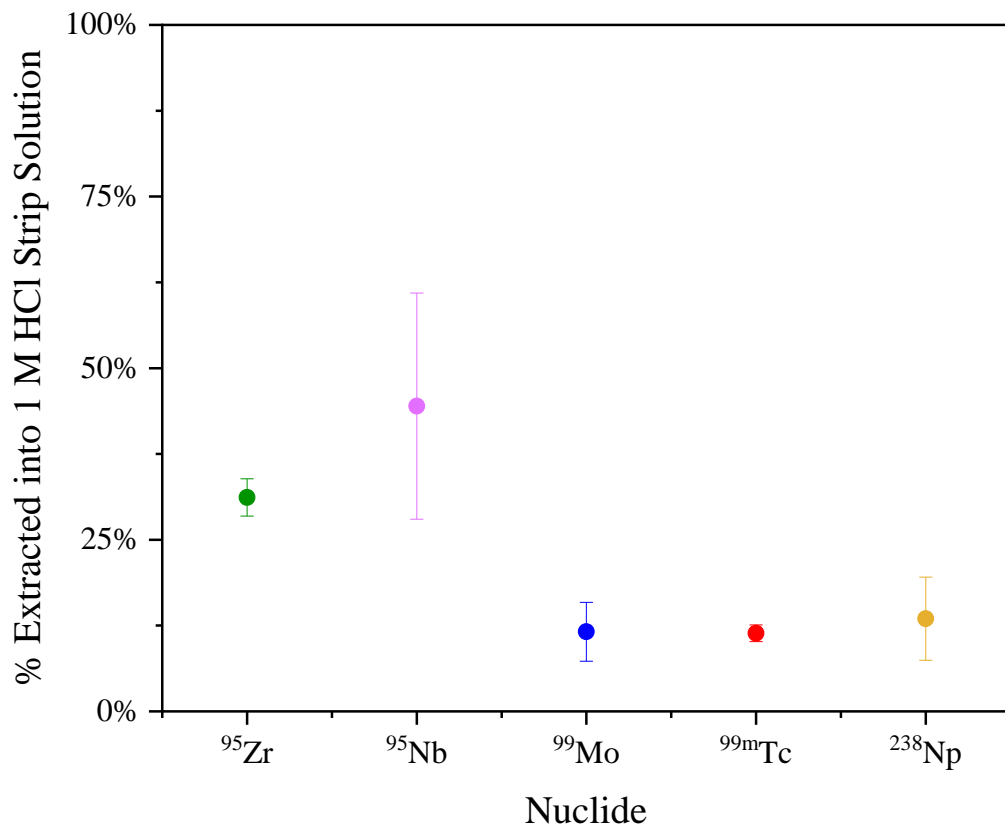


Figure 47: Extraction yields of detected fission products in the strip solution. Fission products that were not extracted into the strip are not shown. Experiment parameters were a flow rate of 5  $\mu\text{L}/\text{min}$ , 12 M  $\text{HNO}_3$  feed, and 1 M HCl strip with bulk U.

A debulking step to remove the U was attempted prior to extracting  $^{95}\text{Zr}$  from the same solution to see if yields could be improved. Adopting the SLM extraction procedure for U by Glennon et al., an SLM experiment was set up with a 3 M  $\text{HNO}_3$  feed containing the bulk U, fission products, and  $^{95}\text{Zr}$ , along with a 0.3 M  $\text{HNO}_3$  strip solution and 30% TBP in dodecane SLM.<sup>115</sup>

This was flowed at 5  $\mu\text{L}/\text{min}$  for 40 minutes. Recovery of U was quantified based off the  $^{237}\text{U}$  tracer and resulted in  $80 \pm 8\%$  in the strip. No  $^{95}\text{Zr}$  was detected in the strip solution, and mass balance was conserved due to all the  $^{95}\text{Zr}$  remaining in the feed. Therefore, no  $^{95}\text{Zr}$  had migrated into the membrane.  $^{237}\text{U}$  presence in the feed could not be verified due to the low count rate being masked by the high Compton background present from the other fission products present in the sample.

The 3 M  $\text{HNO}_3$  feed outlet solution containing  $^{95}\text{Zr}$  was acidified to 12 M  $\text{HNO}_3$ , then flowed through the SLM using the standard TOPO only SLM extraction procedure (0.01 M TOPO extractant, 12 M  $\text{HNO}_3$  feed, 1 M  $\text{HCl}$  strip, 5  $\mu\text{L}/\text{min}$ ). Results here were not conclusive, as  $15 \pm 6\%$   $^{95}\text{Zr}$  was recovered in the strip, and only  $28 \pm 7\%$   $^{95}\text{Zr}$  remained in the feed solution post-extraction.  $57 \pm 10\%$  of the total  $^{95}\text{Zr}$  activity that was not accounted for remained in the membrane. Errors within  $1\sigma$  uncertainty are due to low counting statistics. No  $^{237}\text{U}$  was detected in either the feed or strip solution, likely due to the count rate falling below the LOD. Here it can be assumed that  $^{95}\text{Zr}$  was carried into the membrane by remaining bulk U or other unverified matrix components. While this should be repeated to further track the U and Zr chemistry precisely, it gives insight into the sensitivity of trace Zr extraction with SLMs and the matrix elements present. Using TOPO in an FS-SLM for Zr separation requires a solution debulked of any metals or other impurities to allow for extraction into the membrane and subsequent deposition into the strip. With bulk materials such as U that can co-extract with Zr, their stripping properties should be selected in an SLM separation to prevent Zr entrainment in the membrane.

## Screening Extractants

### HDEHP Chemistry

Several extractants were chosen to test for Zr extraction due to their faster extraction kinetics than TOPO. First was bis(2-ethylhexyl) hydrogen phosphate (HDEHP), an acidic organophosphorus extractant that can extract a wide variety of metals via cation exchange mechanism.

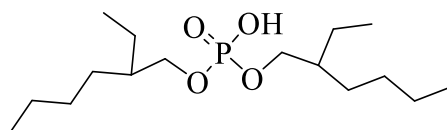
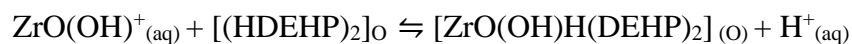


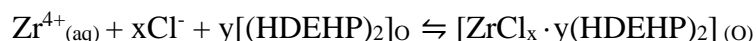
Figure 48: Structure of HDEHP

HDEHP can extract Zr in a wide range of HNO<sub>3</sub> and HCl concentrations. It extracts Zr due to formation of cationic Zr complexes in low acid concentrations, or due to the strong affinity of HDEHP for replacing ions bound to Zr in high concentrations of acid.<sup>123</sup> HDEHP primarily forms dimers in organic solution, but trimers can be present as well in smaller quantities. Once dimerized, it extracts Zr through its phosphoryl oxygen. It extracts cationic Zr through the cation-exchange mechanism:<sup>124</sup>



This stoichiometry can deviate when other cationic hydrolyzed Zr complexes are present in solution but is a suitable approximation for the extraction mechanism.<sup>125</sup>

In higher acid concentrations, the solvation mechanism is more prominent:<sup>53</sup>



HDEHP and TOPO together are known to extract metals synergistically, meaning extraction yields with both ligands together exceeds yields with either ligand alone. Reported widely for the extraction of U, the synergistic effect reaches a maximum at a 1:4 TOPO:HDEHP molar ratio.<sup>89, 126, 127</sup> Favorable synergistic extraction yields of metal ions are claimed to be caused by mixed extractant complexes in solution, however the reasons for improved extraction yields are not completely understood.<sup>128</sup> The synergistic effect may be partially explained by the increased solubility of the extracted complex into the organic phase due to dehydration of the complex by TOPO.<sup>127</sup> TOPO forms hydrogen bonds with acidic organophosphorus reagents (such as HDEHP) in solution, which reduces the viscosity of the organic phase and may contribute to the increased extraction efficiency. However, most extraction systems have an upper limit of extractant concentration before extraction yields are reduced. This is due to the proportional increase of viscosity with extractant concentration in the organic phase, which reduces mass transfer of the analyte into the membrane in SLM systems.<sup>129</sup> Even if not participating in extraction, TOPO acts as a phase modifier by reducing the viscosity of the organic phase, reducing this effect on mass transfer between phases. TOPO and HDEHP form mixed aggregates, which increase in concentration with increasing TOPO concentration relative to HDEHP, while simultaneously

decreasing the amount of HDEHP aggregates. Recent studies suggest the synergistic effect is not due to supramolecular organization in the organic phase prior to extraction of metal ions in the aqueous phase.<sup>126</sup> Therefore, it is assumed that the synergistic effect is primarily caused by differences in the extracted metal complexes with TOPO/HDEHP versus TOPO or HDEHP by themselves.

Tris(2-ethylhexyl)amine (TEHA) and Tris(2-ethylhexyl)phosphate (TEHP), known to extract Zr in high yields and reach equilibrium in less than a minute.

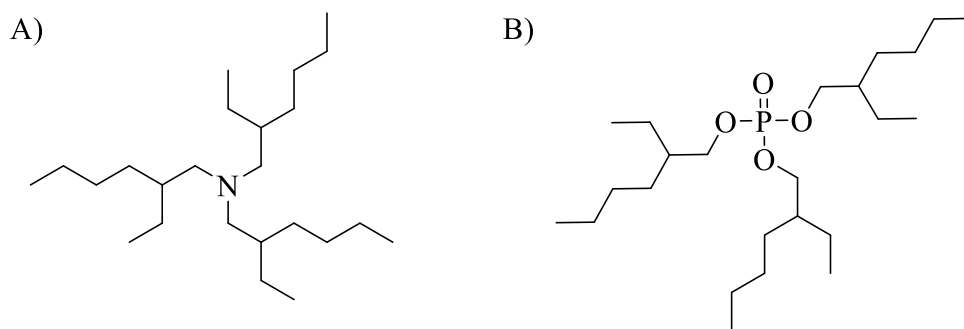


Figure 49: Structures of A) TEHA and B) TEHP.

### Solvent Extraction Methods and Results

Each of these extractants were tested via solvent extraction for efficacy on trace <sup>95</sup>Zr extraction by mixing for 3 minutes with a 1:1 aqueous to organic volume ratio, then separating for nuclear counting. Control extractions were conducted with dodecane containing no extractant, as well as 0.01 M TOPO solutions. All solutions were dissolved in dodecane at a concentration of 0.01 M, except for HDEHP at 0.03 M to keep the TOPO:HDEHP molar ratio at 1:3. A 1:3 ratio

was chosen as a starting point for Zr extraction, as synergism for TOPO and HDEHP is reported to occur in various ratios. 0.03 M HDEHP and 0.01 M TOPO/0.03 M HDEHP were tested to compare to one another along with the previous TOPO extractions. Each extractant was tested for  $^{95}\text{Zr}$  extraction from 1 M  $\text{HNO}_3$ , 6 M  $\text{HNO}_3$  (Figure 50), as well as 1 M  $\text{HCl}$ , 6 M  $\text{HCl}$ , and 8 M  $\text{HCl}$  (Figure 51).

Interestingly, the only solutions that yielded any  $^{95}\text{Zr}$  extraction into the organic phase were those containing HDEHP. The TOPO, TEHA and TEHP solutions did not extract any detectable amounts of  $^{95}\text{Zr}$ . This is an indication that matrix elements hindering  $^{95}\text{Zr}$  extraction are still prevalent, as TOPO is expected to extract  $^{95}\text{Zr}$  in all concentrations of these acids tested based on previous work. HDEHP and TOPO/HDEHP seemingly did not differ in extraction within uncertainty from any nitric acid concentration, ranging from 45-55% extracted into the organic phase. From  $\text{HCl}$ , a similar trend was observed for extraction from 6 M  $\text{HCl}$ , but the TOPO/HDEHP extraction was slightly improved in 8 M  $\text{HCl}$  ( $56 \pm 6\%$  versus  $35 \pm 7\%$ ) and 1 M  $\text{HCl}$  ( $39 \pm 9\%$  versus  $22 \pm 5\%$ ), although this difference may not be statistically significant with repeated trials. From here, SLM extractions using 0.01 M TOPO/0.03 M HDEHP were conducted.

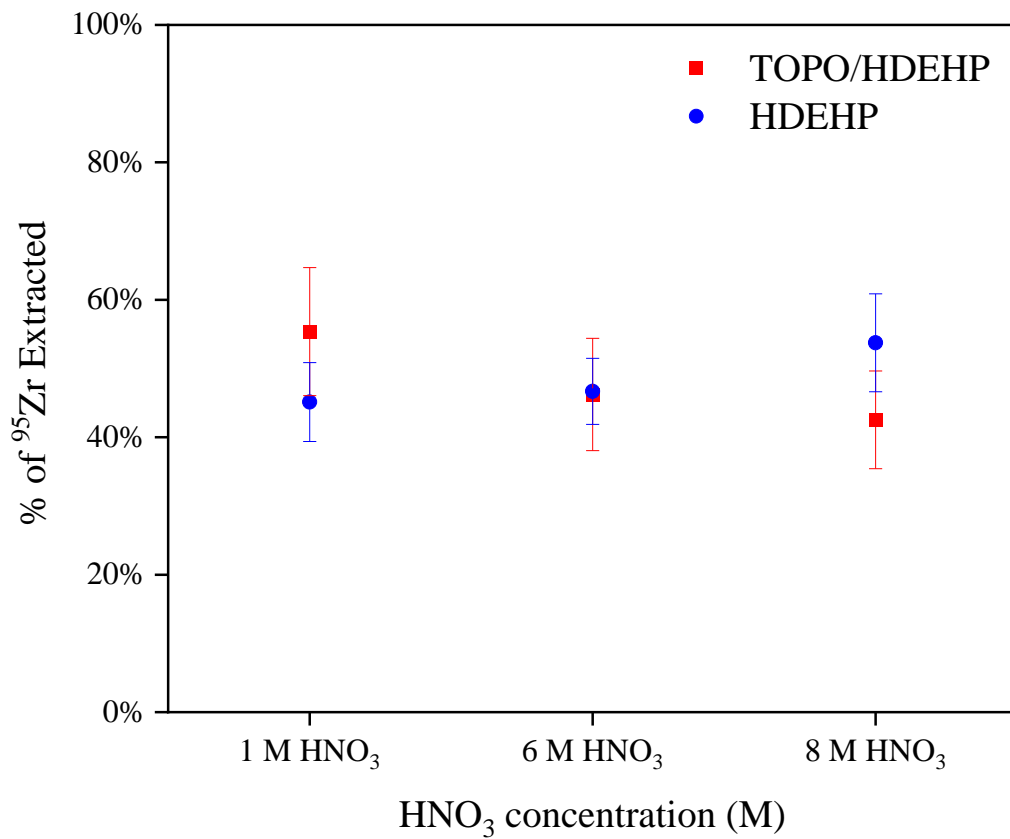


Figure 50: Solvent extractions from HNO<sub>3</sub> solutions with 0.01 M TOPO/0.03 M HDEHP and 0.03 M HDEHP in dodecane diluent.

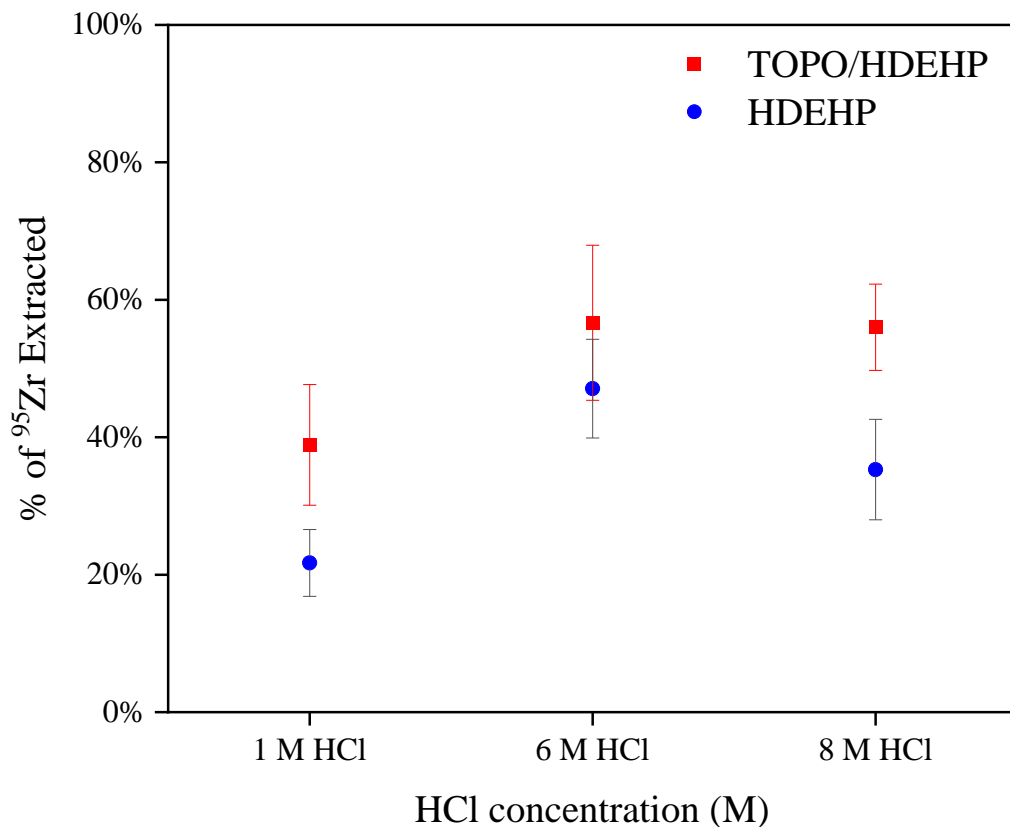


Figure 51: Solvent extractions from HCl solutions with 0.01 M TOPO/0.03 M HDEHP and 0.03 M HDEHP in dodecane diluent.

#### TOPO/HDEHP SLM Extractions

Using 0.01 M TOPO/ 0.03 M HDEHP together with a 6 M HCl, 775 ppm bulk Zr traced with <sup>95</sup>Zr feed solution, the recovery of Zr was improved from  $10 \pm 5\%$  with 0.01 M TOPO to  $58 \pm 6\%$  in the synergistic system (Figure 52). Only 6% accumulated in the membrane, and the remaining

36 ± 5% remained in the feed. HDEHP is known to extract Zr even in its polymerized form, which lead to the improved recovery of Zr from the carrier-added solutions.<sup>101</sup>

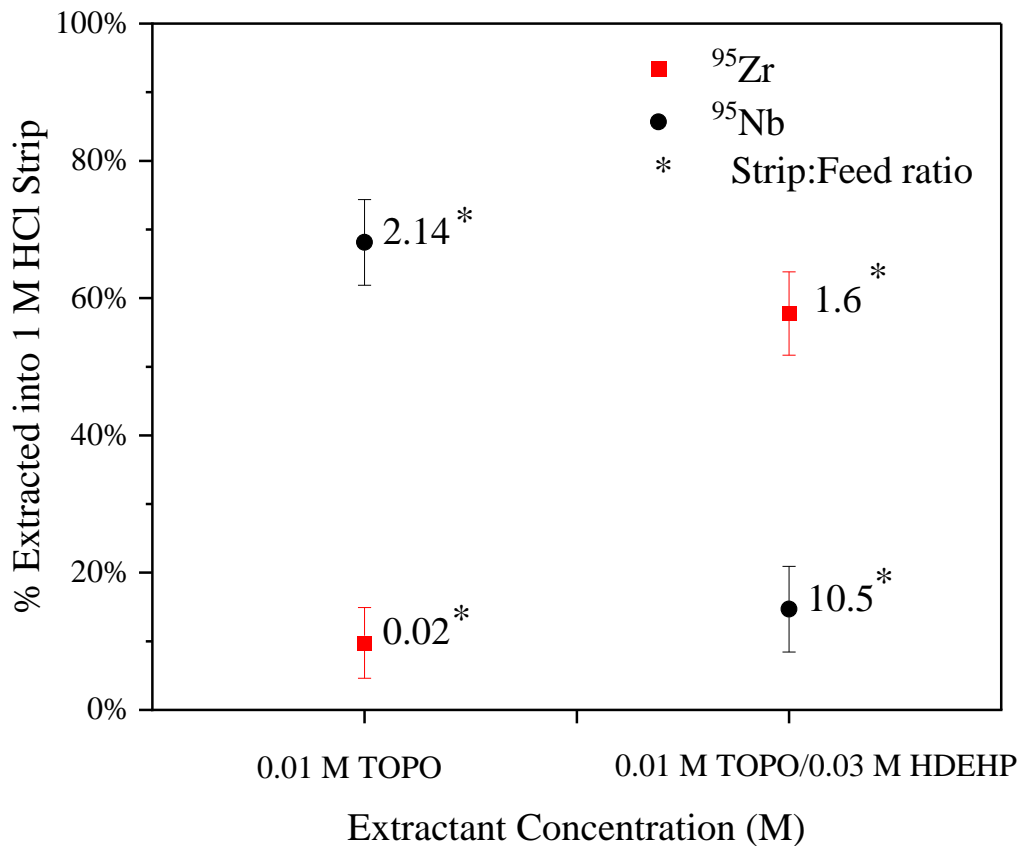


Figure 52: Comparison of extraction with TOPO and TOPO/HDEHP from 6 M HCl feed and 775ppm Zr traced with <sup>95</sup>Zr solution.

SLM extractions from the same 775 ppm carrier-added Zr solution were tested under the same conditions, except with a 12 M HNO<sub>3</sub> feed. With mass quantities of Zr, the extraction yield is improved with TOPO/HDEHP (34 ± 7% yield) versus TOPO alone (18 ± 5%), but is still not

favorable in 12 M HNO<sub>3</sub> due to S:F<1 (Figure 53). The TOPO extraction showed 34% of <sup>95</sup>Zr accumulated in the membrane and 11% for the TOPO/HDEHP extraction, with the remaining <sup>95</sup>Zr in the feed. It is unclear why Zr extraction is still unfavorable in this case, but several factors could contribute. The first is a change in Zr complexation, such as polymerization, although unlikely in 12 M HNO<sub>3</sub>. In HNO<sub>3</sub> concentrations above 2 M, the predominant form of Zr is likely fully chelated Zr(NO<sub>3</sub>)<sub>4</sub>. HDEHP extracts as a dimer complex, which may be sterically hindered to properly extract Zr with four NO<sub>3</sub><sup>-</sup> groups. With HDEHP present, the viscosity of the organic phase is decreased from that of pure dodecane (dodecane=1.34 mPa·s)<sup>130</sup>, so Zr extraction is hindered by phase transfer due to the higher difference in viscosity to 12 M HNO<sub>3</sub> (2.0 mPa·s).<sup>120</sup> Membrane

saturation would not be the cause here, as mass balance of the total Zr was achieved between the feed and the strip alone.

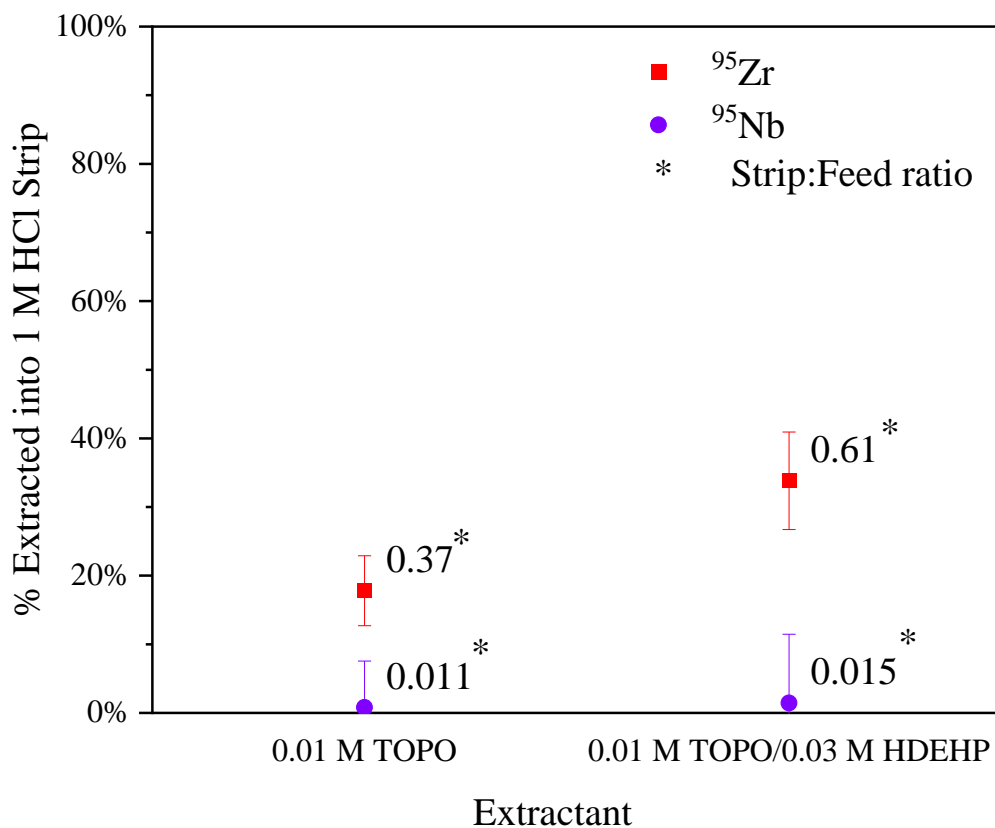


Figure 53: Comparison of extraction with TOPO and TOPO/HDEHP from 12 M HNO<sub>3</sub> feed and 775pm Zr traced with <sup>95</sup>Zr solution.

With trace scale <sup>95</sup>Zr, extraction trends differ in the SLM systems. Under conditions with 6 M HCl feed, 1 M HCl strip solution and 0.01 M TOPO/0.03 M HDEHP, 86 ± 10% of the <sup>95</sup>Zr had extracted from the feed solution, however all of the extracted <sup>95</sup>Zr remained in the membrane, with

no detectable activity in the strip. Back extraction of Zr from HDEHP is unfavorable in dilute HCl, possibly due to steric hindrance of the ligand preventing replacement with  $\text{Cl}^-$ . Therefore, the Zr likely needs to be stripped with a complexant stronger than HDEHP to cause the phase transfer of Zr from the organic layer into the strip. In this case, 0.1 M  $\text{HNO}_3$ /0.1 M HF was used as the strip solution due to the low D value ( $<10$ ) for HDEHP and Zr in these conditions.<sup>131</sup> Repeating the experiment with a 6 M HCl feed and 0.1 M  $\text{HNO}_3$ /0.1 M HF strip,  $84 \pm 6\%$  of the  $^{95}\text{Zr}$  was recovered in the strip. The remaining activity was in the membrane, and no detectable  $^{95}\text{Zr}$  was found in the feed solution. Using 8 M  $\text{HNO}_3$  feed and 0.1 M  $\text{HNO}_3$ /0.1 M HF strip,  $78 \pm 6\%$  of the  $^{95}\text{Zr}$  was recovered in the strip, with the remainder in the membrane. Both extraction results are shown in Figure 54.

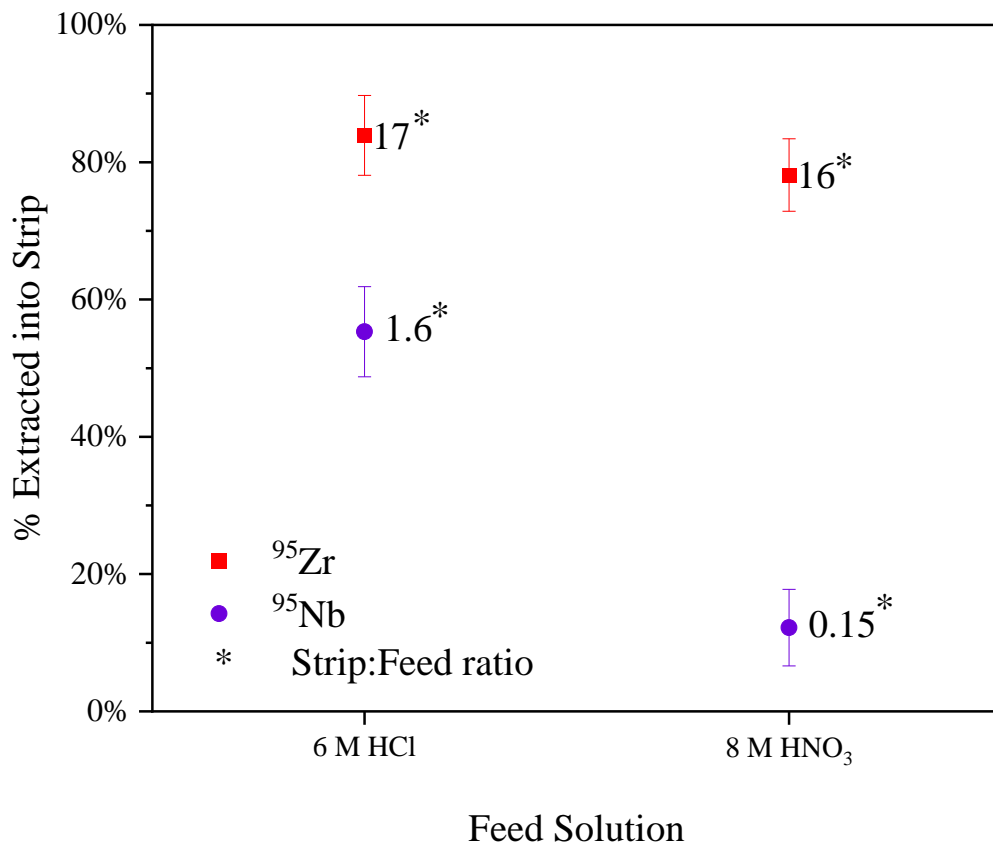


Figure 54:  $^{95}\text{Zr}$  and  $^{95}\text{Nb}$  recovery in the 0.1 M HNO<sub>3</sub>/0.1 M HF strip versus the feed solutions of either 6 M HCl or 8 M HNO<sub>3</sub> using TOPO/HDEHP extractants.

The control extraction of  $^{95}\text{Zr}$  under the same conditions (8 M HNO<sub>3</sub> feed, 0.1 M HNO<sub>3</sub>/0.1 M HF strip) and no extractant in the SLM resulted in  $76 \pm 5\%$  of  $^{95}\text{Zr}$  in the feed, 4% in the strip, and the remaining 20% in the membrane. Compared to the same conditions with 0.03 M HDEHP only,  $93 \pm 6\%$  of  $^{95}\text{Zr}$  was recovered in the strip, with  $8 \pm 5\%$  in the feed. Therefore, it appears the synergistic effect of TOPO and HDEHP together slightly improves the extraction of Zr from the

feed into the membrane, but makes the limiting factor the accumulation of  $^{95}\text{Zr}$  in the membrane. TOPO present in the membrane is likely acting as a phase modifier, improving Zr complex solubility into the organic solution in the membrane. This allows for improved Zr extraction but subsequently slower kinetics for Zr stripping. More studies with mass quantities of Zr are required to elucidate the reasons for reduced extraction compared to those with trace scale Zr.

## Kinetics

Increasing the flow rate of the feed and strip solutions reduces the residence time of the solutions with the SLM as they travel through the channels. Therefore, it is important to determine the effect on Zr extraction and back extraction by changing the flow rate. Figure 55 shows the effect of flow rate on  $^{95}\text{Zr}$  recovery in 1 M HCl. The residence time is calculated by dividing the channel volume for half of a module (volume for either the feed or the strip channels) by the flow rate. At 5  $\mu\text{l}/\text{min}$ , the residence time is 1.7 minutes (101 seconds), which decreases proportionally with flow rate. With increasing flow rate, less Zr is extracted from the feed and simultaneously more Zr accumulates in the membrane due to poor stripping from the organic phase. Above 10  $\mu\text{l}/\text{min}$  from 12 M  $\text{HNO}_3$ , the strip:feed ratio for Zr drops below 1. While increasing flow rates have a large tradeoff in extraction yield, it is important to note that even at 5  $\mu\text{L}/\text{min}$ , the SLM extraction of  $^{95}\text{Zr}$  still results in >80% recovery in the strip solution in less than 30 minutes. For example, 100  $\mu\text{l}$  of strip solution can be obtained in 20 minutes from a 5  $\mu\text{l}/\text{min}$  flow rate, in addition to 10 minutes of steady-state flow prior to sample collection.

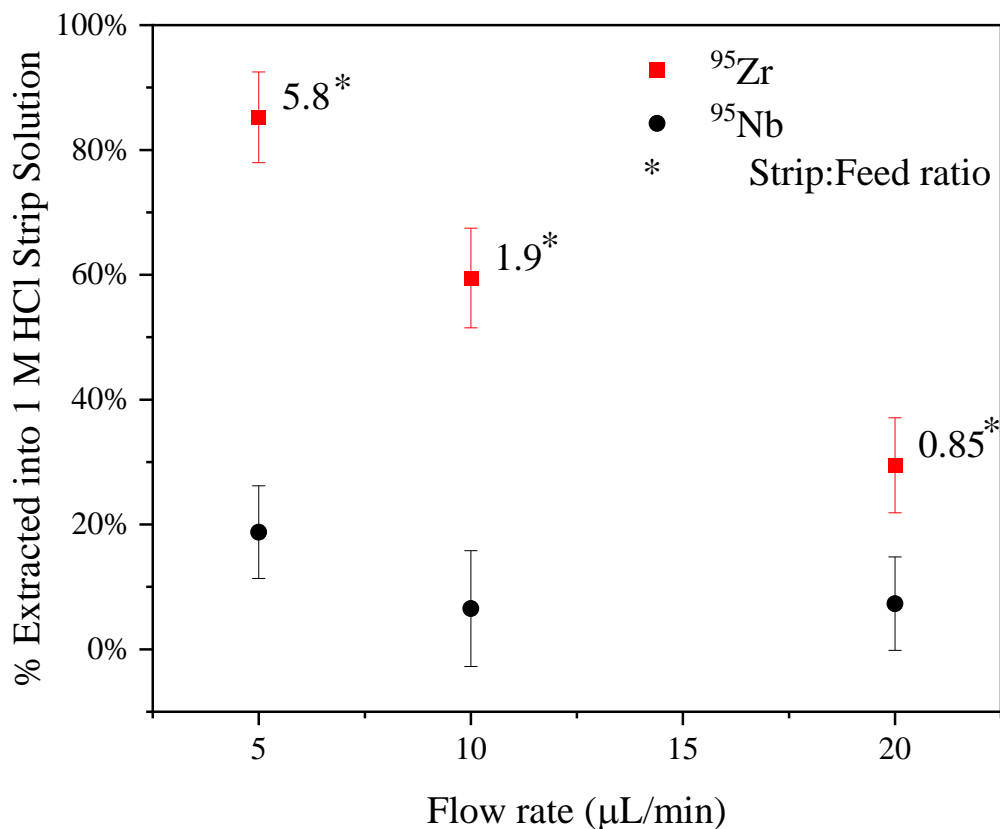


Figure 55: <sup>95</sup>Zr recovery in the 1 M HCl strip versus the flow rate using 0.01 M TOPO.

When testing the effect of flow rate on the TOPO/HDEHP synergistic extractions, the extraction still proceeded with S:F>1 and no appreciable difference in recovery within error up to 20 μl/min. These extraction values and their associated strip to feed ratios are shown in Figure 56. S:F ratios reduce with increasing flow rate due to some <sup>95</sup>Zr not extracting into the membrane. However, each extraction yields >90% of the <sup>95</sup>Zr extracted from the feed and the remaining <sup>95</sup>Zr accumulates in the membrane. <sup>95</sup>Nb extraction yields from the feed solution decrease with flow

rate, but were low even at 5  $\mu\text{l}/\text{min}$  ( $82 \pm 5\%$  remaining in feed post-extraction). At 20  $\mu\text{l}/\text{min}$ ,  $95 \pm 5\%$  of the  $^{95}\text{Nb}$  remained in the feed solution post-extraction.

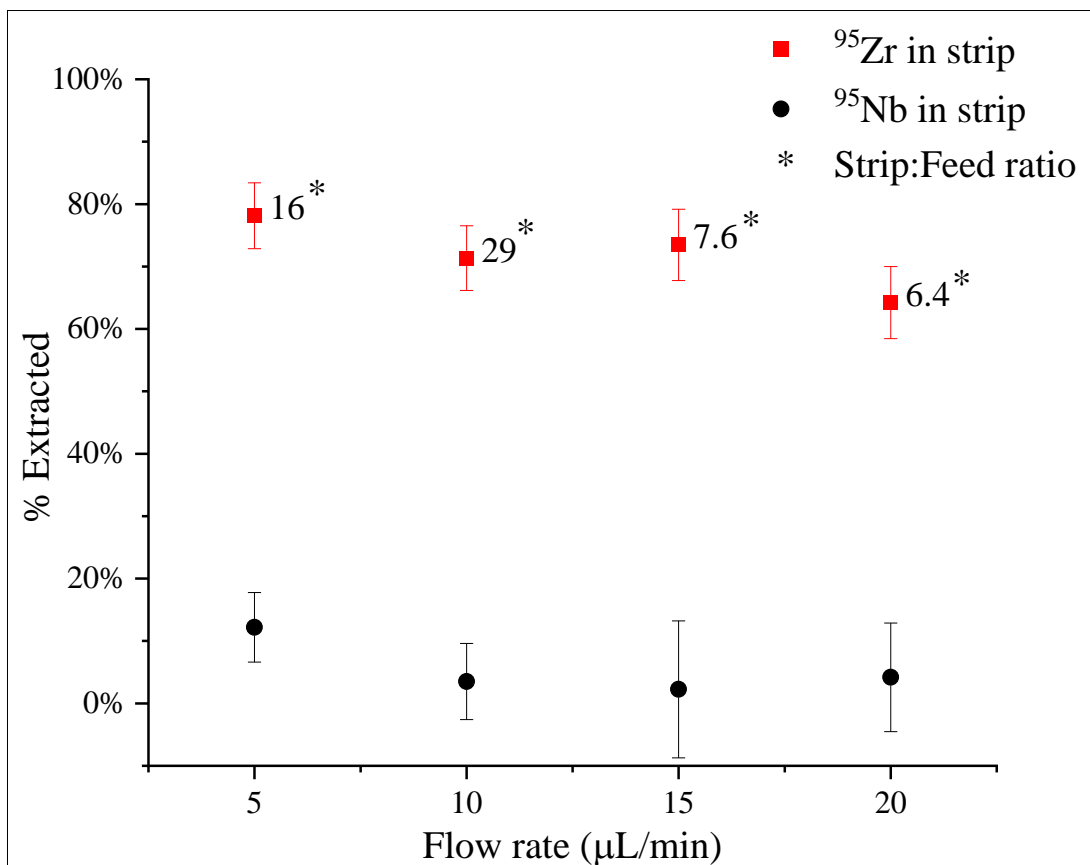


Figure 56:  $^{95}\text{Zr}$  and  $^{95}\text{Nb}$  recovery in the 0.1 M  $\text{HNO}_3$ /0.1 M HF strip versus the flow rate using 0.01 M TOPO/0.03 M HDEHP extractants from an 8 M  $\text{HNO}_3$  feed.

## Extraction of Zr from Bulk Metals with TOPO and HDEHP

### Separation from Bulk Al

Separation of  $^{95}\text{Zr}$  proceeded from a stock solution of approximately 500 ppm Al dissolved in 6 M HCl. Conditions were 0.01 M TOPO/0.03 M HDEHP in dodecane for the extractants, 0.1 M  $\text{HNO}_3$ /0.1 M HF strip flowing at the same flow rate as the feed (5  $\mu\text{L}/\text{min}$ ). Recovery of  $^{95}\text{Zr}$  in the strip was consistent with  $100 \pm 5\%$ , with no detectable activity remaining in the feed solution post-extraction. ICP-OES analysis of the solutions showed the initial stock concentration at 613 ( $\pm 3$ ) ppm, and the feed aliquot post-extraction at 560 ( $\pm 58$ ) ppm. No Al was detected in the strip solution with  $^{95}\text{Zr}$ , so the LOD of 1.5 ppm in the undiluted strip solution was assumed to be the maximum Al concentration. This yields a minimum  $\text{DF}=6.6 \times 10^3$ . A comparison of the extraction yields of  $^{95}\text{Zr}$  and  $^{95}\text{Nb}$  from an Al and Al free solution are shown in Figure 57. Extraction yields from Al are significantly improved. This may be due to the Al hydration sphere, which can pull water molecules out of solution and increase the amount of extractable Zr complexes.<sup>57</sup> This can drive up the formation of zirconium chloride complexes. The net effect is the increased number of Zr and Nb complexes that are soluble and extractable into the membrane.

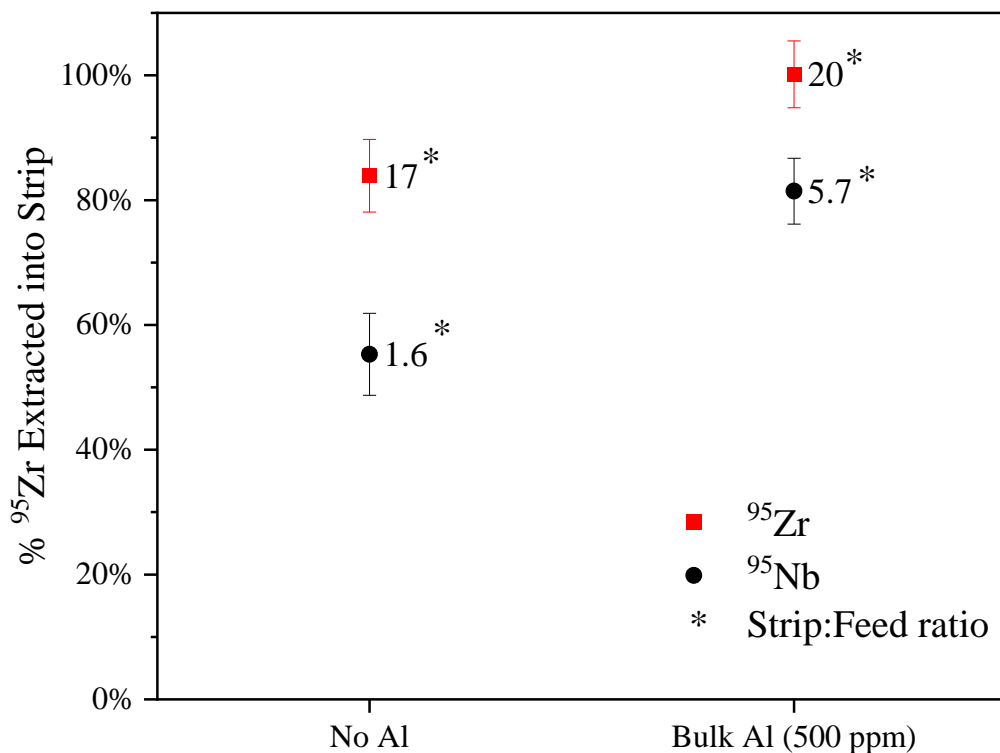


Figure 57: Separation of  $^{95}\text{Zr}$  and  $^{95}\text{Nb}$  from a 500 ppm Al in 6 M HCl solution compared to a solution free of bulk metals.

### Separation from Bulk Cu

Once extraction conditions were established with TOPO/HDEHP, extraction of  $^{95}\text{Zr}$  was conducted from bulk metal matrices. An approximately 10,000 ppm Cu solution was prepared in 8 M  $\text{HNO}_3$  and spiked with  $^{95}\text{Zr}$ , then ran through the SLM with 0.01 M TOPO/0.03 M HDEHP and a 0.1 M  $\text{HNO}_3$ /0.1 M HF strip solution. Compared to extraction from bulk Cu with TOPO

alone (and a 12 M HNO<sub>3</sub> feed), the yield was greatly increased to 80 ± 6%. No detectable <sup>95</sup>Zr was in the feed solution, and 20 ± 5% <sup>95</sup>Zr remained in the membrane. These results are shown in Figure 58. ICP-OES was used to determine the stable Cu content in the feed and strip solutions post-extraction, relative to the initial feed prior to the experiment (quantified with ICP-OES of a stock aliquot). The Cu concentration of the initial feed was determined to be 9,870 ppm, and a relative standard deviation of 6.5%. No Cu was detected in the strip solution, with a LOD of 1.5 ppm based on the dilution factor and 10 ppb LOD for the instrument. The minimum DF for <sup>95</sup>Zr from Cu is 5.2 x 10<sup>3</sup>. The actual DF is likely much higher, as the Cu concentration in the feed solution post-extraction matched the stock aliquot within 2% error. An identical separation was performed with bulk Cu but with a 6 M HCl feed. The recovery of <sup>95</sup>Zr in the strip solution was 89 ± 6%. However, ICP analysis was not performed to verify the Cu concentration in the sample solutions. Visually, the Cu stock solution used as the feed was a deep green, and the strip solution containing the extracted <sup>95</sup>Zr was colorless. Neutral copper chloride complexes can be extracted by organophosphorus reagents, so it is likely there is higher Cu co-extraction into the strip compared to the HNO<sub>3</sub> feed experiment. Therefore, separation of Cu and <sup>95</sup>Zr is preferred from a HNO<sub>3</sub> matrix, however if HCl matrix is desired, this method can at minimum be used as a debulking step, or even achieve suitable DF with sequential separations.

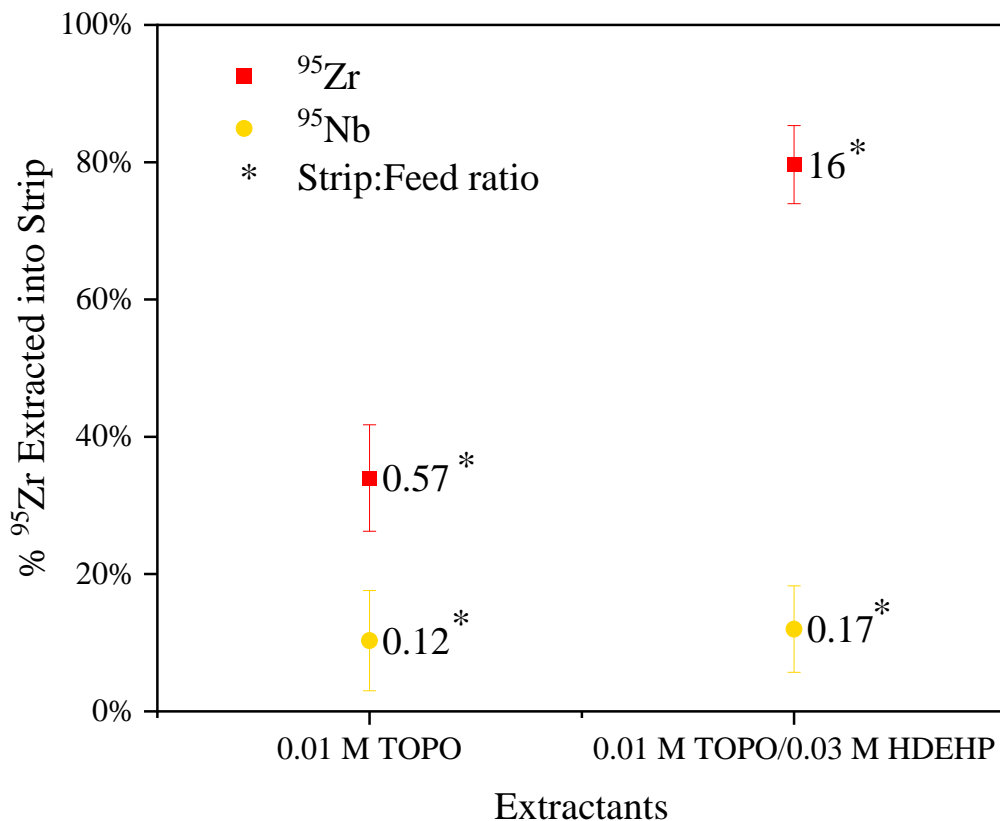


Figure 58:  $^{95}\text{Zr}$  extraction from a 9870 ppm Cu solution with 0.01 M TOPO compared to 0.01 M TOPO/0.03 M HDEHP.

### Separation from Bulk U

Attempting to improve  $^{95}\text{Zr}$  yield, a bulk U/ $^{95}\text{Zr}$  separation was performed with 8 M  $\text{HNO}_3$  and  $^{237}\text{U}$  tracer ([U]= 168 ppm) using the HDEHP/TOPO mixture (Figure 59). The  $^{237}\text{U}$  traced solution was spiked with  $^{95}\text{Zr}$  and reconstituted in 8 M  $\text{HNO}_3$ , then a 100  $\mu\text{L}$  aliquot was counted immediately prior to running the SLM extraction. Using 0.01 M TOPO/0.03 M HDEHP and 0.1

M HNO<sub>3</sub>/0.1 M HF as the strip solution, <sup>95</sup>Zr recovery was 91± 5%, greatly improved from the previous bulk U extractions using only TOPO. Another advantage here was the debulking U step with TBP was not needed. No <sup>95</sup>Zr remained in the feed solution, so the rest of the <sup>95</sup>Zr was likely in the membrane. As for the <sup>237</sup>U/U, 6 ± 2% of the total U was co-extracted into the strip solution, and 19 ± 5% remained in the feed post-extraction. Therefore, a majority of the U was co-extracted into the SLM with <sup>95</sup>Zr, however <sup>95</sup>Zr was preferentially stripped into the 0.1 M HNO<sub>3</sub>/0.1 M HF. While <sup>95</sup>Zr recovery from U was high, the DF was <10 due to the excess mass of U compared to trace <sup>95</sup>Zr. For this to be a suitable separation with DF ≥10<sup>3</sup>, this procedure would likely need to be repeated multiple times by reconstituting the strip in 8 M HNO<sub>3</sub> and repeating the separation. However, complexed F<sup>-</sup> is difficult to remove from Zr by just boiling and reconstituting, so significant workup may be warranted to repeat the SLM separation. Alternatively, the strip solution containing the majority of the <sup>95</sup>Zr could be processed to remove HF and ZrF complexes, acidified, then flowed through an SLM with the same procedure for high recovery and decontamination factor from U. This demonstration shows suitability in debulking of a trace Zr solution from U for further processing.

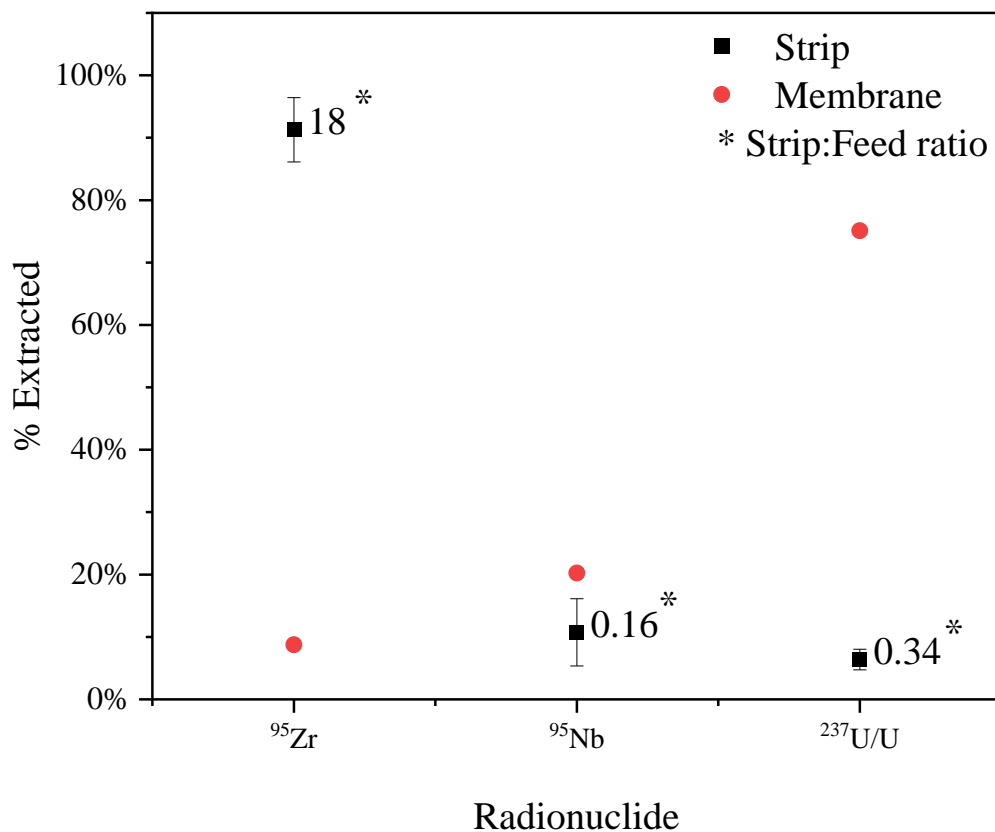


Figure 59: Separation of  $^{95}\text{Zr}$  and  $^{95}\text{Nb}$  from a bulk U matrix. Total [U]=168 ppm traced with  $^{237}\text{U}$ .

### Comparison to Other Zr Extraction Methods

The SLM used for Zr extractions in this work has a distinct advantage over other methods of Zr extraction, and that is operation at microfluidic volumes and with faster timescales. Chemically, they are kinetically limited, as residence times of the analyte feed solution are short. However, separations can be reduced to one step, as the extraction and back-extraction steps typical in a solvent extraction occur simultaneously. The high surface area to volume ratio of the SLM helps

overcome this kinetic limitation, even with the drawback of the reduced surface area an FS-SLM has compared to other types of SLMs. Similar to solvent extraction, a balance between extractant concentration and the acidity of the initial aqueous phase (feed) and back-extraction solution (strip) must be found to optimize Zr recovery. Separation of Zr here from other analytes can be performed using both kinetic and thermodynamic differences between one another, as equilibrium does not need to be established to cause an effective separation. Compared to solid-liquid extraction methods of Zr, quantitative recovery of Zr can be achieved in microfluidic scales of solution, and do not require a strong complexant like fluoride ion in some instances. With the TOPO resin, Zr is only recovered with strong complexant. However, the SLM separation can recover Zr from a debulked solution with TOPO and dilute nitric acid by itself, which is valuable for instances where fluoride ion is undesirable. However, the TOPO based resin is ideal where separations of Zr must occur from large volumes (mL-L scales), as the surface area is greater in the resin ( $87.4 \text{ m}^2/\text{g}$  versus  $62.3 \text{ m}^2/\text{g}$ ) and can be easily scaled up by using larger columns. The SLM is more suitable where fast separations with minimal volumes are required. Also, the 3D printed modules to support the SLMs provide a cheap and simple platform for routine separations with high reproducibility. This may lend well to automation compared to solvent extractions or column separation of Zr, which require more hands-on work to carry out.

## Potential Applications

Use of the SLM in this work can have several applications in radiochemistry. For example, separation of Zr from Nb and Hf isotopes is a challenging endeavor due to their similar chemistry.

Many separations employ their differences in extraction kinetics, which can be amplified using the SLM due to the two different phase transfers that occur in an SLM separation. Zr, Nb and Hf may all be present together in matrices suitable for isotope harvesting at FRIB, such as in solid components that may collect long-lived  $^{88}\text{Zr}$  ( $t_{1/2} = 83.4$  days),  $^{91}\text{Nb}$  ( $t_{1/2} = 680$  years), or  $^{172}\text{Hf}$  ( $t_{1/2} = 1.87$  years).<sup>132, 133</sup> Separation from dedicated isotope production runs may be possible as well. If the target can be rapidly dissolved and passed through an SLM, short-lived Zr isotopes can be quantitatively recovered, such as medically relevant  $^{86}\text{Zr}$  ( $t_{1/2} = 16.5$  hours). These SLMs can minimize dose to the experimentalist since hands on time with radioactivity is reduced, especially if adapted for automation. Preparation of the SLM can occur without the presence of radioactivity, then the sample can be loaded briefly before pumping independent of the operator. The SLMs are also highly tunable, as the feed, strip, and extractant conditions can be easily modified to exploit differences in analyte extraction chemistry. The modules themselves can be modified, for example creating stacked towers where the strip and feed solutions in a single stage extraction can flow into an additional separation step. For example, it may be possible to use the TOPO/HDEHP conditions as described to debulk trace Zr from a solution, then feed it directly into a TOPO SLM for further, more selective purification.

## Conclusion and Future Work

Depending upon the matrix that Zr is in, either TOPO or TOPO/HDEHP can be used as extractants, making the SLM method an easily tunable separation method for Zr. Using TOPO allows for selective extraction of Zr, but with the caveat of sensitivity to matrix element

interference. If high relative concentrations of mass of other elements are present, this can hinder Zr extraction from the feed. TOPO also demonstrates slow extraction kinetics, especially from HCl. As a result, longer residence times are required. Using TOPO synergistically with HDEHP in a 1:3 ratio, or even HDEHP by itself, allows for improved Zr extraction from complex matrices such as bulk metal solutions of Al, Cu and U. TOPO/HDEHP systems are not as selective for Zr, and they require a strong complexant such as fluoride to quantitatively release Zr into the strip solution. Therefore, separation with TOPO only in an SLM offers the advantage of higher selectivity and stripping without complexant. To continue exploring this new method of SLM separation of Zr for isotope harvesting applications, separation efficiency of Zr from other trace radionuclides should be explored, namely Nb and Hf, as separation of Zr from these elements has a wide range of applications in nuclear science. While separation of Nb was touched on in this work, further exploration of ideal extraction parameters needs to be performed to improve the Zr recovery while minimizing Nb co-extraction. Other matrices should be explored as well, such as bulk metals made of W and Au to complement other previous solid-phase isotope harvesting studies.

Overall, several separation methodologies for harvesting Zr isotopes were developed and demonstrated in this work: Anion-exchange and solvent extraction of implanted Zr in solid collector foils, a TOPO impregnated resin for solid-liquid extraction chromatography, and a 3D-printed microfluidic platform for SLM separations. The solvent extraction and anion-exchange methods are well established for Zr recovery, providing a simple means of Zr purification from irradiated target material and co-deposited beam products. The TOPO based resin's effectiveness

in extracting Zr from solution is more amenable to harvesting matrices where large volumes and quantities of bulk metal may be present, which can be easily scaled-up. The microfluidic SLM separation method is suitable for isolating Zr rapidly by reducing the number of total steps needed for a separation. The microfluidic SLM may be more suitable for separations where other radionuclide contaminants are present, or if targeting short-lived isotopes of Zr. All these methods have proven effective for Zr extraction from dissolved bulk metal matrices and can add to our isotope harvesting toolkit for application at FRIB.

## References

- (1) Loveland, W. D.; Morrissey, D. J.; Seaborg, G. T. Modern Nuclear Chemistry. 707.
- (2) Choppin, G. R.; Choppin, G. R.; Liljenzin, J.-O.; Rydberg, J. *Radiochemistry and nuclear chemistry*; Butterworth-Heinemann, 2002.
- (3) Coenen, H. H.; Gee, A. D.; Adam, M.; Antoni, G.; Cutler, C. S.; Fujibayashi, Y.; Jeong, J. M.; Mach, R. H.; Mindt, T. L.; Pike, V. W.; Windhorst, A. D. Consensus nomenclature rules for radiopharmaceutical chemistry — Setting the record straight. *Nuclear Medicine and Biology* **2017**, *55*, v-xi. DOI: 10.1016/j.nucmedbio.2017.09.004 DOI.org.
- (4) Garrison, W. M.; Hamilton, J. G. Production and Isolation of Carrier-Free Radioisotopes. *Chemical Reviews* **1951**, *49* (2), 237-272. DOI: 10.1021/cr60153a001.
- (5) Daraban, L.; Adam Rebeles, R.; Hermanne, A.; Tarkanyi, F.; Takacs, S. Study of the excitation functions for  $^{43}\text{K}$ ,  $^{43,44,44\text{m}}\text{Sc}$  and  $^{44}\text{Ti}$  by proton irradiation on  $^{45}\text{Sc}$  up to 37MeV. *Nuclear Instruments and Methods in Physics Research Section B: Beam Interactions with Materials and Atoms* **2009**, *267* (5), 755-759. DOI: <https://doi.org/10.1016/j.nimb.2009.01.010>.
- (6) Radchenko, V.; Meyer, C. A. L.; Engle, J. W.; Naranjo, C. M.; Unc, G. A.; Mastren, T.; Brugh, M.; Birnbaum, E. R.; John, K. D.; Nortier, F. M.; Fassbender, M. E. Separation of  $^{44}\text{Ti}$  from proton irradiated scandium by using solid-phase extraction chromatography and design of  $^{44}\text{Ti}/^{44}\text{Sc}$  generator system. *Journal of Chromatography A* **2016**, *1477*, 39-46. DOI: <https://doi.org/10.1016/j.chroma.2016.11.047>.
- (7) Va; E., S. C.; Gajecki, L.; Deri, M. A.; Sanders. Current State of  $^{44}\text{Ti}/^{44}\text{Sc}$  Radionuclide Generator Systems and Separation Chemistry. *Current radiopharmaceuticals* **2023**, *16* (2). DOI: 10.2174/187447101666622111154424.
- (8) Radchenko, V.; Engle, J. W.; Medvedev, D. G.; Maassen, J. M.; Naranjo, C. M.; Unc, G. A.; Meyer, C. A. L.; Mastren, T.; Brugh, M.; Mausner, L.; et al. Proton-induced production and radiochemical isolation of  $(^{44})\text{Ti}$  from scandium metal targets for  $(^{44})\text{Ti}/(^{44})\text{Sc}$  generator development. *Nucl Med Biol* **2017**, *50*, 25-32. DOI: 10.1016/j.nucmedbio.2017.03.006 From NLM Medline.
- (9) The Multi-Agency Radiological Laboratory Analytical Protocols (MARLAP) Manual. 2004; Vol. 2.
- (10) Deri, M. A.; Zeglis, B. M.; Francesconi, L. C.; Lewis, J. S. PET imaging with  $^{89}\text{Zr}$ : From radiochemistry to the clinic. *Nuclear Medicine and Biology* **2013**, *40* (1), 3-14. DOI: 10.1016/j.nucmedbio.2012.08.004 ScienceDirect.

- (11) Baimukhanova, A.; Radchenko, V.; Kozempel, J.; Marinova, A.; Brown, V.; Karandashev, V.; Karaivanov, D.; Schaffer, P.; Filosofov, D. Utilization of (p, 4n) reaction for  $^{86}\text{Zr}$  production with medium energy protons and development of a  $^{86}\text{Zr} \rightarrow ^{86}\text{Y}$  radionuclide generator. *Journal of Radioanalytical and Nuclear Chemistry* **2018**, *316* (1), 191-199. DOI: 10.1007/s10967-018-5730-7 (accessed 2022-04-19 19:44:42).Springer Link.
- (12) Sonnabend, K.; Mohr, P.; Zilges, A.; Hertenberger, R.; Wirth, H.-F.; Graw, G.; Faestermann, T. First excited state of the s -process branching nucleus Zr 95. *Physical Review C* **2003**, *68* (4), 048802. DOI: 10.1103/PhysRevC.68.048802 (accessed 2022-04-22 15:24:11).DOI.org (Crossref).
- (13) Hoffman, R. D.; Kelley, K.; Dietrich, F. S.; Bauer, R.; Mustafa, M. G. *Modeled Neutron and Charged-Particle Induced Nuclear Reaction Cross Sections for Radiochemistry in the Region of Yttrium, Zirconium, Niobium, and Molybdenum*; Lawrence Livermore National Laboratory (LLNL), Livermore, CA, US, 2006.
- (14) Reis, V. H.; Hanrahan, R. J.; Levedahl, W. K. The Big Science of stockpile stewardship. *Physics Today* **2016**, *69*. DOI: 10.1063/pt.3.3268.
- (15) McCutchan, E. A.; Sonzogni, A. A. Nuclear Data Sheets for A = 88. *Nuclear Data Sheets* **2014**, *115*, 135-304. DOI: <https://doi.org/10.1016/j.nds.2013.12.002>.
- (16) Shusterman, J. A.; Scielzo, N. D.; Thomas, K. J.; Norman, E. B.; Lapi, S. E.; Loveless, C. S.; Peters, N. J.; Robertson, J. D.; Shaughnessy, D. A.; Tonchev, A. P. The surprisingly large neutron capture cross-section of  $^{88}\text{Zr}$ . *Nature* **2019**. DOI: 10.1038/s41586-018-0838-z Crossref.
- (17) Schmor, P. Review of Cyclotrons for the Production of Radioactive Isotopes for Medical and Industrial Applications. *Reviews of Accelerator Science and Technology* **2011**, *04* (01), 103-116. DOI: 10.1142/S1793626811000574 (accessed 2023/07/14).
- (18) Department of Energy, 2023. <https://isotopes.gov/production-methods>.
- (19) *Meeting Isotope Needs and Capturing Opportunities for the Future: The 2015 Long Range Plan for the DOE-NP Isotope Program, NSAC Isotopes Subcommittee, July 2015*; USDOE Office of Science (SC) (United States), 2015.
- (20) Jha, D. K. *Elements of nuclear reactors*; Discovery Publishing House, 2004.
- (21) Abel, E. P.; Avilov, M.; Ayres, V.; Birnbaum, E.; Bollen, G.; Bonito, G.; Bredeweg, T.; Clause, H.; Couture, A.; DeVore, J.; et al. Isotope harvesting at FRIB: additional opportunities for scientific discovery. *Journal of Physics G: Nuclear and Particle Physics* **2019**, *46* (10), 100501. DOI: 10.1088/1361-6471/ab26cc.

- (22) Domnanich, K. A.; Abel, E. P.; Clause, H. K.; Kalman, C.; Walker, W.; Severin, G. W. An isotope harvesting beam blocker for the National Superconducting Cyclotron Laboratory. *Nuclear Instruments and Methods in Physics Research Section A: Accelerators, Spectrometers, Detectors and Associated Equipment* **2020**, *959*, 163526. DOI: <https://doi.org/10.1016/j.nima.2020.163526>.
- (23) Domnanich, K. A.; Severin, G. W. A Model for Radiolysis in a Flowing-Water Target during High-Intensity Proton Irradiation. *ACS Omega* **2022**, *7* (29), 25860-25873. DOI: 10.1021/acsomega.2c03540.
- (24) Schumann, D.; Stowasser, T.; Dressler, R.; Ayranov, M. Possibilities of preparation of exotic radionuclide samples at PSI for scientific investigations. *Radiochimica Acta* **2013**, *101* (8), 501-508. DOI: 10.1524/ract.2013.2058 Web of Science.
- (25) Margerin, V.; Murphy, A. S. J.; Davinson, T.; Dressler, R.; Fallis, J.; Kankainen, A.; Laird, A. M.; Lotay, G.; Mountford, D. J.; Murphy, C. D.; et al. Study of the  $Ti^{44}(\alpha,p)V^{47}$  reaction and implications for core collapse supernovae. *Physics Letters B* **2014**, *731*, 358-361. DOI: 10.1016/j.physletb.2014.03.003 ScienceDirect.
- (26) Schumann, D.; Ayranov, M.; Stowasser, T.; Gialanella, L.; Leva, A. d.; Romano, M.; Schuermann, D. Radiochemical separation of  ${}^7Be$  from the cooling water of the neutron spallation source SINQ at PSI. *Radiochimica Acta* **2013**, *101* (8), 509-514. DOI: 10.1524/ract.2013.2078 degruyter.
- (27) Ayranov, M.; Schumann, D. Preparation of  ${}^{26}Al$ ,  ${}^{59}Ni$ ,  ${}^{44}Ti$ ,  ${}^{53}Mn$  and  ${}^{60}Fe$  from a proton irradiated copper beam dump. *Journal of Radioanalytical and Nuclear Chemistry* **2010**, *286* (3), 649-654. DOI: 10.1007/s10967-010-0732-0.
- (28) Talip, Z.; Dressler, R.; David, J. C.; Vockenhuber, C.; Müller Gubler, E.; Vögele, A.; Strub, E.; Vontobel, P.; Schumann, D. Radiochemical Determination of Long-Lived Radionuclides in Proton-Irradiated Heavy-Metal Targets: Part I—Tantalum. *Analytical Chemistry* **2017**, *89* (24), 13541-13549. DOI: 10.1021/acs.analchem.7b03952 From NLM ACS Publications.
- (29) Talip, Z.; Dressler, R.; Schacherl, B.; David, J.-C.; Vockenhuber, C.; Schumann, D. Radiochemical Determination of Long-Lived Radionuclides in Proton-Irradiated Heavy Metal Targets: Part II Tungsten. *Analytical Chemistry* **2021**, *93* (31), 10798-10806. DOI: 10.1021/acs.analchem.1c00640 From NLM ACS Publications.
- (30) Pen, A.; Mastren, T.; Peaslee, G. F.; Petrasky, K.; DeYoung, P. A.; Morrissey, D. J.; Lapi, S. E. Design and construction of a water target system for harvesting radioisotopes at the National Superconducting Cyclotron Laboratory. *Nuclear Instruments and Methods in Physics Research Section A: Accelerators, Spectrometers, Detectors and Associated Equipment* **2014**, *747*, 62-68. DOI: 10.1016/j.nima.2014.02.010.

- (31) Abel, E. P.; Domnanich, K.; Clause, H. K.; Kalman, C.; Walker, W.; Shusterman, J. A.; Greene, J.; Gott, M.; Severin, G. W. Production, Collection, and Purification of Ca- 47 for the Generation of Sc- 47 through Isotope Harvesting at the National Superconducting Cyclotron Laboratory. *Acs Omega* **2020**, *5* (43), 27864-27872. DOI: 10.1021/acsomega.0c03020 Web of Science.
- (32) Loveless, C. S.; Marois, B. E.; Ferran, S. J.; Wilkinson, J. T.; Sutherlin, L.; Severin, G.; Shusterman, J. A.; Scielzo, N. D.; Stoyer, M. A.; Morrissey, D. J.; et al. Harvesting 48V at the National Superconducting Cyclotron Laboratory. *Applied Radiation and Isotopes* **2020**, *157*, 109023. DOI: <https://doi.org/10.1016/j.apradiso.2019.109023>.
- (33) Domnanich, K. A.; Vyas, C. K.; Abel, E. P.; Kalman, C.; Walker, W.; Severin, G. W. Harvesting Zn-62 from an aqueous cocktail at the NSCL. *New Journal of Chemistry* **2020**, *44* (47), 20861-20870. DOI: 10.1039/d0nj04411c (accessed 2021-10-07 15:44:51).Web of Science Nextgen.
- (34) Mastren, T.; Pen, A.; Peaslee, G. F.; Wozniak, N.; Loveless, S.; Essenmacher, S.; Sobotka, L. G.; Morrissey, D. J.; Lapi, S. E. Feasibility of Isotope Harvesting at a Projectile Fragmentation Facility: 67Cu. *Scientific Reports* **2014**, *4*, 6706.
- (35) Mastren, T.; Pen, A.; Loveless, S.; Marquez, B. V.; Bollinger, E.; Marois, B.; Hubley, N.; Brown, K.; Morrissey, D. J.; Peaslee, G. F.; Lapi, S. E. Harvesting 67Cu from the Collection of a Secondary Beam Cocktail at the National Superconducting Cyclotron Laboratory. *Analytical Chemistry* **2015**, *87* (20), 10323-10329. DOI: 10.1021/acs.analchem.5b02322.
- (36) Shusterman, J. A.; Scielzo, N. D.; Abel, E. P.; Clause, H. K.; Dronchi, N. D.; Frey, W. D.; Gharibyan, N.; Hart, J. A.; Loveless, C. S.; McGuinness, S. R.; et al. Aqueous harvesting of Zr 88 at a radioactive-ion-beam facility for cross-section measurements. *Physical Review C* **2021**, *103* (2), 024614. DOI: 10.1103/PhysRevC.103.024614.
- (37) Fritz, J. S.; Abbink, J. E. Cation Exchange Separation of Vanadium from Metal Ions. *Analytical Chemistry* **1962**, *34* (9), 1080-1082. DOI: 10.1021/ac60189a014 (accessed 2021-10-10 18:12:51).ACS Publications.
- (38) Takeno, N. Atlas of Eh-pH diagrams. *Geological survey of Japan open file report* **2005**, *419*, 102.
- (39) Connick, R. E.; McVey, W. H. The Aqueous Chemistry of Zirconium. *Journal of the American Chemical Society* **1949**, *71* (9), 3182-3191. DOI: 10.1021/ja01177a070 ACS Publications.
- (40) Dewell, E.; Voight, A. *Zirconium ions in aqueous solution*; 1951.

- (41) Steinberg, E. P. *Radiochemistry of Zirconium and Hafnium*; The National Academies Press, 1960.
- (42) Kraus, K. A.; Johnson, J. S. Hydrolytic Polymerization of Zirconium (IV). *Journal of the American Chemical Society* **1953**, *75* (22), 5769-5769. DOI: 10.1021/ja01118a535 (accessed 2020-06-19 20:10:51).ACS Publications.
- (43) Burger, L. L. *The Chemistry of Tributyl Phosphate: A Review*; General Electric Co. Hanford Atomic Products Operation, Richland, Wash., 1955.
- (44) Asrami, M. R.; Tran, N. N.; Nigam, K. D. P.; Hessel, V. Solvent extraction of metals: Role of ionic liquids and microfluidics. *Separation and Purification Technology* **2021**, *262*. DOI: 10.1016/j.seppur.2020.118289.
- (45) Yao, C.; Zhao, Y.; Ma, H.; Liu, Y.; Zhao, Q.; Chen, G. Two-phase flow and mass transfer in microchannels: A review from local mechanism to global models. *Chemical Engineering Science* **2021**, *229*, 116017. DOI: <https://doi.org/10.1016/j.ces.2020.116017>.
- (46) Mariet, C.; Vansteene, A.; Losno, M.; Pellé, J.; Jasmin, J.-P.; Bruchet, A.; Hellé, G. Microfluidics devices applied to radionuclides separation in acidic media for the nuclear fuel cycle. *Micro and Nano Engineering* **2019**, *3*, 7-14. DOI: 10.1016/j.mne.2019.02.006 ScienceDirect.
- (47) Boyd-Moss, M.; Baratchi, S.; Di Venere, M.; Khoshmanesh, K. Self-contained microfluidic systems: a review. *Lab on a Chip* **2016**, *16* (17), 3177-3192, 10.1039/C6LC00712K. DOI: 10.1039/C6LC00712K.
- (48) Jones, J. Microfluidic Tools for Radiochemical Analysis and High-throughput Radiopharmaceutical Development. UCLA, 2021.
- (49) Parhi, P. K. Supported Liquid Membrane Principle and Its Practices: A Short Review. *Journal of Chemistry* **2013**, *2013*, 618236. DOI: 10.1155/2013/618236.
- (50) 21 - Titanium, Zirconium and Hafnium. In *Chemistry of the Elements (Second Edition)*, Greenwood, N. N., Earnshaw, A. Eds.; Butterworth-Heinemann, 1997; pp 954-975.
- (51) Mailen, J. C.; Eorner, D. E.; Dorris, S. E.; Pih, N.; Robinson, S. M.; Yates, R. G. Solvent Extraction Chemistry and Kinetics of Zirconium. *Separation Science and Technology* **1980**, *15* (4), 959-973. DOI: 10.1080/01496398008076280 Taylor and Francis+NEJM.
- (52) Singhal, A.; Toth, L. M.; Lin, J. S.; Affholter, K. Zirconium(IV) Tetramer/Octamer Hydrolysis Equilibrium in Aqueous Hydrochloric Acid Solution. *Journal of the American Chemical Society* **1996**, *118* (46), 11529-11534. DOI: 10.1021/ja9602399 ACS Publications.

(53) Wang, L. Y.; Lee, M. S. A review on the aqueous chemistry of Zr(IV) and Hf(IV) and their separation by solvent extraction. *Journal of Industrial and Engineering Chemistry* **2016**, *39*, 1-9. DOI: <https://doi.org/10.1016/j.jiec.2016.06.004>.

(54) Nielsen, R. H.; Schlewitz, J. H.; Nielsen, H. Zirconium and Zirconium Compounds. In *Kirk-Othmer Encyclopedia of Chemical Technology*, American Cancer Society, 2013; pp 1-46.

(55) Lister, B. A. J.; McDonald, L. A. 827. Some aspects of the solution chemistry of zirconium. *Journal of the Chemical Society (Resumed)* **1952**, (0), 4315-4330. DOI: 10.1039/jr9520004315 pubs.rsc.org.

(56) Morozov, I. V.; Fedorova, A. A.; Palamarchuk, D. V.; Troyanov, S. I. Synthesis and crystal structures of zirconium(IV) nitrate complexes  $(\text{NO}_2)[\text{Zr}(\text{NO}_3)_3(\text{H}_2\text{O})_3]_2(\text{NO}_3)_3$ ,  $\text{Cs}[\text{Zr}(\text{NO}_3)_5]$ , and  $(\text{NH}_4)[\text{Zr}(\text{NO}_3)_5](\text{HNO}_3)$ . *Russian Chemical Bulletin* **2005**, *54* (1), 93-98. DOI: 10.1007/s11172-005-0222-7.

(57) White, J. C.; Ross, W. J. *The Use of Tri-N-Octylphosphine Oxide in The Solvent Extraction of Zirconium*; United States, 1958. <https://www.osti.gov/biblio/4342898>

<https://www.osti.gov/servlets/purl/4342898DOI>: 10.2172/4342898.

(58) Kobayashi, T.; Sasaki, T.; Takagi, I.; Moriyama, H. Solubility of Zirconium(IV) Hydrrous Oxides. *Journal of Nuclear Science and Technology* **2007**, *44* (1), 90-94. DOI: 10.1080/18811248.2007.9711260 Taylor and Francis+NEJM.

(59) Brown, P. *Chemical Thermodynamics of Zirconium*.

(60) Lu, W.; Anderson, T.; Bowers, M.; Bauder, W.; Collon, P.; Kutschera, W.; Kashiv, Y.; Lachner, J.; Martschini, M.; Ostdiek, K.; et al. Zr/Nb isobar separation experiment for future  $^{93}\text{Zr}$  AMS measurement. *Nuclear Instruments and Methods in Physics Research Section B: Beam Interactions with Materials and Atoms* **2015**, *361*, 491-495. DOI: 10.1016/j.nimb.2015.01.071 ScienceDirect.

(61) Steinberg, E. P. *The Radiochemistry Of Zirconium And Hafnium*; NAS-NS-3011 2016-06-27 NTIS; United States, 1960. <https://www.osti.gov/biblio/4178233>.

(62) Severin, G. W.; Engle, J. W.; Nickles, R. J.; Barnhart, T. E.  $^{89}\text{Zr}$  Radiochemistry for PET. *Medicinal Chemistry* **2011**, *7* (5), 389-394.

(63) Matyskin, A. V.; Stamatopoulos, A.; O'Brien, E. M.; DiGiovine, B. J.; Mocko, V.; Fassbender, M. E.; Vermeulen, C. E.; Koehler, P. E. Production of zirconium-88 via proton irradiation of metallic yttrium and preparation of target for neutron transmission measurements at DICER. *Scientific Reports* **2023**, *13* (1), 1736. DOI: 10.1038/s41598-023-27993-7.

- (64) Zweit, J.; Downey, S.; Sharma, H. L. Production of no-carrier-added zirconium-89 for positron emission tomography. *International Journal of Radiation Applications and Instrumentation. Part A. Applied Radiation and Isotopes* **1991**, *42* (2), 199-201. DOI: [https://doi.org/10.1016/0883-2889\(91\)90074-B](https://doi.org/10.1016/0883-2889(91)90074-B).
- (65) Ivanov, P. I.; Jerome, S. M.; Bozhikov, G. A.; Maslov, O. D.; Starodub, G. Y.; Dmitriev, S. N. Cyclotron production and radiochemical purification of  $^{88,89}\text{Zr}$  via  $\alpha$ -particle induced reactions on natural strontium. *Applied Radiation and Isotopes* **2014**, *90*, 261-264. DOI: 10.1016/j.apradiso.2014.04.018.
- (66) Lahiri, S.; Mukhopadhyay, B.; Das, N. R. Simultaneous production of Zr-89 and Nb-90, Nb-91m, Nb-92m in alpha-particle activated yttrium and their subsequent separation by HDEHP. *Applied Radiation and Isotopes* **1997**, *48* (7), 883-886. DOI: 10.1016/s0969-8043(96)00338-7 Web of Science.
- (67) Zheltonozhskaya, M.; Zheltonozhsky, V. A.; Lykova, E. N.; Chernyaev, A. P.; Iatsenko, V. N. Production of Zirconium-89 by photonuclear reactions. *Nuclear Instruments & Methods in Physics Research Section B-Beam Interactions with Materials and Atoms* **2020**, *470*, 38-41. DOI: 10.1016/j.nimb.2020.03.002 Web of Science.
- (68) Fassbender, M.; Jamriska, D. J.; Hamilton, V. T.; Nortier, F. M.; Phillips, D. R. Radiopharmaceutical Studies and Nuclear Medicine; Simultaneous  $^{68}\text{Ge}$  and  $^{88}\text{Zr}$  recovery from proton irradiated Ga/Nb capsules (LA-UR #03-2319). *Journal of Radioanalytical and Nuclear Chemistry* **2005**, *263* (2), 497-502. DOI: 10.1007/s10967-005-0614-z Springer Link.
- (69) Khan, S. R.; Sharma, B.; Chawla, P. A.; Bhatia, R. Inductively Coupled Plasma Optical Emission Spectrometry (ICP-OES): a Powerful Analytical Technique for Elemental Analysis. *Food Analytical Methods* **2022**, *15* (3), 666-688. DOI: 10.1007/s12161-021-02148-4.
- (70) Bruice, P. Y. *Organic Chemistry*; Pearson Education Inc., 2013.
- (71) Shusterman, J. A. Interactions of Trivalent Lanthanides and Actinides with Solid-Phase Extractants. UC Berkeley, UC Berkeley. <https://escholarship.org/uc/item/4sg7k53t>.
- (72) Reif, B.; Ashbrook, S. E.; Emsley, L.; Hong, M. Solid-state NMR spectroscopy. *Nature Reviews Methods Primers* **2021**, *1* (1), 2. DOI: 10.1038/s43586-020-00002-1.
- (73) Modern Aspects of  $^{31}\text{P}$  NMR Spectroscopy. In *Organophosphorus Chemistry*, 2019; pp 457-498.
- (74) Chapter 7 - NMR of Other Commonly Studied Nuclei. In *Multinuclear Solid-State NMR of Inorganic Materials*, MacKenzie, K. J. D., Smith, M. E. Eds.; Vol. 6; Pergamon, 2002; pp 432-435.

- (75) Hartmann, S. R.; Hahn, E. L. Nuclear Double Resonance in the Rotating Frame. *Physical Review* **1962**, *128* (5), 2042-2053. DOI: 10.1103/PhysRev.128.2042.
- (76) Brunauer, S.; Emmett, P. H.; Teller, E. Adsorption of Gases in Multimolecular Layers. *Journal of the American Chemical Society* **1938**, *60* (2), 309-319. DOI: 10.1021/ja01269a023.
- (77) Brunauer, S.; Deming, L. S.; Deming, W. E.; Teller, E. On a Theory of the van der Waals Adsorption of Gases. *Journal of the American Chemical Society* **1940**, *62* (7), 1723-1732. DOI: 10.1021/ja01864a025.
- (78) Kraus, K. A.; Nelson, F. Anion Exchange Studies of the Fission Products. In *International Conference on the Peaceful Uses of Atomic Energy*, 1956, 1956; United Nations: Geneva, Vol. VII, pp 113-125.
- (79) Kraus, K. A. Anion exchange studies of fission products. In *Proc. Intern. Conf. Peaceful Uses At. Energy*, 1955; Vol. 7, p 113.
- (80) Faris, J. P.; Buchanan, R. F. Anion Exchange Characteristics of the Elements in Nitric Acid Medium. *Analytical Chemistry* **1964**, *36* (6), 1157-1158. DOI: 10.1021/ac60212a067.
- (81) Basu, S. K.; McCutchan, E. A. Nuclear Data Sheets for A = 90. *Nuclear Data Sheets* **2020**, *165*, 1-329. DOI: <https://doi.org/10.1016/j.nds.2020.04.001>.
- (82) Johnson, T. D.; Kulp, W. D. Nuclear Data Sheets for A = 87. *Nuclear Data Sheets* **2015**, *129*, 1-190. DOI: 10.1016/j.nds.2015.09.001.
- (83) Negret, A.; Singh, B. Nuclear Data Sheets for A = 86. *Nuclear Data Sheets* **2015**, *124*, 1-156. DOI: <https://doi.org/10.1016/j.nds.2014.12.045>.
- (84) Singh, B. Nuclear Data Sheets for A = 89. *Nuclear Data Sheets* **2013**, *114* (1), 1-208. DOI: <https://doi.org/10.1016/j.nds.2013.01.001>.
- (85) Ansari, S. A.; Pathak, P.; Mohapatra, P. K.; Manchanda, V. K. Chemistry of Diglycolamides: Promising Extractants for Actinide Partitioning. *Chemical Reviews* **2012**, *112* (3), 1751-1772. DOI: 10.1021/cr200002f.
- (86) Horwitz, E. P.; McAlister, D. R.; Bond, A. H.; Barrans, R. E. Novel Extraction of Chromatographic Resins Based on Tetraalkyldiglycolamides: Characterization and Potential Applications. *Solvent Extraction and Ion Exchange* **2005**, *23* (3), 319-344. DOI: 10.1081/SEI-200049898.

- (87) Pourmand, A.; Dauphas, N. Distribution coefficients of 60 elements on TODGA resin: Application to Ca, Lu, Hf, U and Th isotope geochemistry. *Talanta* **2010**, *81* (3), 741-753. DOI: <https://doi.org/10.1016/j.talanta.2010.01.008>.
- (88) Wang, L. Y.; Lee, H. Y.; Lee, M. S. Solvent Extraction of Zirconium and Hafnium from Hydrochloric Acid Solutions Using Acidic Organophosphorus Extractants and Their Mixtures with TOPO. *Materials Transactions* **2013**, *54* (8), 1460-1466. DOI: 10.2320/matertrans.M2013150.
- (89) Banda, R.; Lee, H. Y.; Lee, M. S. Separation of Zr from Hf in acidic chloride solutions by using TOPO and its mixture with other extractants. *Journal of Radioanalytical and Nuclear Chemistry* **2013**, *298* (1), 259-264. DOI: 10.1007/s10967-012-2349-y.
- (90) Saisho, H. Note on the Solvent Extraction of Some Metals by Tri-n-octyl Phosphine Oxide. *Bulletin of the Chemical Society of Japan* **1962**, *35*, Medium: X; Size: p. 514-515. DOI: 10.1246/bcsj.35.514.
- (91) Biswas, S.; Basu, S. Extraction of zirconium(IV) from hydrochloric acid solutions by tri-octylamine and neutral donors. *Journal of Radioanalytical and Nuclear Chemistry* **1999**, *242* (2), 253-258. DOI: 10.1007/BF02345549.
- (92) Mishra, P. K.; Chakra Vortty, V.; Dash, K. C.; Das, N. R.; Bhattacharyya, S. N. Extraction and separation of Zr, Nb and Hf by Aliquat 336 and its mixtures with TOPO from acidic thiocyanate media. *Journal of Radioanalytical and Nuclear Chemistry* **1992**, *162* (2), 289-298. DOI: 10.1007/BF02035390.
- (93) Pai, S. A.; Subramanian, M. S. Synergistic extraction of uranyl ion with 1-phenyl-3-methyl-4-benzoylpyrazolone-5 (HPMBP) and diphenyl sulfoxide (DPSO), tri-n-butyl phosphate (TBP) or tri-n-octylphosphine oxide (TOPO). *Journal of Radioanalytical and Nuclear Chemistry* **1985**, *89* (2), 423-433. DOI: 10.1007/BF02040606.
- (94) *Product Sheet TK200 Resin*; Triskem.
- (95) Kmak, K. N.; Despotopoulos, J. D.; Scielzo, N. D. Extraction of selenium and arsenic with TOA-impregnated XAD-2 resin from HCl. *Journal of Radioanalytical and Nuclear Chemistry* **2023**. DOI: 10.1007/s10967-023-08818-3.
- (96) Berdous, D.; Akretche, D. E. Recovery of Heavy Metal Using Solvent Impregnated Resin (SIR) Coupled with Donnan Dialysis. *Materials Sciences and Applications* **2012**, *03* (10), 704-712. DOI: 10.4236/msa.2012.310103.
- (97) Navarro, R.; Saucedo, I.; Núñez, A.; Ávila, M.; Guibal, E. Cadmium extraction from hydrochloric acid solutions using Amberlite XAD-7 impregnated with Cyanex 921 (tri-octyl

phosphine oxide). *Reactive and Functional Polymers* **2008**, 68 (2), 557-571. DOI: 10.1016/j.reactfunctpolym.2007.10.027.

(98) Zhang, Z.; Zhou, Y.; Zhou, J.; Qiao, Z.; Zhang, H. Synthesis of TOPO/XAD-16 impregnated resins and effective adsorption of uranium (VI) in acidic solution. *Journal of Radioanalytical and Nuclear Chemistry* **2023**, 332 (4), 1149-1162. DOI: 10.1007/s10967-023-08767-x (accessed 2023-04-08 19:35:52).Springer Link.

(99) Fatah, A. I. L. A. E.; Elashry, S. M. La (III) Separation by Tri Octyl Phosphine Oxide (Cyanex 921) Based on Amberlite Xad-4 Chelating Resin. *Journal of Inorganic and Organometallic Polymers and Materials* **2022**, 32 (7), 2793-2805. DOI: 10.1007/s10904-022-02344-7.

(100) Suneesh, A. S.; Selvan, B. R.; Prathibha, T.; Sriram, S.; Ramanathan, N. Extraction chromatography based separation of zirconium(IV) from simulated high-level liquid waste using N,N-di-octyl-2-hydroxyacetamide impregnated amberlite XAD-7 resin. *Chemical Engineering Journal Advances* **2021**, 8, 100182. DOI: 10.1016/j.ceja.2021.100182 ScienceDirect.

(101) Banda, R.; Lee, M. S. Solvent Extraction for the Separation of Zr and Hf from Aqueous Solutions. *Separation & Purification Reviews* **2015**, 44 (3), 199-215. DOI: 10.1080/15422119.2014.920876 DOI.org (Crossref).

(102) Nayl, A. A.; El-Nadi, Y. A.; Daoud, J. A. Extraction and Separation of Zr(IV) and Hf(IV) from Nitrate Medium by Some CYANEX Extractants. *Separation Science and Technology* **2009**, 44 (12), 2956-2970. DOI: 10.1080/01496390903014169.

(103) Wang, L. Y.; Lee, M. S. Development of a separation process for the selective extraction of hafnium(IV) over zirconium(IV) from sulfuric acid solutions by using D2EHPA. *Hydrometallurgy* **2016**, 160, 12-17. DOI: 10.1016/j.hydromet.2015.11.013 ScienceDirect.

(104) Lommelen, R.; Vander Hoogerstraete, T.; Onghena, B.; Billard, I.; Binnemans, K. Model for Metal Extraction from Chloride Media with Basic Extractants: A Coordination Chemistry Approach. *Inorganic Chemistry* **2019**, 58 (18), 12289-12301. DOI: 10.1021/acs.inorgchem.9b01782.

(105) Banda, R.; Min, S. H.; Lee, M. S. Selective extraction of Hf(IV) over Zr(IV) from aqueous H<sub>2</sub>SO<sub>4</sub> solutions by solvent extraction with acidic organophosphorous based extractants. *Journal of Chemical Technology and Biotechnology* **2014**, 89 (11), 1712-1719. DOI: 10.1002/jctb.4249.

(106) Dey, P.; Basu, S. Synergistic Extraction of Copper from Nitrate Solutions Using  $\beta$ -Hydroxy-Naphthaldoxime and Organophosphorus Compounds into Carbon-Tetrachloride. *Metallurgical and Materials Transactions B* **2011**, 42 (6), 1136-1143. DOI: 10.1007/s11663-011-9552-z.

- (107) Gindler, J. E. *Radiochemistry of uranium*; United States, 1962. <https://www.osti.gov/servlets/purl/5392883DOI>: 10.2172/5392883.
- (108) *XAD-7 Certificate of Analysis*.
- (109) Company, R. a. H. *Amberlite XAD7HP*; 2006.
- (110) He, H.; Klinowski, J. Solid-state NMR studies of the aluminophosphate molecular sieve AlPO<sub>4</sub>-18. *The Journal of Physical Chemistry* **1993**, *97* (40), 10385-10388. DOI: 10.1021/j100142a020.
- (111) Wang, F.; Tang, R.; Kao, J. L. F.; Dingman, S. D.; Buhro, W. E. Spectroscopic Identification of Tri-n-octylphosphine Oxide (TOPO) Impurities and Elucidation of Their Roles in Cadmium Selenide Quantum-Wire Growth. *Journal of the American Chemical Society* **2009**, *131* (13), 4983-4994. DOI: 10.1021/ja900191n.
- (112) Amini, M.; Rahbar-Kelishami, A.; Alipour, M.; Vahidi, O. Supported Liquid Membrane in Metal Ion Separation: An Overview. *Journal of Membrane Science and Research* **2018**, *4* (3), 121-135. DOI: 10.22079/jmsr.2017.63968.1138.
- (113) Servis, A. G.; Parsons-Davis, T.; Moody, K. J.; Gharibyan, N. 3D Printed Microfluidic Supported Liquid Membrane Module for Radionuclide Separations. *Industrial & Engineering Chemistry Research* **2021**, *60* (1), 629-638. DOI: 10.1021/acs.iecr.0c05349.
- (114) Bartsch, R. A.; Way, J. D. Chemical Separations with Liquid Membranes: An Overview. In *Chemical Separations with Liquid Membranes*, ACS Symposium Series, Vol. 642; American Chemical Society, 1996; pp 1-10.
- (115) Glennon, K. J.; Valdovinos, H. F.; Parsons-Davis, T.; Shusterman, J. A.; Servis, A. G.; Moody, K. J.; Gharibyan, N. 3D printed field-deployable microfluidic systems for the separation and assay of Pu in nuclear forensics. *Lab Chip* **2022**, *22* (23), 4493-4500. DOI: 10.1039/d2lc00391k.
- (116) Anna G. Servis, N. G., Kenton J. Moody, Tashi Parsons-Davis. Modular, Disposable 3d Printed Microfluidic Membrane System for Separation And Purification. 11,724,213 B2.
- (117) Scott, M. D.; Schorp, J.; Sutherlin, L.; Robertson, J. D. Isotope harvesting with Hollow Fiber Supported Liquid Membrane (HFSLM). *Applied Radiation and Isotopes* **2020**, *157*, 109027. DOI: 10.1016/j.apradiso.2019.109027 ScienceDirect.
- (118) Anna G. Servis, N. G., Kenton J. Moody, Tashi Parsons-Davis. Modular, Disposable 3d Printed Microfluidic Membrane System for Separation And Purification. 11,724,213 B2, 2023.

(119) Thiemann, M.; Scheibler, E.; Wiegand, K. W. Nitric Acid, Nitrous Acid, and Nitrogen Oxides. In *Ullmann's Encyclopedia of Industrial Chemistry*, 2000.

(120) Lewis, L. C. *The Physical Properties of Nitrate Solutions of EBR-II Fuel Elements*; United States, 1968. <https://www.osti.gov/biblio/4481042>

<https://www.osti.gov/servlets/purl/4481042DOI>: 10.2172/4481042

(121) Nishikata, E.; Ishii, T.; Ohta, T. Viscosities of aqueous hydrochloric acid solutions, and densities and viscosities of aqueous hydroiodic acid solutions. *Journal of Chemical & Engineering Data* **1981**, *26* (3), 254-256. DOI: 10.1021/je00025a008.

(122) Gunnink, R.; Niday, J. B. *Computerized quantitative analysis by gamma-ray spectrometry Volume I Description of the GAMANAL program*; UCRL--51061(Vol1); United States, 1972. [http://inis.iaea.org/search/search.aspx?orig\\_q=RN:04042261](http://inis.iaea.org/search/search.aspx?orig_q=RN:04042261).

(123) Kandil, S. A.; Scholten, B.; Saleh, Z. A.; Youssef, A. M.; Qaim, S. M.; Coenen, H. H. A comparative study on the separation of radiozirconium via ion-exchange and solvent extraction techniques, with particular reference to the production of <sup>88</sup>Zr and <sup>89</sup>Zr in proton induced reactions on yttrium. *Journal of Radioanalytical and Nuclear Chemistry* **2007**, *274* (1), 45-52. DOI: 10.1007/s10967-006-6892-2.

(124) Abdel-Fattah, A. A.; Ali, S. M.; El-Sweify, F. H. Thermodynamics of the solvent extraction of Zr(IV) by Amberlite LA-2, TBP and HDEHP from different aqueous media. *Journal of Radioanalytical and Nuclear Chemistry* **2002**, *253* (3), 465-475. DOI: 10.1023/A:1020433906562.

(125) Eiroa-Lledo, C.; Wall, D. E.; Wall, N. A. Extraction mechanism of Tc(IV) by Di-(2-ethylhexyl)phosphoric acid (HDEHP). *Journal of Radioanalytical and Nuclear Chemistry* **2022**, *331* (6), 2751-2760. DOI: 10.1007/s10967-022-08303-3.

(126) Pecheur, O.; Dourdain, S.; Guillaumont, D.; Rey, J.; Guilbaud, P.; Berthon, L.; Charbonnel, M. C.; Pellet-Rostaing, S.; Testard, F. Synergism in a HDEHP/TOPO Liquid-Liquid Extraction System: An Intrinsic Ligands Property? *The Journal of Physical Chemistry B* **2016**, *120* (10), 2814-2823. DOI: 10.1021/acs.jpcc.5b11693.

(127) Singh, S. K.; Tripathi, S. C.; Singh, D. K. Studies on the Separation and Recovery of Uranium from Phosphoric Acid Medium Using a Synergistic Mixture of (2-Ethylhexyl)phosphonic Acid Mono 2-Ethyl Hexyl Ester (PC-88A) and Tri-n-octylphosphine Oxide (TOPO). *Separation Science and Technology* **2010**, *45* (6), 824-831. DOI: 10.1080/01496391003607498.

- (128) Zhu, Z.; Zhang, W.; Cheng, C. Y. A literature review of titanium solvent extraction in chloride media. *Hydrometallurgy* **2011**, *105* (3), 304-313. DOI: 10.1016/j.hydromet.2010.11.006 ScienceDirect.
- (129) Wannachod, T.; Leepipatpiboon, N.; Pancharoen, U.; Nootong, K. Synergistic effect of various neutral donors in D2EHPA for selective neodymium separation from lanthanide series via HFSLM. *Journal of Industrial and Engineering Chemistry* **2014**, *20* (6), 4152-4162. DOI: <https://doi.org/10.1016/j.jiec.2014.01.014>.
- (130) Dymond, J. H.; O/ye, H. A. Viscosity of Selected Liquid n-Alkanes. *Journal of Physical and Chemical Reference Data* **1994**, *23* (1), 41-53. DOI: 10.1063/1.555943.
- (131) Ekatova, T. Y.; Kazakov, A. G. Extraction-chromatographic behavior of Zr(IV) and Hf(IV) on TRU and LN resins in mixtures of HNO<sub>3</sub> and HF. *Journal of Radioanalytical and Nuclear Chemistry* **2019**, *321* (2), 557-563. DOI: 10.1007/s10967-019-06601-x.
- (132) Satija, S.; Domnanich, K. A.; Bence, J. A.; Vyas, C. K.; Abel, E. P.; Kleinfeldt, C.; Essenmacher, S.; Kalman, M.; Walker, W.; Despotopulos, J. D.; et al. Harvesting <sup>88</sup>Zr from heavy-ion beam irradiated tungsten at the National Superconducting Cyclotron Laboratory. *Applied Radiation and Isotopes* **2023**, *197*, Article. DOI: 10.1016/j.apradiso.2023.110831 Scopus.
- (133) Kmak, K. N.; Despotopulos, J. D.; Scielzo, N. D. Development of Chemical Procedures for Isotope Harvesting: Separation of Trace Hafnium from Tungsten. *Solvent Extraction and Ion Exchange* **2022**, 1-17. DOI: 10.1080/07366299.2022.2079502.

ProQuest Number: 30686782

INFORMATION TO ALL USERS

The quality and completeness of this reproduction is dependent on the quality and completeness of the copy made available to ProQuest.



Distributed by ProQuest LLC (2023).

Copyright of the Dissertation is held by the Author unless otherwise noted.

This work may be used in accordance with the terms of the Creative Commons license or other rights statement, as indicated in the copyright statement or in the metadata associated with this work. Unless otherwise specified in the copyright statement or the metadata, all rights are reserved by the copyright holder.

This work is protected against unauthorized copying under Title 17, United States Code and other applicable copyright laws.

Microform Edition where available © ProQuest LLC. No reproduction or digitization of the Microform Edition is authorized without permission of ProQuest LLC.

ProQuest LLC  
789 East Eisenhower Parkway  
P.O. Box 1346  
Ann Arbor, MI 48106 - 1346 USA